TWO-PHASE FLOW IN THE FREEBOARD
OF A FLUIDIZED BED

by

Yeshayahou Levy B.Sc., M.Sc.
August, 1981

A thesis submitted for the degree of Doctor of
Philosophy in the University of London and for
the Diploma of Membership of the Imperial College

Mechanical Engineering Department
Imperial College of Science and Technology
London, S.W.7

ABSTRACT

Measurements of the gas-phase and particulate-phase velocities in the freeboard of a fluidized bed are reported. The measurements have been performed in order to elucidate the flow behaviour which results in real bed elutriation rates which greatly exceed those predicted by simple 'terminal velocity theories'. The measurements were obtained in a rectangular 0.3 m x 0.6 m bed with the aid of a novel application of laser Doppler anemometry and an elaborate data processing system. The bed material was sand. Results have been obtained for various particle sizes and fluidizing velocities, for both normal bed operation and for single bubble release superimposed on bed operation at the minimum fluidizing velocity. The measurements reveal many detailed features of the freeboard flow.

Large vortices, associated with each bubble burst, were detected in the freeboard. Gas velocity profiles with a <u>lower</u> velocity value in the freeboard centre-line were measured across the freeboard and they are believed to be due to the presence of the large vortices. Turbulence intensities of the gas flow were measured to be about 10 times those of fully developed turbulent duct flow. These high values were due to the air discharge from the bubbles as they burst at the bed surface and to the gas interaction with the sand particle movement in the freeboard. The sand particles were also found to have a wide velocity distribution. Their terminal velocities were greater than the fluidizing velocities and no loss of bed material was expected. The recorded mean velocities of the sand particles were usually close to zero with the fluctuating component exceeding in some cases five times the fluidizing velocity.

It is believed the information presented is of a new kind which will provoke a substantial revision of thought about the freeboard flow.

ACKNOWLEDGEMENTS

TABLE OF CONTENTS

LIST OF FIGURES

Y = 0, Z´ = 400 mm, U_f = 1.03 m/s (experiment group HA1, see Table 6.4.1-1).

6.4.4-12   Variation of dimensionless particle flux with freeboard height for d_p = 0.40 mm, X = Y = 0, U_f = 0.40 m/s (experiment group HB1, see Table 6.4.1-1).

NOMENCLATURE

A	Cross-section area
a	General constant
B	General constant
b	General constant
b_x	Weight fraction of particles size x in the bed material
C	Concentration (weight fraction) of particles
c	Speed of light
C_D	Drag coefficient
D	Diameter
D_{ph}	Pinhole diameter
d	Diameter
d_p	Particle diameter
d_{ph}	Control volume diameter as seen by the photomultiplier
$\dot{E}_x$	Elutriation rate constant of particles of size x
F	Frequency
ΔFu	Frequency interval per binary value of the sweep voltage
Fr1, Fr2	Reference frequencies
f	Focal length
G	Mass flow rate
g	Gravitational acceleration
H	Freeboard height
h	Height
I	Light intensity
I_{time}	Number of step delay cycles
J	Solid projection rate

J	Particles flux
J	Sweep voltage binary value
ΔJ	Step size increment
K	Elutriation velocity constant
L	Length
M	Mass
M	Magnification of collecting optics
m	Refractive index ratio
N_{step}	Number of steps in a sweep voltage cycle
N_e	Number of zero crossing recorded by the frequency counter
N_t	Number of clock pulses recorded by the frequency counter
n	Refractive index
Q	Volume flow rate
r, R	Radius
R_x	Elutriation rate of particles of size x
S_{tsize}	Sweep voltage step size (binary unit)
T	Time
t	Time
t_o	Delay time
ΔT	Step duration
ΔT_g	Duration of gate time pulse
ΔT_c	Duration of modified gate time pulse
Δt_o	Minimum step duration
Δt_d	Duration of a delay cycle
U	Velocity
U'	Instantaneous velocity
$\bar{U}$	Mean velocity
U_o	Interstitial gas velocity at minimum fluidization

$\overline{U}_f$	Fluidizing velocity
U_t	Terminal velocity
U_{mf}	Minimum fluidizing velocity
$U_{\perp}$	Velocity component perpendicular to the planes of the fringes
V	Signal visibility
V	Voltage
V_{init}	Initial sweep voltage binary value
ΔV	Resolution of the digital-to-analogue converter
X	Cartesian co-ordinate
X_1, X_2, X_3	Cartesian co-ordinates
Y	Cartesian co-ordinate
Z	Cartesian co-ordinate
Z	Vertical distance measured from top of distributor
Z'	Vertical distance measured from top of bed surface (static)

Greek Symbols

ϕ	Half beam incidence angle
ϕ	Sphericity or particle shape factor
η	Shape correction factor
μ	Viscosity
τ	Period
λ	Wave length
ν	Frequency
δ	Fringe spacing
θ	Angle, see Fig. 1.1.2-2

Subscripts

b	Bubble
c	Cloud
g	Gas
p	Particle
o	Initial value

NB The MKS system was used

CHAPTER 1

INTRODUCTION

1.1   Preamble

    1.1.1   Preliminary Comments

This thesis is concerned with the loss or carry over of particulate matter from the freeboard of fluidized beds. The phenomenon is commonly termed 'elutriation'. The freeboard heights required to eliminate elutriation are usually unacceptably large. Indeed, it has been found that quite large particles having 'terminal' velocities, significantly higher than the mean fluidizing velocity, are carried over. Consequently, most fluidized bed installations contain equipment to separate off and re-cycle the elutriated material. This represents additional capital investment and while the calorific value of the elutriated material may thereby be recovered, there is still unavoidable loss of sensible heat. This may be interpreted as a loss of combustion efficiency which is not insignificant when compared to a conventional PF burner for which the combustion efficiency is very high.

Previous experimental works were based on elutriation measurements for various freeboard heights and operating conditions. Samples were collected over known time intervals and weighed (see Subsection 1.2.1). These authors have generally attempted to correlate their data with semi-empirical expressions most often based on dimensional analyses. The resulting correlations lack universality and are only applicable to fluidized beds operating at conditions similar to those of the original experiment. Experiments of this kind provide little understanding about the fundamental nature of the elutriation process. The work of Horio et al (1980) (see Subsection 1.2.4), who were concerned with the behaviour of the freeboard flow, represents virtually the sole exception to this background.

1.1.2   The Present Study

More detailed studies of freeboard flow are required before the fundamental nature of the elutriation phenomenon can be understood. Only then will it be possible to explain why the quantity of elutriated material is so large and thus provide universal design criteria for engineers.

The present study was made in the pursuit of such desired fundamental knowledge. It is concerned with the details of the freeboard flow and it centres on a novel application of laser Doppler anemometry (LDA) to the freeboard region. In addition to being a non-intrusive technique, suitably developed LDA has the ability to return information about the velocities of both the solid and gas phases.

Measurements have been taken in a rectangular fluidized bed (0.3 m x 0.6 m x 2.4 m) containing (nearly) monosize sand, combustion being an unnecessary distraction at this stage. Separate development work on the LDA system has been carried out in an axisymmetrical particle-laden free jet. The freeboard flow is two-phased and time dependent thus the amount of data to be processed is unavoidably large. Because of this, a rather elaborate data processing system, based on a mini-computer, was developed. Data has been collected for normal bed operation, for different particle sizes and fluidizing velocities, and for periodic single bubble releases in bed operations at minimum fluidizing velocity.

1.1.3   Summary of Bubble Behaviour in a Fluidized Bed

A low flow rate of fluid passing through a bed of fine particles results in a uniformly distributed velocity between the particles. A hydrostatic pressure across the bed is formed and increases linearly with fluidizing velocity. A minimum velocity exists with which the associated hydrostatic pressure is sufficient

to support the weight of the bed. This is the minimum fluidizing velocity. This value is dependent only upon the particle characteristics which form the bed material. Any further increase in flow rate results in the generation of gas bubbles which transfer the excess air to the bed surface.

According to Davidson and Harrison (1963) the bubble velocity is related to the fluidizing velocity and bubble diameter by:-

$$U_b = \overline{U}_f - U_{mf} + 0.711 \sqrt{g \cdot D_b} \qquad\qquad (1.1.3-1)$$

where D_b is the bubble diameter which has been calculated to be (Darton et al, 1977):-

$$D_b^{5/4} = 0.46 \ (\overline{U}_f - U_{mf})^{1/2} \cdot Z/g^{1/4} + D_{b_o}^{5/4} \qquad\qquad (1.1.3-2)$$

where D_{b_o} is the initial bubble diameter and Z is the height above the distributor.

The above equation is said to agree quite well with most of the literature data on bubble size. For a porous plate distributor, as in the present case, the value of D_{b_o} is given by Mori and Wen (1975):-

$$D_{b_o} = 0.376 \ (\overline{U}_f - U_{mf})^2 \qquad \text{(m.k.s. units)} \qquad (1.1.3-3)$$

As the bubble rises the gas in the bubble circulates in a toroidal shape, the centre moving upwards (see Fig. 1.1.3-1). Usually, for intermediate bubble velocities (where $1 \leq 0.711 \cdot \sqrt{g \ D_b}/\overline{U}_f \leq 5$), the gas flow associated with the recirculation exceeds the bubble's geometrical boundaries and its streamlines penetrate the neighbouring dispersed phase. According to Davidson's model (see Davidson and

Harrison, 1963), which successfully accounted for the movement of both gas and solid and the pressure distribution about rising bubbles, a cloud of finite thickness is formed around the bubble through which most of the bubble's gas circulates (see again Fig. 1.1.3-1). This gas does not tend to mix with the surrounding fluid moving at U_{mf}.

The cloud diameter is given as (Davidson and Harrison, 1963):-

$$R_c^3 = R_b^3 \cdot \frac{U_{br} + 2U_0}{U_{br} - U_0} \qquad (1.1.3-4)$$

where:-

$U_0 = U_{mf}/\varepsilon_{mf}$ (the interstitial gas velocity)

ε_{mf} is the void fraction at minimum fluidization*

U_{mf} is the superficial velocity at incipient (minimum fluidization)

$$U_{br} = 0.711 \sqrt{g D_b} \qquad (1.1.3-5)$$

It seems from Equation (1.1.3-4) that the cloud thins with increasing U_{br}/U_0. The faster the bubble velocity, the thinner the cloud and, therefore, the higher the local velocities inside the bubble. According to Davidson and Harrison (1963) the velocities of the circulating fluid around a rising bubble are given by (for an observer moving with the rising bubble and for $r > R_b$):-

$$U_r = \left[\frac{R_b^3}{r^3} (U_b + 2U_0) - (U_b - U_0) \right] \cos \theta$$

$$U_\theta = \left[\frac{R_b^3}{r^3} \left(\frac{U_b}{2} + U_0 \right) + (U_b - U_0) \right] \sin \theta$$

$$(1.1.3-6)$$

---

* $\varepsilon_{mf} = 0.49$ for 0.4 mm sharp sand (Kunii and Levinspiel, 1977)

where:-

R_b is the bubble radius

and the co-ordinate system is given in Fig. 1.1.3-2.

The volume flow rate of fluid into and out of a bubble has been determined by Davidson and Harrison (1963) to be:-

$$q = 3 \ U_{mf} \ \pi \ . \ R_b^2 \tag{1.1.3-7}$$

Equations (1.1.3-6) and (1.1.3-7) imply that the maximum absolute vertical velocity at the bubble boundary ($r = R_b$, $\theta = 0$, see Fig. 1.1.3-2) is:-

$$U\hat{}_{z(max)} = U_b + \frac{3U_{mf}}{\varepsilon_{mf}} \tag{1.1.3-8}$$

and that the average upwards velocity at the bubble cross-section of maximum area is:-

$$U\hat{}_{z(ave.)} = U_b + 3U_{mf} \tag{1.1.3-9}$$

According to Davidson and Harrison it is these highest upward velocities at the bubble boundaries which prevent the roof from collapsing.

1.1.4   Model Proposal for the Bubble Bursting Phenomena

The author will now offer his own interpretation of the bubble bursting phenomena. As the bubble rises in the bed, the

thickness of the sand layer above it decreases. A stage will come where the gas cloud boundaries will reach the particles at the top of the bubble bulge and the vertical upward component of the drag force will exceed their weight. These particles will accelerate and detach themselves from the bubble bulge. The bubble bulge will subsequently thin at a faster rate, the net vertical force on the bulge will increase and the number of particles ejected will also increase.

As particles separate themselves from the bubble bulge, they disperse and their relative distance increases. Consequently, the interstitial velocity (i.e. the gas velocity between the particles) decreases and so does the drag force on the particles. One can assume that there is only a relatively short acceleration period during which particles of various sizes gain their ejection velocity.

The interstitial velocity and the terminal velocity of the various particles determine the range of particle sizes that will be ejected. Small particles, typically of which $U_t \lesssim \overline{U}_f$, will obtain a high initial velocity. Their velocity will attenuate and obtain a mean vertical velocity similar to the gas flow and eventually will be elutriated. Larger particles, typically of which $U_t > \overline{U}_f$, obtain their vertical velocity only during the acceleration period in the bursting process. During that time the interstitial velocity is greater than their terminal velocity and particles accelerate. As the acceleration period terminates, gravitation overcomes the drag force and eventually these particles will fall back to the bed.

When small bubbles emerge at the bed surface, typically above which the maximum interstitial velocity is smaller than the particle terminal velocity, no acceleration period is created and, therefore, no bursting of the bubble will be observed. The particles at the top of the bulge will only obtain the bulge rising velocity and will descend immediately after the gas within the bubble discharges.

It seems from Equations (1.1.3-1, 2) and (1.1.3-6) that for given bed particle characteristics, the acceleration period and, therefore, the bursting process depends mainly on the bubble's diameter and fluidizing velocities. One might presume, therefore, that a deeper bed and faster fluidizing velocity, both resulting in faster bubble velocities (Equations (1.1.3-1) and (1.1.3-2)), would produce a higher ejection velocity and, therefore, higher elutriation rates. This conclusion agrees with most of the literature on elutriation (see Section 1.2).

1.1.5   Statement of Objectives

The purpose of the work described in this thesis is to investigate the flowfield pattern of the two phases in the freeboard of a fluidized bed. This information is required in order to produce much needed universal elutriation correlations. Traditional measurement techniques, such as hot wires and fibre optics probes, have been found to be inappropriate for the measurements of the gas phase and sand particle instantaneous velocities.

The specific objective of the work may be stated as:-

1.   To design and build a large experimental fluidized bed with the facility of obtaining the periodic release of single bubbles.

2.   To select and develop a technique for the two-phase velocity measurements in the freeboard.

3.   To design, build and evaluate the selected LDA system with adequate traversing mechanism.

4.   To develop, build and evaluate a signal processing system
        for the steady and time dependent two-phase velocity
        measurements.

5.   To develop computer programs for the data acquisition and
        data processing.

6.   To develop, build and evaluate a technique for particle
        flux measurements in the freeboard.

7.   Using the constructed measurement system described above,
        to perform velocity measurements of both the gas flow and
        the sand particles during the periodic release of single
        bubbles and during the normal operation of the fluidized
        bed.

8.   To analyse the recorded results in order to obtain more
        detailed knowledge about the bubble bursting phenomena and
        to increase the understanding of the two-phase behaviour in
        the freeboard of normal operated fluidized beds.

1.1.6   Outline of the Thesis

This outline commences with Section 2 of Chapter 1, which
refers to previous elutriation work both experimental and theoretical.
The section proceeds with a review of previous velocity measurements
in fluidized beds.

The thesis continues in Chapter 2 with a review of the Laser
Doppler Anemometry (LDA). Following an introduction, Sections 2 and
3 of the chapter are concerned with the principles and application
of LDA. Section 4 reviews the previous two-phase flow measurements,

using a standard or a modified LDA system. The chapter terminates

by describing the application of LDA to the present study, and the

modifications required.

A preliminary experiment was conducted (Chapter 3) in

order to test the validity of the selected two-phase velocity measure-

ment technique. Measurements were performed in a particle laden

turbulent free jet and results using various sizes of sand particles

are presented.

Chapter 4 describes the fluidized bed system. Details of

the construction as well as of its accessories are given in Section 2.

Section 3 of the chapter describes the traversing table designed

to carry the optical bench for velocity measurements in the freeboard.

A description of the optical bench with details of the various components

is given in Section 4. The last section of the chapter describes all the

components associated with the periodic release of single bubbles as

applied to the study of the bubble bursting phenomenon.

The signal processing system especially designed and built

for the present investigation is described in some detail in Chapter

5. The chapter commences with a description of the signal processing

structure. Two types of Doppler frequency processors are discussed:

frequency analyser (Section 3) and frequency counter (Section 4).

The measurement of the signal pedestal amplitude in order to indicate

the particle size is discussed in the following section (4).

Recording of the time of measurement is described in the next section

(6). The recording of the time enables the measurements of time-

dependent two-phase flow, the case of which are the experiments

concerning the periodic release of single bubbles. The mini-computer

which is interfaced to the whole of the signal processing units and

which is responsible for the control of the measurements, the data

acquisition and the data analysis is given in Sections 7 and 8.

The technique to measure particle flux (i.e. the number of particles crossing a control volume per unit time) is discussed in the last section. This technique is not yet fully developed. A simple version of the technique with a description of the suggested one are presented.

Experimental results are given in Chapter 6. Measurements performed during the periodic release of single bubbles are presented in Section II. Detailed results of the gas and of the sand particle velocities are presented indicating the generation of large scale vortices associated with each bubble burst. A velocity bias effect which was encountered during the measurements and which reduces the recorded mean and r.m.s. velocity values is reported in the following section. Section IV presents measurement results of normal bed operation for various operating conditions.

The thesis concludes with Chapter 7 where the achievements and findings of the present study are summarised.

1.2   Review of Previous Elutriation Work

Elutriation, which is the process of particle carry over from the freeboard region, is an undesirable feature of fluidized bed combustion. The elutriation of fine coal particles and hot bed material reduces combustion efficiency and necessitates the use of large and expensive separation equipment. Reducing the amount of elutriated material is of great interest to the developers of commercially viable fluidized bed combustors. The amount of elutriation is determined by two principal processes:-

1.   the arrival of the bubbles at the bed surface and their eruption, and,

2.   the individual behaviour of particles in the freeboard.

These two mechanisms are not yet fully understood, and to the author's knowledge no generally accepted and universal description yet exists in the literature.

Several empirical and theoretical elutriation investigations were reported; brief literature reviews are given by Lin et al (1980) and by Kunii and Levenspiel (1977). In general the elutriation literature is of two kinds:-

(a)   where an elutriation formula is predicted by dimensional analysis based on empirical results and on general bed behaviour (Subsection 1.2.1), and,

(b)   where some kind of analysis and explanation is given about the physical processes occurring at the bed surface and in the freeboard (Subsection 1.2.2).

1.2.1   Empirically Based Elutriation Formulae

The first attempt to evaluate elutriation was made by Leva (1951). Based on his own experimental results he suggested that the elutriation, from a batch system (i.e. without recycling of the elutriated material) of a close cut of fines, from fluidized bed proceeds according to:-

$$C = C_o \exp (- 2.303 \ K \ . \ t) \qquad\qquad (1.2.1\text{-}1)$$

where:-

$C \equiv$ concentration of fines in the bed at time $T = t$

$C_0 \equiv$ initial fine concentration

$K \equiv$ elutriation velocity constant, which is mainly a
function of the gas velocity ($K \propto \overline{U}_f^4$), gas properties,
and particles characteristics

Thomas et al (1961) extended this correlation to include a correction
for an uneven fines distribution in the bed and suggested the relation:-

$$\frac{C}{1 + aC} = \frac{C_0}{1 + aC_0} \exp(-K \cdot t) \qquad (1.2.1-2)$$

where "a" is a constant dependent on the classification of particles
within the bed which is not, however, explained in detail. The
operation of a steady state bed (with fines recycled) was investigated
in detail by Lewis et al (1962) and the elutriation correlation
was suggested to be:-

$$E_x/U_f = C \exp\left[-(b_0 + BHU_f)/U_f^2\right] \qquad (1.2.1-3)$$

where:-

$E_x \equiv$ elutriation rate constant ($\equiv$ elutriation for a specific
size x)

$U_f \equiv$ fluidizing velocity

$H \equiv$ freeboard height (below TDH*)

---

*   Transport Disengaging Height is the height above which
entrainment becomes constant (maximum height of rise of
the coarse particles whose terminal velocities are greater
than the maximum local gas velocity)

$$b_o \equiv a \cdot \rho_p \cdot d_p^2$$

$a, C, B \equiv$ constants

Wen and Hashinger (1960), in a batch operated fluidized bed using glass spheres and coal powder, suggested that the elutriation rate constant (E_x) is a function of the terminal velocity U_t and of d_p, $U_f - U_t$, ρ_g, $\rho_p - \rho_g$, μ and g. They suggested the following dimensionless expression:-

$$\frac{E_x}{\rho_g (U_f - U_t)} = 1.52 \cdot 10^{-5} \cdot \left[\frac{(U_f - U_t)^2}{g d_p} \right]^{0.5} \cdot \left(\frac{d_p U_t \rho_g}{\mu} \right)^{0.725} \cdot$$

$$\cdot \left(\frac{\rho_p - \rho_g}{\rho_g} \right)^{1.15} \tag{1.2.1-4}$$

based on their data in the ranges:-

$$0.040 \text{ mm} < d_p < 0.147 \text{ mm}$$
$$0.165 \text{ Kg/m}^3 < \rho_g < 1.20 \text{ Kg/m}^3$$
$$1300 \text{ Kg/m}^3 < \rho_p < 5000 \text{ Kg/m}^3$$
$$0.221 \text{ m/sec} < U_f < 1.320 \text{ m/sec}$$

The data reported is in general agreement with the suggested formula, but there are nonetheless substantial deviations.

Merrick and Highley (1972), who used data obtained from a large square (91 cm x 91 cm) and high (4 metres) fluidized bed combustion pilot plant, suggested that for steady state bed operation, the only significant factors affecting the elutriation rate constant (E_x) of a close-size fraction are the particles' terminal velocity

U_t*, the fluidizing velocity U_f, the minimum fluidizing velocity $U_{mf}**$ of the whole bed and the gas mass flow rate G. By dimensional analysis they isolated three important groups: $\frac{AE_x}{G}$, $\frac{U_t}{U_f}$, $\frac{U_f - U_{mf}}{U_{mf}}$ with boundary condition of:-

1. E_x attains a maximum as $d_p \to 0$

2. $E_x \to 0$ as $d_p \to \infty$ or as $U_f = U_{mf}$

With the experimental data plotted on a semi-log graph they deduced the

---

*   Terminal velocity (Wen and Hashinger, 1960; Leva and Wen, 1971): the free fall terminal velocity calculated from the following expression valid in the range:-

$$2 < \frac{d_p \cdot \rho_g U_f}{\mu} < 500 \qquad \text{(typical of the present work)}$$

is:-

$$U_t = \eta \cdot \frac{0.153 \ d_p^{1.14} \ g^{0.71} \ (\rho_p - \rho_g)^{0.71}}{\mu^{0.43} \cdot \rho_g^{0.29}}$$

where η is a correction for non-spherical particles ($\eta = 1$ for sphere particles):-

$$\eta = 0.843 \ \log \left(\frac{\phi}{0.065} \right)$$

ϕ = particle shape factor (ϕ = 0.83 for rounded sand - Perry and Chilton, 1973).

**   Minimum fluidizing velocity is that at which the particulate bed changes from fixed to a fluidized state and at which pressure drop across the bed is said to become constant with the increasing fluidized velocity.

formula:-

$$E_x = \frac{130G}{A} \cdot \exp\left[- 10.4 \left(\frac{U_t}{U_f}\right)^{0.5} \cdot \left(\frac{U_{mf}}{U_f - U_{mf}}\right)^{0.25} \right] \qquad (1.2.1-5)$$

for experimental data within the range of:-

$$0.2 \leq \left(\frac{U_t}{U_f}\right)^{0.5} \cdot \left(\frac{U_{mf}}{U_f - U_{mf}}\right)^{0.25} \leq 1.3$$

Although the measured elutriation tendency was generally described by the above formula, discrepancies as large as an order of magnitude occurred.

Between all the correlations reported in the literature the one of Merrick and Highley (1972) was obtained using the most realistic (commercially usable) operating conditions such as: bed dimension, particle size range and fluidizing velocity. Their elutriation correlation (1.2.1-5) for the steady state operation is a widely used form.

1.2.2   Theoretically Based Elutriation Formulae

A theoretical approach to the elutriation phenomena was given by Zenz and Weil (1958). They presumed that particles are ejected from the bed surface at a velocity equal in magnitude to the bubble velocity as it emerges from the bed surface. The particles are initially presumed to be thrown into a uniform stream of gas at the fluidizing velocity. Each particle so ejected is acted upon by inertia, gravitation and drag forces such that: inertia force + gravitational force + drag force = 0. The interaction between particles is neglected. The motion of a spherical particle in laminar motion is

.

described by:-

$$\frac{dV}{dt} + \frac{1}{C} - (U_p - U_g) = - g \left[\frac{\rho_p - \rho_g}{\rho_p} \right]$$ (1.2.2-1)

where:-

$$C = \frac{4\rho_p \, d_p^2}{3k}$$

k is a special shape factor = 37.5 for irregular particles

The solution for a particle velocity $U_p = U_{po}$ at H = 0 is (Zenz and Weil, 1958):-

$$U_p = (C \cdot g - U_g) \, (e^{- \, t/C} - 1) + U_{po} \, e^{- \, t/C}$$ (1.2.2-2)

and the maximum height of rise for a particle is:-

$$h_{max} = C \left[U_{po} + (U_g - C \cdot g) \, \ell n \left(1 - \frac{U_{po}}{U_g - C \cdot g} \right) \right]$$ (1.2.2-3)

A further step in their work was to assume that the bed surface may be represented by a plane in which a number of nozzles are located from which gas is injected intermittently into the free board. The nozzles simulate the bursting gas bubbles at the bed surface. The relation of jet velocity variation to height, together with the correlation of the saturation carrying capacity of solids*

---

*   Saturation carrying capacity of solids is the maximum particle concentration which can be held in suspension by the flowing gas without the collapse of the solids onto the bed.

with the fluidizing velocity were used to obtain the particle entrainment rate at TDH. Andrew (1960) in his entrainment calculation below TDH assumed that the kinetic energy of the particles at the bed surface as the bubbles erupt obeys the Maxwell-Boltzman distribution and calculated that entrainment and, consequently, the loss of particles should decrease almost exponentially with the freeboard height (and exhaust pipe level). This conclusion agrees with the work of Lewis et al (1962), see Equation (1.2.1-3).

An explanation of the mechanism of particle elutriation based on the properties of the rising gas bubble is given by Leva and Wen (1971) who assumed the bed to consist of a spherical bubble phase and an emulsion phase. They also assumed that the initial particle velocity is less than the bubble velocity as it emerges at the bed surface. With these assumptions they calculated the rate of solids carried out by the bubbles' wakes. By comparing their calculated values to the elutriation data it was shown that only a fraction of a per cent of these solids are thrown up into the freeboard.

A different approach was published recently by Gugnoni and Zenz (1980). They suggested the treatment of entrainment as an equilibrium state between particle concentration in the freeboard (above TDH) and in the dense bed. An analogy is made with a multi-component liquid system held at a constant temperature above its initial boiling point. The analogy between temperature and velocity suggests that some vapour pressure related properties exist for each of the particle components in the bed as a function of velocity. The following correlation, which appears to be fairly well supported by the data, is derived:-

$$\frac{E_x}{U_f \cdot \rho_g} = \left(\frac{U_f - U_{mb}}{\sqrt{g} \cdot D_{avg}}\right)^a \qquad (1.2.2-4)$$

where:-

a $\simeq$ 3.7

U_{mb} is the minimum bubbling velocity

D_{avg} is the geometric weight mean diameter of the entrained particles

Chen and Saxena (1978) made an attempt to develop a general theory for the first stage of elutriation. They assumed that the solids projected into the freeboard are originally contained in the bulges formed by the response of the bed surface to the approaching bubbles (see Fig. 1.2.2-1) and that the surface tension of the dense bed is sufficiently small so as not to damp the bulge formation. It was further assumed that the solid projection occurs when the bubble is half-way above the bed surface and that the solids in the bulge above the air bubble are thrown up into the freeboard. The total solid projection rate (J) was calculated by multiplying the number of bubbles per unit time per unit area by the amount of solids projected from a bubble yielding:-

$$J = \left[\frac{U_f - U_{mf}}{4/3\pi \cdot R_{b_1}^3}\right] \cdot \left[2\pi \left(\frac{Rb_1 + r_1}{2}\right)^2 \cdot (r_1 - Rb_1) (1 - \varepsilon_{mf}) \cdot \rho_p\right] \qquad (1.2.2-5)$$

where Rb_1 is the bubble radius and $(r_1 - Rb_1)$ is the bulge thickness at the time when the bubble centre reaches the bed surface level. These are determined by the numerical solution of two further equations which form part of the theory.

1.2.3 Gas Velocity Field in the Freeboard of a Fluidized Bed

The trajectory of an ejected particle is influenced by two main parameters (Zenz and Weil, 1958; Do et al, 1972): its initial velocity vector and the gas velocity field which it traverses (ignoring wall effects and particle interaction).

Zenz and Weil (1958) suggested that the intermittent high velocity gas bursts originating from the bubble bursts at the bed surface impose a fluctuating and irregular time dependent velocity profile over the freeboard cross-section. They estimated that the velocity profile will become more stable with freeboard height until a constant velocity profile is achieved. An analogy to pulsating free jets was made and velocity gradient dissipation similar to that of jets is assumed enabling the calculation of the level at which the steady velocity profile is attained.

A relation between gas velocity and freeboard height is given (Zenz and Weil, 1958):-

$$\frac{U_z - U_f}{U_o} = \frac{k \cdot f(D_b)}{Z} \qquad (1.2.3-1)$$

where:-

U_z is the centre-line vertical gas velocity at a level Z above the bed

U_o is the initial gas velocity when issuing from the jet orifice

k is a constant

$f(D_b)$ is an arbitrary function of the bubble diameter

Zenz and Weil (1958) assumed that entrainment will obtain a constant value at the level where velocity profile across the freeboard will remain unchanged. For that level (the TDH) they assumed a uniform (flat) velocity profile with mean value equal to the fluidizing velocity.

Wen and Hashinger (1960) assumed the gas flow field in the freeboard to behave as pipe flow, becoming a fully developed flow at a certain height, defined as the TDH (see Fig. 1.2.3-1). A maximum velocity of 1.2 to 2.0 times the fluidizing velocity is said to exist at the centre-line of the freeboard. No information is given about how to calculate the level at which the profile becomes fully developed.

Both works (Zenz and Weil, 1958 and Wen and Hashinger, 1960) assumed that entrainment remains constant when velocity distribution becomes constant. This implies that the level at which the velocity profile remains constant has to be higher than the maximum height particles attain from their ejection velocity. Neither paper provides any experimental result to confirm their assumption about the gas flow behaviour, although measured particle velocity distribution reported by Horio et al (1980) tends to confirm the velocity profile as suggested by Wen and Hashinger.

1.2.4   Two-Phase Flow Velocity Measurements in a Fluidized Bed - Literature Review

Velocity measurements in a fluidized bed subdivide naturally into: (1) measurements in the dense bed, and (2) measurements in the freeboard. Each requires different techniques and instrumentation. As this work primarily concerns the elutriation in a fluidized bed, the main emphasis will be on measurements in the freeboard.

(1)   Two-Phase Flow Velocity Measurement in the Dense Bed

The main technique which has been employed to measure particle velocity distributions in the dense phase of a fluidized bed is the fibre optic probe. Ohki and Shirai (1976) describe the operating principle of the probe. The middle fibre of three is used to illuminate the individual particles and the two others to collect the reflected light. Photo-detectors convert the collected light into electric signals which are processed to give the cross-correlation function. The time lag distribution of the signals derived from the cross-correlation and the distance between the two outer fibres determines the velocity distribution of the particles. Ishida et al (1980) used a modified fibre probe consisting of a central illuminated fibre surrounded by six equally spaced collecting fibres.

A modified signal processing system for the same technique, allowing the instantaneous velocity to be measured, is described by Ogawa et al (1978). An alternative technique based on thermal impulse response of fine thermocouple has been employed by Yamazaki and Kato (1980). These arrangements permit the velocities of the particles as well as their directions to be detected in a two-dimensional domain. To the author's knowledge there has not been any work published on measurements of the instantaneous local gas velocities in the dense bed.

(2)   Two-Phase Flow Velocity Measurement in the Freeboard
        of a Fluidized Bed

Most of the measurements in the freeboard are concerned with elutriation. The elutriation rate of solid particles (E) can be defined as the average mass flow rate of the solid phase through the exhaust pipe of the fluidized bed. Elutriation measurements are mainly performed by analysing the particles collected at the exit of the freeboard by an air-particle separating device. The technique is

an integral one, the instantaneous local behaviour of the two-phase

flow in the freeboard remains unknown. Data has been reported* on

the amount and size distribution of the collected particles in

relation to various bed geometries and operating conditions for

either batch operation or in steady state with fines recycling. The

outcome of these works was described previously in Subsection 1.2.1.

Particles velocities measurements in the freeboard have

been reported by Do et al (1972). The particle trajectories as

ejected from a single bubble burst was calculated using the following

particle momentum balance equation and then compared with the

measurements:-

$$\frac{d\vec{U}_p}{dt} = -\frac{3}{4} \frac{C_D \, \rho_g \, (\vec{U}_p - \vec{U}_g) \cdot |(\vec{U}_p - \vec{U}_g)|}{\rho_p \, d_p} - \frac{(\rho_p - \rho_g) \, \vec{g}}{\rho_p} \qquad (1.2.4\text{-}1)$$

with the initial condition of $U_p = U_{p_0}$ at $H = 0$, $t = 0$:-

U_p = the vertical component of the particle velocity

U_g = the vertical component of the gas velocity

The solution of Equation (1.2.4-1) requires the value U_{p_0} which was

obtained from the measurements. The velocity measurements were

carried out in a two-dimensional bed (1 cm x 56 cm x 245 cm) with

perspex walls. The bed material consisted of glass beads of 177 to

250 μm size range and the fluidizing velocity was 5.4 cm/sec. A

single bubble was injected near the bottom of the bed via a solenoid

---

*   See for example work by Fournol et al (1973), Merrick and
Highley (1972) and Zenz and Weil (1958).

valve. The measurements themselves were performed using a fast movie camera and a subsequent frame-by-frame analysis of the film. Only one initial particle velocity, 0.95 m/s, at the top of the advancing bubble bulge is reported. The measurements and predictions agree quite well for upward moving particles but for falling ones, the discrepancies are significant. The deviation in the descending part is probably partially due to the assumption of a uniform upward gas velocity (U_f) whereas the real gas velocity is fluctuating.

Gas velocity measurements in the freeboard using the hot-wire technique are reported by Fournol et al (1973). They recorded a flat profile of the vertical velocity across the freeboard. Recently hot-wire measurements as well as solid particle velocity measurements using a fibre optic probe have been reported by Horio et al (1980). Measurements are reported at various freeboard heights for different particle sizes. Their measurements indicated an increase in r.m.s. velocity with fluidizing velocity and bed height and a decrease with particle size. Turbulent intensity values of 20% to 40% were recorded at a height of 0.4 m above the bed level decreasing to 5% to 10% at a height of 2 m. Particle mean velocities higher than the fluidizing velocity were measured in the central area of the bed whereas descending particle motion was measured near the wall. Fluctuating components of particle velocities are not reported.

Serious problems must be expected to arise while using the hot-wire technique for velocity measurements in the freeboard. The difficulties occur mainly for two reasons:-

1.   The presence of solid particles in the flow. Each time a
        particle impinges upon the wire a different heat transfer
        mechanism is obtained affecting the output signal and

thus the accuracy of the results. Mechanical failure of
the wire due to particle collision necessitate the use of
thicker and, therefore, less sensitive wire, or limits the
region of measurement to high freeboard levels where
particles are present in much lower concentration.

2.   Low gas velocity with a relatively high fluctuating component.
The disturbance to the flow by the probe is greater at low
velocity as a result of the buoyance imposed by the heated
wire. Insensitivity to velocity direction (while using a
single wire) usually limits the use of the technique to flow
of turbulence intensity ($\sqrt{\overline{U'^2}}/\overline{U}$) of less than about 40%.
Measurement in regions with higher turbulence intensity will
record erroneous results of lower r.m.s. and higher mean
velocity values.

The mechanical probe technique for particle velocity measure-
ments (as for the fibre optics probe) suffer the disadvantage of
introducing disturbance to the flow. This is especially significant
in flows where small particles (typical of which $U_t \lesssim U_f$) are presented.
Mechanical probes are sensitive only to flow in a certain direction.
The probe will record a correct value only when aligned with the flow.
Measurements of particles velocities in the freeboard of a fluidized
bed, the movement of which is three-dimensional, will, therefore,
suffer a distinct lack of accuracy. The error will depend on the
ratio of the number of particles moving at any direction to the number
of particles moving in the measured direction.

1.2.5   Concluding Remarks

The estimation of elutriation is clearly a difficult problem.

The existing literature contains various and different correlations. At best the following comments may be offered:-

1. For a batch operated fluidized bed, the concentration of fine particles in the dense bed decays exponentially with time.

2. For a specific steady state operated bed, with freeboard height lower than the TDH, the elutriation rate for a specific particle size group (E_x) decays exponentially with bed height.

3. A variety of experimentally and theoretically based correlations for elutriation above TDH as a function of some operating parameter occur in the literature. None of these appears to offer any degree of universality and order of magnitude discrepancies are typical.

4. It seems that none of the previous elutriation studies provided definite information about the particle ejection velocity at the bed surface or about the gas flow field in the freeboard. In the absence of both types of information the physics of the freeboard flow is open to excessive confusion. Fast movie cameras, hot-wires and fibre optic probes have so far proved unable to supply comprehensive information about the two-phase velocity field in the free-board.

CHAPTER 2

SINGLE AND TWO-PHASE FLOW MEASUREMENTS
USING LASER DOPPLER ANEMOMETRY

2.1   Introduction

Only two techniques for freeboard velocity measurements appear in the literature. Do et al (1972) used a fast movie camera to record the initial velocity of the sand particles in the freeboard, and Horio et al (1980) used a hot-wire for the gas velocity measurements and a fibre optics probe for the particle velocities. These works are discussed in detail in Subsection 2.3.2. A potentially very powerful technique for local two-phase flow velocity measurements in the freeboard is Laser Doppler Anemometry (LDA).

The advantages of LDA may be summarised as follows: a high degree of accuracy, no flow disturbance, and sensitivity to velocity direction. Both gas and particle velocities may be determined, and particle size in addition to its velocity can also be estimated. The complexity of the necessary signal processing, and the inability to measure beyond an opaque obstacle, represent the main disadvantages of LDA.

In this chapter both the principles and the properties of LDA are discussed. Fairly comprehensive knowledge is required in order to understand the technique sufficiently well for the present purposes. This chapter attempts to provide some of the knowledge required. Section 2.2 explains the relation of Doppler frequency and velocity, while the spatial resolution of the control volume is discussed in Section 2.3. Section 2.4 reviews the previous two-phase flow literature and demonstrates that none of the existing LDA techniques is applicable to the present case. The selection of a suitable

technique and its description are outlined in the last section (2.5).

2.2   The Laser Doppler Anemometer: Principle of Operation

The laser Doppler anemometer is a linear velocity transducer device. It is based on the principle that light impinging on and scattered by a moving particle has a frequency shift related to its velocity vector. In order to apply the technique to velocity measurements and to interpret the data correctly it is important to understand the principle of this phenomenon. The subject has been discussed by many writers, Durst et al (1976) for example, and only a brief review is necessary here.

2.2.1   The Doppler Effect

1.   Stationary Wave Source

The wave frequency received by a moving observer at a velocity $\{U\}_i$ transmitted from a stationary wave source of frequency ν_0 is:-

$$\nu = \nu_0 \left(1 - \frac{1}{c} \{U\}_i \cdot \{\ell\}_i \right) \tag{2.2.1-1}$$

where $\{\ell\}_i$ is a unit vector in the direction from the source to the observer and c is the speed of light.

2.   Moving Wave Source

The wave frequency received by a stationary observer transmitted from a wave source of frequency ν_0 moving at a velocity $\{U\}_i$ is:-

$$\nu = \nu_0 \ \frac{1}{1 - \frac{1}{c} \{U\}_i \cdot \{\ell\}_i} \qquad\qquad (2.2.1\text{-}2)$$

where $\{\ell\}_i$ is a unit vector in the direction from the moving source to the stationary observer.

2.2.2   Velocity Measurement Using Doppler Effect

A system of two stationary sources of coherent and mono-chromatic beams which are crossed in space and a stationary receiver form the basis for the velocity measurements (see Fig. 2.2.2-1a). When a small particle moving at a velocity $\{U\}_i$ passes through the intersection of the beams, then the frequency received by the particle from source A is:-

$$\nu_{P_A} = \nu_0 \left(1 - \frac{1}{c} \{U\}_i \cdot \{k\}_i \right) \qquad\qquad (2.2.2\text{-}1)$$

while the frequency received by the particle from source B is:-

$$\nu_{P_B} = \nu_0 \left(1 - \frac{1}{c} \{U\}_i \cdot \{m\}_i \right) \qquad\qquad (2.2.2\text{-}2)$$

where $\{U\}_i$ is the velocity of the particle, ν_0 is the source frequency and $\{k\}_i$ and $\{m\}_i$ are unit vectors as shown in Fig. 2.2.2-1a. As the particle receives these frequencies it simultaneously transmits them at the same frequencies. A stationary observer at a point O will detect two frequencies ν_{d_A} and ν_{d_B} transmitted from the moving particle:-

$$\nu_{d_A} = \nu_{p_A} \cdot \frac{1}{1 - \frac{1}{c}\{U\}_i \{\ell\}_i} = \frac{\nu_0 \left(1 - \frac{1}{c}\{U\}_i \cdot \{k\}_i\right)}{1 - \frac{1}{c}\{U\}_i \cdot \{\ell\}_i}$$

$$\nu_{d_B} = \nu_{p_B} \frac{1}{1 - \frac{1}{c}\{U\}_i \cdot \{\ell\}_i} = \frac{\nu_0 \left(1 - \frac{1}{c}\{U\}_i \cdot \{m\}_i\right)}{1 - \frac{1}{c}\{U\}_i \cdot \{\ell\}_i}$$

(2.2.2-3)

where ν_{p_A} and ν_{p_B} are derived from Equations (2.2.2-1) and (2.2.2-2). The two frequencies are superimposed and detected together at the point 0.

In general, laser light is used as the beam source and a photo-detector is placed as the stationary observer at point 0. The superposition of the detected frequencies, ν_{d_A} and ν_{d_B}, in the photo-detector creates several frequency combinations, of which only the frequency difference $(\nu_{d_B} - \nu_{d_A})$ is within the response range of available photo-detectors*. The frequency difference is:-

$$\nu_{d_B} - \nu_{d_A} = \nu_D = \frac{\nu_0 \cdot \frac{1}{c}\left(\{U\}_i \cdot \{k\}_i - \{U\}_i \{m\}_i\right)}{1 - \frac{1}{c}\{U\}_i \cdot \{\ell\}_i}$$

(2.2.2-4)

Since in all practical applications U << c, we have:-

$$\nu_D = \frac{\nu_0}{c} \cdot \{U\}_i \cdot \left(\{k\}_i - \{m\}_i\right) = \frac{1}{\lambda} \cdot \{U\}_i \cdot \left(\{k\}_i - \{m\}_i\right)$$

(2.2.2-5)

where λ is the laser beam wavelength.

Equation (2.2.2-5) shows that the LDA system is a linear

---

*   The frequency of a HeNe laser light and, therefore, nearly of ν_{d_A} and ν_{d_B} is $4.7 \cdot 10^{14}$ Hz and a typical photo-detector frequency response is $\sim 10^8$ Hz.

velocity transducer with the constant of proportionality depending only on the wavelength of the laser beams and on the geometry of the two incident beams.

2.2.3   Measurements in Bi-Directional Flow Field

For velocity measurements where the flow is bi-directional, which in the present context means one having finite negative as well as positive velocity components, as for example in the freeboard of a fluidized bed, a frequency shift technique has to be applied in order to detect the magnitude as well as the direction of the flow. A constant frequency difference between the two incident beams is usually generated by a rotating grating or an acousto-optic cell which is placed in the way of one of the beams, see for example Durst et al (1976).

Let the frequency of one beam be v_0 and the second beam $v_0 + \Delta v$, where Δv is the frequency difference between the two beams, the "frequency shift". A stationary observer at a point 0 (Fig. 2.2.2-1a) will detect two frequencies v_{d_A} and v_{d_B} transmitted from the moving particle:-

$$v_{d_A} = \frac{v_0 \left(1 - \frac{1}{c} \{U\}_i \cdot \{k\}_i\right)}{1 - \frac{1}{c} \{U\}_i \{\ell\}_i}$$

$$v_{d_B} = \frac{(v_0 + \Delta v) \cdot \left(1 - \frac{1}{c} \{U\}_i \cdot \{m\}_i\right)}{1 - \frac{1}{c} \{U\}_i \{\ell\}_i}$$

(2.2.3-1)

where v_{d_A} and v_{d_B} are derived as in Equations (2.2.2-3).

The frequency difference $(v_{d_B} - v_{d_A})$ detected by the photo-detector is:-

$$\nu_{d_B} - \nu_{d_A} = \frac{\Delta\nu \left(1 - \frac{\{U\}_i \{m\}_i}{c}\right) + \nu_1 \frac{\{U\}_i}{c} \left(\{k\}_i - \{m\}_i\right)}{1 - \frac{1}{c} \{U\}_i \{\ell\}_i}$$

and since $U \ll c$:-

$$\nu_D = \nu_{d_B} - \nu_{d_A} = \Delta\nu + \frac{1}{\lambda} \cdot \{U\}_i \left(\{k\}_i - \{m\}_i\right) \qquad (2.2.3\text{-}2)$$

The selection of $\Delta\nu$ is such as to create a positive value for ν_D under all circumstances.

2.2.4 Evaluation of Laser Doppler Velocity Measurements

It was shown in Equation (2.2.2-5) that the LDA system is a linear velocity transducer. In order that the velocity measurements may be evaluated, the equation will be analysed in detail.

Equation (2.2.2-5) is written as:-

$$\nu_D = \frac{1}{\lambda} \{U\}_i \cdot \{n\}_i \qquad (2.2.4\text{-}1)$$

where $\{n\}_i$ is a vector in the direction perpendicular to the bisector of the two incident beams (see Fig. 2.2.2-1b) expressed as:-

$$\{n\}_i = 2 \sin \phi \cdot \{\cos a_1, \cos a_2, \cos a_3\} \qquad (2.2.4\text{-}2)$$

where ϕ is the half angle between the beams and a_1, a_2, a_3 are the angles which the vector $\{n\}_i$ forms with the co-ordinates x_1, x_2, and x_3 respectively.

When a particle passes through the point of intersection of the beams at a velocity $\{U\}_i = \{U_1, U_2, U_3\}$ it will scatter (transmit)

light. The frequency of the light scattered from the particle as detected by the photo-detector will now be derived (starting from Equation 2.2.2-5):-

$$\nu_D = \frac{1}{\lambda} \cdot 2 \sin \phi \cdot \{U_1, U_2, U_3\} \cdot \{\cos a_1, \cos a_2, \cos a_3\} \qquad (2.2.4\text{-}3)$$

or:-

$$\nu_D = \frac{1}{\lambda} \cdot 2 \sin \phi \cdot \left(U_1 \cdot \cos a_1 + U_2 \cdot \cos a_2 + U_3 \cos a_3 \right) \qquad (2.2.4\text{-}4)$$

A more common form of Equation (2.2.4-4) is:-

$$\nu_D = \frac{2 \sin \phi}{\lambda} \cdot U_\perp \qquad (2.2.4\text{-}5)$$

where $U_\perp$ is the instantaneous velocity component in the plane of the two beams and perpendicular to the bisector of the beams.

It must be noted at this stage that as it stands the system cannot distinguish between velocities of opposite sign. To solve this directional ambiguity, frequency shift technique is employed.

2.3   Control Volume and the Fringe Model

As mentioned in Subsection 2.2.2, two coherent and mono-chromatic laser beams are used as wave sources for laser Doppler anemometry systems (see Fig. 2.3-1). The two beams originate from a single laser whose beam is split into two beams of equal intensity. The beams are focussed by a positive lens and intersect at the lens focal plane. A laser beam has a Gaussian intensity distribution. The volume formed by the crossing of the two beams, the "Control Volume", is of finite size. A particle passing through

any part of the control volume will transmit light at frequencies as discussed in Subsection 2.2.2. The intensity will vary with its location within the control volume.

An interference pattern is formed when two coherent and monochromatic light waves intersect, see for example Born and Wolf (1975) and Durst et al (1976). Fringes are created in the control volume in planes perpendicular to the plane of the two beams and parallel to the bisector of the beams (plane $\hat{X}$ - $\hat{Z}$ in Fig. 2.3-1). The distance between two sequential fringes is (Durst et al, 1976):-

$$\delta = \frac{\lambda}{2 \sin \phi}$$ (2.3-1)

This fact leads to an additional, more illustrative and simpler way of explaining the laser Doppler anemometry principle. A small particle passing through the control volume will scatter light according to the light intensity of the fringes. If the particle has a velocity component $U_{\perp}$ in the direction perpendicular to the plane of the fringes, the intensity of the transmitted light will fluctuate at a rate of:-

$$f = \frac{U_{\perp}}{\delta} = \frac{U_{\perp} \cdot 2 \sin \phi}{\lambda}$$ (2.3-2)

This formula is the same as Equation (2.2.4-5); this derivation is usually referred to as the fringe model of LDA.

The properties of the focussed laser beam (see following section) affect the shape and the overall dimension of the control volume. The variation of light intensity inside the control volume (see Subsection 2.3.2) determines the characteristics of the light scattered by particles of various size crossing through it.

2.3.1   Laser Beam - Properties of a Focussed Gaussian Beam

Lasers of moderate power, as used in LDA measurements, operate in the fundamental TEMoo* mode. The beam of such a laser diverges and has a Gaussian intensity distribution about its axis. The characteristics of a Gaussian beam focussed by lenses were investigated by Kogelnik (1965). Fig. 2.3.1-1a shows a Gaussian beam having a waist diameter d_0, defined as the diameter at which the intensity decreases to $1/e^2$ of its maximum value, and with a wave front curvature R(z). At the waist the wave front of the beam is flat. With increasing distance from the waist the beam diverges. The beam diameter of $1/e^2$ intensity level at any axial distance (z) from the waist is:-

$$d^2 (z) = d_0^2 \cdot \left[1 + \left(\frac{4\lambda z}{\pi d_0^2} \right)^2 \right] \qquad (2.3.1-1)$$

The wave front radius of curvature is:-

$$R(z) = z \cdot \left[1 + \left(\frac{\pi d_0^2}{4\lambda z} \right)^2 \right] \qquad (2.3.1-2)$$

And the angle of divergence is:-

$$\Theta = \frac{2\lambda}{\pi d_0} \qquad (2.3.1-3)$$

The size and location of the beam waist depends on the specific mirror geometry of the laser resonator (Bloom, 1963). In our case (5 mw HeNe Spectra Physics Model 120) the beam waist is 0.5 mm in diameter at the front side of the back mirror.

---

*   Transverse Electric and Magnetic mode.

The distance of an imaged waist from a lens (Kogelnik, 1965; see Fig. 2.3.1-1b) is:-

$$Z_1 = f + \frac{(Z_0 - f) \cdot f^2}{(Z_0 - f)^2 + \left(\frac{\pi d_0^2}{4\lambda}\right)^2}$$

(2.3.1-4)

The imaged waist diameter (at $1/e^2$ intensity level) is:-

$$d_1 = \frac{d_0 f}{\left[(Z_0 - f)^2 + \left(\frac{\pi d_0^2}{4\lambda}\right)^2\right]^{1/2}}$$

(2.3.1-5)

where d_0 is the original beam waist diameter at a distance of Z_0 from a lens of focal length f.

The imaged beam waist will be located at the lens focal plane ($Z_1 = f$) if the original waist is at the other focal plane ($Z_0 = f$), or according to Dickson (1970), if the beam at the lens is collimated ($R(z) = \infty$, that is a plane wave front). The waist diameter will be:-

$$d_1 = \frac{4\lambda f}{\pi d_0}$$

(2.3.1-6)

For most of the laser Doppler anemometry system, the laser beam can be considered as a beam with a plane wave front*. For a collimated Gaussian beam, the radial intensity distribution is:-

---

*   The effect of non-parellelism is discussed by Abbiss
        (1974) and Durst and Stevenson (1979).

$$I(r) = I_0 \cdot e^{- 8r^2/d_2^2} \tag{2.3.1-7}$$

where I_0 is the maximum intensity of the beam and d_2 is the diameter where the intensity level is $1/e^2$.

2.3.2   The Control Volume Characteristics

When two collimated coherent Gaussian laser beams intersect in space the light intensity distribution inside the control volume is (Brayton, 1974; Farmer, 1976):-

$$I_{(x,y,z)} = 2 \ I_0 \ \exp \left[- 4 \left[x^2 + y^2 \cos^2 (\phi) + z^2 \sin^2 (\phi) \right]/d_1^2 \right] \cdot$$

$$\cdot \left[\cosh \left[4yz \cdot \sin (2\phi)/d_1^2 \right] + \cos \left(\frac{4\pi}{\lambda} \cdot \sin (\phi) \cdot y \right) \right] \tag{2.3.2-1}$$

The control volume shape is defined as the space in which the light intensity modulation is larger than $1/e^2$ of the centre point value ($x = y = z = 0$) and is described by the formula:-

$$\frac{4x^2}{d_1^2} + \frac{4y^2 \cdot \cos^2 (\phi)}{d_1^2} + \frac{4z^2 \cdot \sin^2 (\phi)}{d_1^2} = 1 \tag{2.3.2-2}$$

which is an ellipsoid whose axes are:-

$$
\left.
\begin{aligned}
X_1 &= d_1/2 \\
Y_1 &= d_1/2 \cos (\phi) \\
Z_1 &= d_1/2 \sin (\phi)
\end{aligned}
\right\} \tag{2.3.2-3}
$$

The co-ordinates x, y and z are as shown in Fig. 2.3-1, and d_1 is

derived from Equation (2.3.1-6).

2.3.3   The Collecting Optics

The dimensions of the detected control volume are also dependent on the geometry of the collecting optics which collect and transmit scattered light to the photo-detector. The collecting optics consist of a collecting lens L_2 (Fig. 2.3.3-1) and a pinhole (same figure) located in front of the photo-detector. The diameter of the lens L_2 affects the quality of the detected signal, the greater the lens diameter the greater the solid angle of detection and the stronger the signal intensity. A lens diameter of 50 mm - 100 mm is commonly used. The magnification M (see Equation 2.3.3-1) of the collecting optics, along with the pinhole diameter, determines the portion of the control volume which is viewed by the photo-detector. Exclusion of the outer part of the control volume, where the light intensity is low, improves the signal quality significantly.

The magnification M is:-

$$M = \frac{X_2}{X_1} \qquad\qquad (2.3.3-1)$$

where X_1 and X_2 are distances as shown in Fig. 2.3.3-1. The relation between X_1, X_2 and the focal length f of the lens is:-

$$\frac{1}{f} = \frac{1}{X_1} + \frac{1}{X_2} \qquad\qquad (2.3.3-2)$$

Consider a pinhole diameter D_{ph} and magnification M. The diameter of the control volume as seen by the photo-detector is:-

$$d_{ph} = \frac{D_{ph}}{M} \qquad\qquad (2.3.3\text{-}3)$$

So the number of fringes viewed is:-

$$N_{fr} = \frac{d_{ph}}{\delta} = \frac{D_{ph}}{M} \cdot \frac{2 \sin \phi}{\lambda} \qquad\qquad (2.3.3\text{-}4)$$

where δ is the fringe spacing as given by Equation (2.3-1).

A value of M of 1 to 3 is generally accepted. Smaller values result in very small control volume images requiring very small pinhole diameters and these in turn create severe alignment problems. Large values of M distort the image and usually necessitate unacceptably long distances between the photo-detector and the control volume.

2.4   Two-Phase Flow Measurements Using LDA

2.4.1   Single and Two-Phase Flow - Definition and Classification

Two-phase flow may be considered the case where two phases (gas, liquid, solids) are moving in a common space at the same time. In two-phase flow measurement using the LDA technique, where each velocity field has to be measured separately, two different types of scattering particles are usually presented: small particles which follow the flow and represent the continuous phase and bigger ones which form the dispersed phase. A spray of droplets with a wide range of size distribution is a flow situation in which it is difficult to distinguish between the two phases. The very small droplets will follow the flow; the bigger ones will have different flow patterns. Each size group should, therefore, be analysed separately, the smallest representing the continuous phase.

In single phase flow particles are usually introduced
artificially to mark the fluid. Two major factors determine the
characteristics required for such particles:-

1.   The particles should follow the instantaneous fluctuation

of the flow within an acceptable tolerance thereby

precisely representing the motion of the fluid, see for

example Durst et al (1976), Chapter 10.

2.   The light scattered from the particles must be of sufficient

intensity and quality to generate a processable signal at

the photo-detector. Durst (1973) suggested an optimal

particle diameter of $d_p = \frac{\lambda}{8 \cdot \sin \phi}$ (see Fig. 2.3-1).

The effect of these particles on the flow structure is generally negligible,
although concentration gradients tend to have some biasing effect on
the resulting measurements (Baker, 1974).

In two-phase flows the particles of the dispersed phase
could be spherical or irregular solid particles, liquid droplets or
gas bubbles. The continuous phase is measured, as in the single phase
flow, by small particles following the flow.

LDA measurements in two-phase flows require the extension
of the basic experimental arrangement. The signal processing system
and sometimes the optics have to be modified. Two main techniques
are applied and they depend on the flow configuration and nature of
the phases:-

1.   Where the velocities of the two phases are of significantly

different magnitude, one can separate the recorded velocity

histograms into two ranges and calculate mean and r.m.s. values for each phase. The same result can be achieved by electronic filtering of the Doppler signals, for example see Rajami and Langer (1972) and Durst (1978).

2.   For general flow situations, the velocities of the two phases with additional information about particle sizes are recorded. Instantaneous phase classification, or optional data recording for analysis at a later state, are possible.

The first technique is generally easier to perform but is less likely to be used since such flow situations are rarely of interest. Most of the work reported in the literature relates to the second category and only those will be reviewed here.

Various techniques are applied in order to evaluate the size as well as the velocity of the particles. Some extract all the information from the photo-detector signal, others require the extension of the optical system for measuring the particle size. The size measuring technique could be divided for convenience into three different particle size ranges:-

(a) $0.1 \ \mu m \lesssim d_p \lesssim 10 \ \mu m$;

(b) $5 \ \mu m \lesssim d_p \lesssim 100 \ \mu m$;

(c)   where d_p is of the order of, or bigger than, the diameter of the beam at the control volume ($100 \ \mu m \lesssim d_p$).

2.4.2   <u>Particle Sizing - Low Range ($0.1 \ \mu m \lesssim d_p \lesssim 10 \ \mu m$)</u>

Small particle sizing, of an order or two of the wave length of the laser beam, is usually based on the Mie theory of light

scattering. The parameter that most affects the intensity of the light scattered from the particles is the particle size. Other parameters are particle shape and refractive index, incident beams and detection geometry, wave lengths and polarization. The book of Durst et al (1976) gives a summary of the general solution of the Mie theory. More details are given by van de Hulst (1957) and Kerker (1969). With a fixed optical setting and particle category, the light intensity collected at the photo-detector varies with particle diameter as (Durst and Umhauer, 1975): $I_{scattered} \propto F(d_p^n)$ where $2 \leq n \leq 6$ and the lower values are appropriate to the larger particles.

Measurements of the ratio of intensity of the light collected at two different angles, or measurements of the absolute light intensity collected from a single position, although very sensitive, can provide the particle size.

Durst and Umhauer (1975) describe a combined system which marks possible simultaneous measurements of velocity and size of individual particles. The optical system consists of two independent units:-

1.   an LDA system for the velocity measurements;

2.   a particle sizing unit based upon light scattered from the particle but originating from a different (white light) source.

The use of white light improves the monotony of the signal amplitude-to-particle size response curve. Measurements of particle size in the order of 0.3 μm to 10 μm are reported.

Bachalo and Hess (1980) describe a system comprising two

units for the measurement of particles in the range of 0.1 μm to 25 μm.
The lower range (0.1 μm to ∿ 5 μm) is analysed by the intensity ratio
measuring technique.

The former technique, Durst and Umhauer (1975) described
above, has the advantage of a smaller (shorter) control volume and of
a better monotonic response curve. The latter described technique,
Bachalo and Hess (1980), as a combined system with the visibility
technique (to be discussed later) has the advantage of a wider
dynamic range. Measurements using the absolute pedestal amplitude
technique to determine the particle size were discussed by Graham and
Gouesbert (1979). They present a calculation method by which a one-
to-one relation can be obtained for absorbing and non-absorbing
particles for the range of submicron particles up to 30 μm. However,
no experimental result is given to compare with their prediction.

2.4.3   Particle Sizing - Intermediate Range (5 μm $\leq d_p \leq$ 100 μm)

Two main techniques were used: visibility and signal amplitude.

The Visibility Technique

Initial work by Farmer (1972) suggested that there is a
close relation between particle geometry and the visibility of the
signal collected at the photo-detector from a particle crossing the
control volume. The visibility of a signal is defined as (see Fig.
2.4.3-1):-

$$\overline{V} = \frac{I_{maximum} - I_{minimum}}{I_{maximum} + I_{minimum}} \quad \bigg| \quad \text{when signal amplitude is at the maximum} \qquad (2.4.3-1)$$

According to his calculation, the visibility for a spherical particle
is:-

$$\bar{V} \simeq \frac{2J_1 \ (2\pi d_p/\delta)}{(2\pi d_p/\delta)} \qquad\qquad (2.4.3\text{-}2)$$

where J_1 (x) is the first order bessel function. As it is not practical to measure a negative value for visibility, only absolute values are considered (see Fig. 2.4.3-2). Farmer concluded that the visibility response curve depends mainly on particle shape. This technique can be applied with forward or backward collection and its effective range for particle sizing is $0.2 \lesssim V \lesssim 0.9$. The lower limit is necessary to avoid ambiguity (see Fig. 2.4.3-2), the upper limit is dictated by the SNR (Signal-to-Noise Ratio) of signal from the small particles. When more than one particle is present in the control volume at the same time, visibility is attenuated by the square root of the number of particles. Adrian and Orloff (1977) further investigated the phenomenon and concluded that visibility also depends on the refractive index ratio m = n_p/n, the direction and magnitude of the solid angle of collection (Ω), and the dimensionless particle diameter, d_p/λ. Adrian and Orloff (1977), and at the same time Chu and Robinson (1977), found that visibility measurements in the backscatter mode are not entirely practical. The two main reasons are:-

1.   The response curve of visibility to d_p/δ was predicted to be dependent upon the absolute particle size (d_p).

2.   It had a much smaller region ($0.7 \lesssim V \lesssim 1.0$) of unambiguity.

Bachalo (1978) calculated the effect on the visibility curve of the beams stops at the collecting optics. He suggested the selection of some optical dimensions as a bypass technique. Later on, Bachalo (1980) analysed visibility as detected at an off-axis angle. The

advantages of this lay in the elimination of the beam stop effect, a higher dynamic range for particle sizing, and smaller effective control volume dimensions. The bigger the off-axis angle, the higher the visibility for a specific size and the higher the corresponding dynamic range. A detailed mathematical expression for the visibility function is given for non-absorbing spherical particles. Brayton (1974) emphasized the importance of fringe visibility in the control volume. Fringe visibility is the initial condition for measurement and prediction of signal visibility. Brayton calculates the fringe visibility for various unequal incident beam conditions. To conclude, it might be said that the technique is suitable for measuring particle sizes in the intermediate range. Initial calibration or prediction is necessary, but then predictions are well-established for simple geometrical non-absorbing particles; they are much more difficult for irregular absorbing ones.

Particle Sizing Using Signal Amplitude

The technique implies a monotonic one-to-one relation between absolute signal amplitude and particle size. Although the response curve can be predicted, calibration is mostly more convenient. For prediction purposes, two additional factors (as for the visibility technique) must be known: laser power and the sensitivity of the photomultiplier.

Holve and Self (1979) analysed particle size by direct amplitude detection and although a single beam was used, their technique is in principle applicable to an LDA system. Their theoretical analysis demonstrated that if the flux of light scattered from a particle is collected coaxially by a lens, the signal will vary monotonically with size regardless of the refractive index of the

particle. Small off-axis detection angles eliminate light collection from the unscattered beam. A large collecting lens and the use of white light tends to attenuate the resonant structure of the Mie scattering response curve. For this reason Durst (1976) also used white light. Holve and Self (1976) found that for a non-absorbing particle (n = n$_1$ + 0 . i) the intensity of the light flux collected is nearly a monotonic function:-

$$I_{scattered} \propto d_p^2$$

For absorbing particles (n = n$_1$ + n$_2$. i; n$_2$ $\approx$ 0.01) with diameters above $\sim$ 10 µm, the response curve is nearly linear:-

$$I_{scattered} \propto d_p$$

Yule et al (1977) carried out a theoretical and experimental investigation of the relation between the maximum pedestal amplitude (see Fig. 2.4.3-1) and the diameter of transparent and non-transparent spheres for 30 µm $\leq$ d$_p$ $\leq$ 300 µm. They demonstrated that with proper selection of the optics geometry, for particles bigger than the fringe spacing and smaller than the control volume diameter, an unambiguous one-to-one relation exists. In the paper by Chigier (1977), some more results, based on Yule et al (1977) are presented. The use of an off-axis detection angle, in order to avoid measuring particles crossing at the edge of the control volume, is given by Ungut et al (1978) and Chigier et al (1979).

The relation between particle size and the Doppler frequency amplitude (the AC component) is given by Lee and Srinivasan (1978). They developed an electronic technique to ensure detection

of only particles crossing at the centre of the control volume. Using

this technique, they demonstrated a linear relation between the

diameter of the particles and the Doppler amplitude for 16 μm $\leq d_p \leq$

34 μm and predicted a linear relation (with a different constant) for

particle size below 4 μm. In between these ranges a monotonic response

function is given.

2.4.4 Particle Sizing - High Range ($100 \mu m \leq d_p$)

To the best of the author's knowledge only three investigations

have been reported on the simultaneous measurement of velocity and size

of particles of the order of the control volume diameter (and bigger).

Wigley (1978) describes a system designed to measure the velocity and

the size of droplets within the range of diameters 0.1 mm to 1.0 mm.

Wigley describes a combined forward and backward LDA system which is

capable of measuring the velocity and crossing time of the particle

through the control volume. The time, when correlated with the

velocity gives information about the particle size. The technique is

limited to the measurement of only one velocity component, and thus

to one-dimensional flows.

Durst and Zare (1975) analysed the measurement of velocity

and the radius of curvature R of large and smooth moving surfaces (as

for example that of a spherical bubble). The surfaces partially or

totally reflect or refract the light impinged upon at different angles

by two laser beams. Spherical particles or gas bubbles (in liquids)

crossing the control volume reflect the impinged beams backwards or

refract them forwards. These beams interfere in space to form a

fringe pattern, linear fringes in the backwards sense and non-linear

in the forward sense. The fringes move in space as the scattering

source moves through the "control volume" (no fringes exist in this

control volume). The fringe spacing is calculated as a function of

the optical parameter and the scattering source radius of curvature. Different formulae are applied for the forward and backward detection. The frequency-to-velocity relation is given, as being different from the standard one (Equation (2.2.3-5)). Detection is achieved by means of a set of two photo-detectors. The radius of curvature is derived through the given formulae and the phase difference between the signals of the two photo-detectors. Measurements of gas bubbles and sphere particles up to 20 mm in diameter are reported, in good agreement with the theory. The same phenomena, but only for transparent sphere, was analysed by Bachalo (1980), who gives a different presentation. Transparent and spherically smooth particles, simultaneously crossing two incident and inclined laser beams, refract the beams and form in space an interference of fringe pattern. The refracted light pattern, when collected by a lens over a certain solid angle, gives rise to signals of various visibilities at the photo-detector. The visibility-to-particle size response function is the same for big particles (bigger than the beam waist diameter) as for small particles. The difference is only the optimization of the characteristics of the collecting optics. The bigger the particle, the smaller the F number (focal length/lens diameter) required. Measurements of particles of up to 2.5 mm diameter are reported. There is no mention of a different relationship between the Doppler frequency and the particle velocity as reported by Durst and Zare (1975) (although a small deviation appears for large L/R, L being the distance from the particle to the detector and R the radius of the sphere's surface).

2.5   Two-Phase Flow in the Freeboard of a Fluidized Bed

2.5.1   Operating Conditions

The following three parameters governed the choice of the measurement technique:-

1.   particle characteristics;

2.   fluidized bed geometry;

3.   flow characteristics.

1.   Particle Characteristics

In order to simulate a two-phase flow in the real freeboard of a fluidized bed, silica sand, of the type normally used in a real bed, was chosen as the bed material. The typical diameter of the sand particles is 1 mm. This value is bigger than an average LDA control volume diameter. Silica sand particles are irregular in shape and the refractive index varies from one particle to another. The particles may have randomly distributed flat surfaces with sharp edges. They vary in colour from bright white to completely opaque black particles, the majority being bright and partially transparent. No information was obtained about refractive index values.

2.   The Fluidized Bed Geometry

The freeboard dimensions of 1' x 2' x 8' (see Fig. 4.2-1) and the need to measure throughout the whole of the freeboard determined the dimensions of the optical bench (see Fig. 4.4-1). Because the dimensions are large any alteration from direct forward or backward detection would result in an unfavourable restriction on the measurement zone, or call for further enlargement of the optical

bench. In order to achieve the maximum crossing angle (with a given beam spacing), a shorter optical bench dimension and the minimum disturbance from sand particles outside the control volume, measurements were performed through the wider walls, across the one foot width of the bed.

3.   The Flow Characteristics

The flow in the freeboard is two-phase. Three categories may be identified:-

(a)   The gas phase - air flows from the distribution through the dense bed to the freeboard and exits to the surrounding atmosphere. It is a turbulent flow of $4000 \lesssim Re \lesssim 50000$ based on the hydraulic diameter of the freeboard. The air velocity has a mean value corresponding to the volume flow supplied through the distributor.

(b)   Fine bed material - solid particles having terminal velocities (see Subsection 2.2.1) smaller than the maximum instantaneous gas velocity will be carried over (elutriated), outside the freeboard. These particles will record a positive mean velocity value.

(c)   Coarse particles - particles having terminal velocities greater than the maximum instantaneous gas velocity in the freeboard. These particles should record a zero, or slightly positive mean velocity due to the drag force from the upward gas flow.

All three flows in these categories are three-dimensional.

The literature review (Section 2.4) demonstrated that no simultaneous size and velocity measurement technique exists for the afore-mentioned particles and flow conditions. Accordingly, a new technique had to be developed for the present case.

2.5.2   Signal Characteristics

In order to analyse the characteristics of a typical sand particle signal, tests were performed with particles fastened to a rotating disc. Different sand particles were used as well as transparent spheres and metal pins of various diameters. The signals were detected in both forward and backward directions. A typical forward scattered signal of a sand particle (partially absorbing) is given in Fig. 2.5.2-1. Three regions may be identified as the particle crosses the control volume: two corresponding to the passages of the leading and trailing sides of the particle (a, b) and the one corresponding to the period of time during which the particle occupies the whole control volume (c). Location D and E represent the instant in time when the leading and trailing sides of the particle cross the control volume centre. Most of the sand particles produced a processable signal in the forward direction with adequate Doppler modulation and SNR values. The back scattered signal is of a much smaller pedestal amplitude and AC Doppler modulation. The gas signals, from the very fine particles representing the gas flow, were unprocessable.

In some of the sand particle signals the effect of multi-scattering appeared (i.e. modulation in the Doppler signal envelope shape). It is obvious that the phenomenon derives not from several particles - rather it has the following two sources:-

1.   Several edges of the particle enter the control volume each
        generating a Doppler signal. Whenever the spacing between
        any two edges (see Fig. 2.5.2-2) does not satisfy the
        following relation k . δ = a sin Θ, their corresponding
        Doppler signals are not coherent, producing modulation in
        the envelope shape of their combined signal (k being any
        integer, a the spacing between the edges, δ the fringe's
        spacing and Θ the angle between the line joining the two
        edges and a plane of a fringe - see again Fig. 2.5.2-2).

2.   A Doppler frequency variation might exist between signals
        of various edges of a particle, as a result of its rotation.
        For a particle of 1 mm diameter rotating at 1 r.p.s. the
        maximum velocity difference within a burst is:-

        $$U = 2\pi f . r_p = 0.00314 \text{ m/sec}$$

        Two important observations resulted from the rotating pin
test:-

1.   The existence of a certain maximum for the pedestal
        amplitude above which amplitude does not increase with
        particle size. Maximum pedestal amplitude was about 20 to
        100 times bigger than that of a particle marking the gas
        flow.

2.   The possibility of obtaining a processable signal from the
        sand particle as well as from a gas representing particle
        with the same operating conditions.

2.5.3   A Possible Particle Size Measurement Technique

During the search for an automatic technique to determine particle size, it became obvious that the surface of the particle, being in the order of the control volume diameter, contains no information about its overall dimensions. A technique based on the "time of flight" of the particle through the control volume seemed more likely to provide this information. A simplified adaptation of the technique reported by Wigley (1978) would be suitable for the present case, its only limitations being cost and operational complexity.

Description of the Suggested Technique

A three channel LDA system can simultaneously recover the three velocity components of a sand particle as it crosses the control volume; thus its absolute velocity and direction can be obtained. The particle velocity (Equation (2.2.4-4)), the control volume dimension (Equations (2.3.2-1) to (2.3.2-3)) and the crossing time (equal to the signal duration) can be used to determine the size of the particle at the crossing point (see Fig. 2.5.3-1).

The signal duration (see Fig. 2.5.2-1):-

$$T = T_a + T_b + T_c \qquad\qquad (2.5.3-1)$$

is the same for all three channels. It corresponds to the traversing distance $\overline{X}$ in Fig. 2.5.3-1. The particle diameter can then be calculated to be (for $M \geq 1$, see Equation (2.3.3-1):-

$$d_p = \overline{U} \cdot T - d_{ph}/\cos \alpha \qquad\qquad (2.5.3-2)$$

α being the angle between $\overline{U}$ and a plane perpendicular to the planes of the fringes and d_{ph} being the control volume diameter as seen by the photodetector in the collecting optics (see Equation 2.3.3-3). Particles crossing outside the centre of the control volume can be eliminated by using for example the method of off-axis detection described by Ungut et al (1978). However, this sizing technique was not used in the present study because of the cost of nearly triplicating the optical and electronic equipment. The technique could quite easily be applied for relatively big particles in the order of the control volume diameter d_{ph}, for the special case of one-dimensional flow, where a standard single component LDA system could be used, or in two-dimensional or axially symmetrical flows using dual channel LDA systems (which are much more commonly used than three channel systems).

2.5.4   The Chosen Technique

As it was found to be impractical to determine particle size at the present time, a different strategy was adopted: several mono-size particle beds have been used, effectively eliminating the necessity to measure the absolute size of the scattering particle and reducing the problem to that of simply identifying the phase to which it belongs.

The most convenient technique for discriminating between the signals of the two phases is by measuring the pedestal amplitude. Signals of high pedestal amplitude are generated by the solid phase, while lower ones are attributable to the gas phase. No classification technique based on differences in velocity between the two phases could be applied (see for example Durst, 1978) as the velocity histograms of the two phases usually overlapped. A partially similar technique is reported by Durst (1978) who used spherical glass balls of

$100 \ \mu m \leq d_p \leq 800 \ \mu m$. The signals were classified with respect to the two phases according to their pedestal amplitudes, their velocity and with the use of two additional photo-detectors located as beam stops, which provided a timing signal for particle passage through the control volume.

In order to explore the technique a preliminary measurement test was carried out performing two-phase velocity measurements in a particle-laden turbulent free jet (see Chapter 3). A variable threshold level for the pedestal amplitude was used to distinguish the two phases. After achieving satisfactory results, the same principle, although somewhat modified, was applied to the measurements in the fluidized bed. Instead of using a pre-selected threshold level as the parameter of classification, the actual pedestal amplitude value was recorded and stored together with the velocity. At the end of the data collection an optimum (programmable) threshold level was applied and classification was performed as part of the data processing.

CHAPTER 3

VELOCITY MEASUREMENTS IN A PARTICLE
LADEN TURBULENT FREE JET

3.1   Introduction

It seemed proper to verify the technique selected for two-phase

flow measurement in the particularly simple circumstances of a particle

laden free jet. Quite apart from this basic consideration, measurements

in a jet flow would yield much needed new data. The behaviour of small

particles in turbulent jet flows is of particular importance in oil and

pulverized coal combustion. With these considerations in mind, preliminary

data were obtained in a sand particle laden free turbulent jet directed

vertically downward, (see Fig. 3.1-1).

A substantial amount of work has been published on the subject

of two-phase jet flows, most of which concerns small particles with dp $\leq$

100 μm. Abramovich (1970) made some analytical explorations. He

suggested that the transverse component of the velocity fluctuation,

which directly affects jet growth should: decrease in proportion to

the mass flow ratio of the two phases (particle loading); increase with

the particle transverse velocity; and be greater when the particles lag

behind the gas flow (which may be the case near the jet exit). Al Taweel

(1977) surmises that energy dissipation results from the relative

velocity between the particle and the instantaneous gas motion, due to

sheer forces. This energy is subtracted from the total kinetic energy

of the jet, especially from the high frequency eddies. The process

increases with particle loading and decreases with particle size.

Danon et al (1977) also concluded that there is a reduction

in the turbulence energy level due to the presence of the dispersed

phase, and that a simple explanation based on viscous energy

dissipation is not enough to evaluate the phenomenon. Measurements

conducted by Hetzroni and Sokolov (1971) using hot-wire techniques confirmed the reduction of gas phase turbulence intensity due to the introduction of oil droplets of 13 μm diameter. Popper et al (1974) carried out comprehensive LDA measurements in various flow conditions using particles smaller than 50 μm. They demonstrated that the radial velocity profiles for the particles are similar along the centreline and that two-phase jets are narrower than free air jets having the same nozzle exit velocities.

Rajani and Langer (1972) conducted an experiment using spherical glass particles of 110 μm diameter discharged vertically downwards. They concluded that the particles had a uniform velocity distribution across the nozzle exit, unaffected by the particle loading, and that the velocity along the jet exit reaches a maximum just beyond the point where the relative velocity between the fluid and the particle is reversed. As for the gas flow it was found that in comparison to a single phase flow under the same conditions, the potential core is shorter, the rate of the centreline velocity reduction is faster and the width of the jet is larger in the upstream region (near the nozzle). The velocity is slowed at a reduced rate with narrower jet width further downstream.

All the previously mentioned reports broadly agree on the general phenomena consequent upon introducing dispersed particles to a gaseous free jet. However, none of them refer to the particle size range of current interest (200 - 1200 μm). To the author's knowledge, only the work by Abuaf and Gutfinger (1971) exists for flows laden with large particles (diameter of 250 - 417 μm). Their experiments were performed on a horizontal jet in which the particle trajectories were strongly affected by gravitation.

3.2   Arrangement of the Experiment

Sand particles were admitted to an injection pipe from a

screw feeder powered by a variable speed motor (see Figs. 3.1-1 and 3.2-1). The injection pipe ran straight for 40 diameters in order to obtain an approach to fully-developed conditions at its exit. Experiments were performed using moderately large sand particles of mean diameter: 215, 400, 540, 725 and 1060 μm. The sand was screened to limit size distribution. The minimum and maximum diameters are specified in Table 3.2-1 and a representative size distribution curve is shown in Fig. 3.2-2. At first, silicon oil droplets were introduced to the flow as scattering particles to facilitate the gas phase measurement. This incurred the disadvantage that the oil droplets tended to agglomerate with sand particles. Seeding with solid particles (T_i O_2) did not solve the problem. It was later found that the natural attrition of the sand particles produced a fine dust sufficient to eliminate the necessity for artificial seeding.

Velocity measurements were effected using a standard forward scatter laser Doppler system with frequency shift* (see Fig. 3.2-1). The signals from the photomultiplier were admitted to a threshold selector (Section 3.3) for the purpose of classification according to phase. The signal output from the threshold selector unit was processed by a micro-processor controlled frequency analyser (Durão et al, 1978).

3.3   The Threshold Selector

The principle of discrimination between the two phases was based on the relation between particle size and its pedestal amplitude (Section 2.4). It is evident that by imposing a variable threshold

---

*   Effected by a rotating radial diffraction grating made by
         Technisch Physische Dienst Tno-Th (TPD), Stieltjesweg 1,
         Delft 2208, Postbox 155, Netherlands. The frequency shift
         was 1835 kHz.

TABLE 3.2-1

EXPERIMENTAL SPECIFICATION

Code	Particle sand range (μm)	Air flow rate $\left(\dfrac{kg}{sec}\right)$	Sand flow rate $\left(\dfrac{kg}{sec}\right)$	Sand-to-air ratio	$\overline{U}_g$ at r = 0 and X = 20 D (m/s)	$\overline{U}_p$ at r = 0 and x = 20 D (m/s)
A	850 - 1200	$4.29 \cdot 10^{-3}$	$15.0 \cdot 10^{-3}$	3.5	7.3	8.74
B	600 - 850	$3.62 \cdot 10^{-3}$	$8.78 \cdot 10^{-3}$	2.42	6.12	8.20
C	300 - 700	$3.62 \cdot 10^{-3}$	$8.12 \cdot 10^{-3}$	2.24	6.0	8.52
D	300 - 500	$3.62 \cdot 10^{-3}$	$4.42 \cdot 10^{-3}$	1.22	8.79	13.32
E_1	180 - 250	$3.62 \cdot 10^{-3}$	$4.13 \cdot 10^{-3}$	1.14	9.06	14.90
E_2	180 - 250	$3.62 \cdot 10^{-3}$	$8.45 \cdot 10^{-3}$	2.33	7.57	11.55
F	Clean gas	$4.29 \cdot 10^{-3}$	-	-	9.6	-

level on the pedestal amplitude signal one can distinguish between the
scattered light originating from the sand particles and that from the
fine particles representing the gas flow. A threshold selector was
devised in which a continuous comparison was made between the selected
threshold level and the detected pedestal amplitude. Two operational
modes enabled a Doppler signal to be processed according to whether
its corresponding pedestal amplitude was either higher or lower than
the selected level (Fig. 3.3-1). Sand particle velocity measurements
were obtained by selecting a high threshold level which would allow
only those signals with higher pedestal amplitudes to pass through.
Signals with pedestal amplitudes less than a lower threshold level were
considered to emanate from the gas phase. A threshold level ratio of
about 20 for the two phases was found to be adequate. During gas
phase measurement, the effect of sand signal residue (the portion of
the signal below the threshold level, see Fig. 3.3-1) was found to be
negligible. When measuring the sand phase, each particle produces two
Doppler frequency bursts (see Fig. 3.3-1). The double burst effect
does not bias the results because the phenomenon affects all the sand
particles.

A demonstration for the threshold selector operation is
given in Fig. 3.3-2. Three different measurements were performed in
the flow E_2 (see Table 3.2-1): gas flow measurements (A curve in the
figure); sand velocity measurements (B curve); and measurements in
which signals were processed without discrimination (C curve of the
figure). All the curves were normalized to illustrate probability
histogram values. It became apparent that by using the threshold
selector (curves A and B), the velocity distribution of each phase
could be isolated. This is especially evident in the area of over-
lapping between the velocity fields, 8.3 (m/s) < U < 13 (m/sec). It
was further seen that the mean sand velocity value (as represented by

the peak of curve B and the right peak in curve C) remained unchanged, but that the mean gas velocity was somewhat lower than the gas peak in curve C. The reason for the latter is that curve A is composed only of the signals originating from fine particles with very low pedestal amplitudes representing the gas flow, whereas the gas peak in curve C is the result of much wider particle size range extending to higher size values. The smaller sand particles are travelling at higher velocity, shifting the gas velocity peak to the right. These particles scatter light of intermediate pedestal amplitudes, and are usually excluded from measurement by selecting a low threshold level.

3.4 Discussion of the Results

The particle velocity must obey the equation:-

$$\frac{\rho_p}{\rho_g} \frac{d\vec{U}_p}{dt} = \frac{1}{2} C_D A_p' (\vec{U}_g - \vec{U}_p) |\vec{U}_g - \vec{U}_p| + \frac{\rho_p}{\rho_g} \vec{g} \qquad (3.4\text{-}1)$$

where ρ is density, $\vec{U}$ is the instantaneous velocity vector, t is time, C_D is the drag coefficient, A' is the cross-sectional area per unit particle volume, $\vec{g}$ is the gravitational acceleration vector and the subscripts g and p designate the gas and particle phases. For very small particles, of the order 1 μm (typical of those used in LDA to measure gas velocities), the first term on the right hand is very large and the particles closely follow even the smallest motions of the turbulence spectrum. Larger particles are less and less responsive and their tendency to fall through the mean gas flow under the influence of gravity increases with increasing particle size.

We may identify three regimes. The first two correspond to the above-mentioned extremes:-

(i)   The particles are very small and respond to all turbulence
        irregularities. Within the range of extremely small sizes
        they have no influence on the flow apart from increasing
        its effective density in proportion to their extra mass.
        The otherwise important parameter ρ_p/ρ_g (constant in this
        study) for high jet Reynolds numbers is not significant in
        this case.

(ii)   The particles are very large and drag the mean gas flow along
        as they fall. In so doing, they increase the mean velocity
        gradients in the gas phase and, consequently, its kinetic
        energy.

(iii)   The particles belong to an intermediate size range tending
        to move with, rather than fall through, the mean flow. But
        they partially respond to fluctuations in the gas phase
        turbulence thereby reducing gas phase kinetic energies.

        It is evident that the particles in categories (ii) and (iii)
have opposite effects on the gas flow and the magnitude of these effects
must increase as the mass of particulate matter is augmented. These
effects generally agree with the previous investigations discussed in
Section 3.1.

        The turbulent transport in, and consequently the rate of
spread of, the gaseous jet must be expected to be directly linked to
the magnitude of the turbulence kinetic energy. This is verified by
comparison of Figs. 3.4-1 and 3.4-2. The largest particles (case A)
behave according to the expectations of category (ii) and result in a
significant increase in gas phase kinetic energy (Fig. 3.4-2). The
smallest particles in the present experiments behave according to the

expectations of category (iii) for the higher seeding rate (case E_2) reducing the gaseous kinetic energy, the effect being smaller for the lower seeding rate (case E_1). The opposing tendencies of categories (ii) and (iii) tend to cluster the velocities and kinetic energies about the clean gas result (case F).

The kinetic energy of the turbulent fluctuations of the largest particles (Fig. 3.4-3, lower curves) is greater probably because these particles re-absorb some of the turbulence energy induced in the gas flow by their free flow. The apparent independence of particle fluctuating energy on particle loading indicated by the curves for E_1 and E_2 suggests, not unexpectedly, that the absorption of gas phase turbulence energy by the particles in this size range is not strongly linked to the loading. The results for particle mean velocity (Fig. 3.4-3 , upper curves) indicate that the particle spread is a rather sensitive phenomenon. The greatest spreading occurs for particles of intermediate size (case C) suggesting a delicate balance between the response of the particle to the turbulent diffusion of momentum of the fluid and to the gravity vector.

It is generally observed that an increase in particle loading causes a reduction in mean gas velocity (Table 3.2-1, see also Rajani and Langer, 1972) and a decrease in jet width (cases E_1 and E_2 in Fig. 3.4-1). These results indicate lower gas entrainment from the surroundings. This phenomenon, which seems to have finely balanced dependence on the particle loading and size distribution, has wide-ranging industrial importance and should be further analysed.

Abbas et al (1980), who presented a computational technique for particle laden flows, referred in their paper to the author's experimental results reported in Levy and Lockwood (1981). Good agreement was found with the data for both gas and sand particle velocities although the predicted particle spreading rate was an underestimate.

CHAPTER 4

THE FLUIDIZED BED SYSTEM

4.1   Introduction

The term fluidized bed system is meant to include all the
experimental hardware excluding the signal processing which is
described in Chapter 5. The system consists of the fluidized bed
(see Section 4.2), a three-dimensional traversing mechanism (see
Section 4.3), an optical bench for the LDA measurements (see Section
4.4) and a periodic single bubble release facility (see Section 4.5).

Many previous elutriation experiments have been conducted
using a fluidized bed of relatively small dimensions*. It was
Gugnoni and Zenz (1980) who criticized the conditions of such
experiments which have served as bases for the particle entrainment
correlations which were subsequently employed in the design of large
industrial equipment. Comparatively large dimensions were selected
for the present fluidized bed in order to minimize wall effects, but
not so large as to prevent convenient optical measurements. The
present bed has a rectangular cross-section to enable the investigation
of geometrical asymmetry effects on the freeboard flow.

A rigid traversing mechanism was designed to carry the heavy
and unevenly distributed optical bench constructed mainly of
relatively light-weight and rigid aluminium sections. An indication
of its good performance is that no difficulty was experienced due to

---

*   For example, Zenz and Weil (1958) used a two-dimensional
        bed of 5.1 x 61 cm, Wen and Hashinger (1960) used a bed of
        2" and 4" diameter, Osberg and Charlesworth (1951) used a
        bed of 3" diameter and Leva (1951) used a tube of 1.32"
        diameter. Bigger bed dimensions were employed by Horio
        et al (1980) (0.24 m I.D.) and one of still larger
        dimensions, 91 x 91 cm square, was used by Merrick and
        Highley (1972).

vibration and no realignment of the optical components is required when traversing the whole cross-section and height of the freeboard. The single bubble release facility was incorporated to make it possible to study the emerging and bursting bubble.

4.2   The Fluidized Bed

The present fluidized bed is an experimental one permitting a variety of operating conditions and laser Doppler measurements throughout the freeboard. It is based on two separate frames (see Fig. 4.2-1): one for the plenum chamber and the other for the bed section.

4.2.1   The Plenum Chamber

This is a rectangular pressure vessel designed to sustain up to 6 psi of pressure; its internal dimensions are: 0.6 m x 0.3 m x 0.45 m high. It is constructed from $\frac{1}{8}$" thick walls. The plenum chamber (and the bed) are mounted on a 60 cm high base frame (constructed of N.P.C. 4" x 3/16). The fluidizing air inlet is a 2" B.S.P. line with an additional $\frac{1}{4}$" B.S.P. air inlet to supply air to a centrally mounted nozzle used to produce single bubbles. A 2" safety valve (Willcox Model 134) was installed to discharge air should the pressure inside the plenum chamber exceed 5 psi.

4.2.2   The Bed Section

The bed section is 305 mm x 610 mm x 2.4 m high*. It has a metal frame (N.P.L. $2\frac{1}{2}$" x $2\frac{1}{2}$" x 3/16") with the two shorter ends

---

*   The height of the bed is defined as that from the top of the air distributor to the end of the parallel walls where the inclined roof begins (see Fig. 4.2-1).

(305 mm x 2.4 m) formed of metal plates 1/16" thick. Transparent glass walls (which give access for laser Doppler measurements) form the larger sides of the bed, slotted into lower and upper metal frames.

The glass plate dimensions are 655 mm x 1190 mm. Thickness was determined by the pressure distribution along the wall. A thickness of 19 mm, and later 15 mm, was found to be appropriate for the initial experiments.

Plate glass walls were preferred because they are flat, rigid, less susceptible to scratching from sand movement during bed operation and clear enough to enable the laser beam to penetrate with minimal disturbance. During some of the experiments, when U_f = 1.7 m/s (U_f/U_{mf} = $\sim$ 3) with sand particles of mean diameter 1.06 mm and bed height 400 mm, the maximum glass deflection was measured to be about 0.1 mm. Because of the need for thick (and, therefore, expensive) glass, it was used only for the lower walls while cheaper perspex was used for the upper walls. When measurements are to be performed in the upper section, the glass and perspex can be interchanged.

The connection of the glass walls to the frame is shown in Fig. 4.2.2-1 and the type of connection between the lower and upper sections is shown in Fig. 4.2.2-2. This connection allows the use of flat glass with free cut edges, provides adequate sealing and allows relatively easy glass replacement. Access to the bed for servicing is achieved through three openings, one of which is a 2" gate valve to enable draining of the sand with the aid of a vacuum cleaner.

4.2.3   The Air Distributor

The bed air supply is fed from the plenum chamber through a distribution plate. A porous bronze plate (Accumatic Engineering Sintercom Bronze grade "D" $\frac{1}{4}$" thick) was chosen to achieve a uniform

air distribution. Since the initial experiments required a smaller air flow rate than originally envisaged, an additional PVC porous plate was installed under the bronze one. The connection of the distributor to the bed is shown in Fig. 4.2.3-1. The pressure drop across it versus the air flow rate is shown in Fig. 4.2.3-2.

4.2.4   Air Supply

Cool, dry and oil-free air was supplied at constant pressure from a large rotary type compressor. The air flow, metered by an orifice plate (calibrated to British Standard No. 1042), is controlled by a 2" gate valve, with an associated bypass ½" gate valve for fine adjustment, and is then fed to the plenum chamber. After passing through the distributor and the sand particles which form the bed material, the air disperses via the freeboard region into the surroundings. The air flow supply rate was checked and found to vary by less than 1% over a period of 6 hours.

4.3   The Traversing Table

The purpose of the traversing table is to carry the optical bench. It was desirable from the beginning to be able to measure throughout the whole of the freeboard space. The dimensions of the freeboard (Fig. 4.2-1) are 0.3 m x 0.6 m x about 2.0 m high, depending on the bed height. The traversing table was initially designed to enable continuous movement over the whole range, but this was later considered to be too big, heavy and expensive to build. A compromise solution was adopted to allow the whole height of the freeboard to be traversed in two steps with an overlap range. In the event, this was a largely irrelevant problem since the region of interest turned out to be confined to the lower part (below 1 m) of

the freeboard.

4.3.1   Vertical Traversing Mechanism

Separating the vertical traverse into two parts permitted the use of standard commercial equipment. The traversing mechanism has to carry the weight and moment of the optical bench and to traverse in all directions, especially vertically, in a smooth, continuous and stable manner. A lower part of a vertical drilling machine (Pollard Model 150) was found to be very suitable (see Fig. 4.3.1-1). The unit has a base (710 mm x 430 mm), a vertical column (210 mm x 194 mm cross-section) with a guiding slide bar (152 mm x 16 mm) and a moving platform table (table area 610 mm x 527 mm). The vertical movement is achieved by a handle and gear mechanism which rotates a screw jack. The maximum vertical traverse is 480 mm. To increase the vertical traverse a duplicate column was installed on top of the original one. After proper connection and alignment, and using extension tubes under the screw jack, the vertical traverse was increased to 1250 mm.

4.3.2   Horizontal Traversing

A lightweight, two-dimensional traversing table (Unimatic Engineer Limited, Type 600) was bolted to the table of the drilling machine. It allows traversing of about 600 mm in each direction. The maximum permissible load on top of the traversing table is 250 kg.

4.3.3   General Assembly

Displacement scales were installed in each of the traversing directions. A scale division of 1 mm was used although movements as small as 0.1 mm could be achieved. The vertical table was connected

to a wide base to increase its stability. The base (1.2 m x 1.2 m) was made of rectangular hollow steel section (100 mm x 100 mm x 6 mm). The base has 5 adjusting screws to enable fine horizontal alignment. A further 4 screws bolt the base to the laboratory floor and eliminate any possible movement of the whole traversing table due to vibration in the laboratory or to accidental pushing.

When measurements are required in a higher region of the freeboard, two procedures are possible:-

1.   For measurement level up to about 170 cm above the air distributor, the fluidized bed can be removed from its base giving an effective additional height of 60 cm.

2.   For measurements above 170 cm from the air distributor, a box frame with the same horizontal dimension as the base frame and having the required vertical height could be constructed.

After the fluidized bed and the traversing table were installed, the relative alignment between the two was checked. In the lower half of the bed, it was found that the parallelism (the distance between a point attached to the traversing table and the glass wall at various locations) was less than 1.5 mm out of true when traversing 1 m vertically, and less than 0.5 mm out of true in the full horizontal traversing (0.6 m).

4.4   The Optical System

A standard forward scatter laser Doppler anemometer (LDA) optical system with frequency shift formed the basis of the

instrumentation (see Fig. 4.4-1).

The distances between the optical components were determined by the dimensions of the fluidized bed cross-section together with some optical criteria (Section 2.3). As these distances were very long, the optical axis had to be rotated twice (using mirrors), to form a ⌐ shape and so reduce the total bench dimension (see again Fig. 4.4-1). All the optical components were connected to a frame mounted on top of the traversing table. The frame was mainly constructed of standard 4" x 2" x 3/16" aluminium channel. It had to be especially lightweight and rigid as it could only be supported at one corner at the top of the traversing table, leaving most of the frame including its centre of gravity free from support. After assembly the optical system was found to be insensitive to vibration at normal working conditions.

The optical system comprises the following standard components:-

1.   A 5 mw HeNe Spectra Physics model 120 laser;

2.   A beam splitter and Bragg cell unit, DISA 55X modular LDA optics;

3.   A photomultiplier EMI 9817b with a high voltage power supply Hewlett Packard 6110A.

In addition, two boxes were built to contain: (a) a mirror and a focussing lens and (b) a collecting lens and a second mirror. The photomultiplier unit was modified and its components were chosen to provide as linear a response as possible over the whole of the detected light range. The optical dimensions of the system are:-

Beam spacing	60 mm
Half beam crossing angle	3.90°
Magnification of collecting optics	3.0
Pinhole diameter	0.50 mm

4.5   Single Bubble Release Facility

The single bubble release mechanism was designed to produce repeatable air bubbles of constant shape at regular intervals in the fluidized bed so that the process of bubble eruption could be analysed in detail. To produce a repeatable bubble, controlled pulses of air are injected through a central nozzle located in the air distributor, the bed being operated at minimum fluidization. Analysis of bubble processes by examining single bubble release has been effected in several previous studies (see, for example, Harrison and Leung, 1962; Rowe, 1971).

The description of the single bubble mechanism can be divided into three sections:-

1.   The air supply (see Subsection 4.5.1);

2.   The solenoid valve and its control (see Subsection 4.5.2);

3.   The nozzle (see Subsection 4.5.3).

4.5.1   The Air Supply

A special air supply was devised for the single bubble release mechanism (Fig. 4.5.1-1). Shop air is fed through an air filter (Norgren No. F50308A) and a fine pressure regulator (Fairchild No. 1400) to a pressure vessel (100 litre propane gas container). A pressure gauge with 1 psi resolution indicated the

vessel pressure. The shop air pressure is at 80 - 100 psi and the vessel pressure was usually maintained at about 50 psi. The purpose of the pressure vessel is to create a constant pressure reservoir for the derivation of the bubble release uninfluenced by the output flow rate. The air from the vessel is supplied to a solenoid valve, and then to the nozzle.

4.5.2   The Solenoid Valve and its Control

The solenoid valve periodically releases pulses of air. The valve (Beech Pneumatics model 1JLSGA3RS) is operated by a specially built control unit which governs the valve cycle and opening times. Two additional options enable single shot (with adjustable opening duration) or continuously open operation. Typical cycle and opening times are 1.30 and 0.20 s. An output signal which follows the opening of the valve is used (see Subsection 5.6.2) to reset the time clock in the interface unit.

4.5.3   The Nozzle

The air passes from the nozzle into the sand particles which form the bed. The geometry of the nozzle and the nature of the supply line from the valve to the nozzle have a significant influence on the bubble shape (and quality). Several nozzle configurations were tested and the best bubble shape was achieved with a nozzle of 8.5 mm diameter covered with a fine wire mesh to prevent sand back flow (Fig. 4.5.3-1). The air supply line from the solenoid valve was about 0.6 m long and 6 mm in diameter (total volume 17 cm^3). It was necessary to keep the supply line volume as small as possible to minimize its influence on the output air pulse shape.

4.5.4   Bubble Size and its Measurement

When a pulse of air is released through the nozzle, an air bubble is created in the bed. As a first approximation it can be said that the bubble air mass in the bed is the same as the mass of air passed by the solenoid valve while open (Davidson and Harrison, 1963). An experiment was performed to measure the air released as a function of the opening time and upstream pressure. In reality the actual bubble volume is slightly smaller than that determined by the mass of air passing through the solenoid valve as air escapes from the bed during the creation of the bubble. Because the local pressure near the nozzle exceeds the plenum chamber static pressure, air flows backwards through the distribution plate to the chamber. The latter phenomenon was confirmed by the fact that the static pressure of the plenum chamber increased every time a bubble was released.

One way of determining the bubble volume is to close the inlet to the pressure vessel and release several air pulses through the solenoid valve while measuring the drop of pressure in the vessel (usually no more than about 5% of the initial pressure). The pressure drop, vessel volume and number of air releases determines the average volume of air released at each valve opening. In the present case, the exact volume of the pressure vessel was unknown and could not be conveniently measured. Consequently, a different measurement technique was developed (Fig. 4.5.4-1). The basic principal was to be able to capture a fast pulse of air, to store it and later to measure its volume in a convenient manner.

Air from the solenoid valve is directed via tap (1) to a (child's) balloon, with tap (2) closed. The valve is operated once (on single shot mode) releasing a certain amount of air. Tap (1) is closed (required because the solenoid valve is not perfectly sealed)

trapping the lump of air inside the balloon. Tap (2) is opened and
tap (3) is set to position (b). The air from the balloon passes to
a cylindrical glass vessel, the open bottom of which is immersed in
a container of water. The air from the balloon displaces water into
the container. The volume of water displaced is the "bubble" volume.
The volume itself is measured with a scale (height multiplied by the
cross-sectional area). Tap (3) is then turned to position (c)
allowing a suction pump to remove the air. Tap (3) is turned to
position (a), tap (2) is closed, tap (1) is opened and the system is
ready to measure a subsequent air volume.

In general the technique was successful. The balloon was
able to absorb fast and short duration jets and the balloon volume
measurement was convenient and accurate. Measurements were performed
for a vessel pressure of 50 psi and for different gate time openings.
About 30 seconds were required to measure each volume; some results
are given in Table 4.5.4-1 and plotted in Fig. 4.5.4-2. Some
variation was found in the results for equivalent operating
conditions, probably due to lack of synchronization between the
control pulse timing and the frequency of the main (240 volts 50 Hz)
which drives the solenoid valve. This effect would be expected to be
more significant for shorter gate opening periods and this was found
to be the case. Leaking taps and difficulties in operating the
three-way tap (3) were other sources of error. The measurement of
the 200 millisecond gate time pulse was subject to an additional
error as the volume of the glass vessel was smaller than the air
pulse volume and the balloon volume had to be measured in two parts.

The overall error of the system is not expected to exceed
± 5%. This was considered sufficient for the present purposes. The
main difference between the calibration system and the bed system

arises because of the difference in the flow paths to the balloon and to the nozzle.

TABLE 4.5.4-1

AIR PULSE VOLUME MEASUREMENTS,
PRESSURE VESSEL AT 50 psi

Pulse duration (m sec)	Mean height of air displacement (cm)	Standard deviation of height (cm)	Mean volume of air pulses (cm^3)
50	7.8	0.45	296
100	15.5	0.57	586
150	23.0	0.84	873
200	30.9	1.42	1170

CHAPTER 5

SIGNAL PROCESSING SYSTEMS FOR
FLUIDIZED BED MEASUREMENTS

5.1 Introduction

The nature of the signal processing system was dictated by the necessity to measure steady and unsteady two-phase flows. The flows considered in the present study may be classified as follows:-

1.   Single phase (gas) flow.

2.   Two phase (gas plus sand) flow.

3.   Unsteady two phase flow.

Each flow type required its own signal processing. The basic system dealt with the single phase flow. The two-phase flow system consisted of the basic signal processing plus facilities to distinguish between the two phases. The time dependent two-phase system incorporated the two-phase flow system plus a facility for recording the time of measurement relative to a reference time. The single phase flow processing is an option contained in the whole signal processing system.

Two techniques were used to process the Doppler frequency signals: frequency analysis and frequency counting. The counting technique, applied later in the project, is a faster and more accurate measurement technique but requires more subsidiary electronic components. Signal processing was controlled by a minicomputer which was interfaced to all the experimental components. The computer was responsible for data acquisition and processing and provided the print-out of the experimental results.

5.2   Signal Processing Structure

Three principal components (units) were developed to enable the collection of corresponding types of data as follows:-

Unit 1   The Doppler signal processor (see Sections 5.3 and 5.4) for Doppler frequency detection.

Unit 2   The signal pedestal maximum amplitude detector (see Section 5.5).

Unit 3   The time of measurement recorder (see Section 5.6).

The three units were interfaced to a minicomputer (see Section 5.7). By combining the above units, the measurement system was designed to accommodate the following possibilities:-

(a)   Unit 1, Doppler frequency signal processing (for single phase flow).

(b)   Units 1 and 2, for Doppler frequency signal processing and signal pedestal maximum amplitude detection (for two-phase flows).

(c)   Units 1, 2 and 3, for Doppler frequency signal processing, signal pedestal maximum amplitude detection, and time of measurement recording (for time dependent two-phase flow).

(d)   Units 1 and 3, for Doppler frequency signal processing and time of measurement recording (for time dependent

single phase flow).

Possibility (a) was used in preliminary tests to check the accuracy
of the Doppler frequency signal processing system and, while using
the frequency analyser, for quick frequency calibration tests at the
beginning of and during long period measurements. (b) processing
was used in two-phase flow measurements in the freeboard with
different operating conditions. (c) processing was used for the
"single bubble" experiments which were time dependent and two-phase.
The (d) option was not in use.

Selection of the particular processing possibility to be
employed in an experiment was effected by specially developed computer
programs* The kind of measurement to be made was determined by
different control commands. Three basic programs were written for.
the (a), (b) and (c) possibilities respectively. Running the
appropriate program automatically produced the signal processing
combination required. For each possibility the program determined
the experimental parameters, controlled the signal processing and data
acquisition, and stored the measurement data on a magnetic disk. At
a later stage the data was processed by other programs.

5.3   Doppler Frequency Measurements Using Frequency Analyser

Because of the relatively poor signal-to-noise ratio, the
difference in the Doppler signal amplitude between the phases
(Section 2.4), and the results of the preliminary experiments
(Chapter 3), a frequency analyser (Hewlett Packard 8553B) was chosen
to process the Doppler frequency signals. This suffered from the
disadvantages of a relatively low accuracy and low data collection
efficiency. The use of a frequency analyser for Doppler signal

---

*   Available from the author by request.

processing is described, for example, by Durão (1976) and Durst et al (1976).

A schematic diagram of the Doppler frequency processing system is shown in Fig. 5.3-1. The frequency analyser is capable of detecting the frequency which corresponds to its instantaneous sweep voltage. A sweep voltage is externally produced as a periodic sawtooth which causes the frequency analyser to scan over a corresponding frequency range (Durão et al, 1978). The frequency range is defined by the sweep voltage limits, and by the centre frequency and the scan per division setting of the frequency analyser. When the frequency analyser detects a frequency, it reacts by producing an output voltage. The detected frequency value is the one which corresponds to the sweep voltage value at the time of the output voltage detection.

The principle of computer control over the frequency analyser can be divided into two main parts:-

1.   The generation of the sweep voltage;

2.   The detection of a frequency measurement.

5.3.1   The Generation of the Sweep Voltage

The sweep voltage (Fig. 5.3.1-1) is generated in a computer program as a series of binary numbers. These numbers are loaded to the output buffer register of the interfacing card and are simultaneously converted to an analogue voltage by an 8-bit Digital-to-Analogue Converter (DAC). The output of the DAC is connected to the sweep voltage input of the frequency analyser. Since the maximum input sweeping voltage of the frequency analyser is 10 V, the resolution of the DAC is 39.22 mV (10 V for a binary value of 255).

Because of the sawtooth sweep voltage, and the consequent sharp voltage change at the end of each cycle (from 10 V to 0 V) a

delay time is set to ensure completion of the voltage decrement to the initial value of the new cycle. In the routine to produce the sweep voltage, the following parameters can be set:-

1.   the initial voltage (Vinit);

2.   the step size (Stsize);

3.   the number of steps (Nstep);

and if specially required:-

4.   the extension for the duration of each step (Itime).

The sweep voltage parameters can be chosen in any combination satisfying the following relation:-

$$Vinit + Nstep \times Stsize \leq 255 \qquad (5.3.1\text{-}1)$$

The flowchart of the sweep voltage routine is as follows:-

```
                  ( START )
                     │
         ┌───────────▼───────────┐
         │ define initial parameter │
         └───────────┬───────────┘
    ┌────────────────▼────────────────┐
    │  set sweep voltage to initial value │
    └────────────────┬────────────────┘
         ┌───────────▼───────────┐
         │   execute delay cycle   │
         └───────────┬───────────┘
      ┌──────────────▼──────────────┐
      │    increment sweep value     │
      │      by the step size        │
      └──────────────┬──────────────┘
                     │
              ╱──────▼──────╲
        No   ╱     have       ╲
       ◄────  the number of steps 
             ╲ been completed? ╱
              ╲──────┬──────╱
                     │ Yes
```
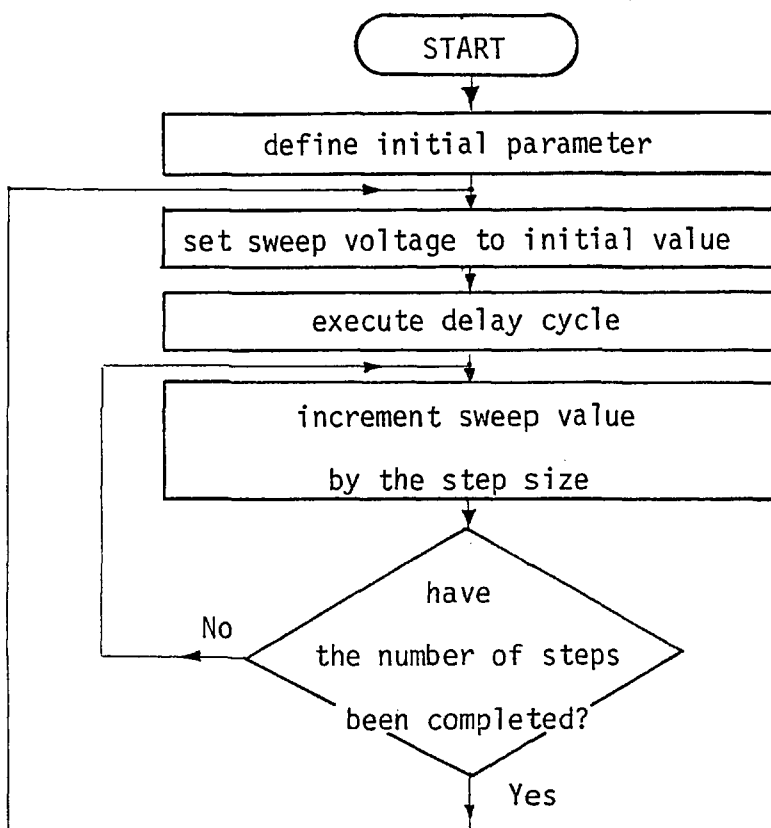
The sweep voltage output is calculated by the formula:-

$$V(j) = J \cdot \Delta V \tag{5.3.1-2}$$

where:-

$$J = J_0 + \left[\frac{t - t_0 - \{t/\tau\} \cdot \tau}{\Delta t} \right] \Delta J$$

$$\tau = t_0 + Nstep \times \Delta t \tag{5.3.1-3}$$

$$\Delta t = \Delta t_0 + Itime \times \Delta t_d$$

where:-

J = sweep voltage binary value

J_0 = initial sweep voltage binary value (Vinit)

ΔJ = a step increment

τ = period time

t = instantaneous time

t_0 = initial delay time

Δt = step duration

Δt_0 = minimum step duration (currently 22.5 μsec)

Δt_d = duration of each step delay cycle

ΔV = DAC resolution

$\{ \}$ ≡ the integer part of the value inside the brackets to be used

5.3.2   Detection of a Frequency Measurement

Detection of Doppler frequencies is performed with the aid

of the computer interrupt facilities which allows continuous
generation of the sweeping voltage until it is "interrupted" by a
signal, initiated by the frequency analyser, indicating that a
Doppler frequency has been detected. When an interrupt occurs, the
computer switches from executing the main program and starts to
execute a special service routine which records the detected Doppler
frequency. The effect of an interrupt on the sweeping voltage is
shown in Fig. 5.3.2-1.

When a frequency is detected by the frequency analyser it
produces an output voltage (Vertical Output). A special Frequency
Analyser Output Detector (FAOD) unit was devised to produce a pulse
when this output voltage is above a minimum preset level and at the
time of its maximum amplitude. The output of the FAOD is connected
to the interrupt line at the Input/Output parallel interface card.
When the interrupt line is set, the computer automatically preserves
the machine state immediately prior to the occurrence of the interrupt
(in order that the main program may be reaccessed from the time of
the interrupt) and starts to execute a service routine (Digital 1978);
the sweep voltage value at the output buffer register is read and
stored in the computer. When the computer terminates the execution
of the service routine it returns to the sweeping routine in the main
program and is then ready to be interrupted again by another interrupt
pulse.

5.3.3   Calibration of Frequency Measurements

The relation between frequency and the sweep voltage binary
value is:-

$$\Delta Fu = \frac{F_{max} - F_{min}}{255}$$

(5.3.3-1)

where ΔFu is the frequency interval for each binary unit:-

$F_{max} - F_{min}$ = frequency range of the analyser which is defined by

its Scan/Division setting

In order to calculate the frequency from the sweep voltage binary value:-

$$F = F_{min} + J \cdot \Delta Fu \qquad (5.3.3-2)$$

where J is the sweep voltage binary value.

A different and more accurate technique for evaluating ΔFu is to measure two reference frequencies Fr1 and Fr2:-

$$\Delta Fu = \frac{Fr2 - Fr1}{\Delta J} \qquad (5.3.3-3)$$

where ΔJ is the difference between the sweep voltage binary values of the two reference frequencies.

5.4   Doppler Frequency Measurement using Frequency Counter

It became evident that the Doppler signals obtained during measurements in the freeboard of the fluidized bed, were of sufficient quality to be processed by a frequency counter. The motives for making use of a counter were: (a) to overcome the long durations required while using the frequency analyser, and, (b) to improve accuracy. The counter chosen (Hewlett Packard 5345A including option 011) requires a signal of the highest possible quality and with a Doppler frequency amplitude above 60 mV peak-to-peak. Accordingly, the Doppler signal had to be amplified and filtered before processing.

5.4.1   Principle of Operation

The frequency counter is a zero crossing counting device. During a specified gate time, the counter counts the number of cycles ('events') (N_e) made by the input signal and calculates an average frequency. The gate time (ΔT_g) can be set by a knob on the counter panel or externally via a gate time control pulse. The counter measures a number of complete cycles. Counting commences with the first zero crossing point following the beginning of the gate pulse, and terminates with the completion of the last cycle within it (see Fig. 5.4.1-1). The duration of the modified gate time pulse over the sequence of complete cycles (ΔT_c) is measured by counting internal pulses of 2 nano-seconds resolution (N_t). The frequency is calculated to be:-

$$F = \frac{N_e}{\Delta T_c}$$

or:-

$$F = \frac{N_e}{N_t} \times \frac{10^9}{2} \quad (Hz)$$

(5.4.1-1)

At the end of each measurement the counter can supply either the frequency (F) information or, (in the computer dump mode) the values of N_e and N_t. To increase the accuracy of a frequency measurement, a gate time pulse as long as possible is required. For the randomly occurring Doppler frequency signals a unit has been devised to generate the gate time pulses synchronized to the envelope shape of the Doppler signals (see Fig. 5.4.1-2).

5.4.2   Interface and Control

To enable automatic measurements the counter has to be interfaced to a mini-computer (see Fig. 5.4.2-1). It is connected via an HPIB* card and it can function either as a "talker" or as a "listener" device. As a listener the computer instructs the counter to operate in the computer dump mode. It then becomes a talker, a mode in which it is able to send measurement results to the computer. The counter interrupt line is switched on and is then capable of responding to the synchronised gate time pulses. As soon as the counter performs a measurement, further interrupts are disabled avoiding multimeasurements out of a single particle signal. The interrupt line is reset at the end of the measurement data transfer.

For each measurement, the counter transfers the values of N_e and N_t numbers to 16 decimal places each. All digits have to be transferred before a new measurement can be made. For the present velocity ranges some of the most significant digits do not contain any information and are automatically ignored. The 32 decimal digits are transferred sequentially, N_e followed by N_t, in the ASCII** format. The two decimal numbers are converted within the computer to the floating point format, in which arithmetical operations can be performed. To minimize the measurement of electronic noise, a condition is set for a minimum number of cycles $(N_{e\ minimum})$. Only signals with $N_e > N_{e\ minimum}$ are then accepted.

5.5   Measurement of Signal Pedestal Amplitude

Information about the particle size is contained in the

---

pedestal amplitude of the signal. The pedestal amplitude changes as the particle travels through the control volume. The maximum of the pedestal amplitude can be viewed as characterising the particle size as discussed in Section 2.4. A system was devised to record the value of the maximum pedestal amplitude of a detected Doppler signal. The system comprised the following:-

(a)   A peak detector which detects and holds the maximum value of the signal amplitude during a prescribed time interval;

(b)   An Analogue-to-Digital Converter (ADC) which converts the analogue value of the maximum amplitude to a binary number;

(c)   A section to control the system and the data transfer to the computer.

The pedestal amplitude measurement system is deployed with the aid of the two-phase flow and the time dependent two-phase flow computer programs.

5.5.1   The Peak Detector

The purpose of the peak detector is to detect the maximum amplitude of the instantaneous pedestal signal within a defined time interval. During that time interval it compares successive instantaneous amplitudes and stores the maximum value. The unit is based on a capacitor which is being charged by a differential amplifier whose output is related to the difference between the input signal and the capacitor voltage.

5.5.2   The Analogue-to-Digital Converter (ADC)

At the end of a defined time interval, the peak detector holds the value of the maximum pedestal amplitude. This value is converted to a binary number by the ADC. The ADC is a linear 10-bit device which gives digital output values of 0 to 1023 to an input analogue voltage of 0 to 5 volts. The amplitude of the signal at the exit of the photo multiplier depends mainly on the particle size. An amplifier was built to amplify the pedestal signal so that for all the various experiments with different particle sizes, the maximum binary value of the pedestal amplitude would be in the range of about 800 to 1000. If signals with an amplitude higher than the maximum range were detected, their recorded amplitude binary value would be 1023.

5.5.3   Control Section

The procedure for measuring the signal pedestal amplitude using the frequency analyser and frequency counter is described below. Timing diagrams and schematic block diagrams incorporating the peak detector are correspondingly given in Figs. 5.5.3-1 and 2 for the frequency analyser, and in Figs. 5.5.3-3 and 4 for the frequency counter based system. The pedestal signal is recovered by passing the photomultiplier signal through a low pass filter. A trigger pulse is generated from the pedestal signal whenever it is above a preset trigger level which initially was set to be just above the background noise. The peak detector produces an analogue voltage with an amplitude equal to the highest value inside the trigger pulse. At the end of the pulse the analogue voltage is converted to a digital number.

The digital information is placed in the input buffer register of the Input/Output parallel interface card. When a frequency is detected by the frequency analyser or the counter an

interrupt signal is set. If the interrupt request signal is set during the time of the trigger pulse, a "size indicator" signal is also set. The interrupt service routine stores the frequency information and also, if the size indicator is set, the digital value of the pedestal amplitude. The data in the computer buffer memory is stored in sequential pairs of frequencies and pedestal amplitudes when using the frequency analyser, and in two different data blocks when using the frequency counter. When a frequency is detected and the related pedestal amplitude is lower than the trigger level, as is the case for most of the gas signals, the size indicator is not set (see Fig. 5.5.3-5 for a counter based system). In the service routine the frequency information is stored, and a zero value is stored for the pedestal amplitude.

5.5.4   System Testing

A test was performed to check the linearity of the signal amplitude measuring system. A simulated Doppler signal was generated with a pedestal amplitude range of 0 to - 2.4 volts. The test was controlled by a program which displayed the pedestal amplitude digital value on the VDU. Tests were performed at various pedestal amplitudes and the results are shown in Fig. 5.5.4-1. The following comments on the results of the tests may be made:-

1.   The linearity of the system is very good. The correlation factor (of a linear regression test) for the effective range is r = 0.9999.

2.   A DC offset is evident in Fig. 5.5.4-1 which is difficult to eliminate.

3.   The digital value of the amplitude is zero until the

analogue voltage exceeds the trigger level at which the

amplitude "jumps" to its appropriate value.

One concludes that the accuracy is sufficient for the

purposes required. When calculating the pedestal amplitude from its

binary value both the slope of the graph and the DC offset must be

taken into consideration.

5.6   Time of Measurement Record

In addition to frequency and maximum pedestal amplitude,

time is also recorded for the "single bubble" experiment. This

operation is assumed to be periodic for every bubble burst. Time is

measured by a continuously operated clock, initialized (at a

reference time) each time a bubble emerges on the bed surface. The

timing system incorporates two principal functions:-

1.   Generation of the reference time marker (see Subsection 5.6.1).

2.   Time measurement (see Subsection 5.6.2).

5.6.1   Reference Time Marker

Single bubbles were generated by the periodic opening of a

solenoid valve (see Section 4.5). As the time required for the bubbles

to traverse the bed is not exactly periodic, a device was introduced

to sense the emergence of the bubbles above the fluidized bed and to

set a reference time marker pulse.

Principle of Operation

An infra-red beam of light, pulsating at 10 KHz is trans-

mitted horizontally through the width of the freeboard at a height of 3 to 5 cm above the bed surface. The beam is aligned to impinge on a photo-detector on the opposite side of the bed (see Fig. 6.2.2-1). The uninterrupted beam produces a 10 KHz pulsating electric signal on the photo-detector. When the beam is blocked, the signal ceases and triggers a pulse, the reference time marker pulse. A light source in the invisible infra-red light range was chosen because of the ease this afforded of obtaining a relatively cheap narrow beam angle light source. The sensitivity of the system, that is the size of obstruction triggering a marker pulse, depends on the beam diameter and on the relative alignment between the light beam and the photo-detector.

Beam Diameter

The effective beam diameter is defined by the sensitive area of the photo-detector. The original sensitive area was so small that particles of the order of 1 mm diameter would block the light path. In order to reduce the sensitivity, a collecting lens was mounted in front of the photo-detector, and a focussing lens in front of the light source. The two lenses increased the effective beam diameter to the extent that only obstructions of about 2.5 mm diameter or greater would block the light path.

Alignment .

To simplify the alignment, the invisible light source was switched on and off at a rate of 10 KHz. The electronic circuitry converts the photo-detector signals, which are above a trigger level, to logic pulses. Since the trigger level is constant, the higher the detected signal amplitudes (i.e. the better the alignment), the wider the trigger pulses. The alignment is effected by observing the trigger pulses on an oscilloscope screen. The light source-detector

position which generates the widest trigger pulses constitutes the best alignment.

5.6.2 Time Measurement

The method of measuring time can be separated into the clock control and the time reading.

(a) Clock Control

An electronic circuit having a 1 MHz crystal oscillator generates pulses at a preselected rate. As the bubble cycle is in the range of 0.5 to 3 seconds, and the time information is stored in a 16-bit binary word, the pulse rate chosen was 10 KHz. These pulses were recorded for each bubble cycle by a clock counter (see Fig. 5.6.2-1). The clock is activated by the reference time marker pulse and is reset to zero at the beginning of the opening pulse of the solenoid valve. The value recorded from the clock counter represents the time information required.

(b) Time Reading

A schematic block diagram including the time measurement control using the frequency analyser is shown in Fig. 5.6.2-2. The time information is transferred to the computer through the input lines of the Input/Output interfaced card. As the maximum pedestal amplitude information is also transferred through these lines, a multiplexer was employed. After the time information has been transferred to the computer, the multiplexer is automatically directed towards the pedestal amplitude ADC to transfer the maximum pedestal amplitude.

When a frequency is detected, the first instruction in the

service routine is to read the time value of the clock. The frequency and the maximum pedestal amplitude of the signal are detected in the same manner as that used for the two-phase flow program (Subsection 5.5.3). The data for each measurement are stored in sequential triplets (frequency; pedestal; time) when using the frequency analyser; or in two data blocks, one block for frequency and the other for pairs of amplitude and time, when using the frequency counter.

5.7   The Mini-Computer

Because of the complexity of the data acquisition and processing requirements, it was clear that no standard commercial equipment was available, and that a mini-computer would be necessary to control the experiments. The selection of a suitable mini-computer was subject to the following requirements:-

1.   Fast 16-bit words central processing unit.

2.   Easily interfaceable to external devices.

3.   Convenient and sophisticated operating system.

4.   Large internal memory for user programs as well as fast access to external storage facilities.

5.   Acceptance of machine and higher level language programs.

6.   Comprehensive well-documented software.

After a market survey, it was concluded that for the present purposes, the DEC LSI 11/03 was the most suitable mini-computer available. It comprised (see Fig. 5.7-1):-

1.   A DEC LSI 11/03 processor with 32,000 16-bit words of memory.

2.   A dual floppy disk unit for 8" single side, single density IBM standard format diskettes.

3.   A parallel Input/Output (I/O) interfacing card (DRV11).

4.   An instrument bus interface card (IBV11-A, also known as IEEE 488 or HPIB).

5.   A Visual Display Unit (VDU) Datamedia Elite 3000.

6.   A DEC LA36 line printer.

7.   A machine language (Macro) and Fortran software package.

5.8   Data Collection

The three signal processing control programs store different quantities of data information. In each program a buffer memory is allocated in the computer memory for temporary data storage (before transfer to the magnetic disk). As a computer data block contains 256 words, for convenience the buffer size is made a multiple of 256. A different memory buffer structure is applied depending on whether a frequency analyser or frequency counter is used.

Frequency Analyser

In the single phase flow program, one word of frequency information is stored for each measurement. The buffer size allocated is 512 words. The two-phase flow program stores two words of information for each measurement, a word for frequency and a word for pedestal amplitude. The buffer size allocated is 512 words for 256 velocity measurements. The time dependent two-phase program stores three words for each measurement; frequency, pedestal, and time. The buffer size allocated is 768 words for 256 velocity measurements.

Frequency Counter

In the time dependent two-phase flows, two different buffers, one for each of the two types of data formats, are allocated. The buffers, one for frequency and one for pedestal and time, are of 1024

each for 512 velocity measurements.

At the beginning of every experiment the program opens a
data file on the diskette in which all the data collected are to be
stored. During the experiment, data are stored in the buffer memory.
Once the buffer is full, a transfer routine is executed and data are
transferred from the buffer memory to the diskette.

The amount of data to be collected in each experiment is
defined at the beginning of each run with respect to the number of
buffer size groups of measurements. The minimum number of data to be
collected is one group. The maximum is limited by the capacity of the
diskette (480 blocks). When the amount of data required is collected,
the last data transfer is executed. The data file is closed and the
experiment terminates.

5.9   Particle Flux Measurement

A further quantity which it would be most desirable to measure
is the number of particles crossing a defined control volume per unit
time. Knowledge of this quantity could be of much assistance in
determining freeboard height based on the concentration of particles
at different levels.

Several investigations are presented in the literature which
predict (see Subsection 1.2.2) and measure (see Subsection 1.2.1) the
decrease in particle concentration with height. These measurements are
usually mechanical. Analysing elutriated particles from a fluidized
bed of different freeboard levels, or isokinetic sampling probes are
usually the techniques applied. These techniques are good, relatively
easy to perform and accurate, the disadvantage being the flow
disturbance and the relative long sampling time. It was thought that
it would be fruitful to expand the present system to enable the particle

counting. Two techniques were investigated.

5.9.1   A Peak Detector Based System

This technique, which required virtually no hardware modification to the measurement system, is based upon counting the number of trigger pulses generated by the peak detector unit (see Subsection 5.5.3) during a known time interval. The ratio of trigger pulse count to time interval would result in particle flux information (number of particles crossing the control volume per unit time).

The trigger pulse would be generated for every signal with pedestal amplitude above the trigger level, the case for sand particle signals as well as for large dust and some fine sand particles. In order to isolate the information on the sand particle flux a correction factor of $N_S/(N_T - N_G)$ should be applied for every measurement:-

$$J_{sand} = J_{trigger\ level} \cdot \frac{N_S}{N_T - N_G} \qquad (5.9.1-1)$$

where:-

J indicates particle flux (number of particles crossing the control volume per unit time)

N_T is the total number of measurements detected during a specific measurement

N_G is the number of gas measurements within the total (N_T) sample

N_S is the number of sand particles measurements within the total (N_T) sample, as classified in the data processing program (see Subsection 2.5.4).

The photomultiplier will detect light scattered from particles inside the control volume as well as from some surrounding region. For a given particle and LDA system, the pedestal amplitude of the detected signal is dependent upon the distance of the particle from the control volume. Fig. 5.9.1-1 describes a typical variation of the pedestal amplitude of a signal from a sand particle fastened to a rotating disc, with increasing distance from the centre of the control volume. This phenomenon implies that trigger pulses will also be obtained from particles outside the control volume with a rather complicated relation between the signal amplitude, the particle size and the intersection location of the particle and the laser beam. For the moment these difficulties prevent the evaluation of absolute values of particle flux.

As the light scattering characteristics is constant for a given system, qualitative information can be obtained by observing the relative flux values after applying the correction 5.9.1-1. This type of information could be useful during investigation of particle flux variation with operating conditions and freeboard location. The values obtained will represent a relative number of particles crossing the control volume per unit time from any direction. The direction ambiguity of the flux information is due to the insensitivity of pedestal amplitude to velocity direction (being different to the Doppler information of a signal). To overcome part of this problem, the flux information should be correlated with the velocity histogram of the sand particle as detected during a specific experiment (see for example Fig. 6.4.4-2) in order to determine the percentage of ascending particles as against the descending ones. The repeatability of the recorded flux values was better than 95% over measurement period of 30 minutes.

5.9.2 A Photodiodes Based System

A different approach to obtaining the absolute flux information

which incorporates some additional electro-optical equipment is currently under development (see Fig. 5.9.2-1). The two laser beams which form the measurement control volume impinge upon two photodiodes located on the collecting lens housing. The beams are usually undisturbed and penetrate through the freeboard striking the two photodiodes. Whenever a sand particle traverses one of the beams, the light will cease to impinge upon the photodiode, a change in its output signal will be detected thus triggering a logic pulse.

When a particle crosses the exact centre of the control volume, it will generate simultaneous signals at the two photodiodes. By imposing certain logic conditions (such as threshold level, overlapping conditions, minimum duration and arrival time difference), selective detection of particles crossing the control volume from any direction could be achieved. There is, however, a good chance of detecting simultaneous signals from two different particles each crossing a different beam, satisfying the logical conditions. Such a possibility cannot be avoided but can be estimated. Sample measurements using two non-crossing beams (see Fig. 5.9.2-2) could measure the probability for the occurrence of such events. These values should be subtracted from the recorded flux values. Currently some optimization of the lens type (L in Fig. 5.9.2-1) and modification of the electronic circuitry are in progress.

5.9.3   Concluding Remarks

When comparing the two techniques, the photodiodes based technique (Subsection 5.9.2) is far superior for the following reasons:-

(a)   the spatial resolution is smaller and easier to
       define;

(b) the system could be adjusted to sense only big particles ($d_p \gtrsim 0.3$ mm) thus eliminating the recording of, and thus confusion with, smaller particles.

Measurements presented in this thesis were recorded using the peak detector based system (Subsection 5.9.1).

CHAPTER 6

RESULT AND DISCUSSION

6.1   Introduction

Several theoretically based attempts have been made to predict elutriation, but much less has been done to confirm the assumptions used by these predictions. With the bed operating condition given, two parameters were recognized as determining the elutriation rate: the initial velocity of the particles at the bed surface and the gaseous flow field in the freeboard. Given this information, the equation of particle motion (for example Equation (1.2.2-1)) can be solved, and the trajectories and maximum height of flight of the particles evaluated. The immediate significance of such information is the ability it confers to define the TDH level below which particle concentration continues to decrease in proportion to freeboard height. Knowing the TDH value is essential for the proper design of the freeboard.

Slightly different information which can be determined is the condition of particle flow at any level below the TDH. This is of special interest where the freeboard height is limited as for example in the case of a horizontal shell boiler (Gibson, 1977a and Gibson, 1977b). As for turbulent systems in nature, mean flow values are not exclusively representative of most real situations. A velocity probability distribution exists for each phase.

The present measurements attempt to expose some of the flow patterns inside the freeboard. Normal bed operation consists of many bubbles simultaneously moving upwards through the bed, coalescing and bursting on the surface. Although bubbles do not always preserve their individual forms and characteristics, it was felt that an investigation of the flow pattern related to single bubble bursts would provide some basic information which could not otherwise be obtained. Two types of

studies were performed: investigation of the flow pattern during the burst of a single bubble, and of the entire flow under normal operating conditions.

Initial measurements with the bed operating under various conditions and during the periodic release of a single bubble were performed using the frequency analyser (see Section 5.3). The counter system which was developed later (Section 5.4) was used for further analysis of normal bed operation.

Sands of two different kinds were used as bed material: sand type A of mean diameter 1.00 mm and sand type B of mean diameter 0.40 mm. Typical size distribution of the two types of sands is given in Fig. 6.1-1. The two types of sand are related to two different particle categories as reported by Geldart (1972). Sand type A particles are within the group d_p > 600 μm and/or of a density characterised by slow bubble velocity, usually slower than the interstitial fluidizing gas velocity. Sand type B on the other hand belongs to the group 40 μm < d_p < 500 μm and 1.4 gr/cm^3 < ρ_p < 4 gr/cm^3 characterised by fast rising bubbles, most of which are faster than the interstitial fluidizing gas velocity. Particles of the same group have broadly similar fluidization properties and generalisation may be made within a category.

6.2   Two-Phase Velocity Measurements in a Periodic "Single Bubble" Bed Operation

During the initial stage of measurements in the freeboard it was realised that many parameters are involved in determining the flow pattern of the two phases. It was felt that an investigation of the gas and the sand particle flow during the burst of a single bubble would result in further understanding of the flow in normal bed operation.

6.2.1 Experimental Conditions

The experimental arrangement is described in Section 4.5.

Time related measurements in the freeboard were carried out at about

minimum fluidization ($U_f = U_{mf}$). Single bubbles were injected

periodically through the nozzle and the measurements were averaged for

each phase over 50 sequential time intervals commencing at the instant

of the bubble's emergence on the bed surface. Mean and r.m.s. values

were calculated for each of these time intervals. A period of 20

milliseconds was deliberately chosen so that the whole cycle would be

longer than the actual time taken by the burst of the bubble and the

descent of the sand particles. In this way, interference between

consecutive bubble cycles could be avoided. The measurements were

performed using the frequency analyser as described in Section 5.6.

The bed operating conditions were (see also Section 4.5):-

Particle mean diameter	0.40 mm
Bed height (static)	340 mm
Fluidizing velocity U_f	0.125 m/s
Bubble release cycle time	1.3 secs
Solenoid valve opening time	0.2 secs
Pressure at air supply vessel	50 psi
Volume of air passed through the valve	1170 cm³

The infra-red light detector (which generated the reference

time marker as described in Subsection 5.6.1) was located about 30 mm

above the static bed surface level. This level is just above the

height of the small bubbles bursting on the bed surface during

operation at the minimum fluidizing velocity. Measurements were

carried out at various heights along the freeboard centre-line (X = 0,

Y = 0 in Fig. 6.2.1-1) which is also the symmetry axis of the bursting

bubble and along the vertical locations X = 100 mm, Y = 0 and X = 200 mm, Y = 0.

As the rate of data collection was low, measurements were carried out over about an hour at each point. The results presented are, therefore, the average of more than 2500 bubble burst cycles.

6.2.2   Result and Discussion

The bubble bursting process is illustrated by sequential photographs and sketches in Fig. 6.2.2-1. Measured data are plotted in Figs. 6.2.2-2, 3, 4. The co-ordinate system is specified in Fig. 6.2.1-1.

We see from these figures that bubble bursting is a repeatable procedure. Accordingly, for constant flow conditions, the two-phase flow can be illustrated by means of "ensemble" averaging over the bubble release cycle. To the eye, successive bubble bursts seem to exhibit small variations but the figures indicate that the phenomenon is constant; this is also evidence that the time recording system performs satisfactorily. Fig. 6.2.2-1 suggests three principle stages of measurements during the bursting of the bubble:-

(a)   The growth of the bubble bulge after the triggering of the reference time marker (see Subsection 5.6.1), but before reaching the lowest level at which sand particle velocity can be measured. Here the LDA system detects mainly gas velocities.

(b)   The extension of the bubble bulge beyond the lowest measurement level limit. At this stage it is nearly impossible to measure, the reason being that during a burst, it is mainly

the particles of the upper part of the bulge that are dispersed by an upward and radial ejection, whereas the particles in the base of the bulge retain a more or less compact structure presenting a "wall" which the laser beam is unable to penetrate.

(c)   After the descent of the major portion of the bubble base material, there is sufficient beam penetration for data to be collected.

A more detailed exposition of the bubble release mechanism is given in Fig. 6.2.2-2. At a level of 60 mm above the static bed level (panel "a" of the figure), an initially high gas velocity was recorded. The velocity increased with time up to a value of 1.5 m/s. During that time the sand velocity was smaller (1.1 m/s). There is no gas or sand velocity information for the following 0.25 seconds (as explained for panel "b" of Fig. 6.2.2-1). Particles are detected only after the dense lower part of the bulge falls away from the path of the laser beams by which time the velocities of the two phases are already negative. The velocity of the downward flowing gas increases, reaching a maximum value of - 0.6 m/s. It then decreases to zero and subsequently attains a positive velocity value. The sand has an absolute negative velocity which is larger than that of the gas. The negative sand velocity increases with time, reaching a maximum value of - 1.7 m/s. It is clearly seen from Fig. 6.2.2-2a that the duration of the gas flow variation is longer than that for the sand. It takes the gas phase about 0.3 seconds longer than the sand to regain the steady state.

At a higher level (Z´ = 110 mm, Fig. 6.2.2-2b), it can be seen that during the initial stage of the burst, the sand particle

velocity (1.5 m/s) exceeds the gas velocity (0.7 m/s). When comparing section (a) and (b) of the figure it appears that the bubble bursts between these levels (60 mm and 110 mm). The fact that the particles at level 110 mm are travelling faster than at the lower level (60 mm), shows that they must have been accelerated (by the gas) between these heights. It would be convenient to define the bursting time as the moment at which the vertical component of the particle velocity exceeds that of the gas. The gas velocity decreases because of the transfer of momentum to the particles through the drag force and because of turbulent diffusion.

At the 110 mm level (section (b) of the figure) there is a shorter period than at (a) during which no information is recorded. Information is missing only during the positive part of the velocity distribution. This indicates that the base of bulge has less effect at this height. The negative gas velocity seems to have a lower magnitude compared with its value at the lower measurement level (Fig. 6.2.2-2a), but it takes longer to reach the steady state. It is also seen in this part of the figure (b) that it is actually the fast descending particles which are now dragging the gas downwards (as we see that they descend first). There is an analogy here with a piston in a cylinder on a suction stroke. The effect of energy being transferred from the sand particles to the gas phase was also observed in the free jet experiment (see Section 3.4). At a higher level, (c) and (d) of the figure, the pattern of the sand particle flow remains the same as in (b). At a level 260 mm above the bed surface, panel (e), virtually no sand particles were detected. (The number was insufficient to obtain velocity measurements). That is, nearly all the particles ejected during the bubble eruption had dropped back to the bed surface. The attenuation of the gas velocity gradients along the freeboard height (probably because of turbulent diffusion) is

seen in panels (c), (d) and (e). The velocity amplitude variation decreases, as height increases, until at a height of 260 mm almost no change of velocity with time is detected.

At the 210 mm and 260 mm levels (Fig. 6.2.2-2) the vertical component of the gas velocity detected was almost zero. This means that in order to maintain the volume of air flow through the freeboard, air is moving vertically faster (than U_f) around the bubble to compensate for the zero velocity in the area directly above the bubble cross-section. Measurements taken along the vertical axis at some distance off the bubble centre-line confirm this assumption. Data along the axis at X = 100 mm, Y = 0 (see Fig. 6.2.1-1) are illustrated in Fig. 6.2.2-3. No positive sand velocity was detected. This was to be expected as the radial component of the sand particles is relatively small and only during the descending parts of their trajectories do they achieve a radial displacement of 100 mm (see Fig. 6.2.2-5). The gas velocity is dragged downwards by the descending particles and slowly regains a positive value. Measurements were also taken at X = 200 mm, Y = 0, with results shown in Fig. 6.2.2-4. The gas velocity is mostly positive. As it is far from the bubble centre-line, no sand particles are present.

A comparison of Fig. 6.2.2-4 with Fig. 6.2.2-2 demonstrates another feature of the gas flow. During the initial bulging of the bubble, some of the gas which forms the cloud surrounding the bubble escapes upwards through the sand particles forming the bulge. This gas is responsible for the increase in velocity measured just above the bed surface on the bubble axis. The bulge growth and the jet-like movement of the fluid entrains surrounding fluid. This is confirmed by panel (a) of Fig. 6.2.2-4, where nearly zero (vertical) velocity is recorded indicating that gas flow must be moving horizontally in order to satisfy mass continuity.

After the bubble burst an effect opposite to the one just described is recorded. At about 0.4 seconds from the beginning of the bubble rise, the negative gas velocity (Fig. 6.2.2-2a) generated by descending sand particles results, at a greater radial distance (about X = 200 mm, Fig. 6.2.2-4a), in a positive (up-going) gas flow. This effect creates a large-scale toroidal shape recirculation zone, the down-flowing gas being on the inner side and the up-flowing gas on the outside. This circulation (the effect of which can sometimes be seen by the eye) is translated upwards as a whole by the main fluidizing velocity. A schematic description of this effect is given in Fig. 6.2.2-6.

6.3   Bias Effect

There is a major biasing effect on velocities measured in the lower part of the freeboard, in the region where the bubbles are still in the process of bursting. This effect is present during normal bed operation but can be more easily demonstrated with the single bubble release operation. The eruption of the bubbles tends to occur in such a way that during the initial part of the process velocity measurements cannot be made (see Subsection 6.2.2 and Fig. 6.2.2-2a and b). As this phenomenon is repeated continually at that part of the cycle at which the velocities are positive (up-going), a tendency for the recorded mean velocity to be biased towards lower values is inescapable. The biasing affects both phases with the same tendency and decreases as the measurement level increases.

The particulate phase is affected because only the first layer of particles, at the top of the bulge, can be measured. The succeeding particles, still within the top part of the bulge, are prevented from being measured because of the blockage of the laser beams. An additional cause of the same effect is the curvature of the top of the

bulge (see Fig. 6.3-1 Part a). Theoretically no particle can be measured while the bulge is ascending (as the beams would be blocked before they could cross to form the control volume). To overcome this problem measurements should be performed at some angle of inclination to the horizontal level (Fig. 6.3-1 Part b). Such measurements were not currently undertaken because of attendant and related difficulties (arising mainly from the required modification of the optical bench). However, some particles were detected, as can be seen in Fig. 6.3-2 (the velocity results are the same as in Fig. 6.2.2-2b). It can be seen from the figure that the number of ascending particles measured was far lower than those detected while descending and they probably existed somewhat in advance of the main bulge. Operating the bed with high fluidizing velocities which cause a more sluggish situation, all previously mentioned effects were encountered with the addition of some large agglomerations of particles which were ejected upwards (see Fig. 6.3-3). These agglomerations tend to preserve some of their shape as they ascend, separating to a more dispersed form and thus becoming measurable while descending, a characteristic which reinforces the sand particle bias effect.

Gas phase velocity measurements could be performed until the bulge encountered the laser beams which prevented the measurement of the gas contained inside the bubbles. Gas is discharged during the bursting process of the bubbles and is measurable at higher levels. As the mean gas velocity inside the bubbles is positive, a biasing towards lower velocity values will be recorded at low freeboard levels.

The level at which the bias effect becomes insignificant depends on the operating conditions of the bed, mainly upon the bed height and fluidizing velocity; for example, with a bed height of 200 mm, particle mean diameter d_p = 0.40 mm and fluidizing velocity

$\overline{U}_f$ = 0.40 m/s, a level of about 250 mm above the static bed level
($\overline{U}_f$ = 0) is the upper limit of the region influenced by the bias
effect (see Fig. 6.4.3-9).

As in the present experiments, the mean fluidizing velocity
is much smaller than the particle terminal velocity, no particle loss
would be expected from the very high freeboard. As the sand particles
are relatively large, the influence of the drag force on them due to
the surrounding gas flow is small. Assuming even flow distribution
across the bed, falling particles will have final velocities of less
than or equal to their initial ascending vertical velocities. The
actual mean local particle velocity would, therefore, be expected to be
positive and close to zero, with a nearly symmetrical velocity
distribution about the mean. The biasing effect usually shifts their
measured mean velocity to negative values. A first order correction of
the bias error could be achieved by reflecting the negative part of the
velocity histogram on the positive side $\left[U_p^{'} (x) = U_p^{'} (- x) \right]$; the
resulting mean velocity would be zero.

6.4   Two-Phase Velocity Measurements with Normal Bed Operation

6.4.1   Experimental Conditions

The measurements in the freeboard of the fluidized bed were
performed at different freeboard heights and cross-sectional locations
with different values of some of the operating parameters. An attempt
was made to try to understand the general gas flow field pattern in
the freeboard and to acquire some general knowledge about the behaviour
of the sand particles.

The measurements were performed using two types of sand
(d_p = 1.00 mm; d_p = 0.40 mm). For each sand type several fluidizing

velocities were applied and measurements were performed mainly along the freeboard centre-line ($X = Y = 0$, Fig. 4.2-1) as well as in horizontal planes along $\hat{x}$ and $\hat{y}$ directions. The various operating conditions are listed in Table 6.4.1-1.

Measurements of the vertical components of the two-phase velocities were performed at various heights from the lowest possible level (at which the beams were not completely obscured by the sand particles) to the highest level (at which sand could hardly be found). Because of the long period required for each measurement (1 to 2 hours per point), only a few points could be analysed.

Towards the end of the measurement programme it was realized that the gas flow pattern holds more interest than the sand flow and so at the later stage (in the main while using the frequency counter system) more attention was paid to the gas measurements. By lowering the settings of the trigger level in the Doppler signal envelope detector unit (see Subsection 5.4.1), the gas signal data rate increased rapidly (while the sand signal rate remained constant), reducing the measuring time to about 10 minutes per point. Faster data collection rates are not recommended as the average period of the bubble bursting phenomenon is 1 to 2 seconds, and a few hundred cycles are required to achieve a statistically reliable result. Eight blocks of data were usually collected at each point of measurement. Using the frequency analyser system, an average sample size of about 1000 was achieved at each location for the gas phase and of about 500 for the sand particles. Using the frequency counter system about twice as much information could be obtained. By concentrating on the gas phase measurements the sample size could be raised to nearly 4000 measurements per point.

Minimum fluidizing velocities for the two types of sand were

TABLE 6.4.1-1

EXPERIMENTAL OPERATING CONDITIONS

Experiment group	d_p - Particle mean diameter (mm)	U_f - Fluidizing velocity	Bed height (static) (mm)	Processing system*
A1	1.00***	0.65	365	FQA
A2	1.00	0.875	365	FQA
HA1	1.00	0.75 - 1.175	300	CNTR
HA2	1.00	1.17	350	CNTR**
B1	0.40****	0.195	200	FQA
B2	0.40	0.235	200	FQA
B3	0.40	0.400	200	FQA
HB1	0.40	0.400	200	CNTR
HB2	0.40	0.400	100 - 300	CNTR

*   FQA $\equiv$ Frequency analyser based system
        CNTR $\equiv$ Frequency counter based system

**   With dividing wall inside the bed (see Subsection 6.4.1)

*** U_{mf} (d_p = 1.00 mm) = 0.50 m/s, see Fig. 6.4.1-1

**** U_{mf} (d_p = 0.40 mm) = 0.135 m/s, see Fig. 6.4.1-2

established by pressure measurements across the bed, the values being extracted from Figs. 6.4.1-1 and 6.4.1-2. The pressure drop across the distributer is a function of the velocity of the flow and, therefore, varied from one experiment to another (see Fig. 4.2.3-2). The relation between the fluidizing velocity and the pressure drop ratio across the bed and across the distributer is given in Fig. 6.4.1-3. As it was not practical to change the distributer, some experiments were conducted with a pressure drop across the distributer below the recommended values $(\Delta P_{bed} \leq \Delta P_{distributor} \geq 0.03$ bar) whereas some were conducted at a value of nearly twice as much. However, because of the high quality of the distributor the low pressure drop did not seem to create difficulties and the quality of distribution appeared to be entirely satisfactory. In order to investigate the source of the velocity profile across the freeboard obtained during the measurements, a dividing wall was installed in the bottom part of the bed (see Fig. 6.4.1-4), separating the dense bed into two equal beds of 305 mm x 305 mm each. The height of the dividing wall was 350 mm, the same as the static bed level for those experiments.

Towards the final period of the experiment some degree of consistent assymmetry in the flow distribution was detected (see for example Fig. 6.4.3-5). It is assumed that some dust penetrated the distributor and created some disturbance, resulting in an uneven pressure drop across the distributor surface.

6.4.2   Experimental Results

At each measurement point about 500 to 4000 velocity measurements were averaged to produce mean and r.m.s. values. For each point velocity histograms were displayed on the VDU screen to ensure the accuracy of the measured result. A sample of these

histograms is presented in Figs. 6.4.2-1 to 6. All measurements results are presented in Figs. 6.4.3-1 to 6.4.4-12.

Description of Figures

Figs. 6.4.2-1 and 6.4.2-2 show the gas and sand velocities histograms using the 1.00 mm diameter sand particles as the material for U_f = 0.65 m/sec for Z' = 210 mm (measured from the static bed height) and for U_f = 0.875 m/sec and Z' = 480 mm (experiment group A1 and A2 respectively, see Table 6.4.1-1). Figs. 6.4.2-3, 4 and 6.4.2-5, 6 present the histograms for the 0.40 mm particle diameter sand for U_f = 0.195 m/sec, Z' = 110 mm and for the 1.00 mm particle diameter for U_f = 0.875 m/sec, X = 295 mm, Y = 0, Z' = 480 mm (experiments groups B1 and A2 respectively, see Table 6.4.1-1). The latter figures are the actual print-outs from the data processing system.

The abscissa describes the instantaneous velocity of each phase. It is divided into 64 segments for the first two figures and into 128 for the latter four printed by the computer. Each segment represents a velocity range defined by the processing system, and by the optical dimension. The ordinate shows the normalized frequency of events (i.e. the number of times the measured velocity lies within a specific velocity range divided by the total number of measurements). The letters F and M in the printed figures designate the fluidizing velocity and the calculated mean velocity. A letter C appears whenever F and M overlap.

The distribution of mean and r.m.s. velocity values along horizontal and vertical axes for different fluidizing velocities, bed material and bed height are shown in Figs. 6.4.3-1 to 6.4.4-11 and discussed in the following sections; Subsection 6.4.3 summarizes

the gaseous phase results and Subsection 6.4.4 that of the particulate phase.

6.4.3 Discussion of the Result - Gas Phase

Extensive measurements were performed with the emphasis on the gas phase and a substantial amount of data is available.

The most significant, as well as surprising, result obtained from the measured flow field was while performing a horizontal traversing across the bed. The location of maximum velocity was found to be not on the centre-line of the freeboard, as predicted by previous investigators (for example Wen and Hashinger, 1960), but somewhere close to the freeboard walls. A typical velocity distribution is shown in Fig. 6.4.3-1. The velocity is zero at the walls (because of no slip boundary condition), increases rapidly to a maximum somewhere near the wall (at a distance of about 30 - 50 mm) and decreases to a minimum value at the centre. This velocity profile, which is further discussed below, suggests in three dimensions a profile having a volcano crater shape. This type of distribution has, to the best of the author's knowledge, never before been discovered and it was, therefore, further analysed under different operating conditions. The author has decided to name this phenomena after its discoverer - the Levy dip.

With sand type B (d_p = 0.40 mm) and a constant fluidizing velocity of $\bar{U}_f$ = 0.4 (m/s) ($\bar{U}_f/\bar{U}_{mf} \simeq 3$) velocity measurements are presented along the $\hat{x}$ axis (Y = 0, Z´ = 500 mm), Fig. 6.4.3-1, and along the $\hat{y}$ axis (X = 0, Z´ = 500 mm), Fig. 6.4.3-2. The two figures demonstrate the three-dimensionality of the dip. It is clearly seen from the two figures that a higher value is recorded near the short wall (Y, X = 305 mm) than near the long one (X, Y = 152 mm). This illustrates

an assymmetric flow effect due to assymmetry in the freeboard cross-section. A three-dimensional sketch of the velocity distribution is given in Fig. 6.4.3-3.

Two other horizontal velocity profiles were obtained at different vertical levels and together with the information of Fig. 6.4.3-1 are plotted in Fig. 6.4.3-4. It is clearly seen that for the three levels presented ($Z' = 300, 500, 700$ mm) neither the shape nor the magnitude of the velocity distribution is significantly changed. The measured differences of about $\pm 5\%$ in the absolute mean velocity values can be considered negligible. What can also be clearly seen from the figure is the significant decrease in the velocity fluctuations (r.m.s. velocity values; $\sqrt{\overline{U'^2}}$) with the increase in distance from the bubbling bed surface. This phenomenon will be discussed later.

Velocity distributions displaying the same features were discovered while using the type A sand ($d_p = 1.00$ mm). The existence of the dip profile and its variation with fluidizing velocity is demonstrated in Figs. 6.4.3-5 and 6.4.3-6. It can clearly be seen that as the fluidizing velocity increases, centre-line velocity and r.m.s. values increase as well. The shape of the distribution, i.e. $\left(\frac{d\overline{U}_g}{dx}\right)_{\hat{x}}$, stays nearly the same. Fig. 6.4.3-7 demonstrates a nearly linear relation between fluidizing velocity and the measured free-board centre-line velocity. If we extrapolate towards the low values, a common velocity value of 0.5 (m/s) will be encountered which is actually the minimum fluidizing velocity for these sand particles.

Two explanations can be offered to explain the dip velocity distribution. The first is the possibility of an uneven effect created by the dense bed on the flow in the freeboard (for example a systematic and uneven bubble flow distribution inside the bed). The

second is the possibility of some effect originating in the freeboard itself.

Werther and Moulerus (1973) found a systematic bubble flow pattern inside the bed in which bubbles are more likely to be generated near the wall close to the distributer, and to expand as they approach the bed centre.

A possible freeboard source for the dip profile is the gas vortex generated each time a bubble bursts. The possible existence of these toroid vortices has been discussed in Subsection 6.2.2 (the suggested flow is sketched in Fig. 6.2.2-6). They have a direction of rotation which moves upwards at the outer boundaries and downwards on the inside. When several bubbles burst randomly in time and location, their corresponding vortices superimpose to form a general net of vertical velocity which increases on the periphery and decreases in the centre, thereby creating the dip shape of the profile. The dip profile could very well be the outcome of both effects, i.e. more bubbles near the wall generate vortices super-imposed on each other to produce the resultant dip shape of velocity profile.

A further argument which lends support to the occurrence of this phenomenon is contained in Fig. 6.4.3-4. The fact that the velocity distribution does not change with height indicates a flow influenced by vortex conservation because since the flow rate and vorticity are constant, so must be the velocity profile. If the vertical velocity gradients were to be generated solely from the pulses of air being discharged from bubbles bursting on the bed surface in such a way as to generate the dip shape, then sheer stress and turbulent energy dissipation would cause both r.m.s. velocity fluctuation and mean velocity gradients to attenuate rapidly

with height. This was demonstrated in the single bubble experiment (Fig. 6.2.2-2) in which the gas pulse discharged during the bubble bursting dissipated and no variation of velocity with time was recorded at a level of 300 mm above the bed surface.

In order to further investigate the source of the dip shape of the velocity profile, measurements across the freeboard were performed with a dividing wall installed in the bed (Subsection 6.4.1; see Fig. 6.4.1-4). Any wall effect inside the dense bed affecting the gas flow in the freeboard should also exist near the dividing wall with nearly similar influence on the freeboard flow. Measurement results with sand type A (d_p = 1.00 mm) and U_f = 1.1 m/s ($\overline{U}_f/\overline{U}_{mf}$ = 2.2) indicated no significant influence by the dividing wall (see Fig. 6.4.3-8). Although a smaller variation in the mean velocity values was detected across the freeboard, the dip shape of the velocity distribution could be identified.

Measurements using sand type B (d_p = 0.40 mm) with constant fluidizing velocity ($\overline{U}_f$ = 0.4 m/s) along the vertical axis $\hat{z}$ at the bed centre-line (X = Y = 0) demonstrated the velocity bias effect (see Section 6.3). The effect which tends to reduce the mean velocity values recorded in the region where the bubbles are still bursting can be seen in Fig. 6.4.3-9. As soon as the measurement level was above the region of the bursting bubbles (Z' = 250 mm), the measured mean velocity value approaches a nearly constant level and did not vary up to the highest measuring level (Z' = 900 mm). If the dip shape of the velocity distribution across the bed was attenuated with freeboard height, a steady increase in the mean velocity (to satisfy mass continuity) would have been recorded.

r.m.s. velocity fluctuations decrease as height increases (see Fig. 6.4.3-9). The turbulent intensity values ($\sqrt{\overline{U_g'^2}}/\overline{U}_f$)

reduce from a level of 140% ($Z' = 200$) down to about 40% ($Z' = 900$). These values are of an order of magnitude bigger than those which are recorded in turbulent flow rectangular ducts, as described for example by Melling and Whitelaw (1976). The decrease of r.m.s. velocity fluctuation ($\sqrt{\overline{U_g'^2}}$) with height was also described in the work of Horio et al (1980). They assumed a freeboard turbulent intensity decay of similar characteristics to those of a steady free jet.

A plot of the logarithm of the r.m.s. velocity fluctuation compared to freeboard height (Fig. 6.4.3-10) indicates that a nearly exponential decay exists from about 400 mm to 500 mm above the static bed level. This level (specific to certain bed operating conditions) is about the maximum level where a significant number of sand particles are still flowing, generating turbulence in the gas phase. A correlation for the variation of normalized velocity fluctuation with freeboard height was found from Fig. 6.4.3-10 (for $0.9 \geq Z' \geq 0.5$ m):-

$$\frac{\sqrt{\overline{U'^2}}\ (Z')}{\overline{U}_f} = 1.14\ e^{-1.275\ \cdot\ Z'} \qquad\qquad (6.4.3-1)$$

The influence of bed height upon the velocity fluctuations was also examined. Measurements were made for three bed heights (experiment group HB2, see Table 6.4.1-1). Smaller fluctuating velocities were recorded for lower bed heights and the effect is clearly seen in Fig. 6.4.3-11. The reason for this effect is that shallower beds are characterized by smaller and slower moving bubbles (see also Subsection 1.1.3). Consequently smaller and slower bursts of gas are discharged thus generating smaller fluctuating velocities.

6.4.4   Discussion of the Results: Sand Phase

Interpretation of the sand measurement results is somewhat more difficult than that for gas. The bias effect (Section 6.3) and the relatively smaller sample size of data per point of measurement affect the quality of the results. Horizontal and vertical traverses were performed for different fluidizing velocities and for two types of sand particles.

As previously mentioned, the sand mean velocity is expected to be close to zero, the reason being that nearly all up-moving sand particles return to the bed at about the same velocity. As a first approximation (i.e. ignoring the drag force on the particles and possible horizontal variations), the velocity probability function at a fixed point in the freeboard of the up-going particles should be equal to that of the down-moving particles with equal absolute mean values $\left[\overline{U}_p(up) = \overline{U}_p(down)\right]$. Although difficulties were encountered the author was able to demonstrate this phenomenon. Fig. 6.4.4-1 schematically illustrates the variation of velocity probability function with freeboard height. Figs. 6.4.4-2 and 3 (which are the print-out of the particles velocity histograms for d_p = 1.00 mm, $\overline{U}_f$ = 1.03 m/s, Y = 0, Z´ = 400 mm and X = 0, and X = 122 mm respectively - see Fig. 4.2-1) clearly show two peaks, one on the negative side and one on the positive side of the histogram. The overall mean value is close to zero.

In theory the distance between the two peaks should be greater in the lower part of the freeboard level, should overlap at the higher level and disappear at the height of maximum particles flight (Fig. 6.4.4-1). In practice, when measuring at low freeboard levels, the bias effect (see Section 6.3) attenuates the positive part of the histogram and sometimes prevents almost any positive velocity measurements (for example for d_p = 0.40 mm, X = Y = 0, Z´ = 50 mm, $\overline{U}_f$ = 0.195 m/s,

see Fig. 6.4.4-4). A consequence of that phenomenon is that the r.m.s. values of the detected velocity histograms in the lower part of the freeboard are lower than their real values. As the measurement level increases and the bias effect weakens, more up-going particles are detected, the velocity distribution becomes wider and velocity r.m.s. values increase. This feature is clearly see for example in Figs. 6.4.4-5. In some situations there is some kind of balance between the increase in the recorded r.m.s. values as a consequence of bias effect attenuation and the decrease because of higher measurement level. In reality, for given flow conditions, r.m.s. values should decrease with freeboard height.

As the whole of the velocity probability function should not and usually does not obtain a normal (Gaussian) distribution*, the interpretation of the measurement results is, therefore, not straightforward. The calculated mean value (arithmetic mean) is not necessarily the median (the middle value) nor is it the mode (the value which occurs with the greatest frequency) of the measured values. It should further be indicated that the standard deviation (r.m.s. value) which represents the deviation of the measurement values from the mean, cannot be directly used with tables of normal distribution in order to evaluate the percentage of the histogram above a certain level**.

Although a quantitative interpretation of the measurement results is difficult, useful qualitative information may be deduced.

Measurements were performed along the freeboard centre-line, using sand type B (d_p = 0.40 mm) with three fluidizing velocities. Fig. 6.4.4-5 demonstrates the velocity variation with freeboard height for a

---

* Calculation of the skewness and kurtosis (third and fourth moment) of the measured data usually indicated deviation from normal distribution.

** For example, for normal distribution, 15.8% of the sample population would be above the $\bar{U} + \sqrt{\overline{U'^2}}$ value

fluidizing velocity of 0.195 m/sec ($U_f/U_{mf} \simeq 1.4$). This flow condition gives a relatively small amount of small bubbles with lower bursting and ejection velocities. The bubble bulge usually preserves its shape even during the air discharge and consequently particles exist only in the lowest freeboard region. Two effects are seen in the figure:-

(a)   the mean velocity value is increasing (obtaining less negative values) with freeboard height;

(b)   r.m.s. values increase as well, probably as bias effect becomes less significant (more ascending particles are detected as measurement level increases).

An additional possible contribution to the negative tendency of the velocity distribution is the very low measurement level (see Fig. 6.4.4-5), some of which are below the level where the maximum ejection velocities are obtained. As the particles descend to the low levels, they obtain a negative velocity of the order of their maximum positive velocity, thus recording a negative mean value.

Higher fluidizing velocities ($\overline{U}_f$ = 0.235, $U_f/U_{mf} \simeq 1.7$) result in a stronger bubbling bed, stronger eruptions and higher ejection velocities. Mean velocity values approach zero value at a height of about 180 mm above the static bed level (see Fig. 6.4.4-6) while the r.m.s. values increase up to that height and then stabilize. Absolute r.m.s. values are higher than those of the gas phase and values as high as 0.66 m/sec ($\sqrt{\overline{U_p'^2}}/\overline{U}_f \simeq 2.5$) were recorded. With even higher fluidizing velocities, $\overline{U}_f/\overline{U}_{mf} = \sim 3.0$ (Fig. 6.4.4-7), the particle attained higher levels and measurements could be performed up to 500 mm above the bed surface. The mean velocity values

approached zero at a level of about 300 mm above the bed surface, but r.m.s. values remained relatively constant with height, indicating some balance between the biasing and the r.m.s. decay with measurement heights.

Measurements with the bigger sand particles (type A, d_p = 1.00 mm) show similar features. For low fluidizing velocities ($\bar{U}_f/\bar{U}_{mf}$ = 1.3) the mean values monotonically approach zero as the measurement level increases (see Fig. 6.4.4-8). Sand particles were not found much beyond 210 mm above the (static) bed surface in sufficient numbers to enable an accurate measurement. Higher fluidizing velocities (U_f/U_{mf} = 1.7, see Fig. 6.4.4-9) result in particle flow to much higher levels. The mean particle velocities approach zero as the measurement level increases and the r.m.s. values increase as well reaching a value of $\sqrt{\overline{U_p'^2}}$ = 1.5 (m/sec).

Vertical traversing at 10 mm from the wall (along Z' where X = 295 mm, Y = 0, see Fig. 4.2-1) revealed slightly higher negative values than along the freeboard centre-line, see Fig. 6.4.4-10. The detected sand particles r.m.s. velocity values as well as the gas mean and r.m.s. velocity values generally remain constant.

Results of horizontal scanning of velocity measurements at 400 mm above the static bed level for a slightly higher fluidizing velocity ($\bar{U}_f$ = 1.03 m/s, $\bar{U}_f/U_{mf}$ ≃ 2) and a lower static bed level (300 mm) are presented in Fig. 6.4.4-11. The mean velocity values of the sand particles are detected to be around zero. Sand particles r.m.s. values were all near 1.1 (m/s) ($\sqrt{\overline{U_p'^2}}/\bar{U}_f$ ≃ 1.05), whereas the gas phase fluctuation ($\sqrt{\overline{U_g'^2}}/\bar{U}_f$) varied from 0.7 in the centre-line to about 1.1 near the wall. No significant variation with horizontal location was encountered. This implies that there is virtually no influence of the gas flow field (especially in the high velocity region near the wall) on the sand behaviour. A similar phenomenon was found for the free jet

experiment (see particle category II, Section 3.4). This set of measurements (performed with the frequency counter system) provided results of high quality. The bias effect is nearly negligible and, therefore, the r.m.s. of the sand velocities do represent the real values. The velocity histograms presented in Figs. 6.4.4-2 and 3, demonstrating a nearly symmetrical distribution around the mean ($\overline{U}_p \simeq$ 0), actually form part of this set of measurements.

Although the particle flux measurement system is still under development some approximate data have been collected along the free-board centre-line. The results are shown in Fig. 6.4.4-12. The dimensionless particle flux clearly describes an exponential decay with freeboard height (part (b) of the figure). This tendency agrees with the results of previous investigations (for example see Gilliland et al, 1962).

There is virtually no similar work with which to compare the present sand velocity results. Only the results of Horio et al (1980) are available. Their work was performed in a 0.24 metre diameter bed with particle diameter of 57 μm. The fluidizing velocity was 0.3 m/sec (above the particle terminal velocity, U_t = 0.24 m/sec). They identified two distinct regions: an inner one where the particle mean velocity was essentially constant with values of about 150% of the superficial gas velocity ($\overline{U}_p \simeq$ 0.5 m/s), and an outer zone (ring layer near the cylindrical wall) within which the velocities are negative and of about the same magnitude ($\overline{U}_p \simeq$ - 0.5 m/s). In the present work no such high mean velocities were encountered. Their findings may be due to the use of much smaller particles with fluidizing velocities higher than their terminal velocities, resulting in the particles tending to follow the gas velocity fluctuations.

CHAPTER 7

CLOSURE

The work described in this thesis has been concerned with the investigation of two-phase flow behaviour in the freeboard of a fluidized bed. Velocity measurements of the gas phase and of the sand particles were performed during the periodic release of a single bubble, and during a bed operation in various conditions at different freeboard locations. The results of the measurements indicated some new and interesting phenomena regarding the behaviour of the gas and sand flow.

Existing elutriation prediction methods are usually experimentally based and in consequence lack universality. In general, the various experiments which have been performed by the different research groups using different operating conditions, have been correlated with the aid of some dimensionless groups. Extrapolation from these correlations to different and real operating conditions became the technique available to predict elutriation. Different wall effects and the use of particles of various types (see Geldart, 1972) reduces the accuracy of these correlations. When applied to other conditions differences of up to 1000% have sometimes been recorded.

Given the initial particle velocities (close to the bed surface) and the gas flowfield in the freeboard for different operating conditions, more accurate entrainment prediction could be obtained for different freeboard heights. However, few references exist about velocity measurements in the freeboard. The hot-wire techniques have been used for gas measurements and cine-camera and fibre optic probes for the solid particle. The main difficulty of the hot-wire technique is the restriction of measurement to places where there

are no particles (which can damage the probe), and to where the local

gas turbulence intensity is below about 40%. The cine-camera can only

work accurately in a two-dimensional domain of low particle

concentration; while the use of the fibre optics probe introduces a

disturbance to the particulate flow which must inevitably produce some

error, the magnitude of which should be further analysed.

A different technique for the velocity measurements of the

two-phase flow is described herein. An extended laser Doppler

anemometer system with the facility to indicate the size of the

particles as well as their velocities was developed. The discrimination

between the signals from the two phases is based upon the difference

in the signal's pedestal amplitude associated with each phase.

The technique was tested and found to be successful in its

ability to discriminate signals with different associated pedestal

amplitudes. It was tested initially using electronically simulated

signals, as well as by a specially conducted two-phase jet flow

experiment. In the latter, velocity measurements of the gas and

sand particles of different sizes were performed. The operation of

the discrimination technique is clearly illustrated in Fig. 3.3-2.

The response of the particles to the gas turbulence has been discussed

and different behavioural ranges of particles' diameters have been

defined.

A fluidized bed (Fig. 4.2-1) with glass walls to enable the

optical measurements together with an optical bench and a traversing

table were constructed. A special electronic system interfaced to a

mini-computer to control the experiment, collect the data and process

the measured results was developed. The system is capable of

controlling either of two Doppler frequency processors - a frequency

analyser or a frequency counter. For every velocity measurement,

the pedestal amplitude is recorded as an indication of the detected

particle size. With this system the time of measurement may also be

recorded.

Velocity measurements of the two phases were performed in

the freeboard for a periodic release of single bubbles. The gas flow

pattern, as demonstrated by the experimental results, suggested the

generation of vortices associated with each bubble release cycle (see

Fig. 6.2.2-6). The gas volume discharged during the bubble burst

dissipated rather quickly and was undetectable at relatively short

heights (see Fig. 6.2.2-2). The velocity measurements of the sand

particles indicated (see Fig. 6.2.2-2) that particles are ejected with high

velocities in the order of the maximum gas velocity circulating inside

the rising bubble (Equation (1.1.3-6)). The short lateral displacement

of the particles indicated that the ejection direction is close to

vertical. This observation, which agrees with the suggested bubble

bursting phenomena (see Subsection 1.1.4), indicates that the kinetic

energy of the particles is mainly obtained through the momentum transfer

from the circulating gas within the bubble rather than from the bubble's

internal pressure. A bias effect on the measured velocity, which

originates from the nature of the flow, was encountered. The bias,

which mainly affects the sand measurements, reduces the recorded mean

and r.m.s. velocity values. Its effect lessens as measurement level

increases.

The two-phase flow in the freeboard was measured at various

normal bed operating conditions. A gas flow pattern which was

essentially different from that of turbulent duct flow was detected.

The location of the maximum velocity is not along the freeboard centre-

line but rather at a small distance from the wall (Fig. 6.4.3-1),

forming a velocity distribution which dips to a minimum value at the

bed centre-line. To the best of the author's knowledge the dip shape of the velocity profile has not previously been predicted or detected by any study and he believes that it also exists in other fluidized bed systems of similar operating conditions. The source of the dip-shaped distribution is suggested, at least partially, to be the vortices generated during the bursting of the bubbles. This idea is supported by the fact that the shape of the velocity distribution does not change with freeboard height. The possibility that the dip shape originates solely from wall effect inside the dense bed was excluded by detecting the dip shape even when introducing a dividing wall inside the bed (see Fig. 6.4.3-8).

The mean fluctuating velocities were found to be much higher (about 10 times) than those in turbulent duct flow. The diminution of turbulence with freeboard height follows an exponential curve, starting from the level where the bubbles complete their burst and where particle agglomeration disperses.

As the terminal velocity of the particles is greater than the maximum local gas velocity, no particle elutriation was expected in the present system. In general the mean sand velocity was found to be close to zero with no significant variation across horizontal planes. An illustration of the estimated variation of sand velocity distribution with freeboard height is given in Fig. 6.4.4-1. Normalized sand r.m.s. velocities ($\sqrt{\overline{U_p'^2}}/U_f$) of the smaller particles ($d_p = 0.40$ mm) were found to be larger than those for bigger particles ($d_p = 1.00$ mm).

The velocity measurements of the sand particles were subjected to a bias effect which reduces the recorded mean and r.m.s. values (see Section 6.3). Sand r.m.s. velocities are expected to diminish with freeboard height. No such effect is seen in the present results probably due to this bias effect. The level at which the effect

becomes insignificant varies with the operating conditions of the fluidized bed, and can be considered to be the level at which the recorded mean (sand) velocity is zero.

A full comparison between the current single bubble results and the results of normal bed operation is not yet possible. To achieve this the following must be done:-

1.   An analysis of the bubble size distribution at the surface of a normally operated fluidized bed must be made.

2.   An estimate of the rate of bubble burst per unit bed area is required.

3.   Measurements during the periodic release of single bubbles but with operating conditions as for item 1 must be carried out.

4.   The data from the various single bubble measurements together with the information from item 2 must be combined to give the two-phase behaviour of a normal bed operation.

The particle flux information together with that of the gas velocity distribution (as for example Figs. 6.4.3-4) and of the sand velocity histogram (as for example Fig. 6.4.4-2) are sufficient to illustrate accurately the complete flow pattern in the freeboard. The use of such information could considerably assist the development of computer programs to evaluate the freeboard flow. For such programs it will be required to state the initial condition of the flow. This information could be obtained either from measurements at low freeboard

level, or by extrapolating the information from the single bubble experiments as described previously in this chapter.

To the fluidized bed designer the information of this thesis can be of much use. The knowledge of the existence and location of high gas velocity regions in which the mean velocity reaches about 1.7 . $\bar{U}_f$, and of the existence of a fluctuating component of more than four times the mean fluidizing velocity value, could assist in determining the entrained particle size range. The design of exhaust pipes for fluidized beds is another application which could be influenced by the present information. For a given mass flow rate through the exhaust pipe, inlets located at an area of large velocity gradients would result in localized high velocity regions and, therefore, larger particles would be entrained. Eliminating those regions or the use of specially designed baffles to attenuate such velocity gradients could result in elutriation rate reduction.

For a fluidized bed combuster, where combustion of the volatiles proceeds in the freeboard, the gas velocity variation across the bed could result in different combustion pattern regions. This could be of importance considering the relatively high percentage of heat generated by the volatiles in the freeboard.

REFERENCES

ABBAS, A. S., KOUSSA, S. S. and LOCKWOOD, F. C. (1980)
The prediction of the particle laden gas flow.
Mechanical Engineering Department, Imperial College of Science and
Technology, Internal Report No. FS/80/1.

ABBISS, J. B., CHUBB, T. W. and PIKE, E. R. (1974)
Laser Doppler anemometry.
Optics and Laser Technology, December.

ABRAMOVICH, G. N. (1970)
The effect of admixture of solid particles or droplets, on the
structure of a turbulent gas jet.
Soviet Physics - Doklady, Vol. 15, No. 2.

ABUAF, N. and GUTFINGER, C. (1971)
Entrainment of solid particles in a turbulent air jet - a preliminary
study.
Israel J. of Technology, Vol. 9, No. 4, pp. 389-395.

ADRIAN, R. J. and ORLOFF, K. L. (1977)
Laser anemometer signals: visibility characteristics and application
to particle sizing.
Applied Optics, Vol. 16, No. 3, pp. 677-684.

AL TAWEEL, A. M. and LANDAU, J. (1977)
Turbulence modulation in two-phase jets.
Int. J. Multiphase Flow, Vol. 3, pp. 341-351.

ANDREW, J. M. (1960)
Kinetic study of fluidized solid entrainment.
Industrial and Engineering Chemistry, Vol. 52, No. 1, pp. 85-88.

BACHALO, W. D. (1978)
On-line particle diagnostics systems for application in hostile
environments.
Presented at Third International Workshop on Laser Velocimetry, Purdue
University, July 11 - 13.

BACHALO, W. D. (1980)
Method for measuring the size and velocity of spheres by dual-beam
light-scatter interferometry.
Applied Optics, Vol. 19, No. 3. pp. 363-370. ·

BACHALO, W. D. and HESS, C. F. (1980)
Optical diagnostics techniques for particulate and turbulence
measurements in combustion research.
Western States Section, The Combustion Institute, Spring Meeting,
April 21 - 22, University of California, Irvine, California.

BAKER, R. J. (1974)
The influence of particle seeding on laser anemometry measurements.
AERE M 2644, Harwell.

BLOOM, A. L. (1963)
Properties of laser resonators giving uniphase wave fronts.
Spectra Physics Laser Technical Bulletin No. 2.

BORN, M. and WOLF, E. (1975)
Principles of optics, electromagnetic theory of propagation,
interference and diffraction of light.
Fifth Edition, Pergamon Press.

BRAYTON, D. B. (1974)
Small particle signal characteristic of a dual-scatter laser velocimeter.
Applied Optics, Vol. 13, No. 10.

CHEN, T. P. and SAXENA, S. C. (1978)
A theory of solids projection from a fluidized bed surface as a first
step in the analysis of entrainment processes.
Fluidization, Cambridge University Press, pp. 151-156.

CHIGIER, N. A. (1977)
Instrumentation techniques for studying heterogeneous combustion.
Prog. Energy Combust. Sci., Pergamon Press, Vol. 3, pp. 175-189.

CHIGIER, N. A., UNGUT, A. and YULE, A. J. (1979)
Particle size and velocity measurement in flames by laser anemometer.
From Seventeenth Symposium (International) on Combustion, The Combustion
Institute.

CHU, W. P. and ROBINSON, D. M. (1977)
Scattering from a moving spherical particle by two crossed coherent
plane waves.
Applied Optics, Vol. 16, No. 3.

DANON, H., WOLFSHTEIN, M. and HETZRONI, G. (1977)
Numerical calculations of two-phase turbulent round jet.
Int. J. Multiphase Flow, Vol. 3, pp. 223-234.

DAVIDSON, J. F. and HARRISON, D. (1963)
Fluidised particles.
Cambridge University Press, Cambridge.

DICKSON, L. D. (1970)
Characteristics of propagating Gaussian beam.
Applied Optics, Vol. 9, No. 8.

DIGITAL (1978)
Micro-computer processors.
Digital Equipment Corporation.

DO, H. T., GRACE, J. R. and CLIFT, R. (1972)
Particle ejection and entrainment from fluidised bed.
Ponder Technology, 6, pp. 195-200.

DURÃO, D. F. G. (1976)
The application of laser anemometry to free jets and flames with and
without recirculation.
Ph.D. Thesis, Imperial College, University of London.

DURÃO, D. F. G., LAKER, J. and WHITELAW, J. H. (1978)
A microprocessor controlled frequency analyser for laser Doppler
anemometry.
Imperial College, Mechanical Engineering, FS/78/21, University of London.

DURST, F. (1973)
Scattering phenomena and their application in optical anemometry.
J. of Applied Mathematics and Physics (ZAMP), Vol. 24.

DURST, F. (1978)
Studies of particle motion by laser Doppler techniques.
Proceedings of the Dynamic Flow Conference, pp. 345-372.

DURST, F., MELLING, A. and WHITELAW, J. H. (1976)
Principles and practice of laser-Doppler anemometry.
Academic Press.

DURST, F. and STEVENSON, H. (1979)
Influence of Gaussian beam properties on laser Doppler signals.
Applied Optics, Vol. 18, No. 4.

DURST, F. and UMHAUER, H. (1975)
Local measurements of particle velocity, size distribution and
concentration with a combined laser Doppler particle sizing system.
Proc. of LDA-75 Symposium, Technical University of Denmark.

DURST, F. and ZARE, M. (1975)
Laser Doppler measurements in two-phase flows.
University of Karlsruhe, Sonderforschungsbereich 80, Report SFB 80/TM/63,
July.

FARMER, W. M. (1972)
Measurement of particle size, number density, and velocity using a laser
interferometer.
Applied Optics, Vol. 11, No. 11, pp. 2603-2612.

FARMER, W. M. (1976)
Sample space for particle size and velocity measuring interferometers.
Applied Optics, Vol. 15, No. 8.

FOURNOL, A. B., BERGOUGNOU, M. A. and BAKER, C. G. J. (1973)
Solid entrainment in large gas fluidized bed.
The Canadian J. of Chemical Eng., Vol. 51, pp. 401-404.

GELDART, D. (1972)
The effect of particle size and size distribution on the behaviour of
gas fluidized beds.
Powder Technology, 6.

GREHAN, G. and GOUESBET, G. (1979)
Mie theory calculations: new progress, with emphasis on particle sizing.
Applied Optics, Vol. 18, No. 20, pp. 3489-3493.

GIBSON, J. (1977a)
Present status of fluidised-bed combustion.
Applied Energy, 3, pp. 87-99.

GIBSON, J. (1977b)
Recent developments in fluidized bed combustion and potential benefits
to the coal industry.
The Mining Engineer, July, pp. 599-606.

GUGNONI, R. J. and ZENZ, F. A. (1980)
Particle entrainment from bubbling fluidized beds.
From Fluidization, Proceeding of the 3rd Foundation Conference on
Fluidization, Plenum Publication, England (Eds. Grace and Matser).

HARRISON, D. and LEUNG, L. S. (1962)
The coalescence of bubbles in fluidised beds.
Symposium on Interaction between Fluids and Particles, Instn. Chem.
Engrs., London, pp. 127-134.

HETSRONI, G. and SOKOLOV, M. (1971)
Distribution of mass, velocity and intensity of turbulence in a two-
phase turbulent jet.
J. Appl. Mech., 88, pp. 735-747.

HOLVE, D. and SELF, S. A. (1979)
Optical particle sizing for in situ measurements, part 1.
Appl. Opt., Vol. 18, No. 10, pp. 1632-1645.

HORIO, M., TAKI, A., HSIEH, Y. S. and MUCHI, I. (1980)
Elutriation and particle transport through the freeboard of a gas solid
fluidized bed.
From Fluidization, Proceeding of the 3rd Foundation Conference on
Fluidization, Plenum Publication, England, (Eds. Grace and Matser).

van de HULST, H. C. (1957)
Light scattering by small particles.
Wiley, New York.

ISHIDA, M., SHIRAI, T. and NISHIWAKI, A. (1980)
Measurement of the velocity and direction of flow of solid particles
in a fluidised bed.
Powder Technology, 27, pp. 1-6.

KERKER, M. (1969)
The scattering of light.
Academic Press.

KOGELNIK, H. (1965)
Imaging of optical modes resonators with internal lenses.
Bell System Technical, 44, pp. 455-494.

KUNII, D. and LEVENSPIEL, O. (1977)
Fluidization Engineering.
Robert E. Krieger Publishing Co., Huntington, New York.

LEE, S. L. and SRINIVASAN, J. (1978)
Measurement of local size and velocity probability density distributions
in two-phase suspension flows by laser-Doppler technique.
Int. J. Multiphase Flow, Vol. 4, pp. 141-155.

LEVA, M. (1951)
Elutriation of fines from fluidized systems.
Chemical Engineering Progress, Vol. 47, No. 1, p. 39.

LEVA, M. and WEN, C. Y. (1971)
Elutriation.
Fluidization (eds. Davidson, J. F. and Harrison, D.), Chapter 14,
Academic Press, New York.

LEVY, Y. and LOCKWOOD, F. C. (1981)
Velocity measurements in a particle laden turbulent free jet.
Combustion and Flame, 40, pp. 333-339.

LEWIS, W. K., GILLILAND, E. R. and LANG, P. M. (1962)
Entrainment from fluidized beds.
Chemical Engineering Progress Symposium Series, No. 38, Vol. 58, pp. 65-78.

LIN, L., SEARS, J. T. and WEN, C. Y. (1980)
Elutriation and attrition of char from a large fluidized bed.
Powder Technology, 27, pp. 105-115.

MELLING, A. and WHITELAW, J. H. (1976)
Turbulent flow in a rectangular duct.
J. Fluid Mech., Vol. 78, Part 2, pp. 289-315.

MERRICK, D. and HIGHLEY, J. (1972)
Particle size reduction and elutriation in a fluidized bed process.
A.I.Ch.E. Symp. Sem., 70, No. 137, pp. 366-378.

OGAWA, K., SATO, H., ISHIDA, M. and SHIRAI, T. (1978)
Continuous measurement of the velocity of particles in unsteady state motion.
J. of Chemical Eng. of Japan, Vol. 11, No. 5.

OHKI, K. and SHIRAI, T. (1976)
Particle velocity in fluidized bed.
Fluidization Technology, Hemisphere Publication, Washington; Vol. 1,
pp. 95-110.

OSBERG, G. L. and CHARLESWORTH, D. H. (1951)
Elutriation in a fluidized bed.
Chemical Engineering Progress, pp. 566-570.

PERRY, R. H. and CHILTON, C. H. (1973)
Chemical engineers' handbook.
International Student Edition, McGraw-Hill.

POPPER, J., ABUAF, N. and HETSRONI, G. (1974)
Velocity measurements in a two-phase turbulent jet.
Int. J. Multiphase Flow, 1, pp. 715-726.

RAJANI, J. B. and LANGER, G. (1972)
Turbulent mixing in an air jet laden with solid particles.
International Flame Research Foundation, 20th Meeting of Aerodynamics
Panel, Grenoble.

ROWE, P. N.
Experimental Properties of bubbles.
Fluidization (eds. Davidson, J. F. and Harrison, D.), Chapter 4,
Academic Press, New York.

THOMAS, W. J., GREY, P. J. and WATKINS, S. B. (1961)
Effect of particle size distribution in fluidisation.
British Chemical Engineering, pp. 176-181.

UNGUT, A., YULE, A. J., TAYLOR, D. S. and CHIGIER, N. A. (1978)
Simultaneous velocity and particle size measurements in two-phase flow
by laser anemometry.
AIAA 16th Aerospace Sciences Meeting, Huntsville, Alabama, January 16-18.

WEN, C. Y. and HASHINGER, R. F. (1960)
Elutriation of solid particles from a dense-phase fluidized bed.
A.I.Ch.E. Journal, Vol. 6, No. 2, pp. 220-226.

WERTHER, J. and MOLERUS, O. (1973)
The local structure of gas fluidized beds II. The spatial distribution
of bubbles.
Int. J. Multiphase Flow, Vol. 1. pp. 123-138.

WIGLEY, G. (1978)
The sizing of large droplets by laser anemometry.
J. Phys. E: Sci. Instrum., Vol. 11.

YAMAZAKI, M. and KATO, Y. (1980)
Measurement of particle velocities in a fluidized bed by a thermal
response method.
Int. Chemical Engineering, Vol. 20, No. 3.

YULE, A. J., CHIGIER, N. A., ATAKAN, S. and UNGUT, A. (1977)
Particle size and velocity measurement by laser anemometry.
J. Energy, Vol. 1, No. 4, pp. 220-228.

ZENZ, F. A. and WEIL, N. A. (1958)
A theoretical-empirical approach to the mechanism of particle
entrainment from fluidised bed.
A.I.Ch.E. Journal, Vol. 4, No. 4.
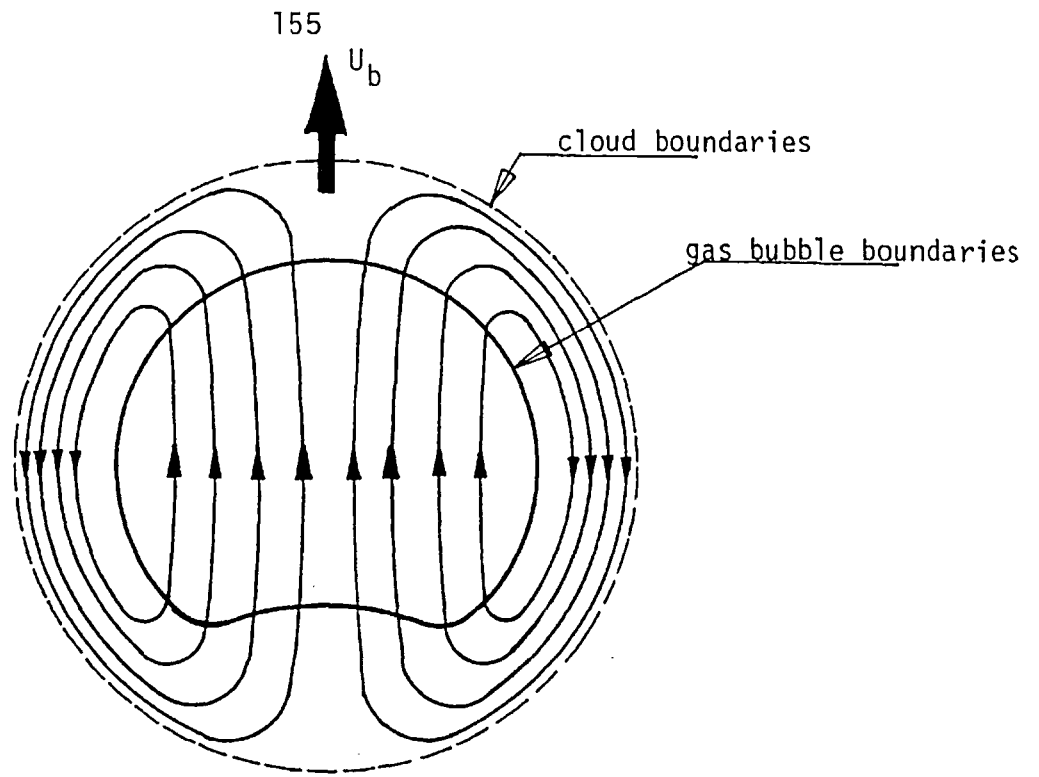
Fig. 1.1.2-1 Gas circulation inside a rising bubble
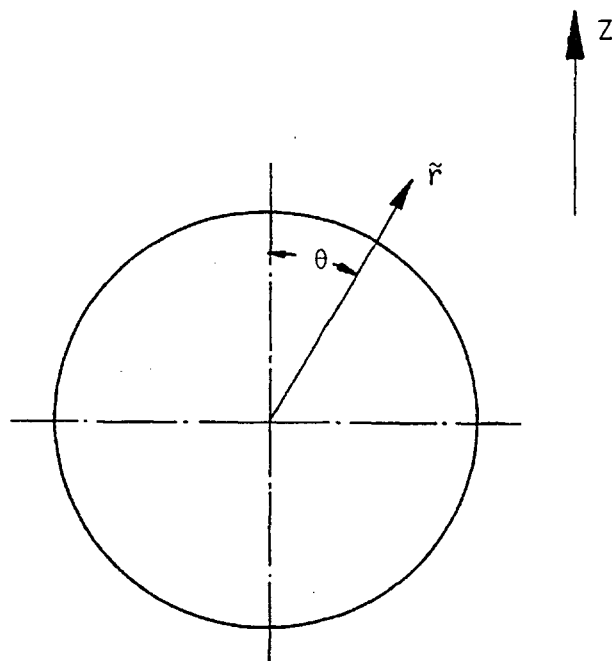
Fig. 1.1.2-2 Bubble geometry
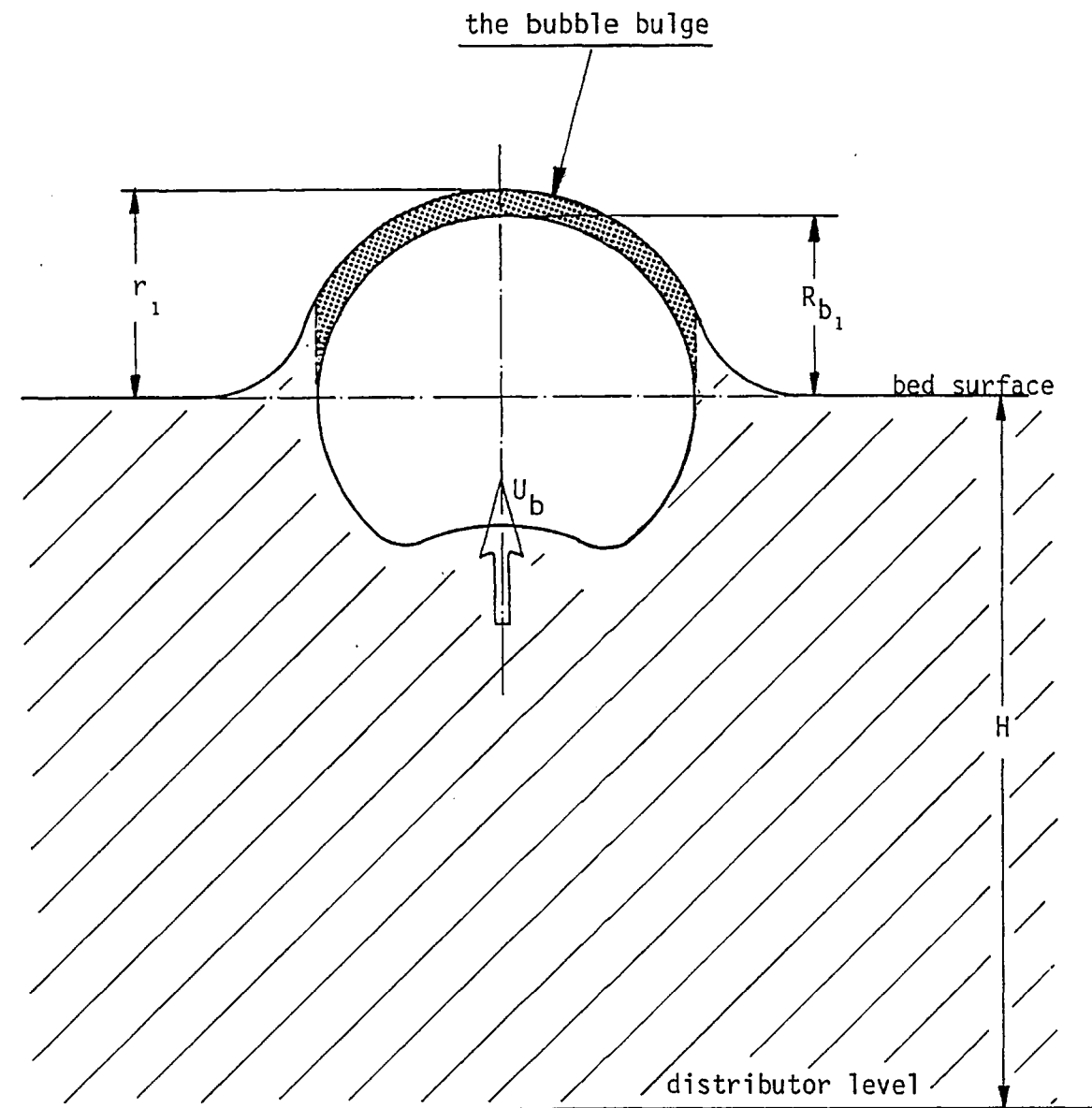
Fig. 1.2.2-1   Schematic representation of the bulge when a bubble
is half above the bed surface and is about to erupt
(by Chen and Saxena, 1978)

$\Delta U \approx$ particle velocity

$\overline{U}_{avg.}$

U_t

$\Delta U \approx$ particle velocity

critical height (TDH)

$\overline{U}_{avg.}$

U_t
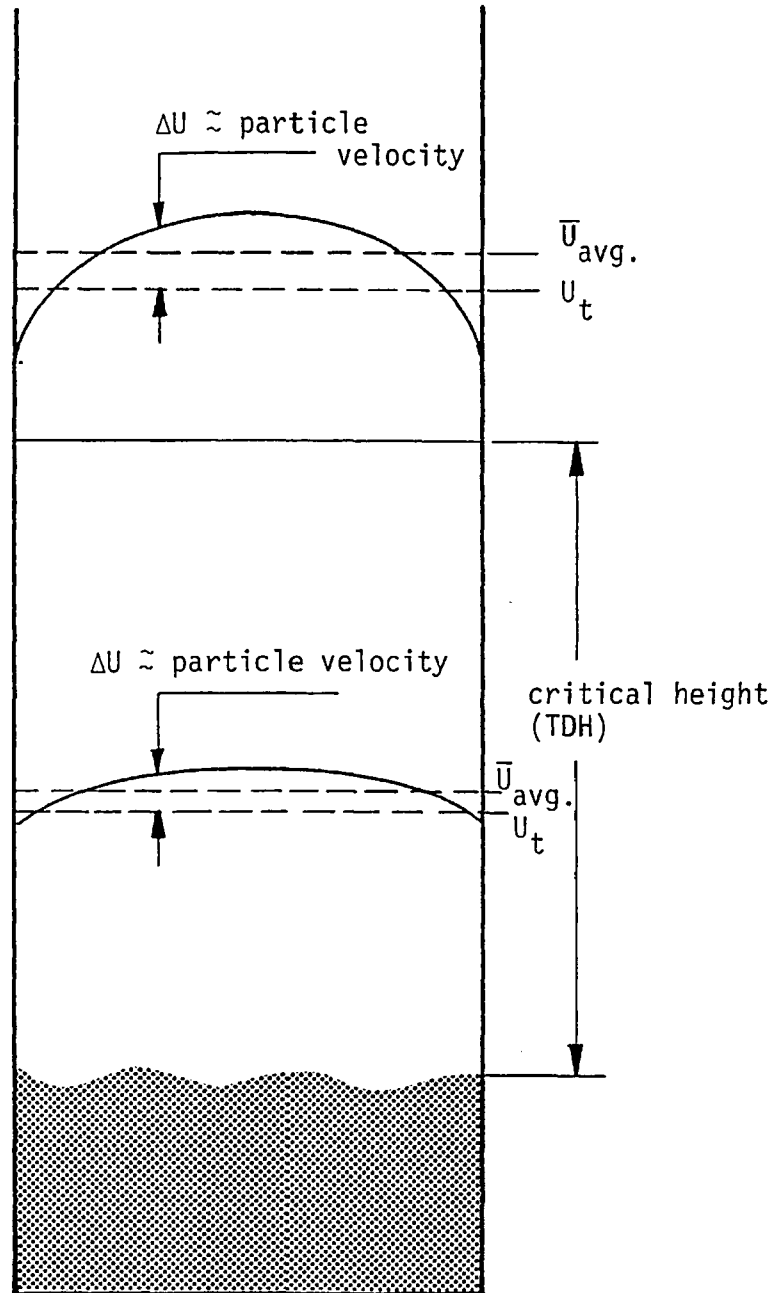
Fig. 1.2.3-1   Variation of the gas velocity across the freeboard at different levels (by Hashinger and Wen, 1960)

- a -

$$\{n\}_i = |\{k\}_i - \{m\}_i| = \{2 \sin\phi\}_i$$

- b -
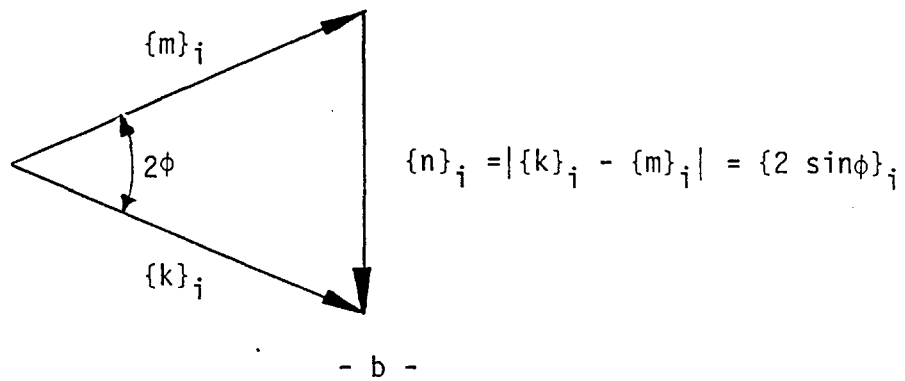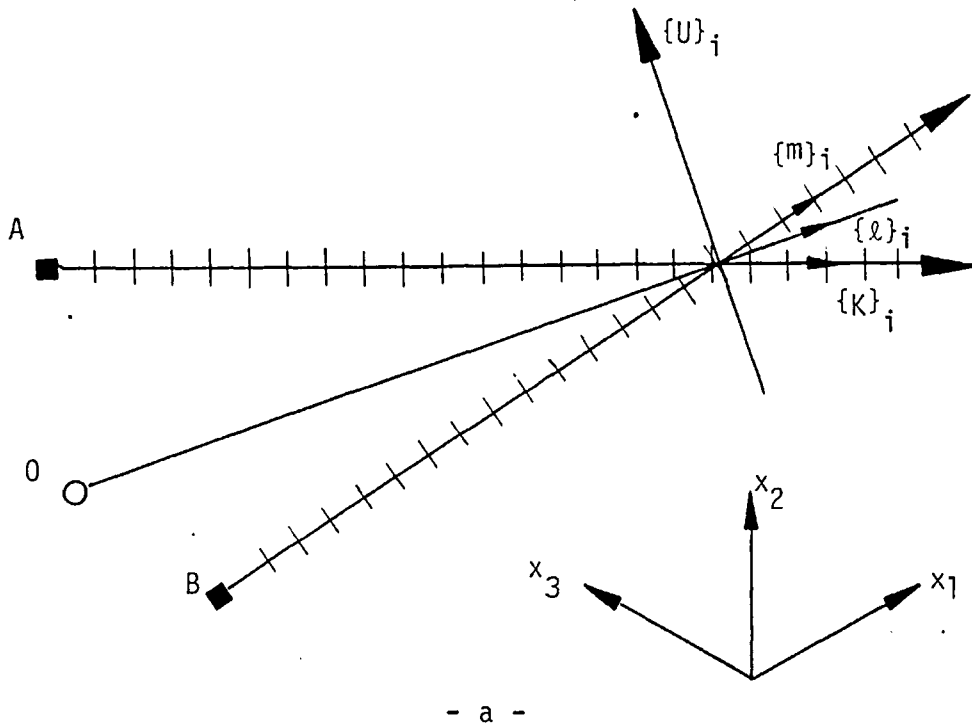
Fig. 2.2.2-1 Wave geometry for velocity measurements.
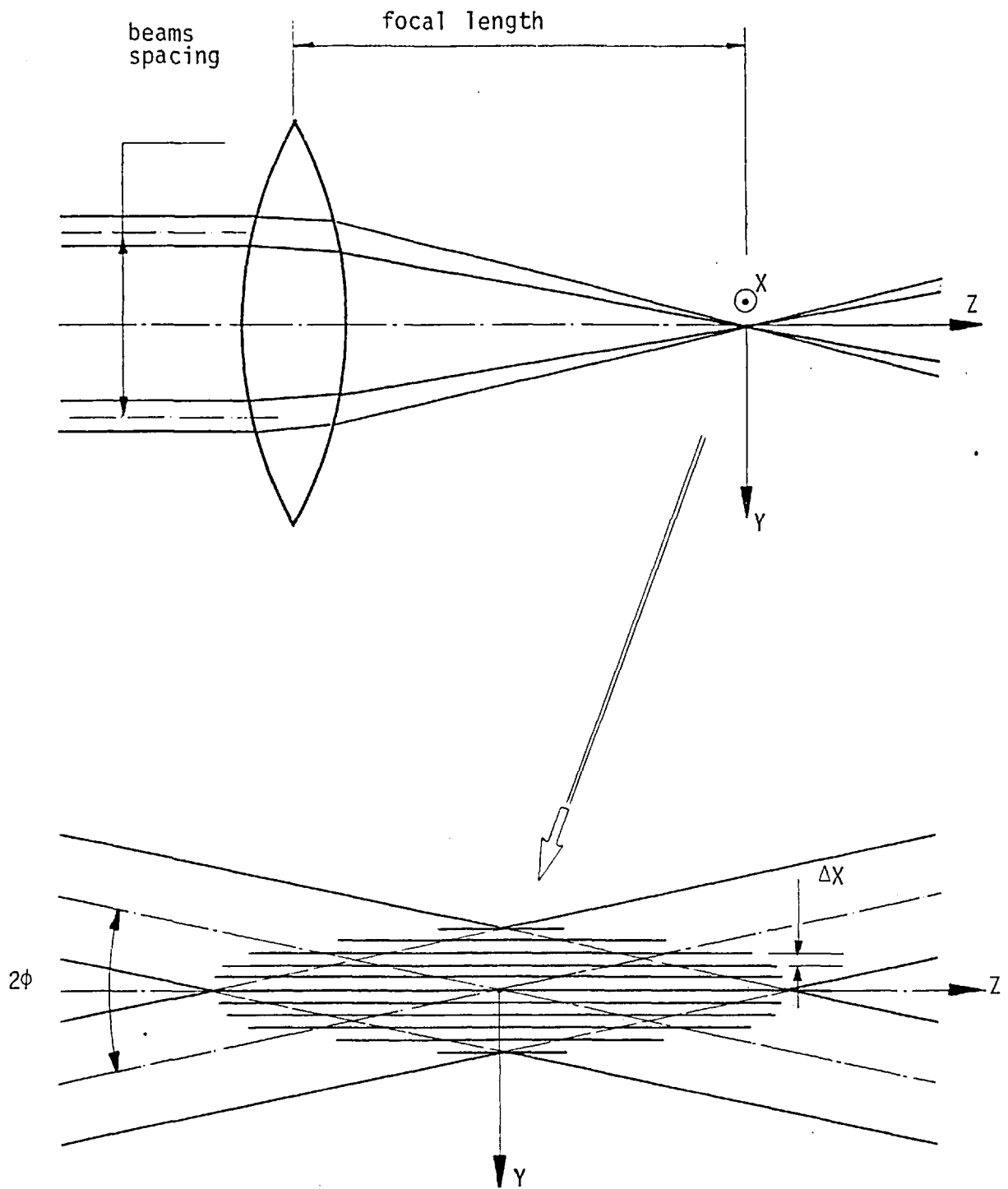
Fig. 2.3-1 Beam geometry and the control volume

Waist plane
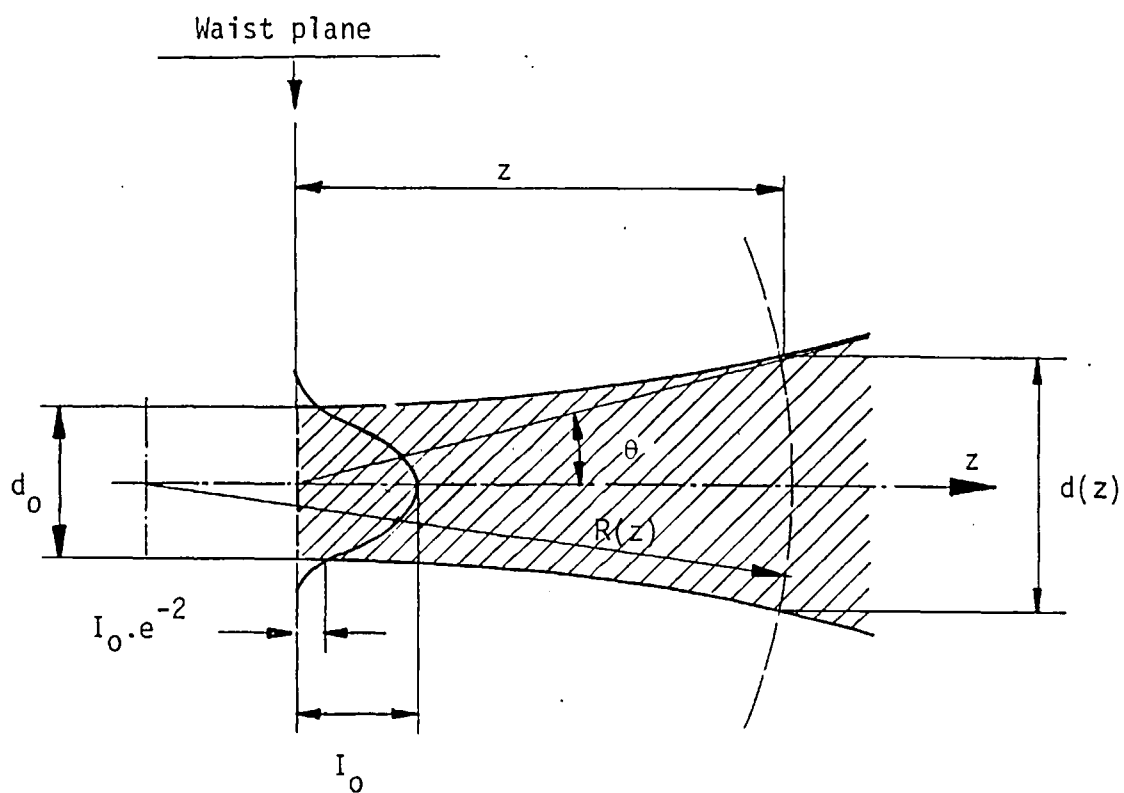
Fig. 2.3.1-1a   Contour of a Gaussian beam
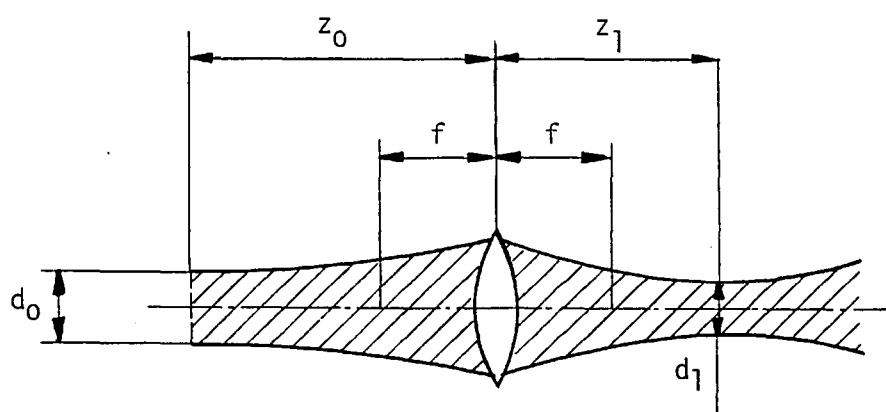
Fig. 2.3.1-1b   Gaussian beam transformed by a lens

transmitting optics   receiving optics

L_1 L_2

laser   pinhole photomultiplier

x_1 x_2
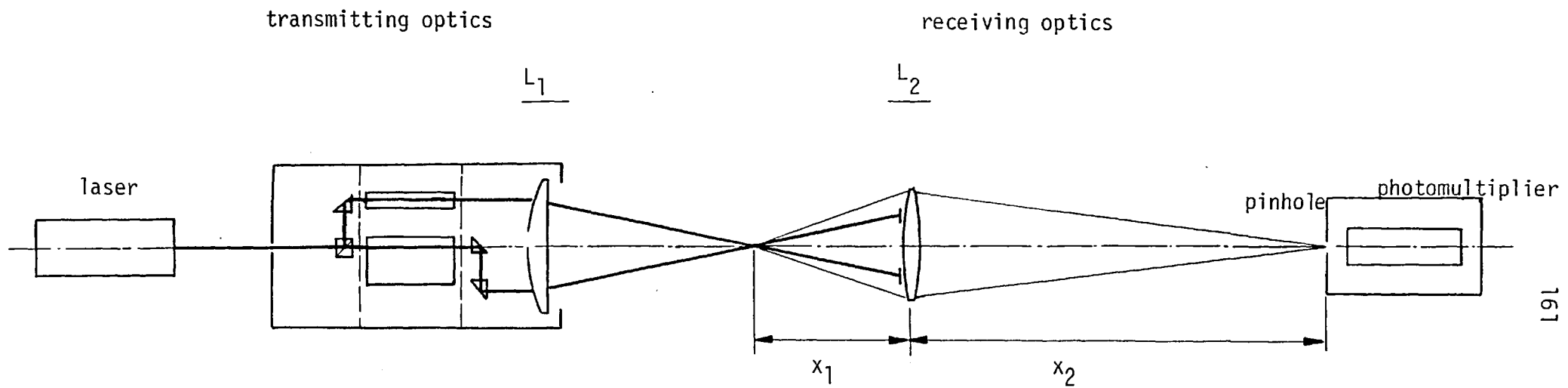
Fig. 2.3.3-1 Schematic diagram of the LDA system
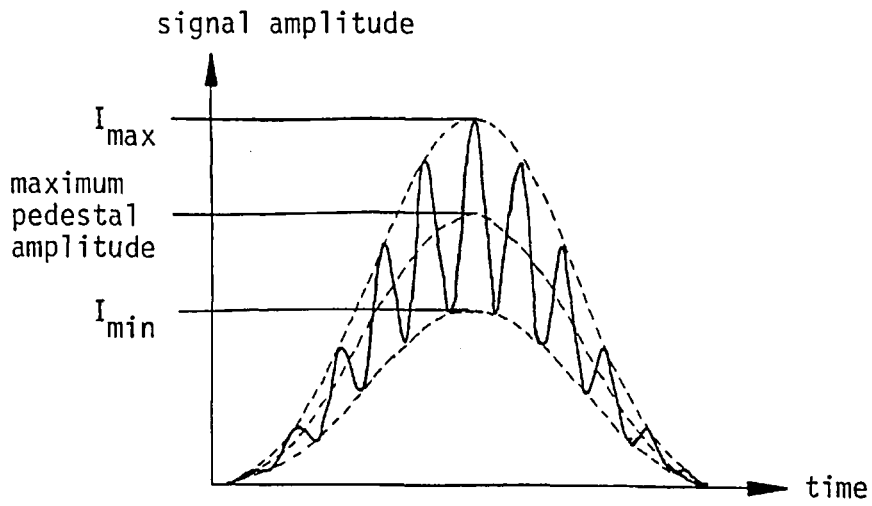
Fig. 2.4.3-1 Signal characteristics
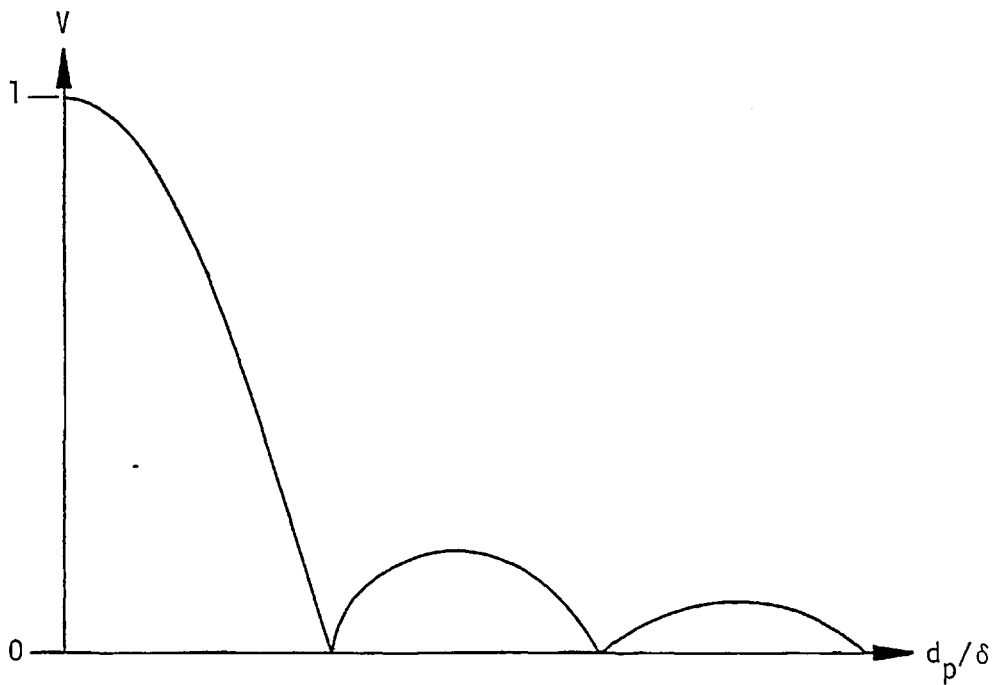
Fig. 2.4.3-2 Variation of visibility with particle diameter
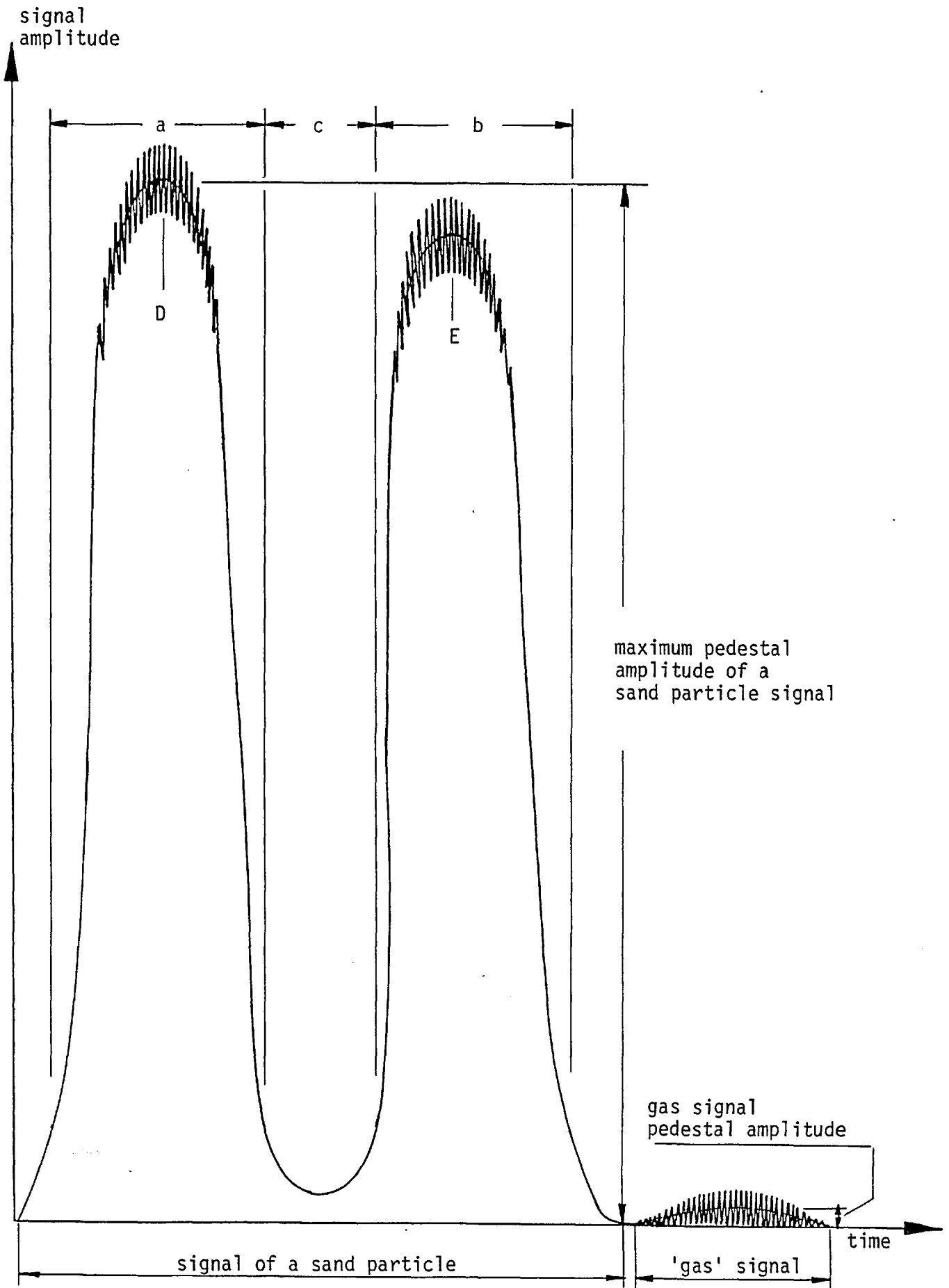
Fig. 2.5.2-1   Typical forward scattered signal of a sand particle
(partially absorbing)
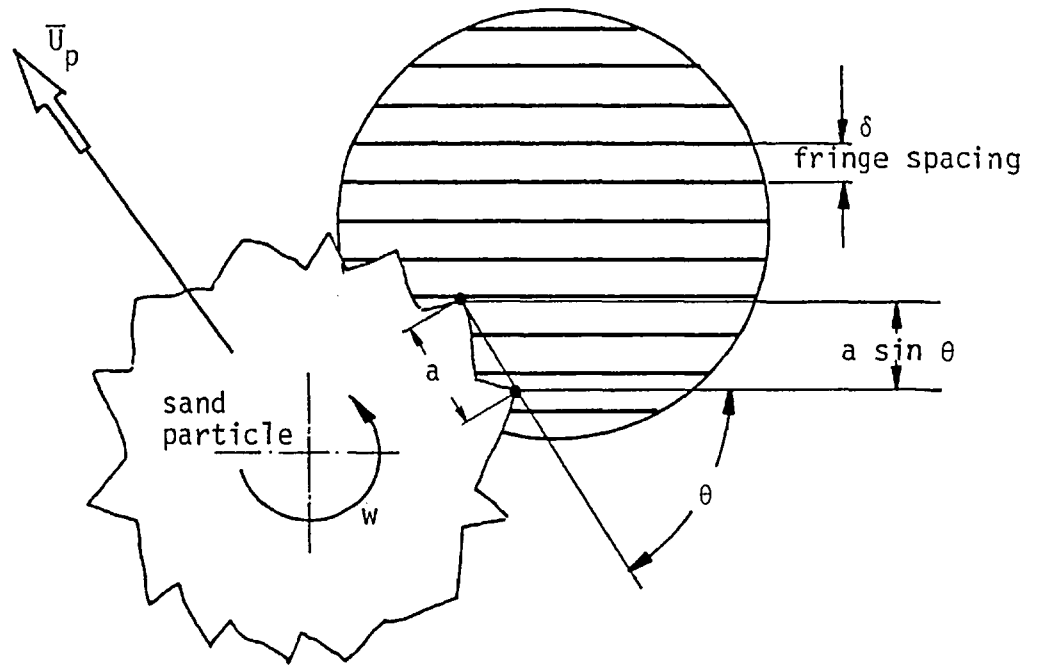
Fig. 2.5.2-2 Schematic illustration of a sand particle crossing the control volume
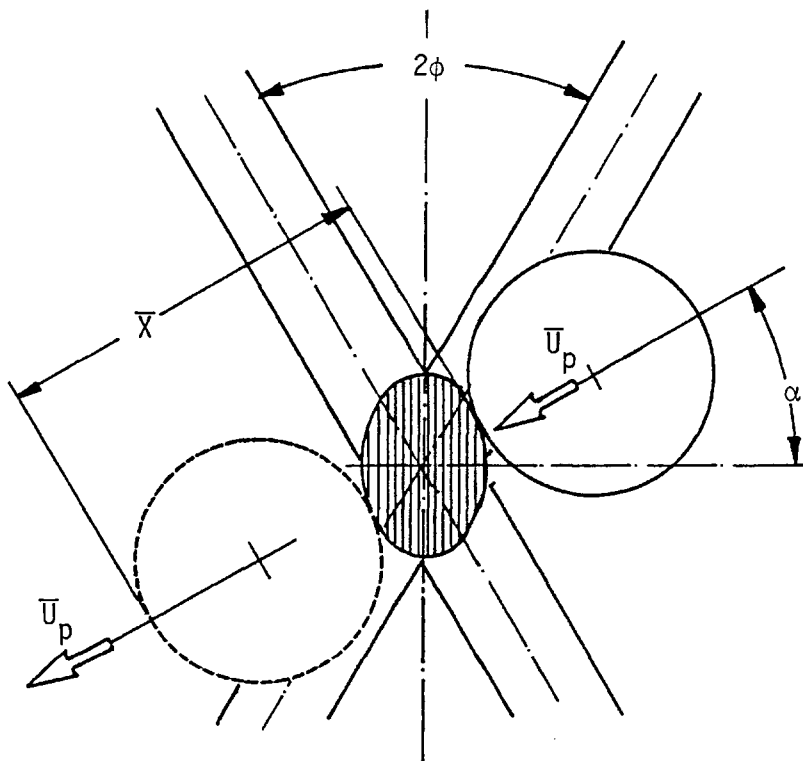
Fig. 2.5.3-1 Sand particle crossing the control volume
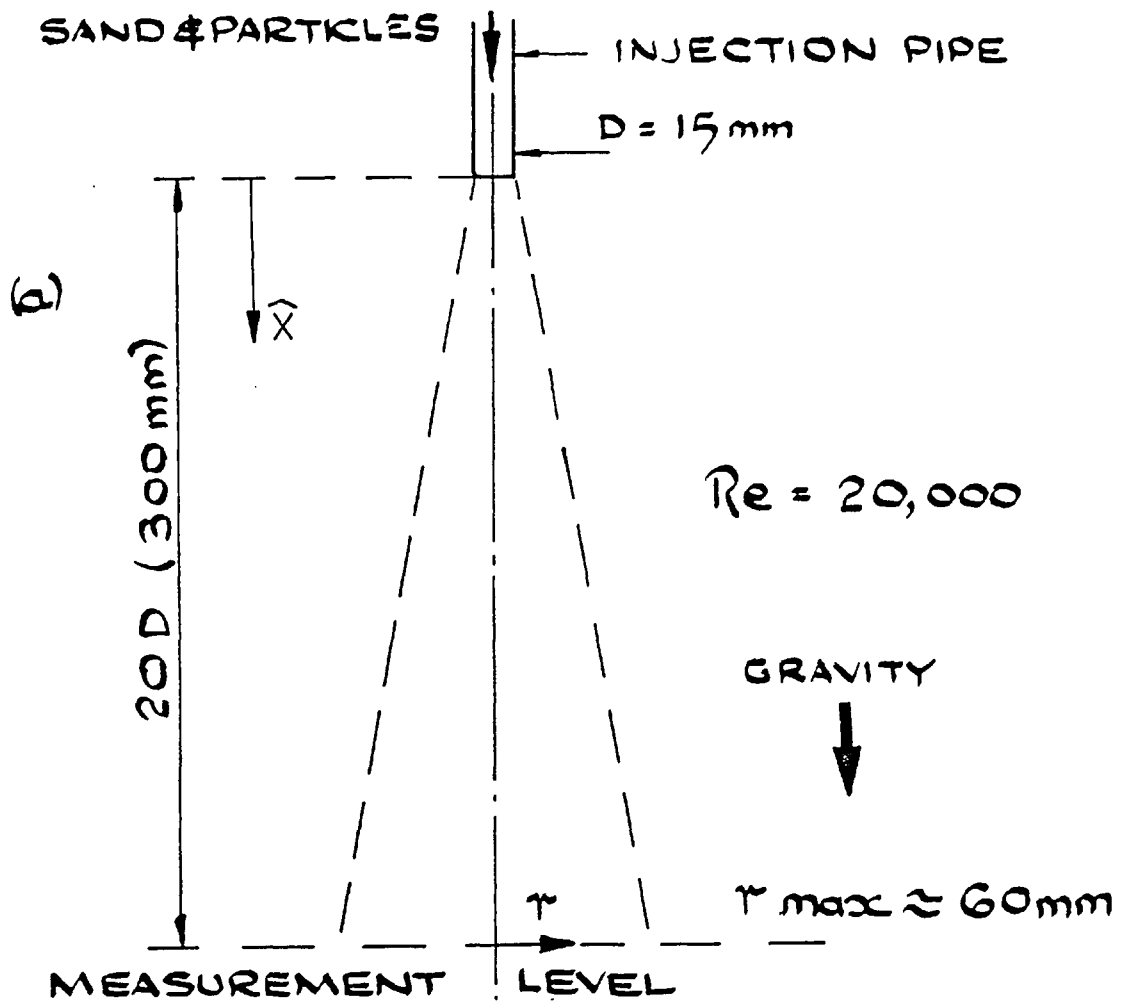
Fig. 3.1-1 The flow arrangement
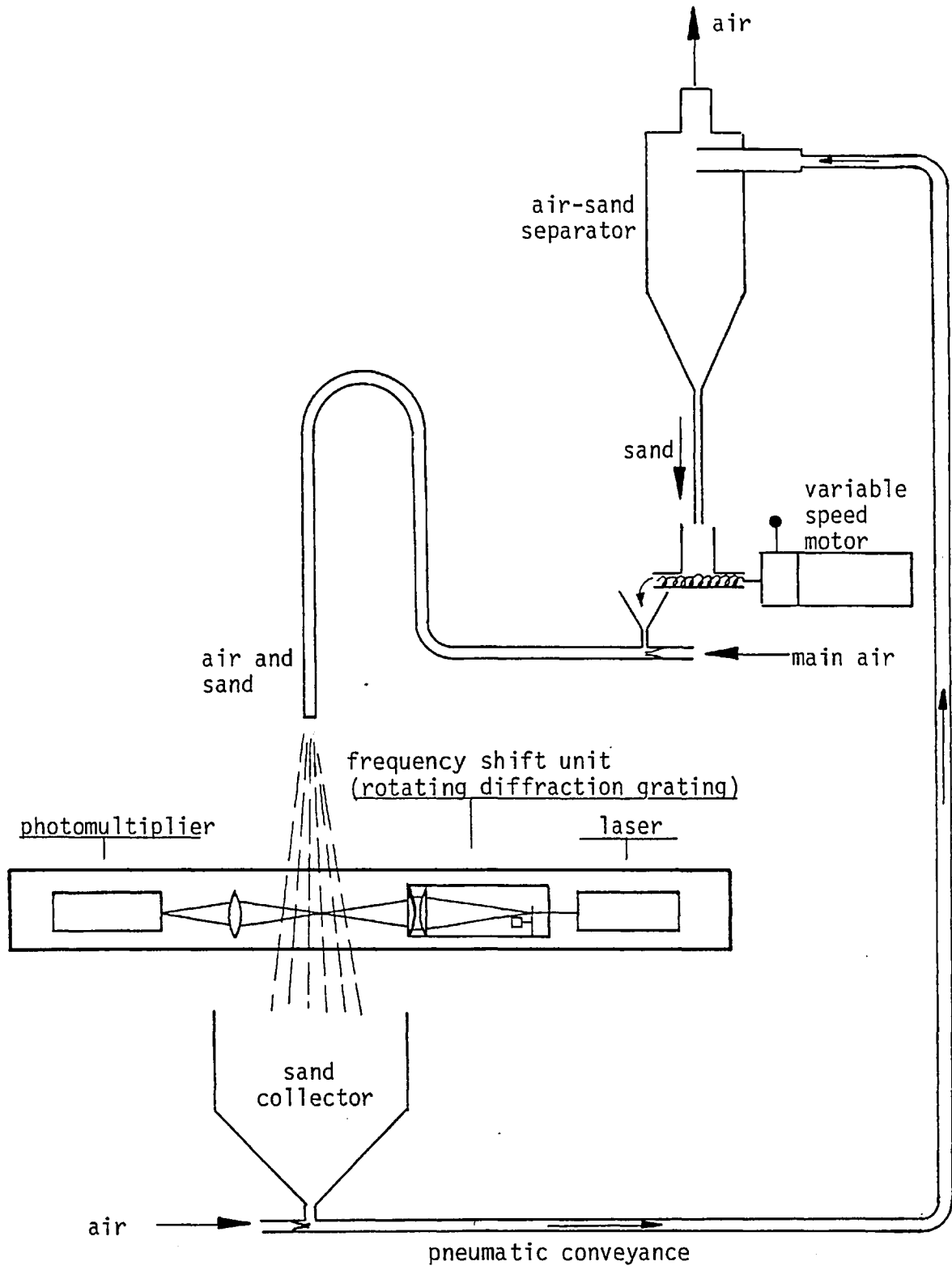
Fig. 3.2-1 Sketch of the experimental arrangement

% WEIGHT PERCENTAGE PASSING

(b)

SAND GRADE 12/24
MEDIAN SIZE 1060 μm

SIEVE SIZE μm

500 700 900 1100 1300 1500 1700 1900
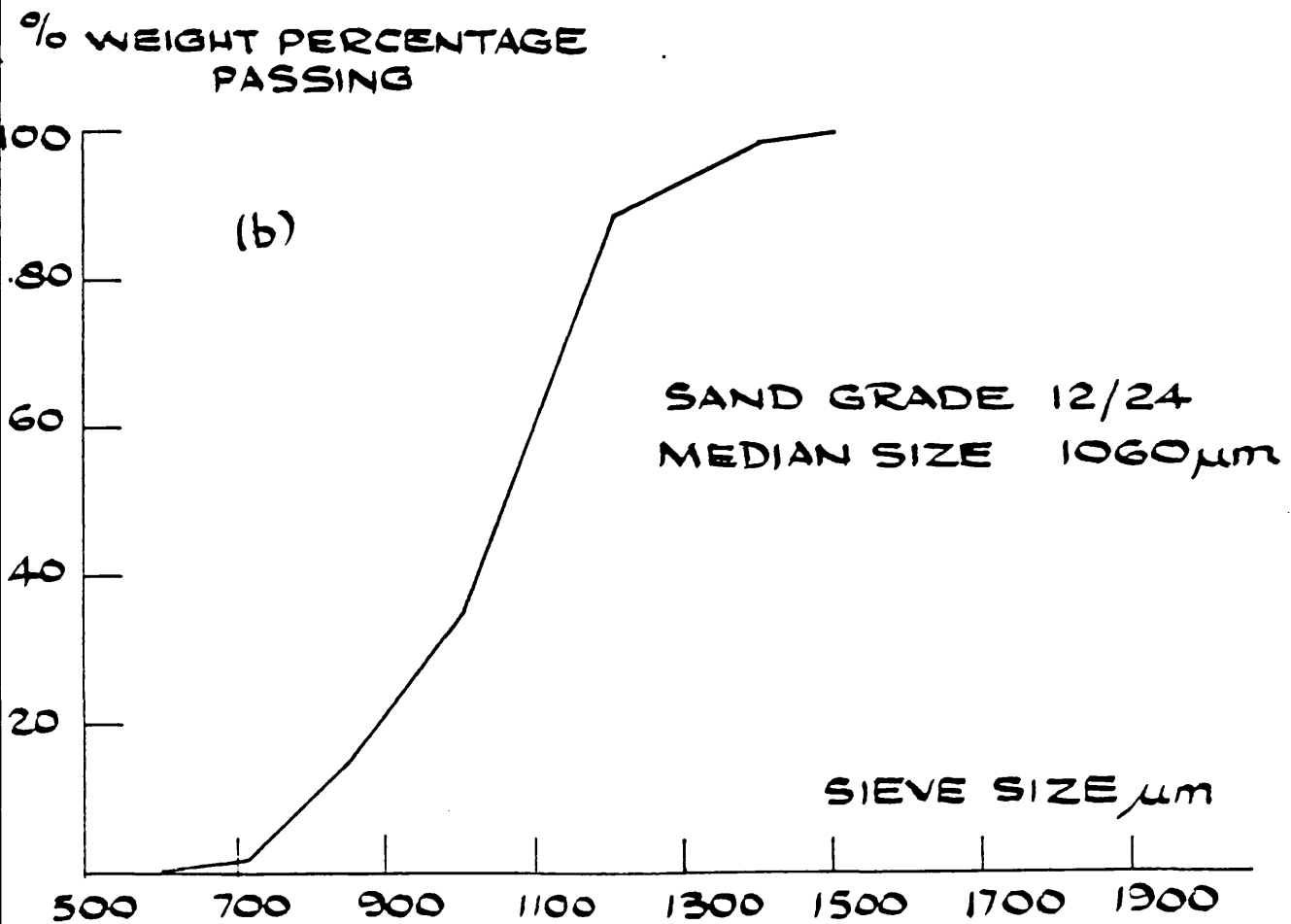
Fig. 3.2-2   The size distribution for 12/24 grade sand (case A,
Table 3.2-1)
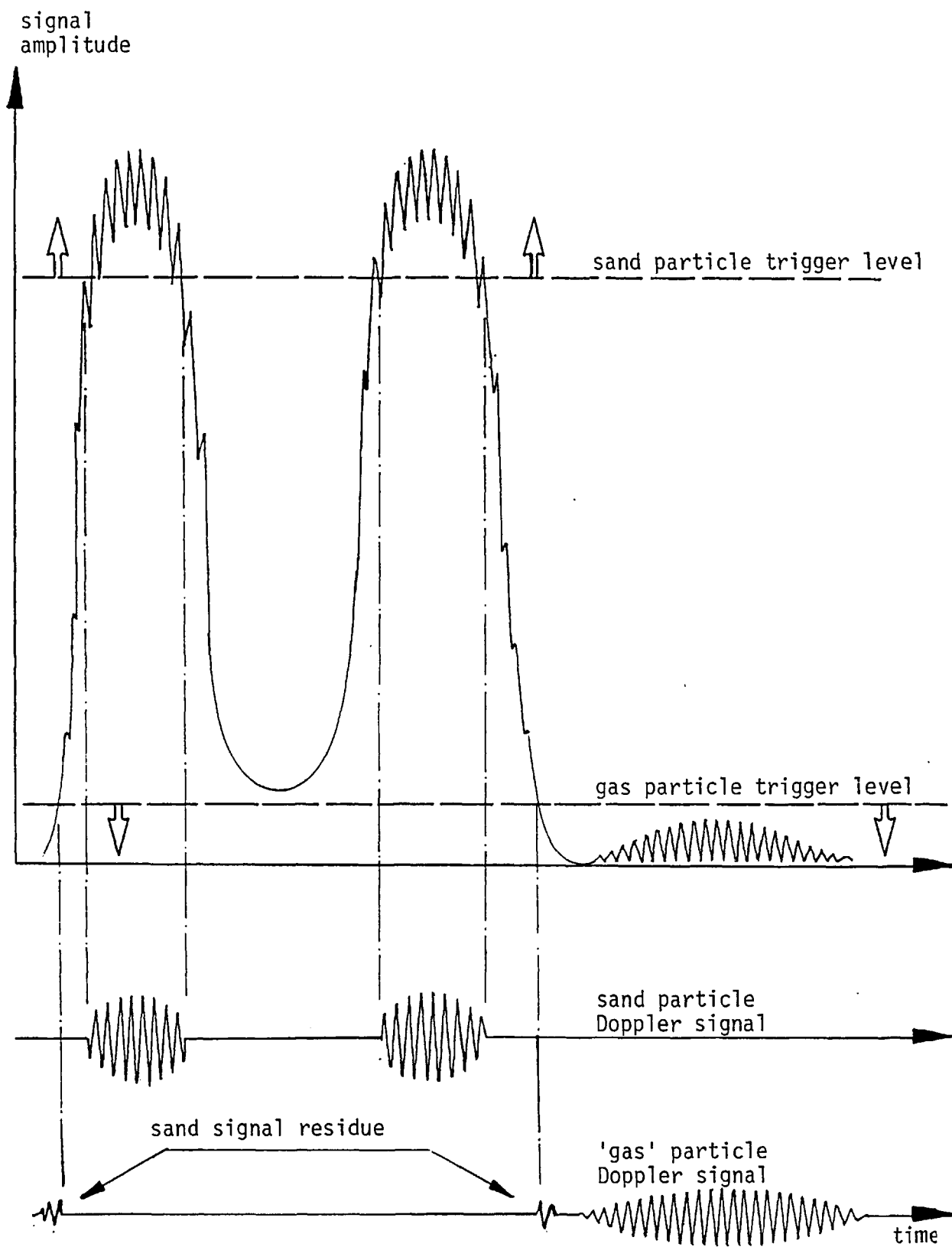
Fig. 3.3-1 Signal output from threshold selector
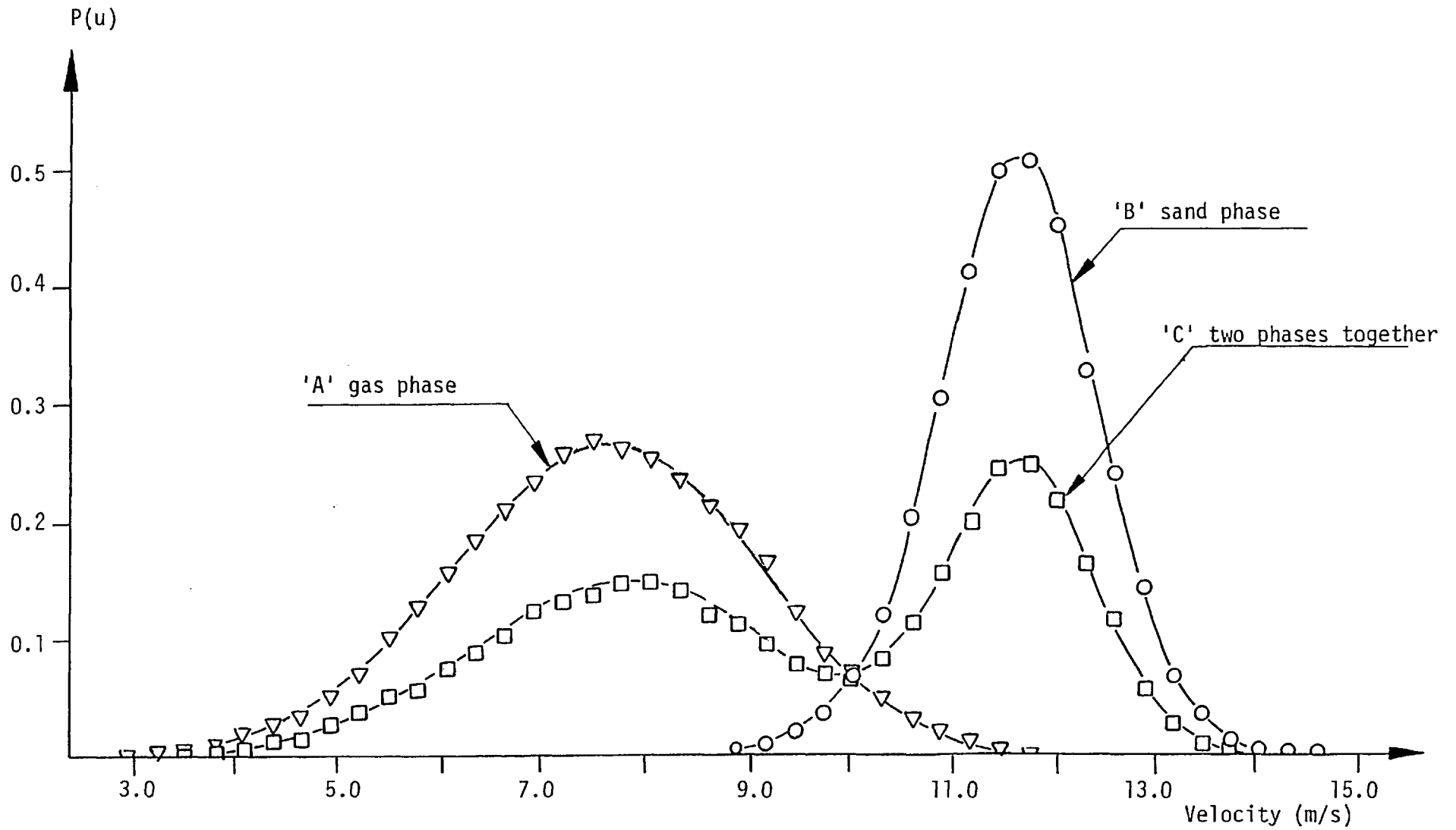
Fig. 3.3-2   Velocity probability histogram of the gas, sand and with no phase discrimination (flow case E2, see Table 3.2-1)
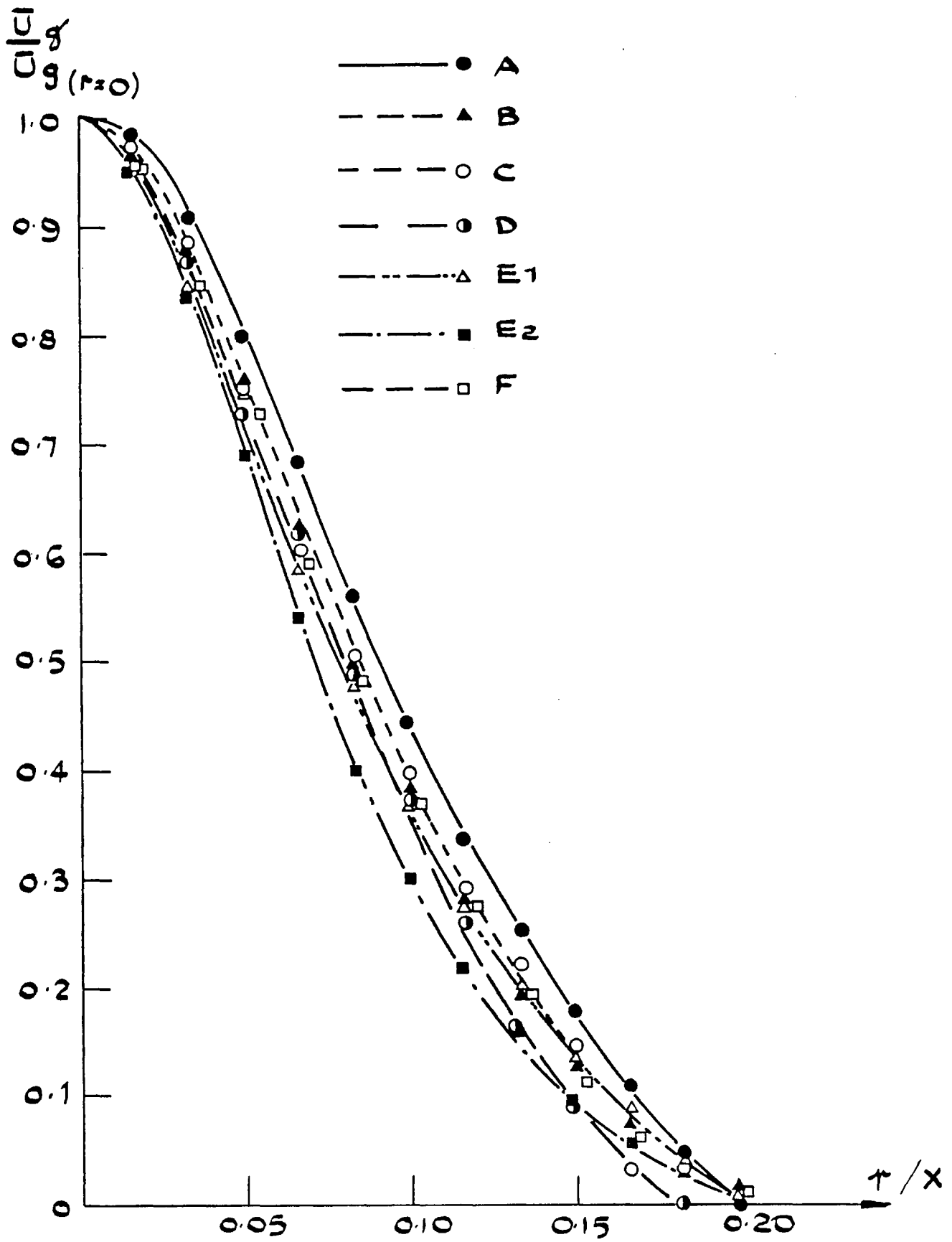
Fig. 3.4-1 Experimental result: mean axial gas velocity
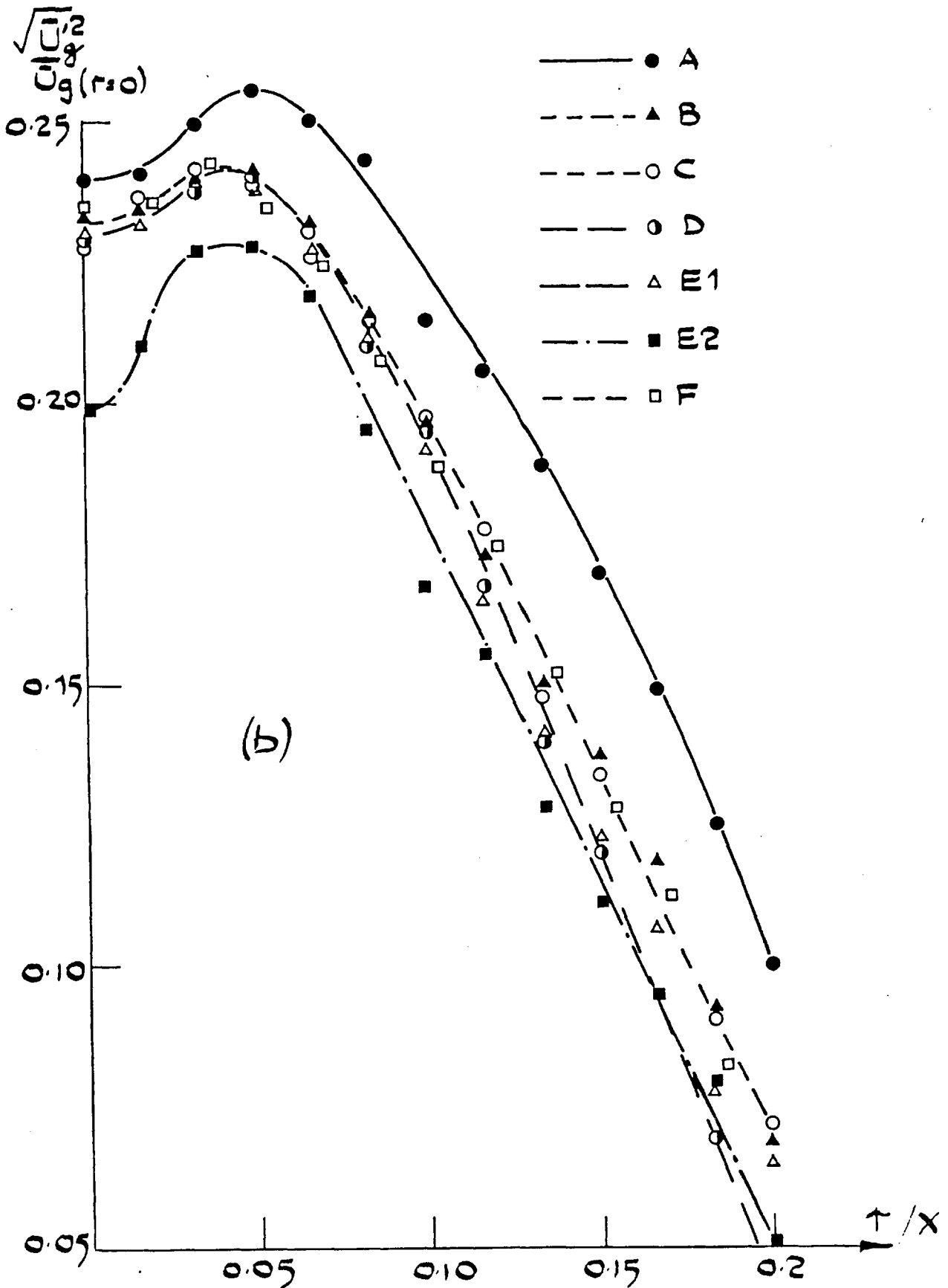
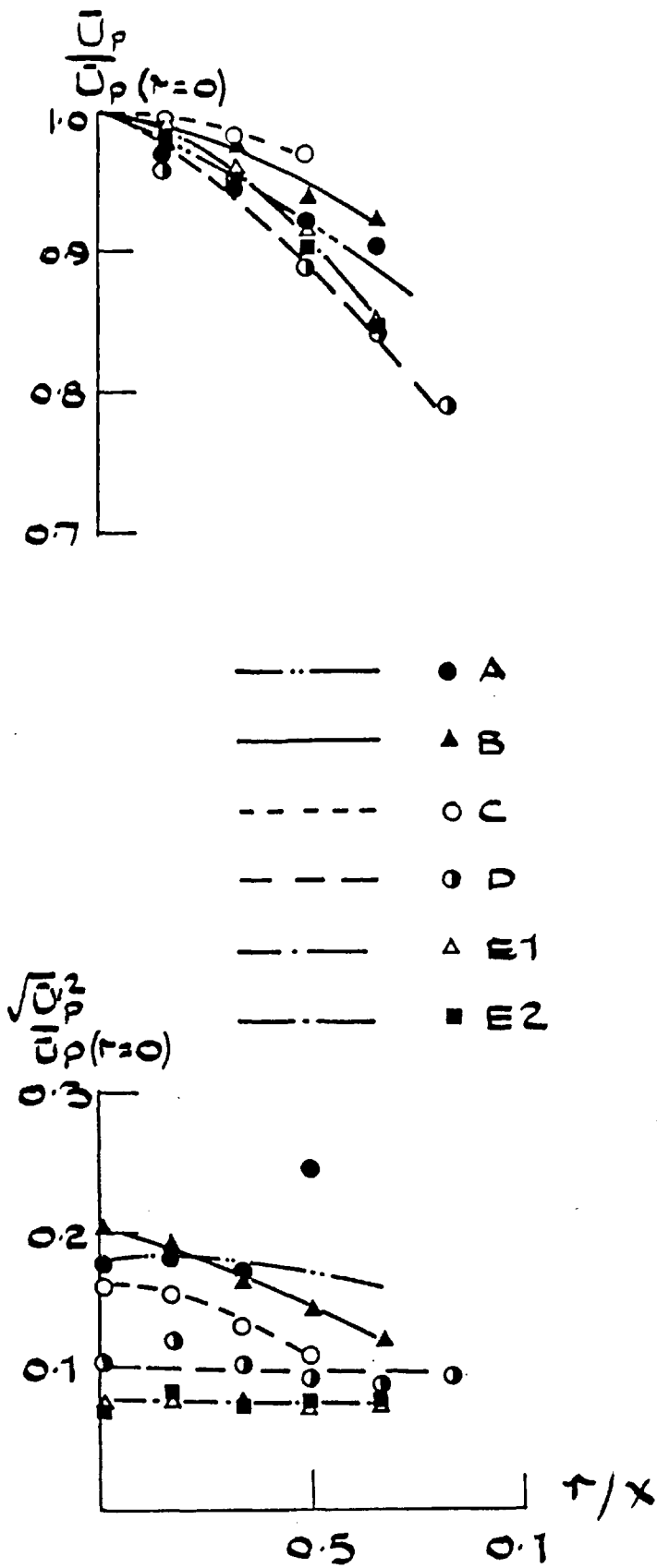Fig. 3.4-2 Experimental result: r.m.s. axial gas velocity

Fig. 3.4-3 Experimental result: mean and r.m.s. axial velocities of sand particles

air out

freeboard

2400 mm

sand

distribution plate

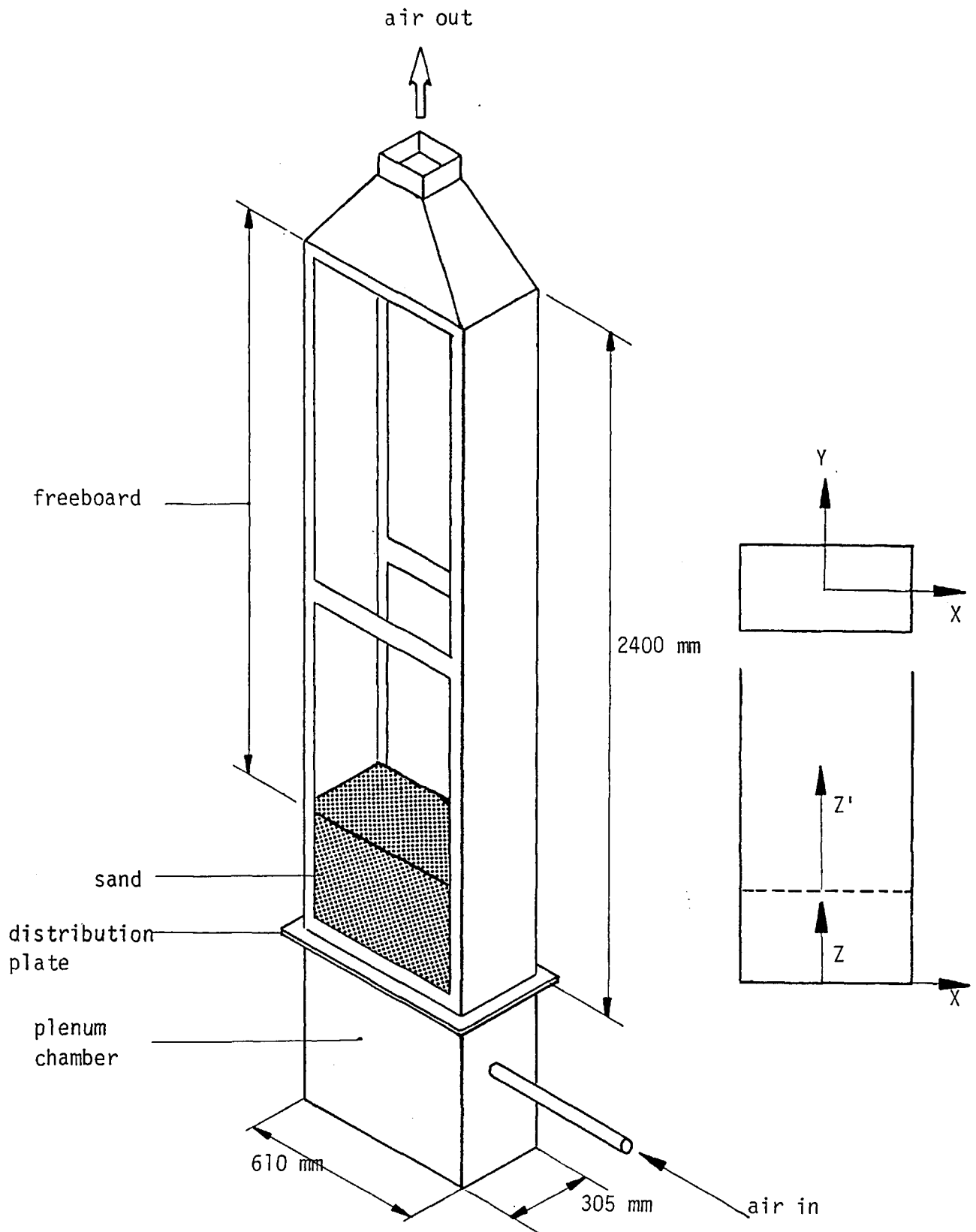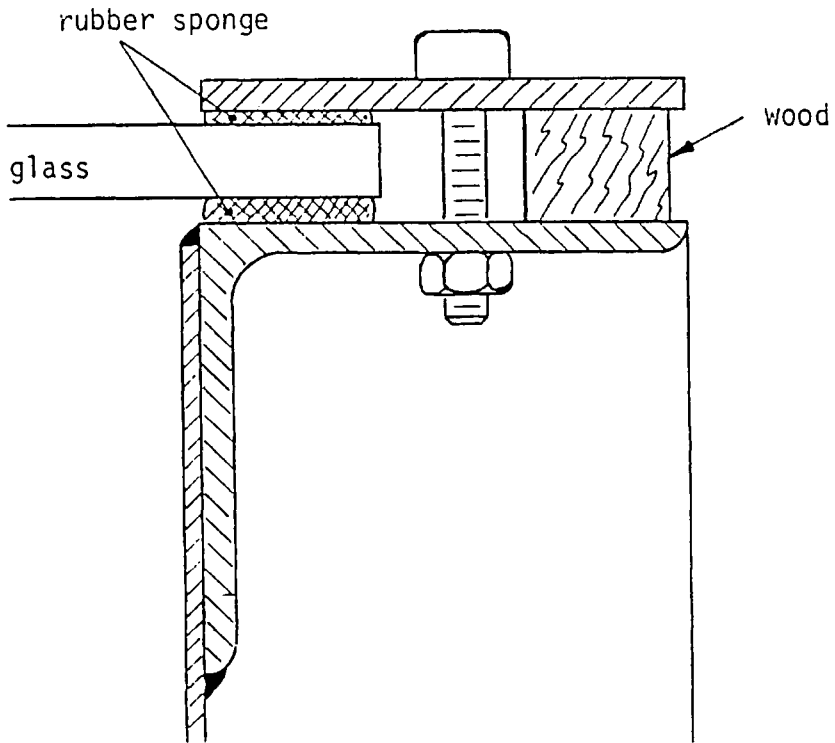plenum chamber

610 mm

305 mm

air in

Y

X

Z'

Z

X

Fig. 4.2-1   Sketch of the fluidized bed

Fig. 4.2.2-1 Glass panel to frame connection
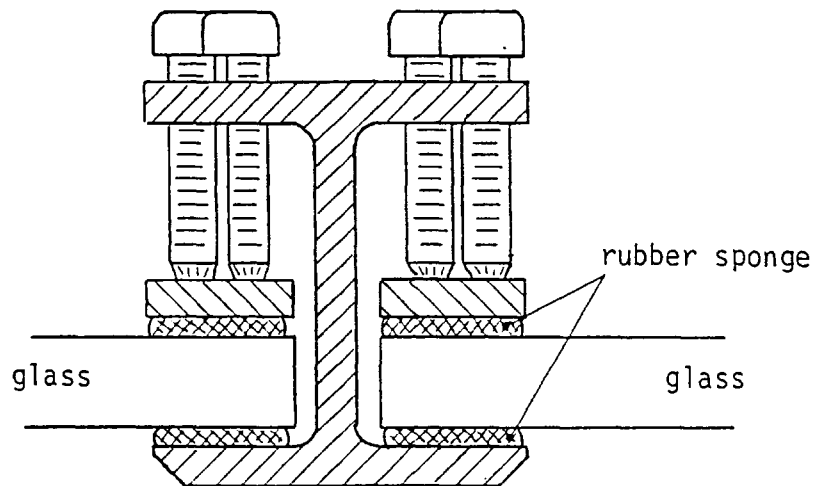
Fig. 4.2.2-2 Connection between lower and upper glass panels

porous bronze

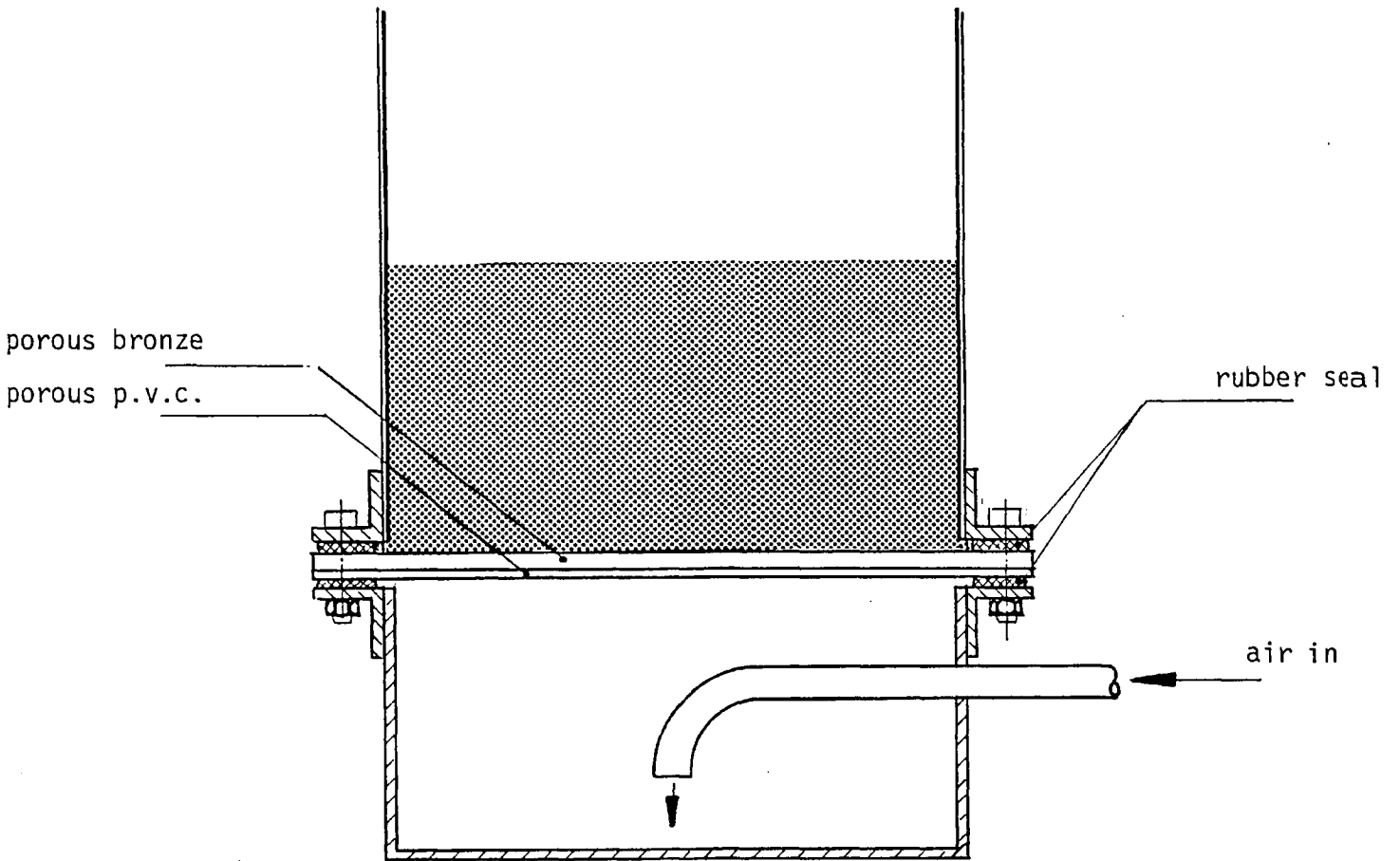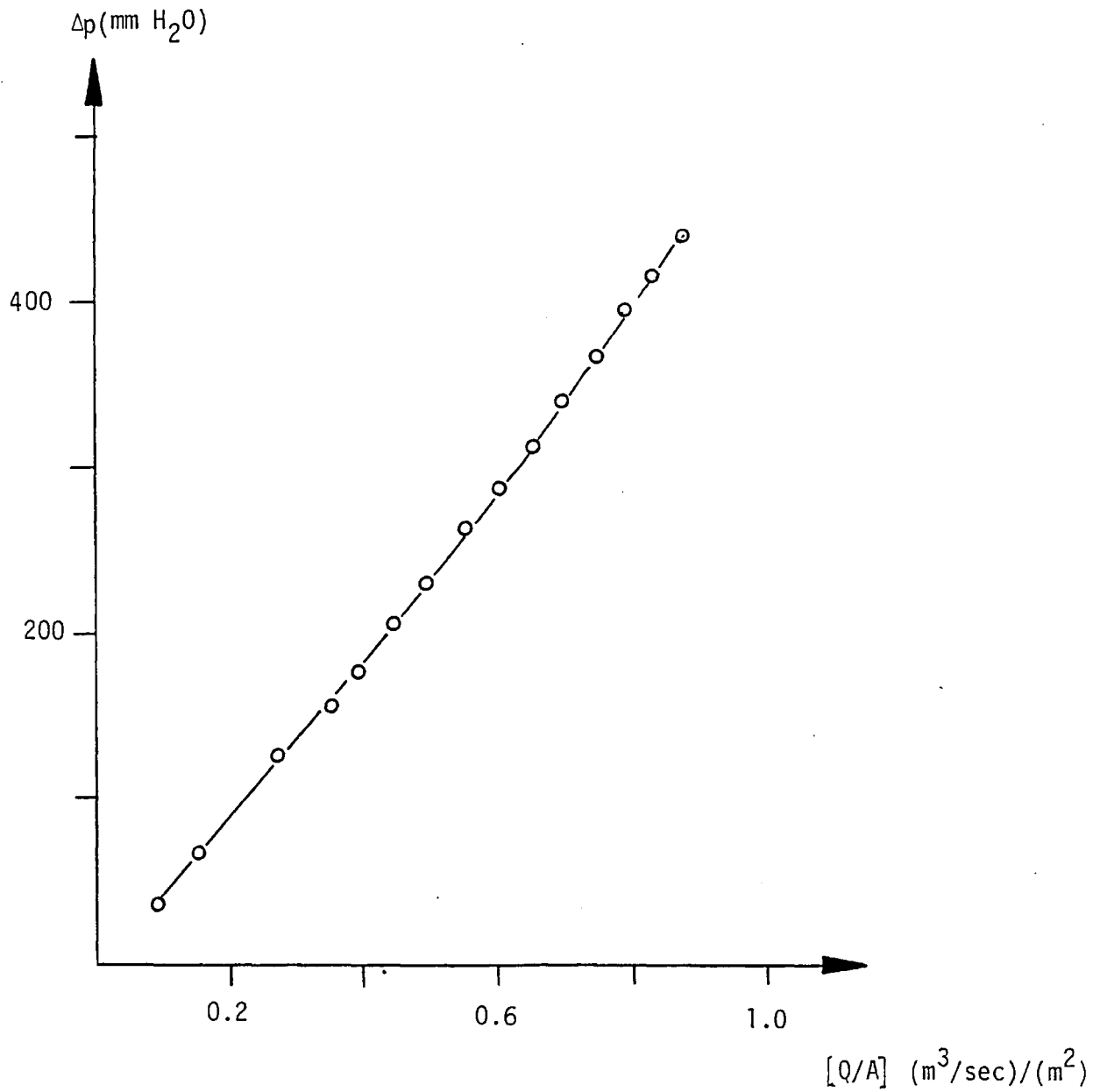porous p.v.c.

rubber seal

air in

Fig. 4.2.3-1   Distributor to bed connection

Fig. 4.2.3-2 Distributor pressure drop
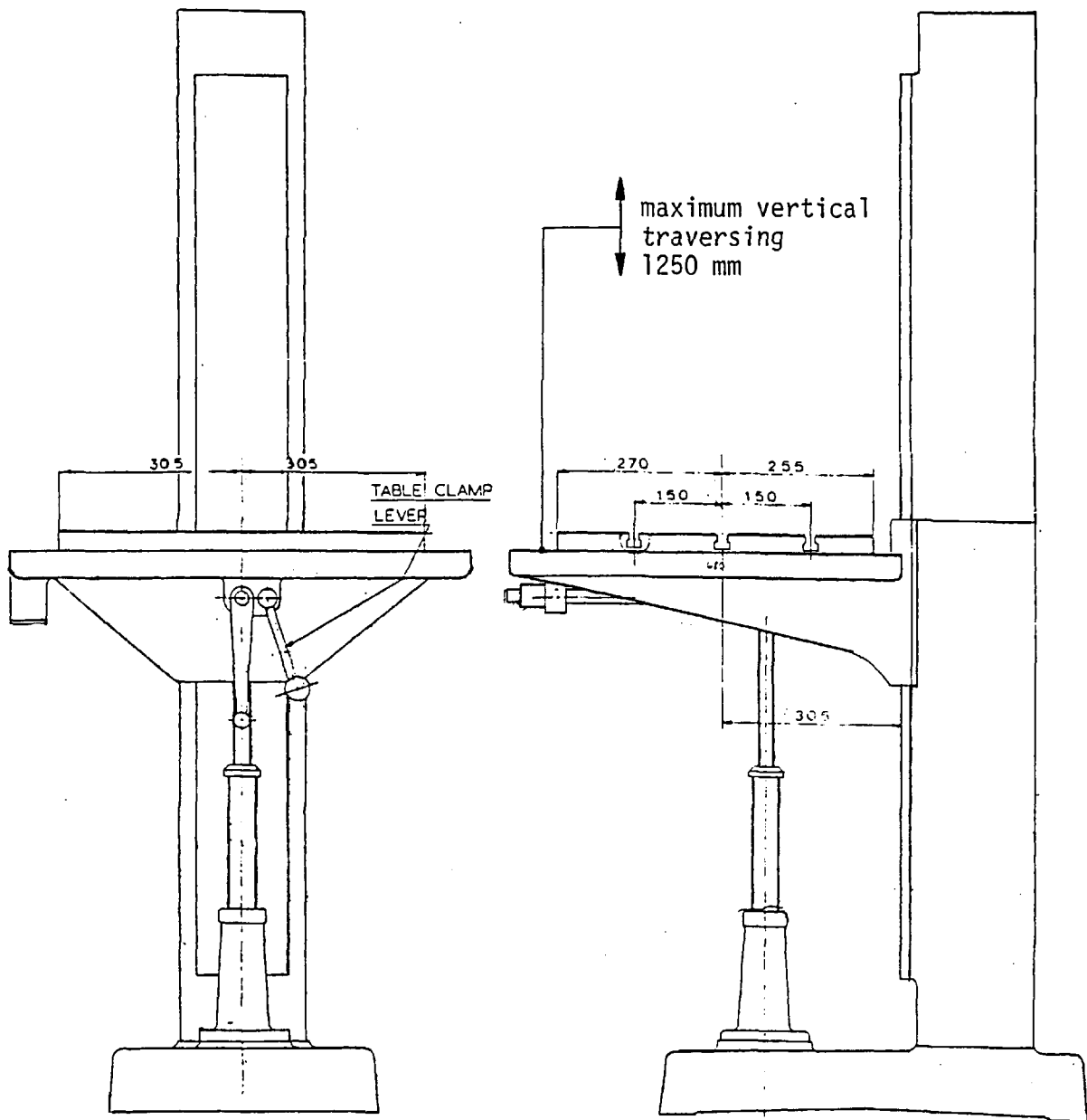
Fig. 4.3.1-1   Vertical traversing table

photomultiplier

fluidized
bed

X ← Z
    ↓
    Y

beam splitter
and Bragg cell

laser

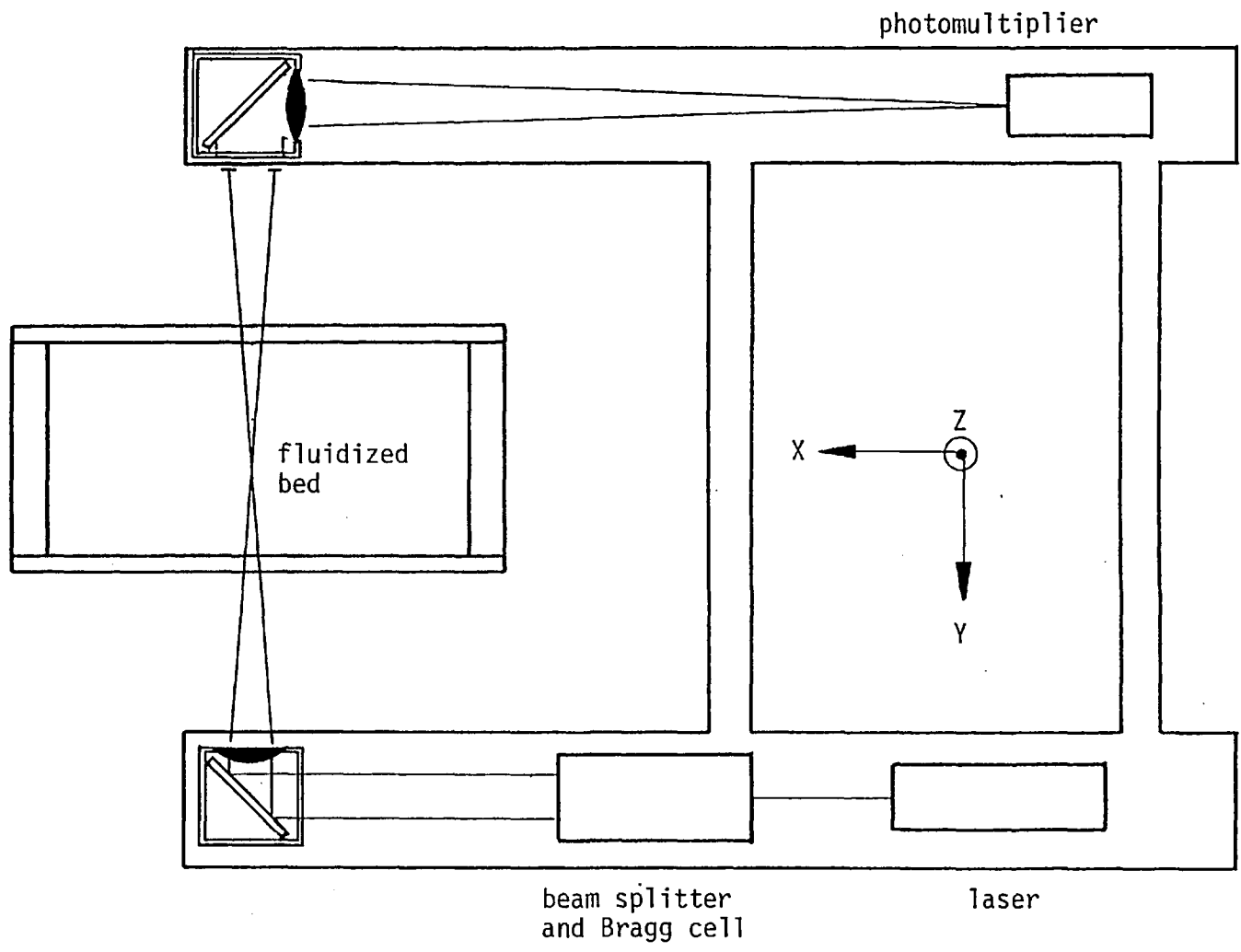Fig. 4.4-1   Optical bench
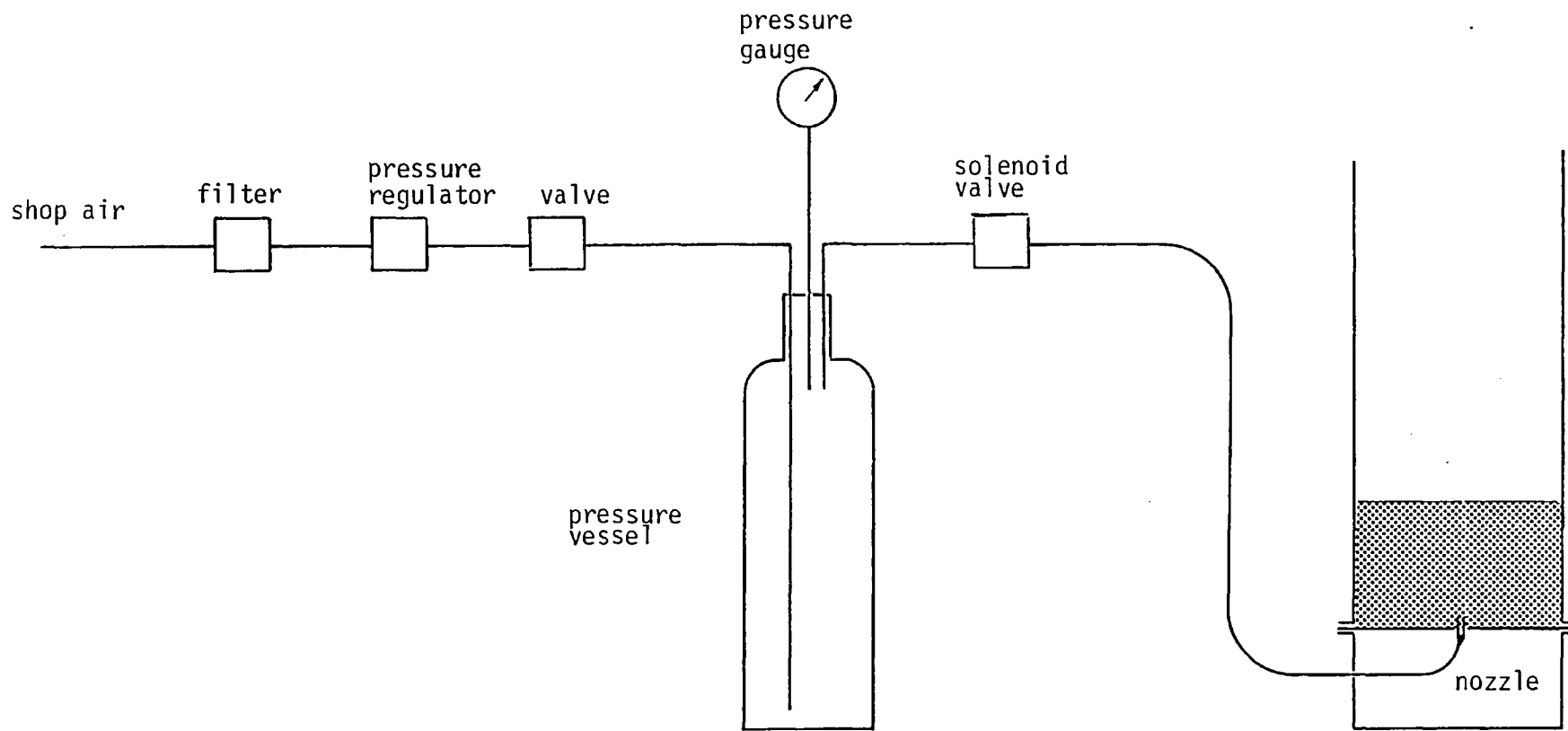
Fig. 4.5.1-1 Single bubble release air supply
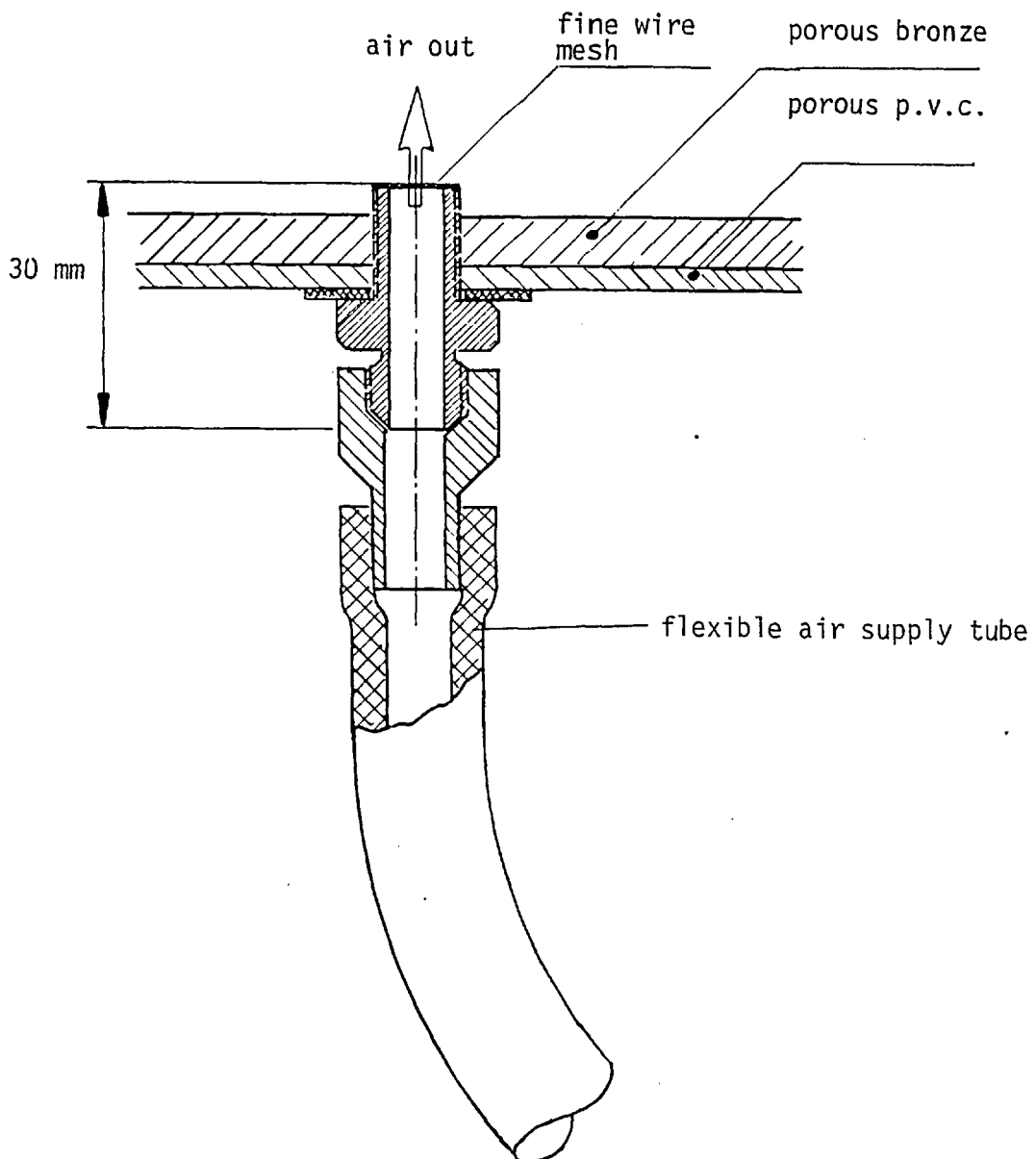
Fig. 4.5.3-1   Sketch of the single bubble nozzle
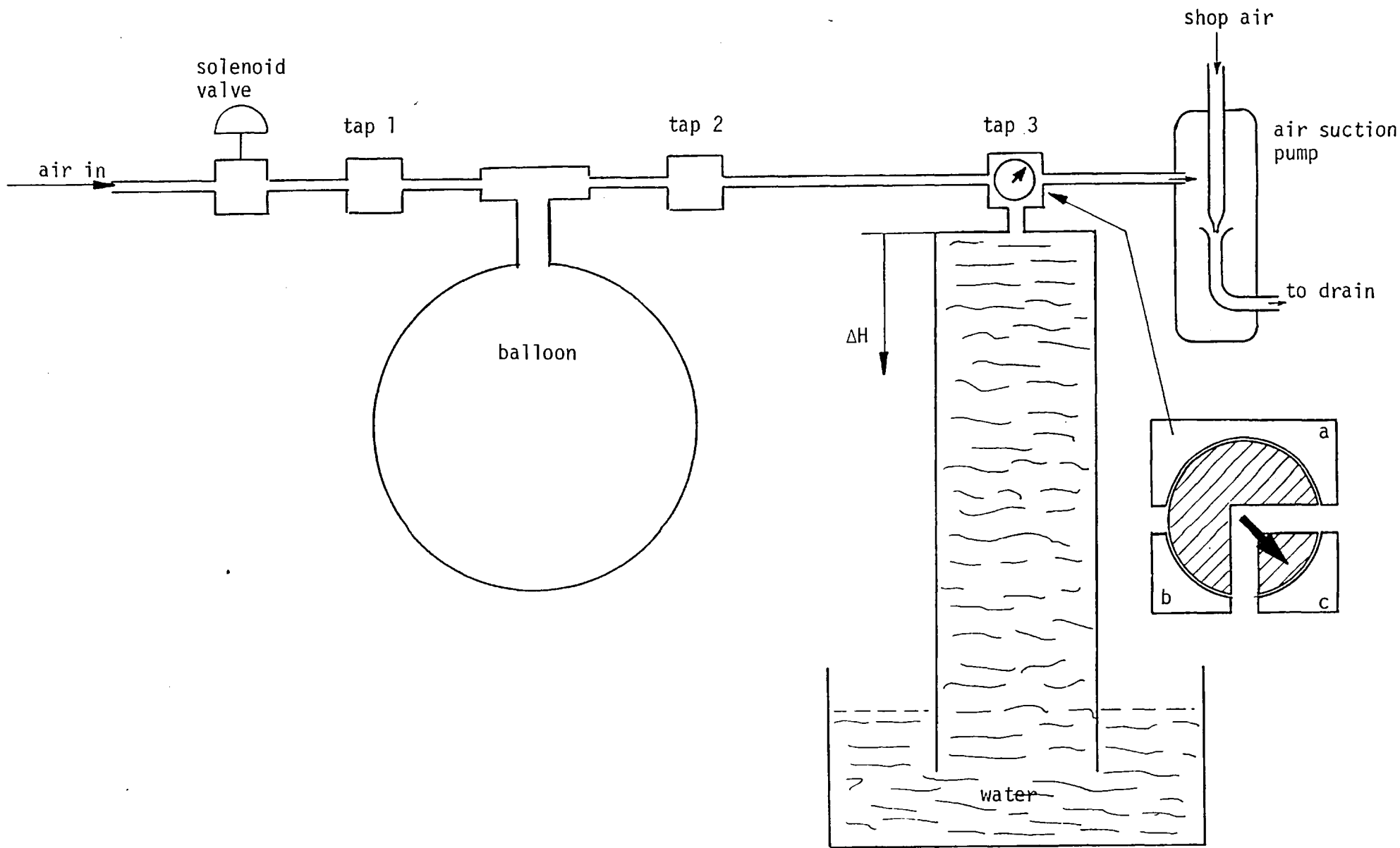
Fig. 4.5.4-1 Air pulse volume measurement system
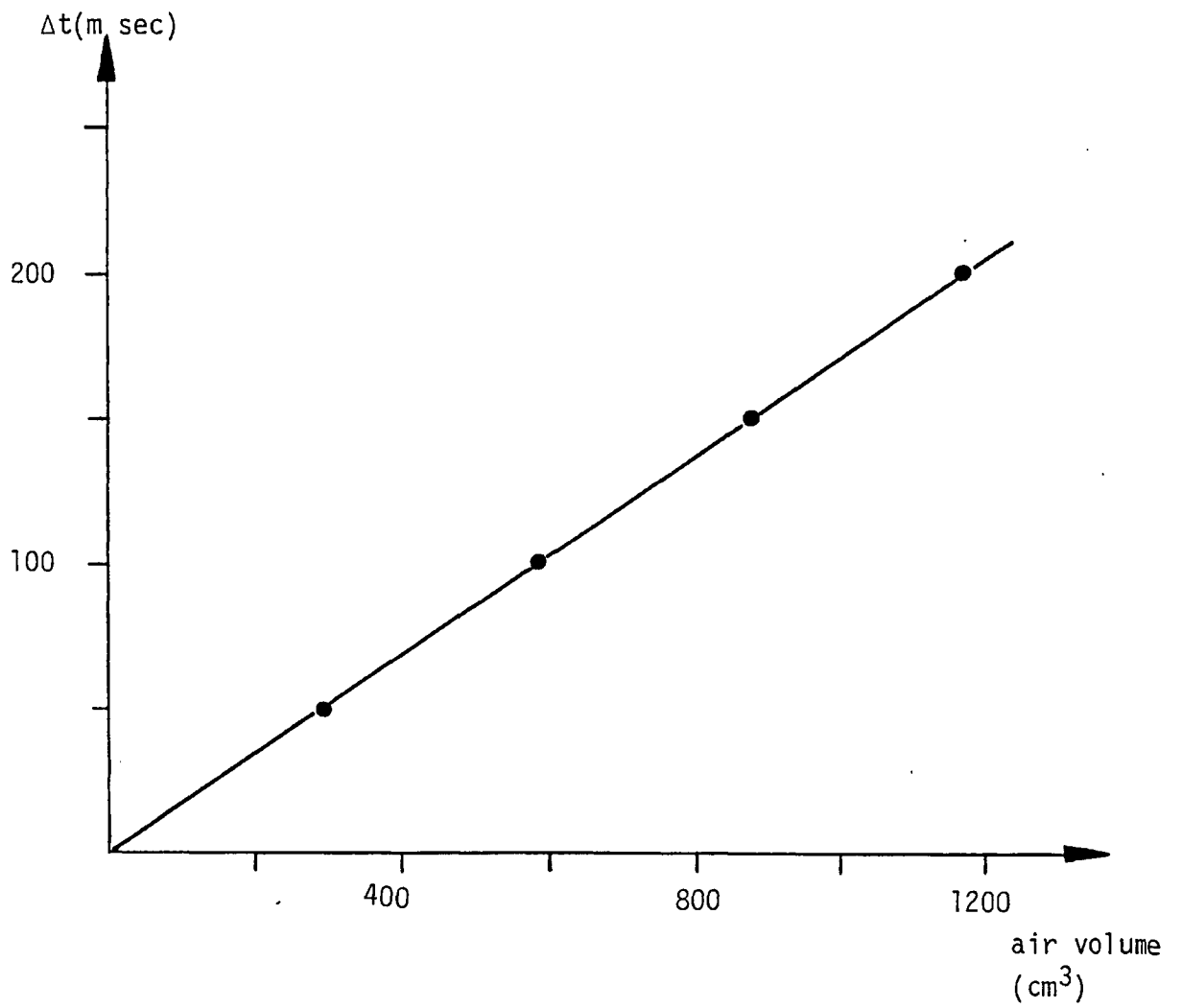
Fig. 4.5.4-2 The variation of air volume with valve opening time
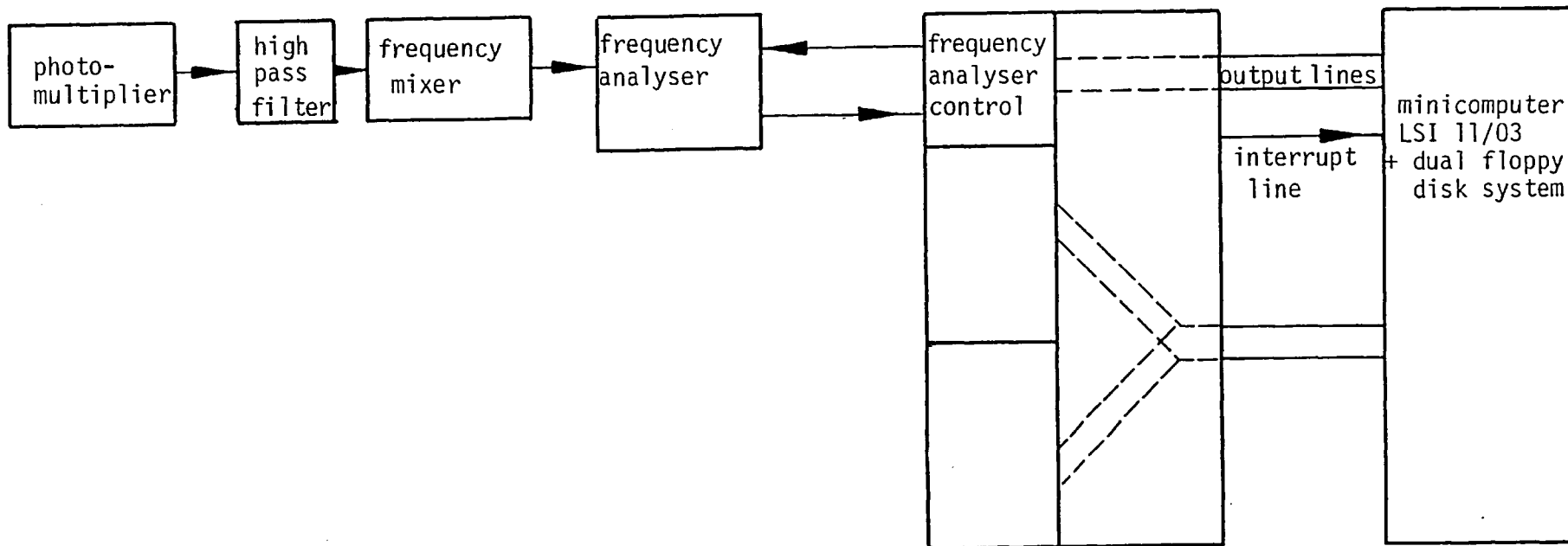
Fig. 5.3-1 Schematic block diagram of the Doppler frequency signal processing
system using frequency analyser
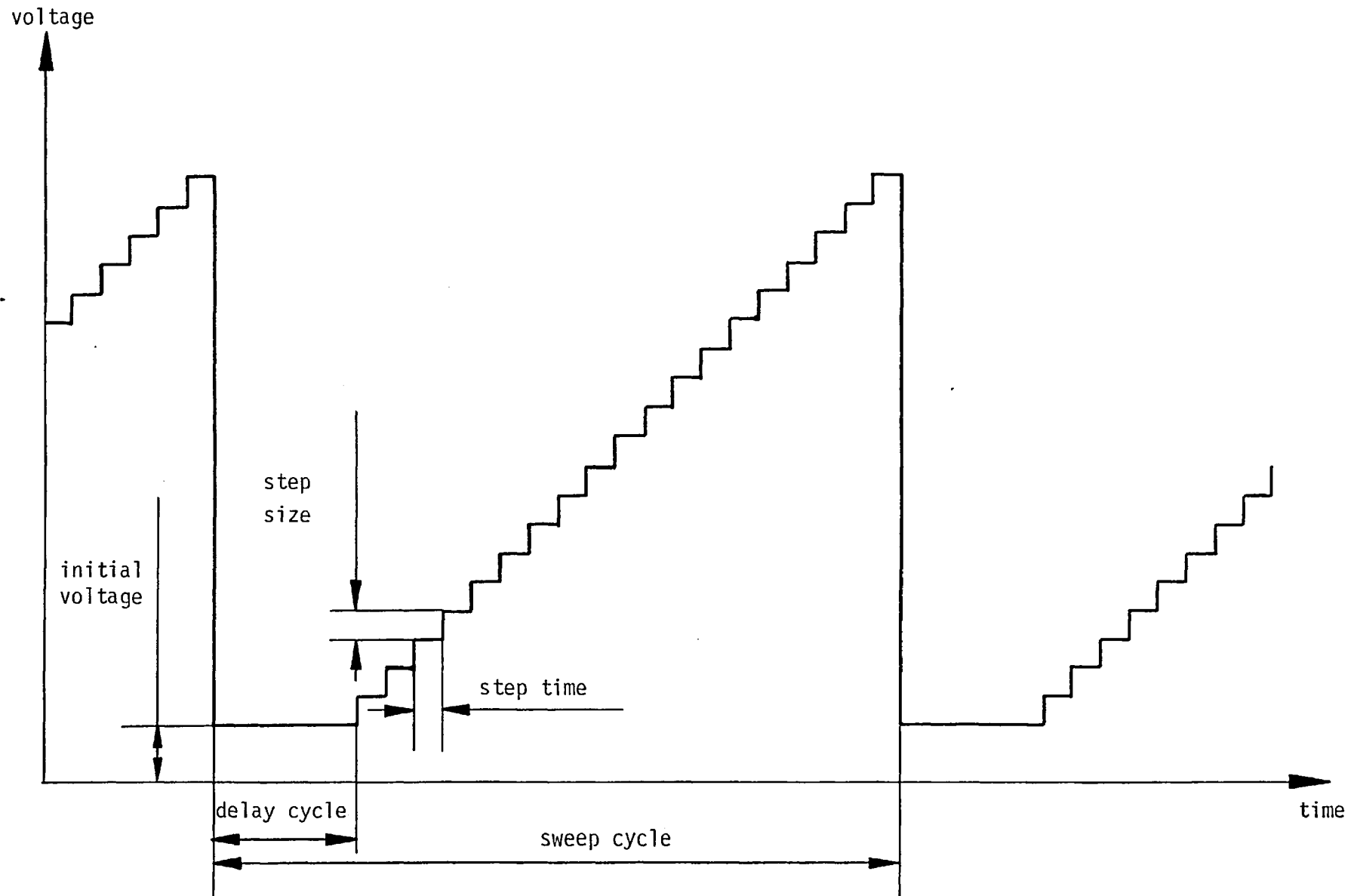
Fig. 5.3.1-1 The sweep voltage wave form
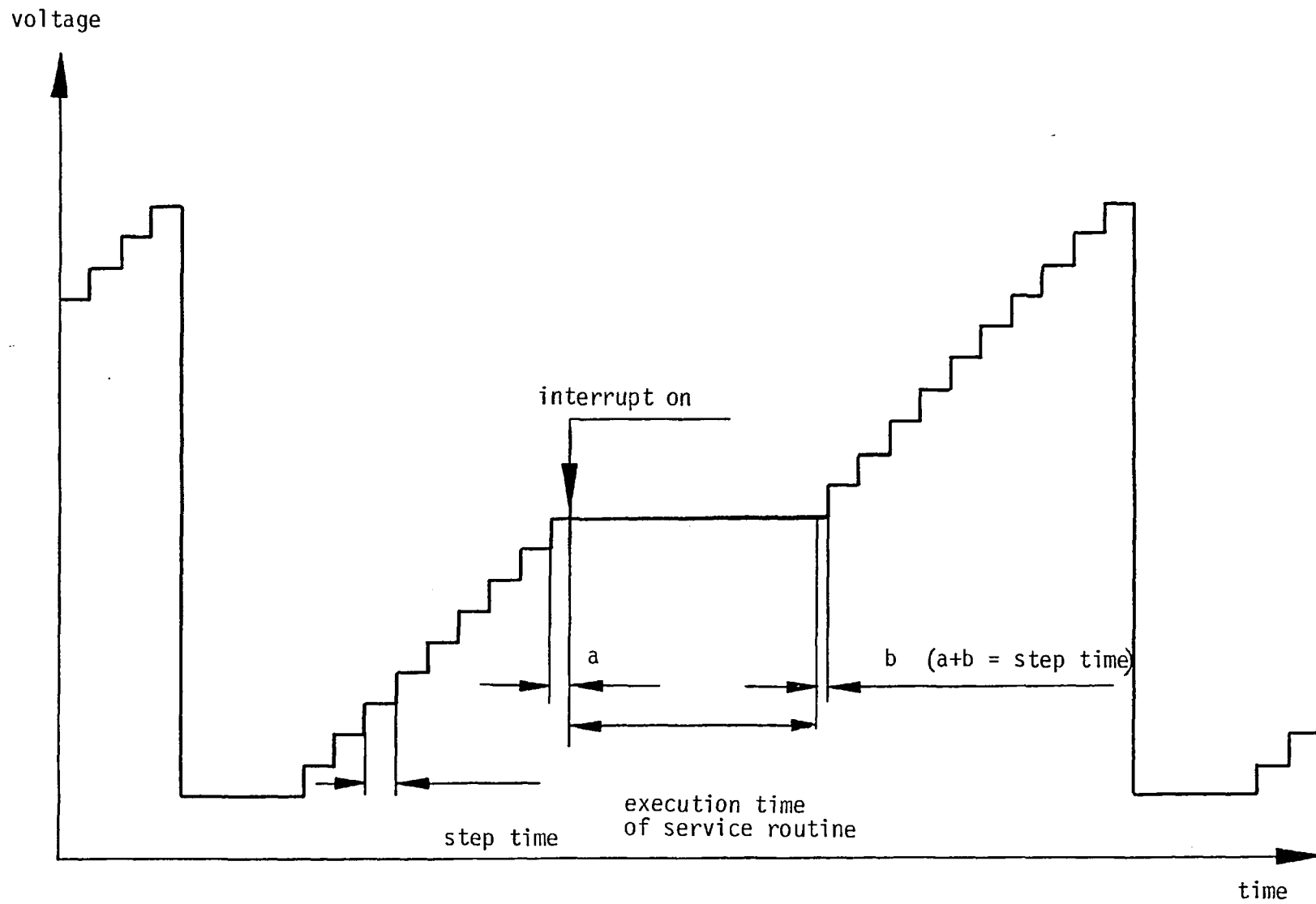
Fig. 5.3.2-1   Effect of an interrupt on the sweep voltage

input signal

external gate time pulse

ΔT_g

counter's gate time pulse

time

ΔT_c
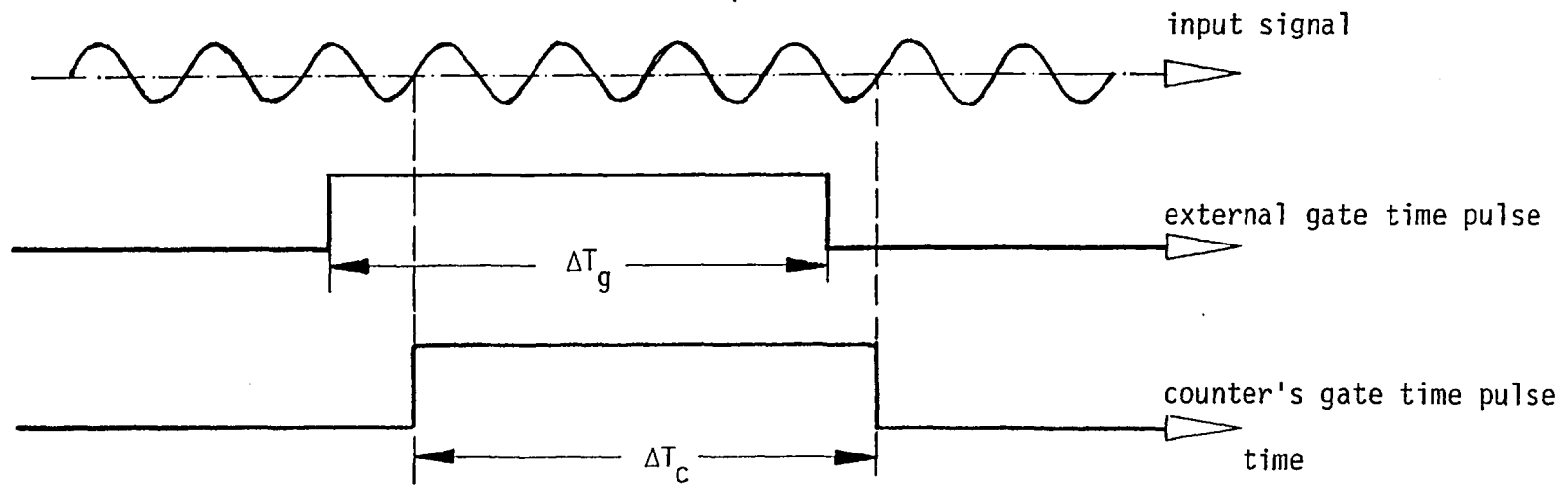
Fig. 5.4.1-1 Generation of the counter's gate time pulse

Doppler signals
(high passed signal)

gate time pulse
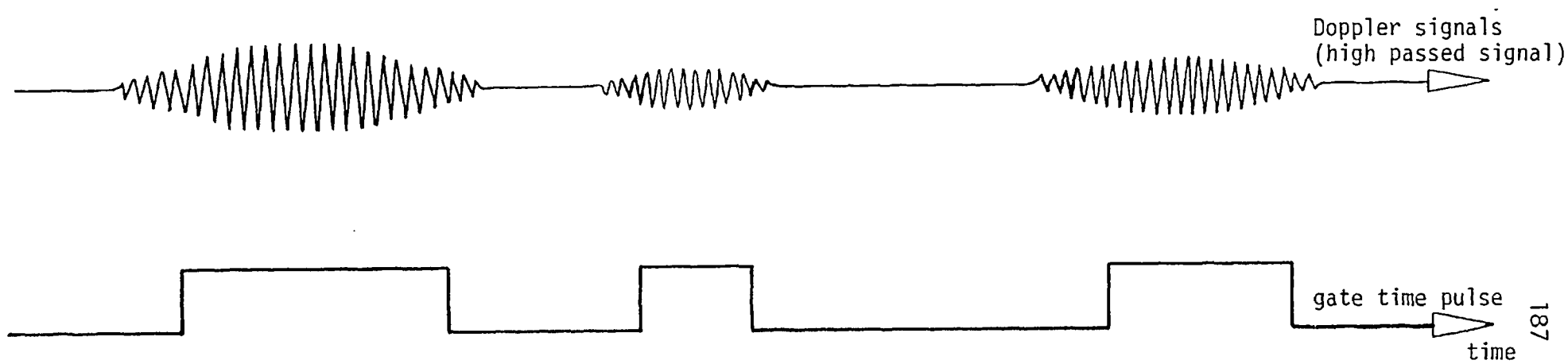
time

Fig. 5.4.1-2 Synchronization of gate time pulse to Doppler burst envelope shape

COUNTER SYSTEM

photo-
multiplier → high pass filter → frequency mixer → amplifier → low pass filter → frequency counter

HPIB → minicomputer

counter's gate time pulse

LSI 11/03 + dual floppy disk system

low pass filter → gate time pulse generator

188
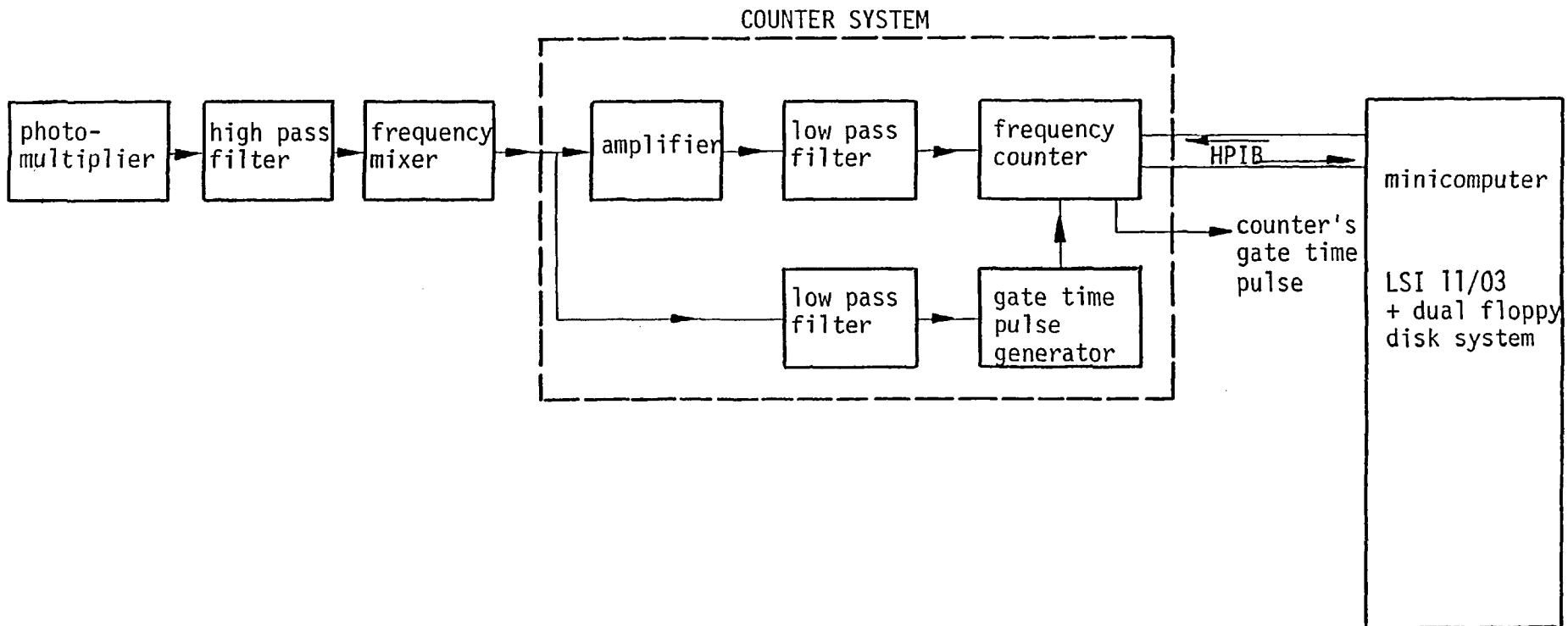
Fig. 5.4.2-1   Schematic block diagram of the Doppler frequency signal processing system using frequency counter

pedestal amplitude t

trigger level

trigger pulse

t

analog output
of peak detector

t

vertical output of frequency
analyser

t

end of service
routine

interrupt
request

t

size indicator

t

analog to digital
conversion

t

pedestal amplitude binary value

old data   reset to zero   new data

time
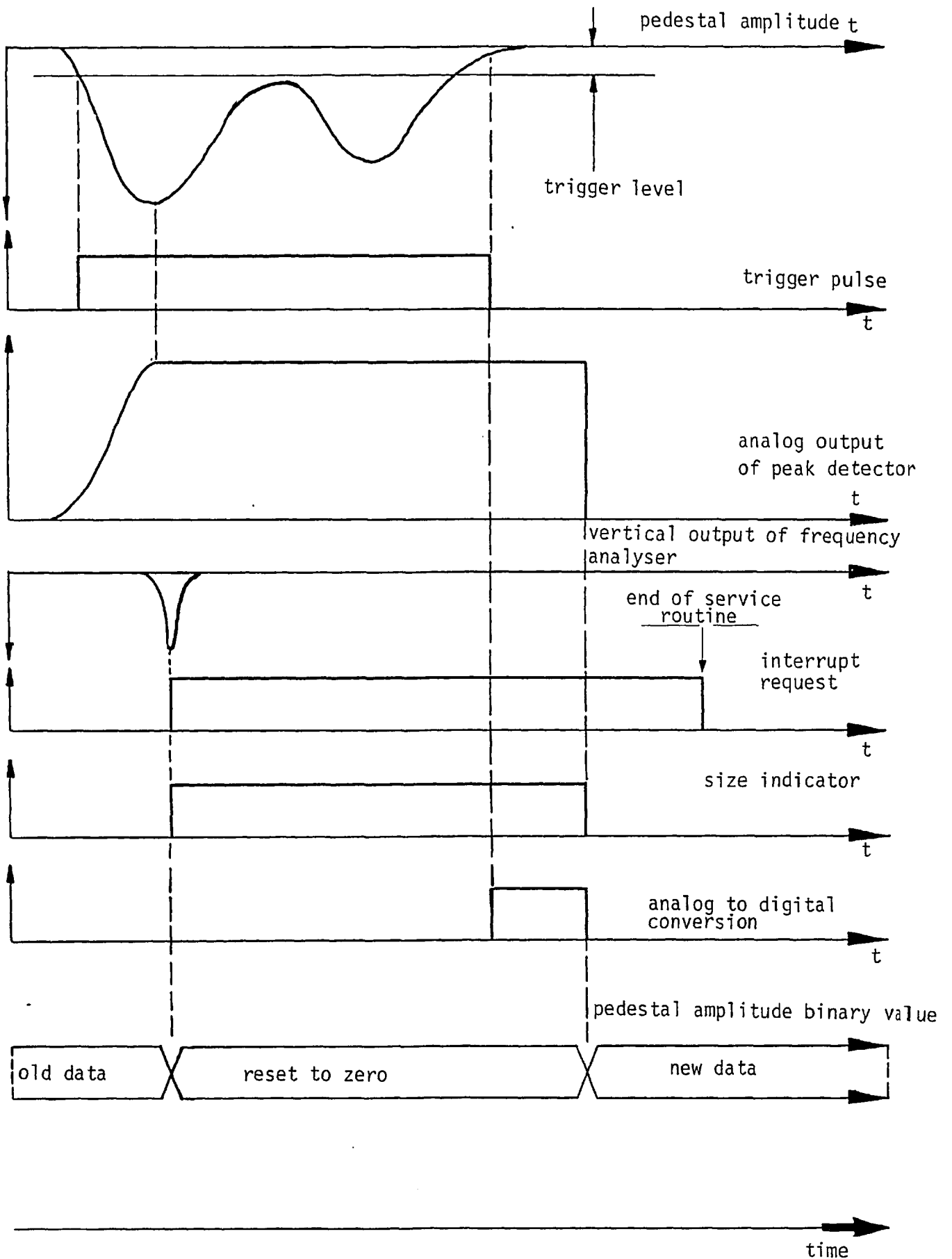
Fig. 5.5.3-1   Timing diagram of the two-phase flow signal processing
using the frequency analyser
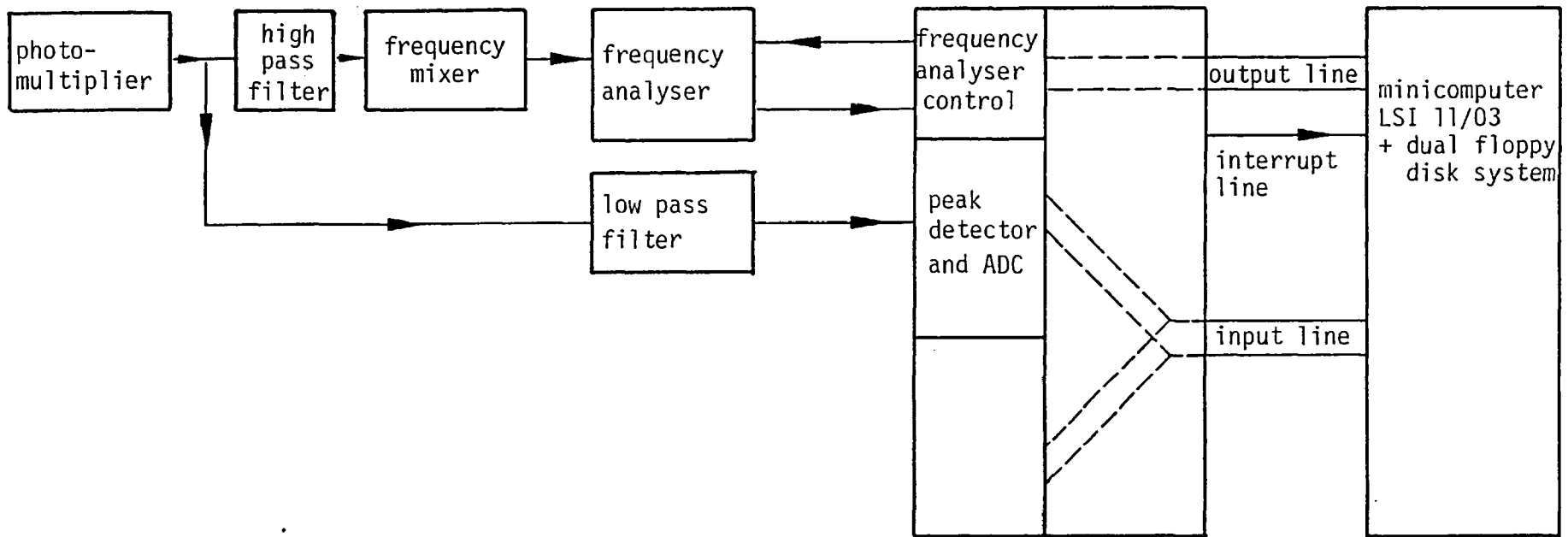
Fig. 5.5.3-2   Schematic block diagram of the two-phase flow signal processing using the frequency analyser

Doppler frequency
(high passed signal)

pedestal amplitude
(low passed signal)

peak detector
trigger pulse

analogue output
of peak detector

counter's gate
time pulse

interrupt request

counter interrupt status

- enable -

- disable -

analogue to
digital conversion

size indicator

pedestal amplitude binary value

old data   reset to zero   new data   TIME

counter
data
transfer
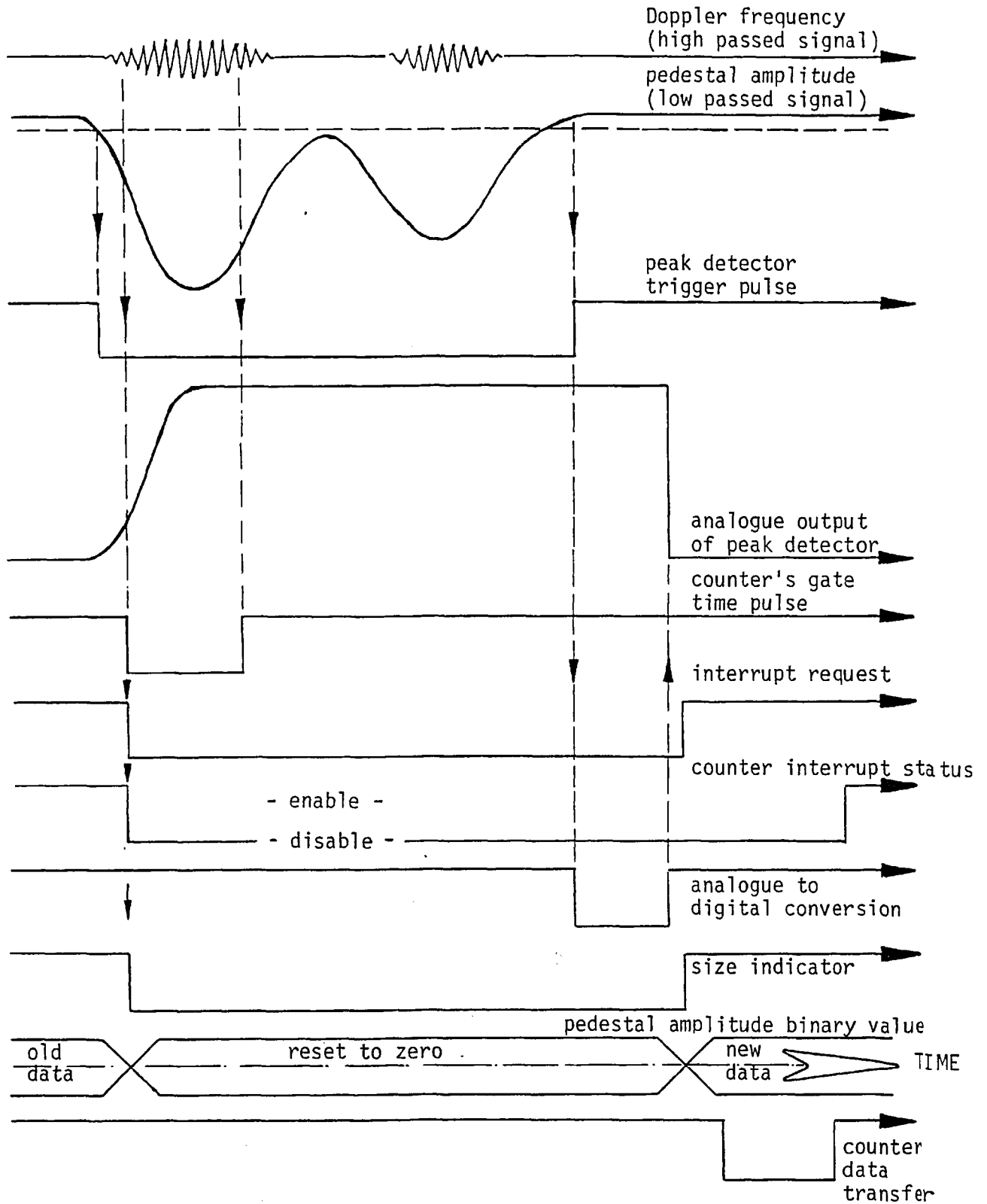
Fig. 5.5.3-3   Timing diagram of the two-phase flow signal processing
using the frequency counter
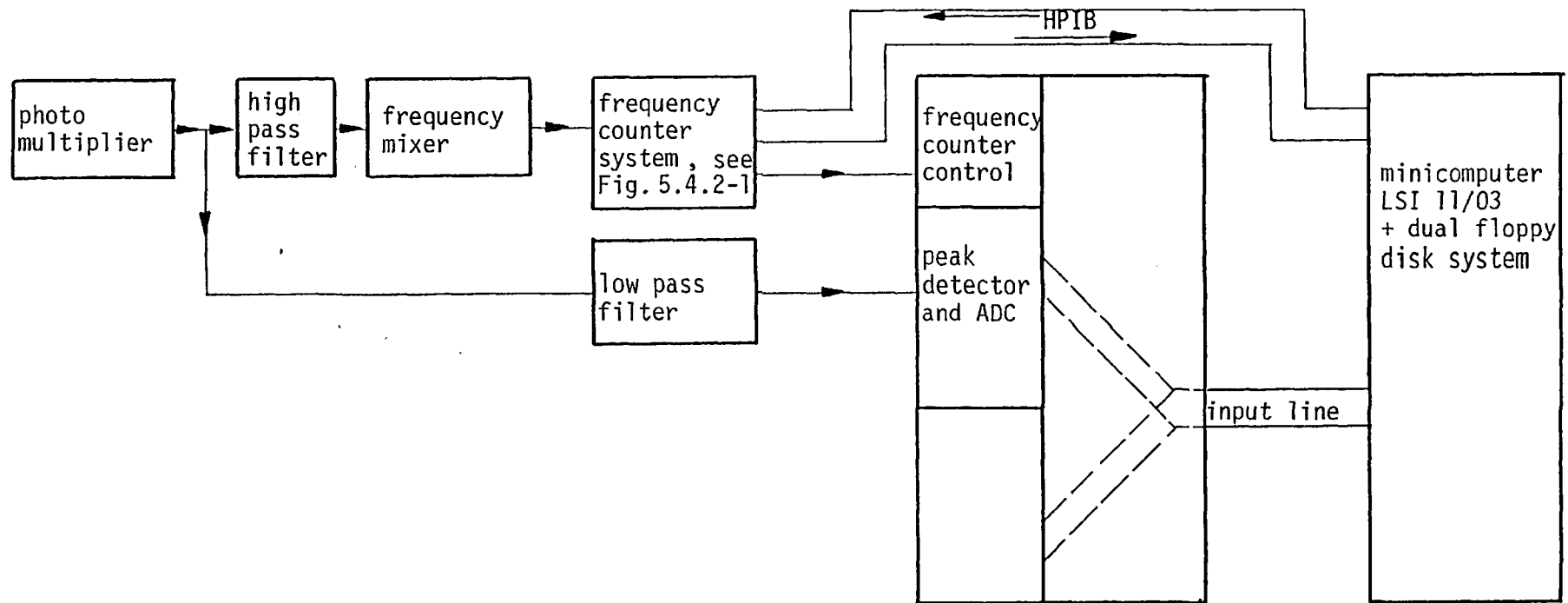
Fig. 5.5.3-4 Schematic block diagram of the two-phase flow signal processing using the frequency counter

Doppler frequency
(high passed signal)

pedestal amplitude
(low passed signal)

trigger level

peak detector
trigger pulse

analogue output of
peak detector

counter's gate
time pulse

interrupt request

- enable -

delay
time

counter's
interrupt
status

-disable -

ADC

size indicator

pedestal amplitude binary value

old data

counter's data
transfer

TIME

end of service routine
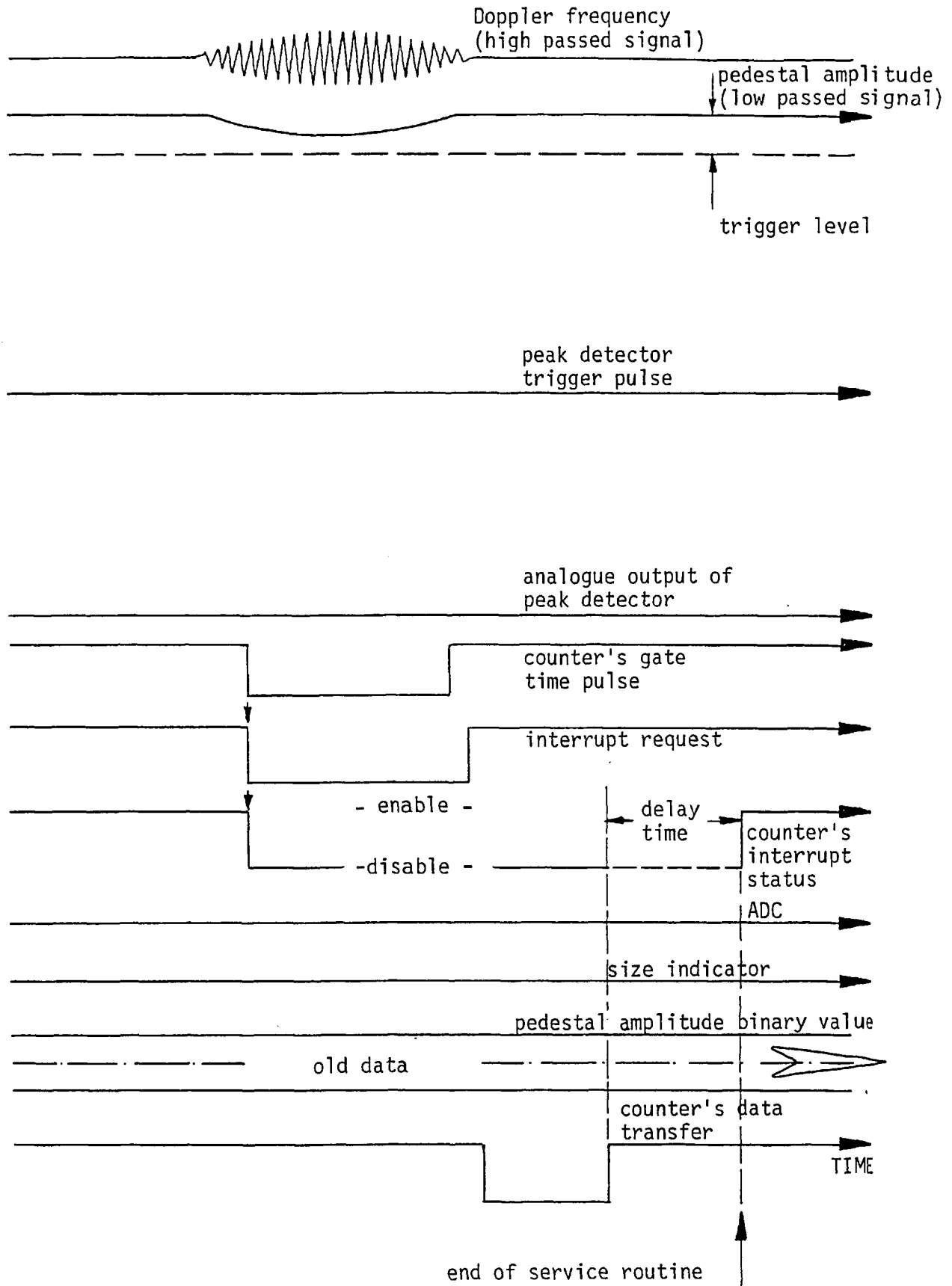
Fig. 5.5.3-5   Timing diagram for the case of a small particle signal
(gas measurement) using a counter based system
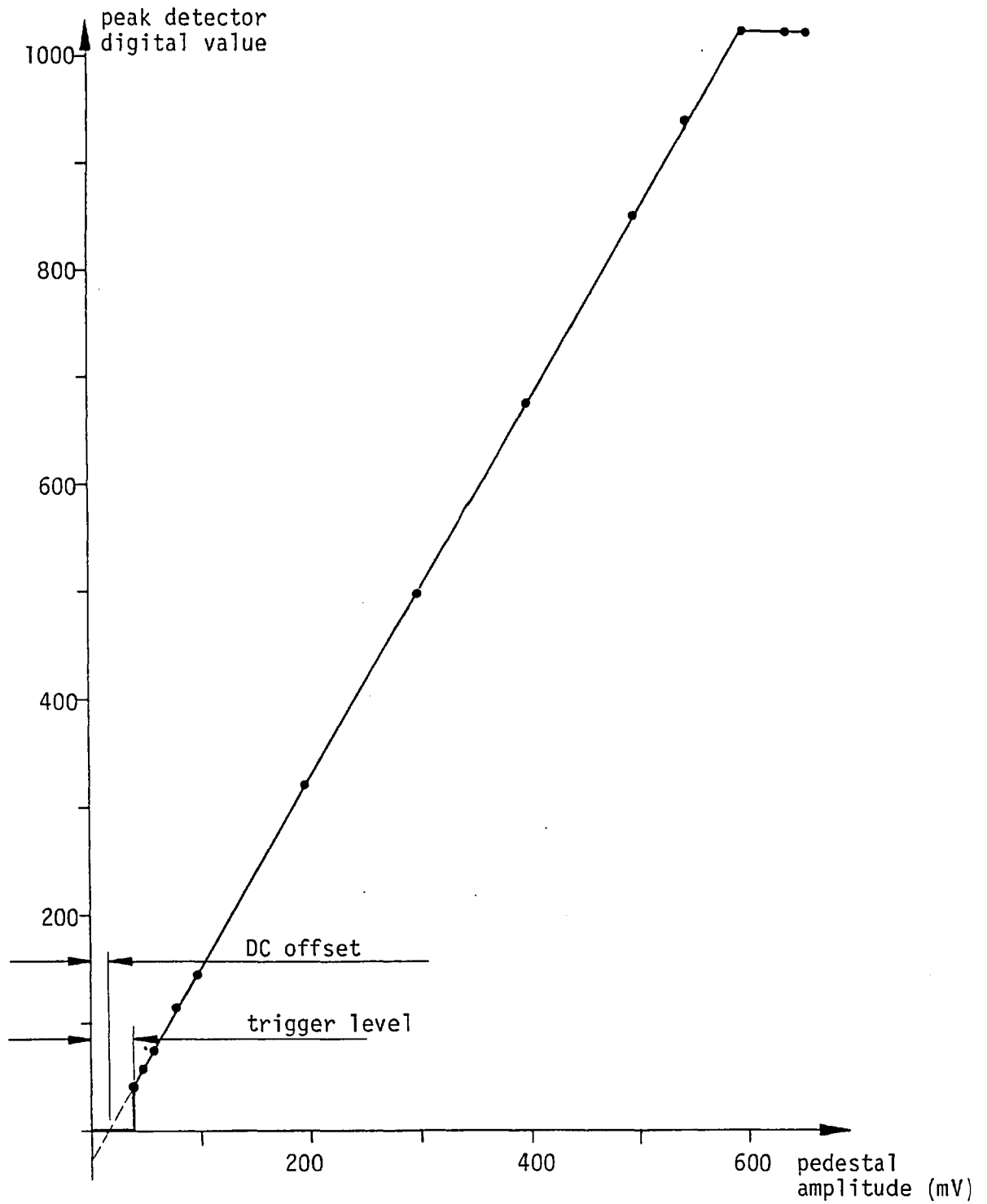
Fig. 5.5.4-1 Variation of the peak detector digital output with pedestal amplitude

solenoid valve
control pulse

the ejected sand
general movement

level of
detection

height

reference
time
pulse
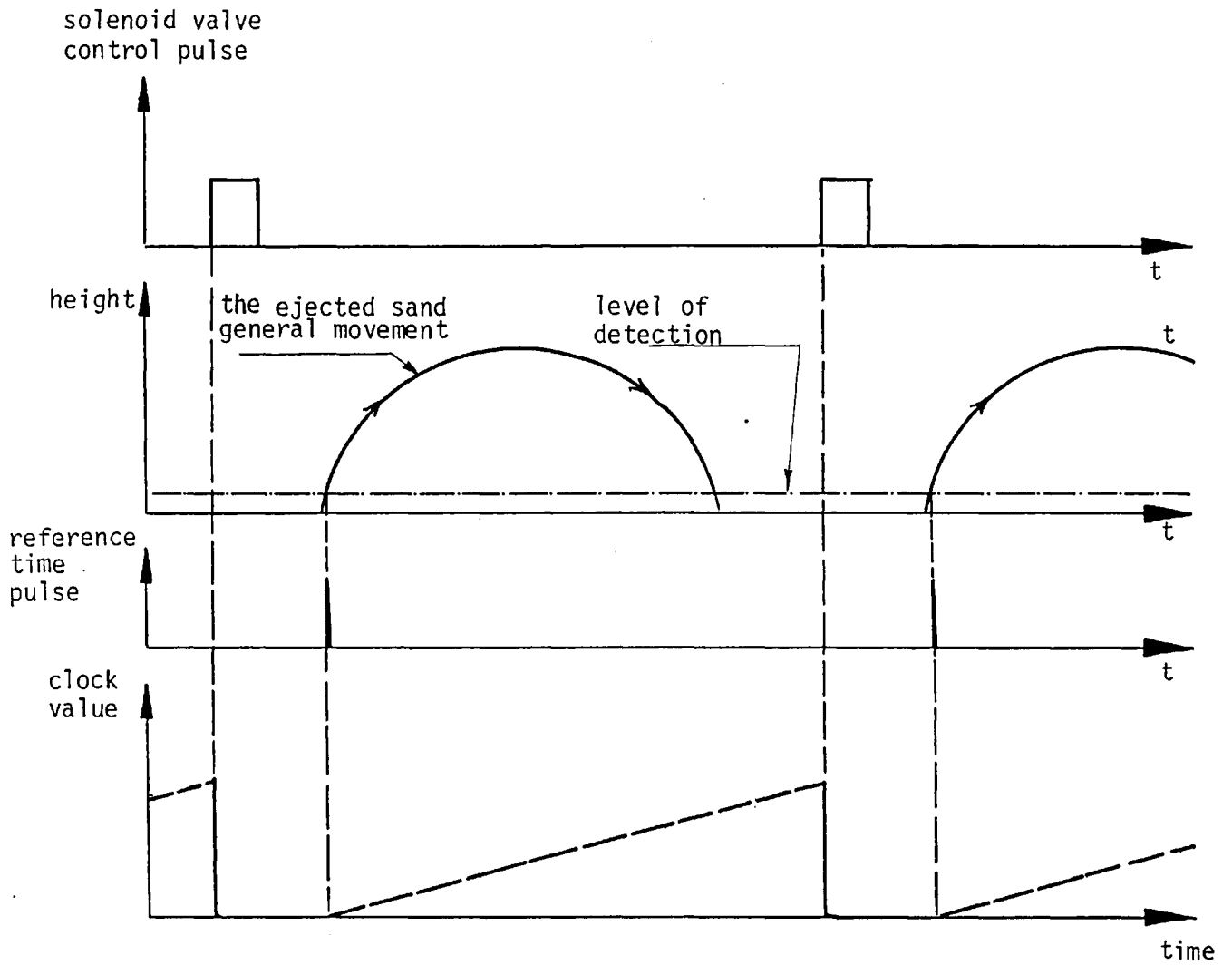
clock
value

time

Fig. 5.6.2-1 Timing diagram of the clock counter control
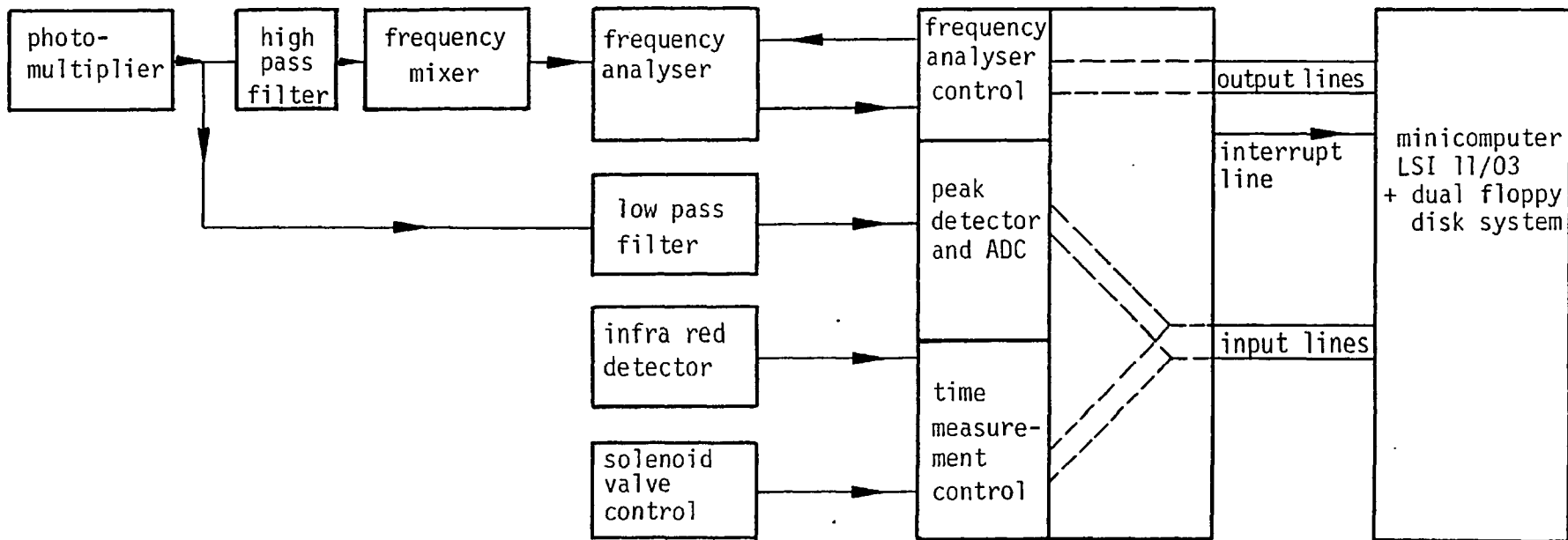
Fig. 5.6.2-2 Schematic block diagram of the time dependent two-phase flow signal processing using the frequency analyser

```
        ┌──────────────┐          ┌──────────────┐
        │              │          │ line         │
        │     VDU      │          │ printer      │
        │              │          │              │
        └──────────────┘          └──────────────┘
```

┌───┐
│   │
│   ┌──────────────────┐   ┌──────────────────┐   │
│   │   │   │ dual floppy disk │   │
│   │ DEC LSI 11/03   │◄────►│ unit for 8"   │   │
│   │ processor   │   │ diskettes   │   │
│   │   │   │   │   │
│   └──────────────────┘   └──────────────────┘   │
│   ◄────►   │
│   ┌──────────────────┐   ┌──────────────────┐   │
│   │ parallel I/O card│   │ bus interface   │   │
│   │ DRV11   │   │ IBV11-A (HPIB)   │   │
│   └──────────────────┘   └──────────────────┘   │
│   │
└───┘

to the interface unit of   to frequency counter
the frequency analyser,
the peak detector and the
time of measurement record
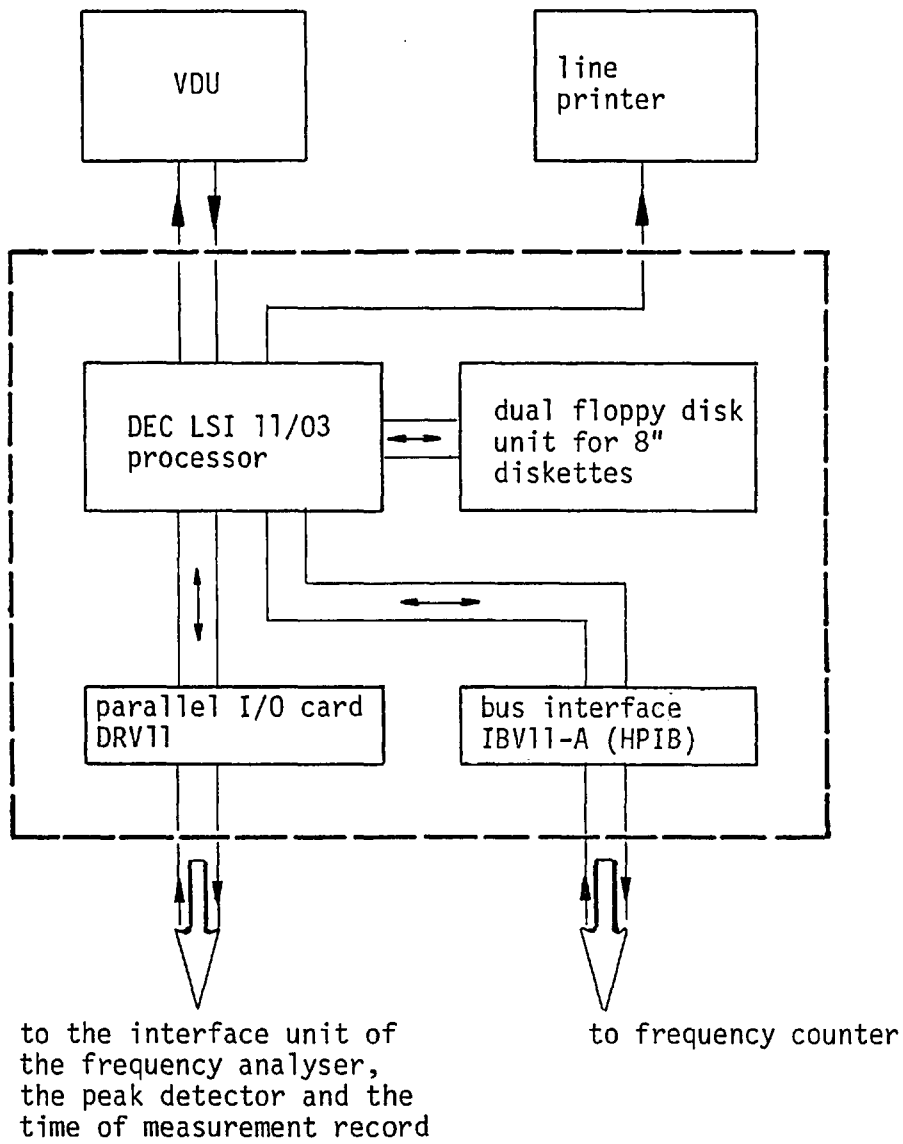
Fig. 5.7-1   The mini-computer system
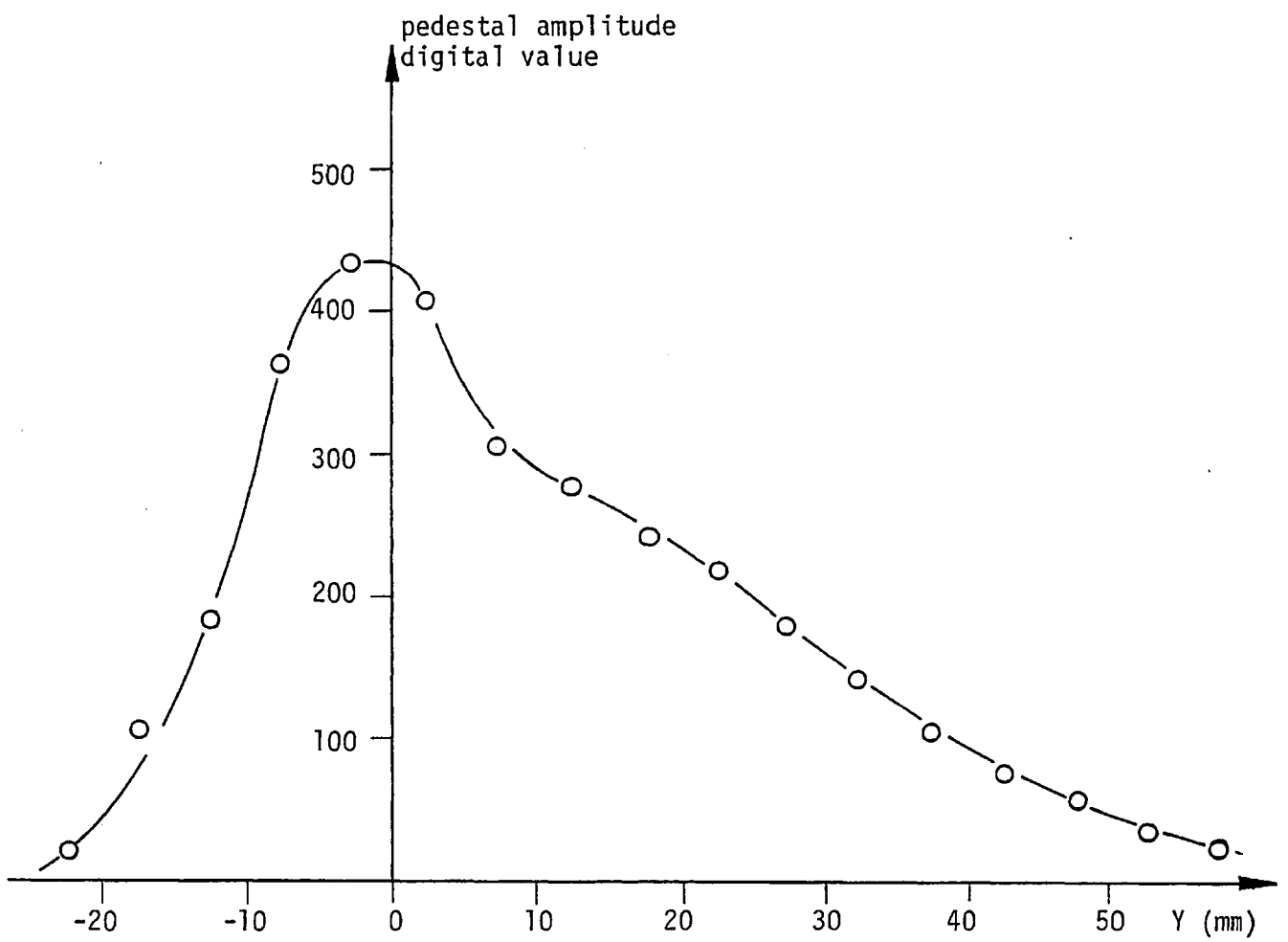
Fig. 5.9.1-1   Typical variation of the signal's pedestal amplitude of
a sand particle with distance from the centre of the
control volume
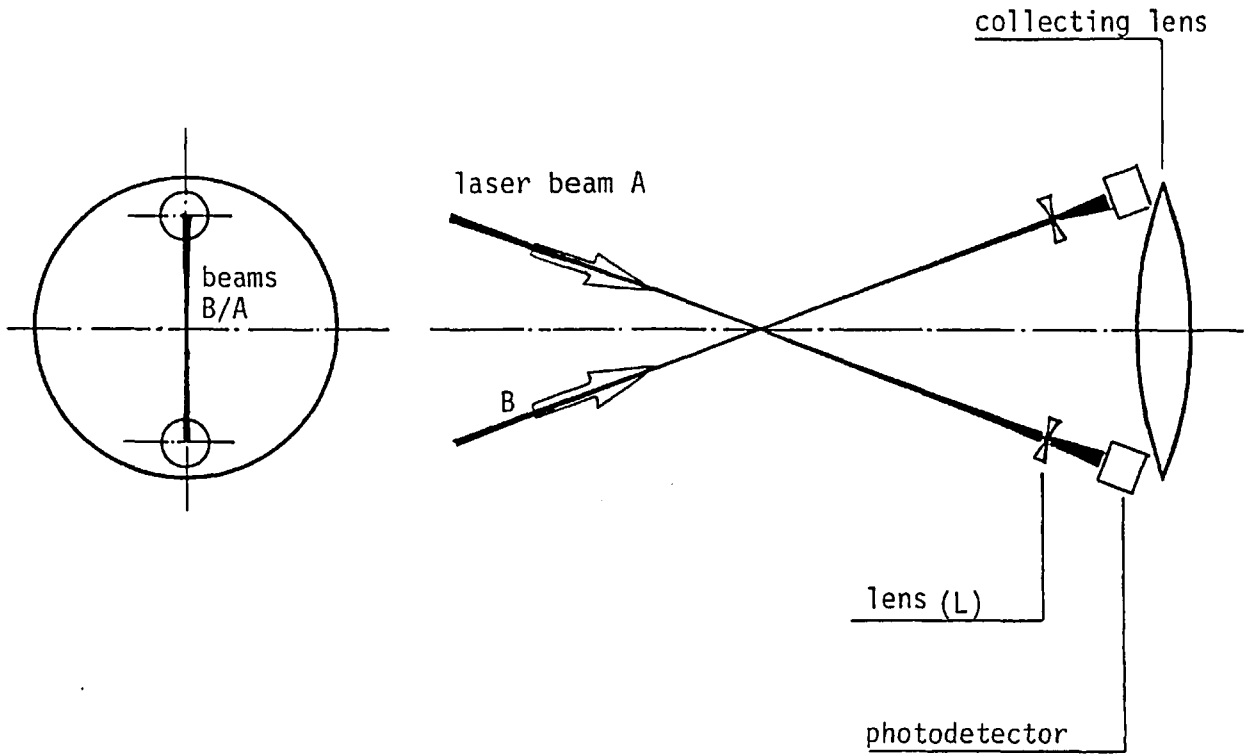
Fig. 5.9.2-1   Optical arrangement for the particle flux measurement
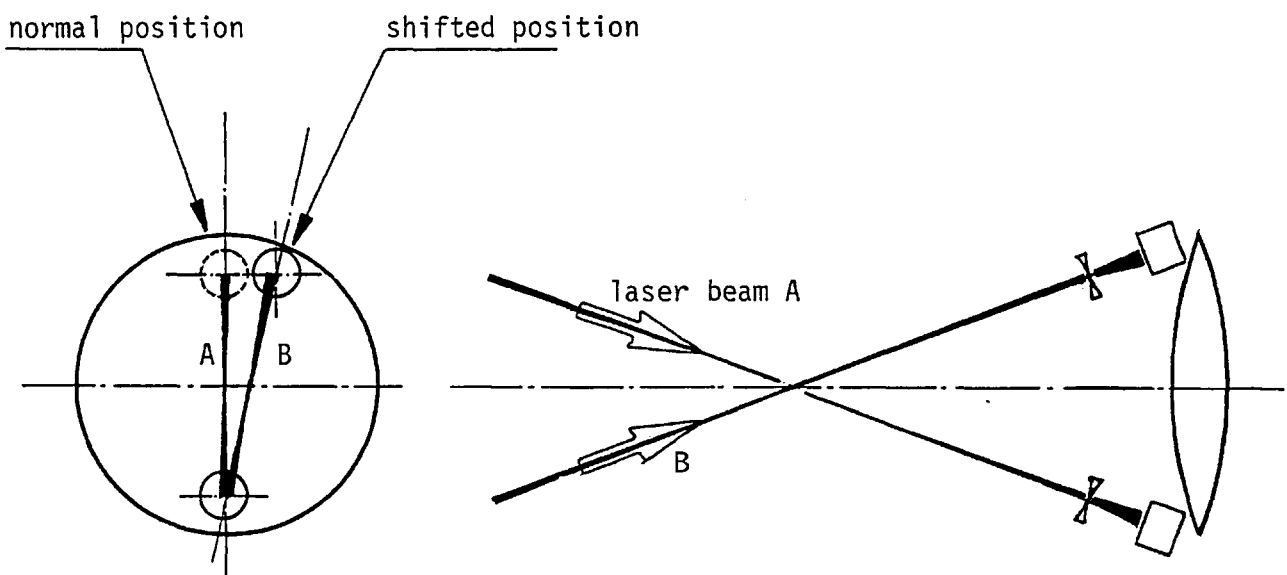
Fig. 5.9.2-2   Optical arrangement for the detection of flux signal
from particles which do not cross the control volume
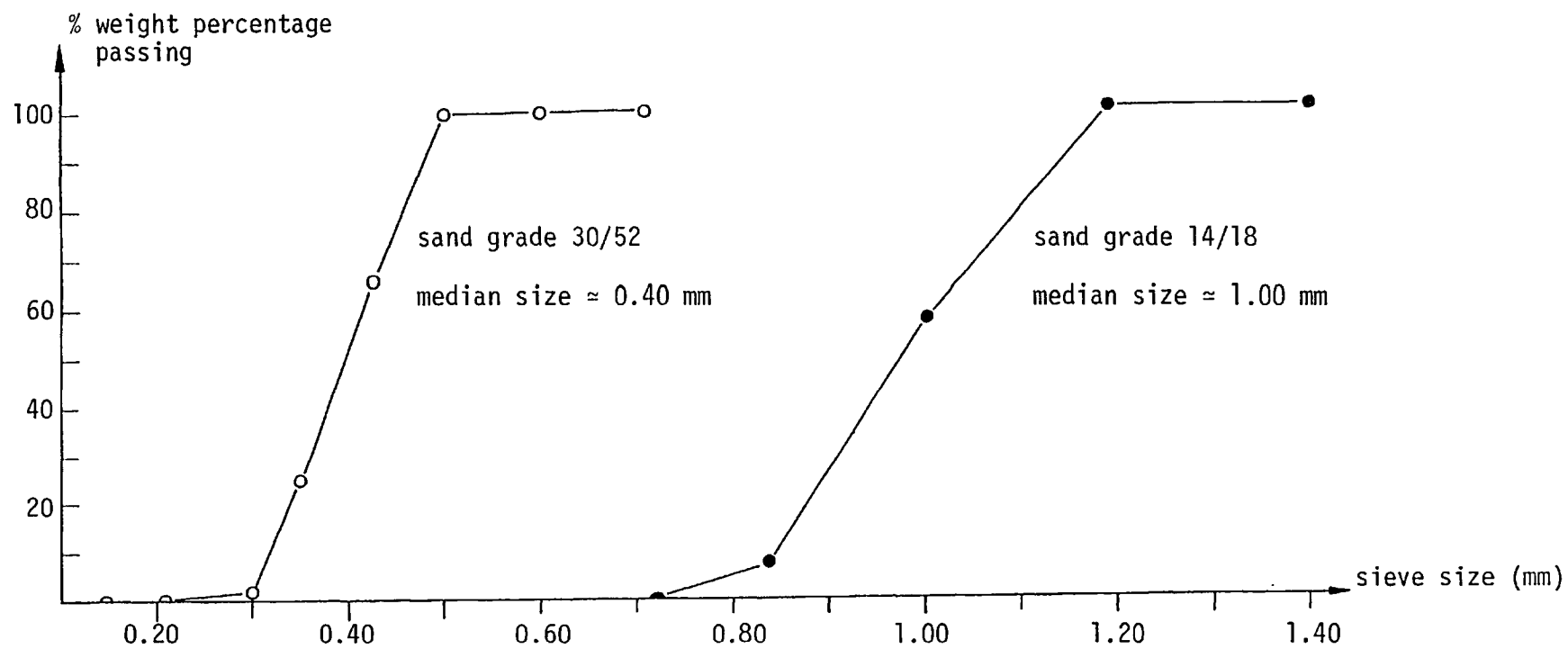
Fig. 6.1-1 Particle size distribution of two types of bed material
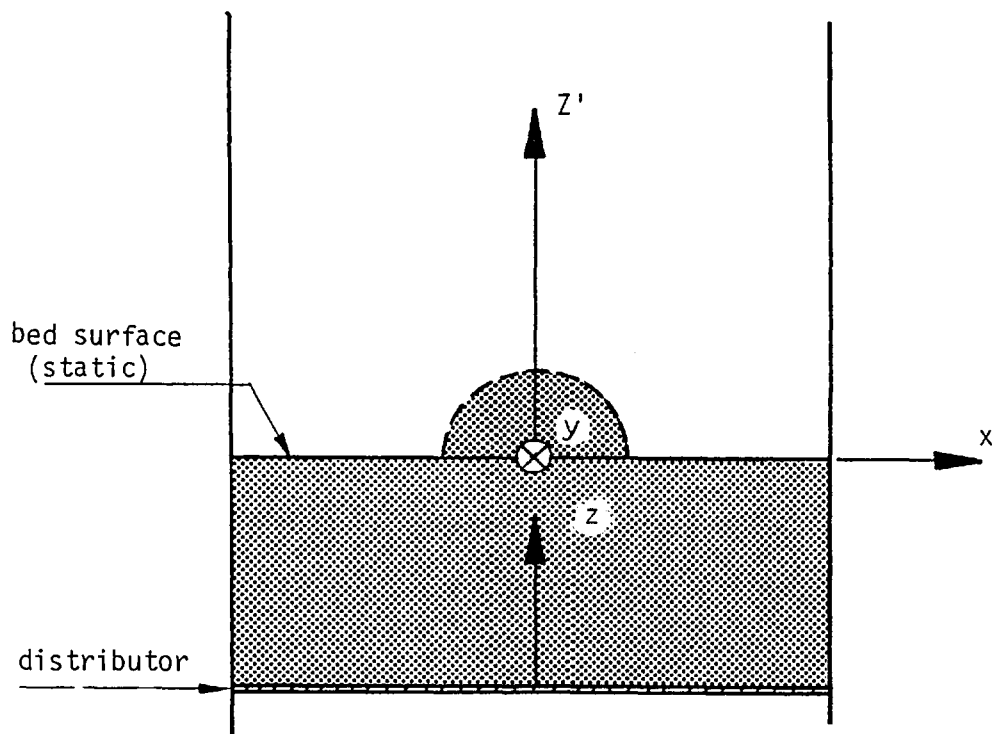
Fig. 6.2.1-1   The co-ordinate system: note Z´ is measured from
the static bed surface

202
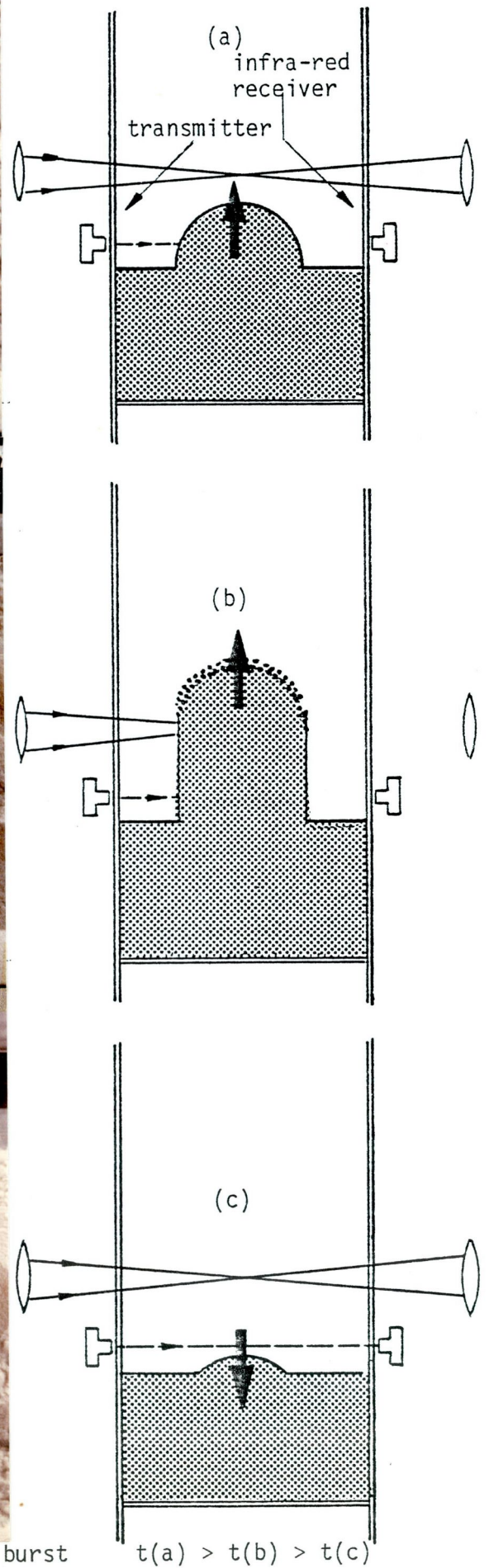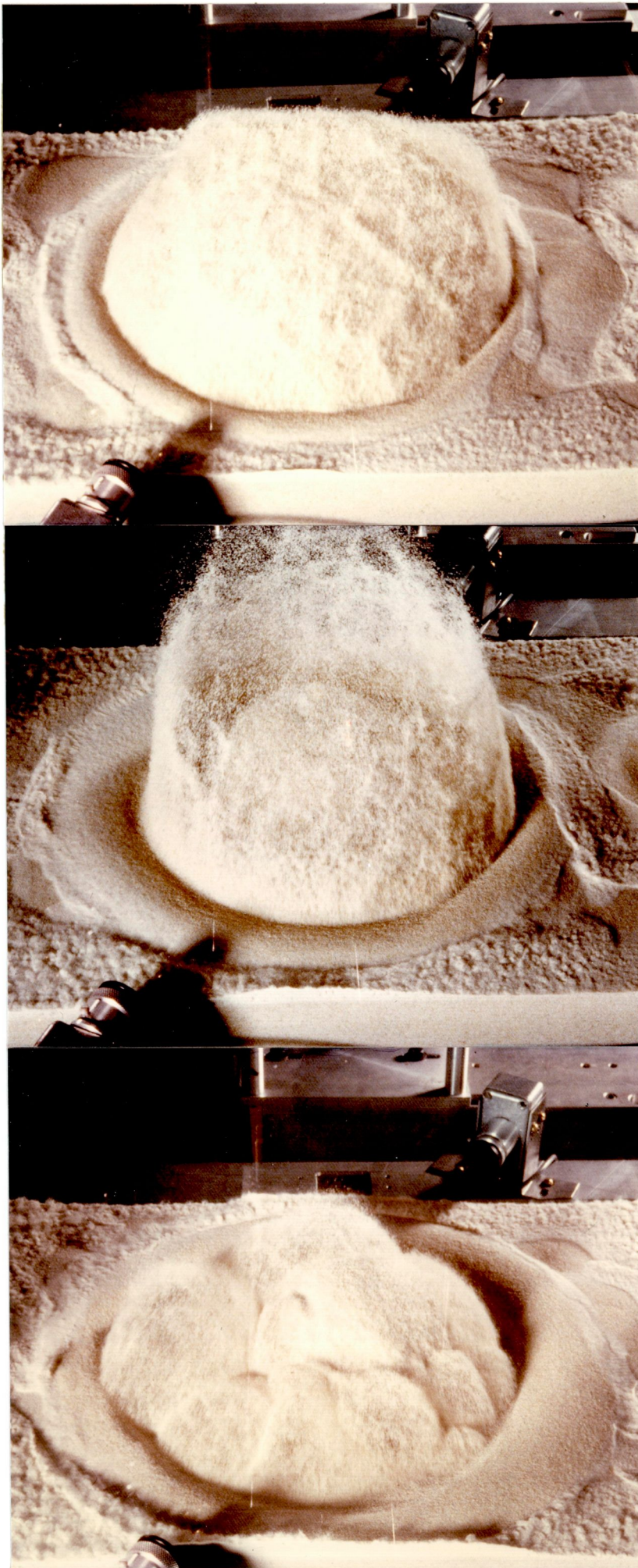
Fig. 6.2.2-1 Illustration of the bubble burst process

(a) infra-red receiver

transmitter

(b)

(c)

t(a) > t(b) > t(c)
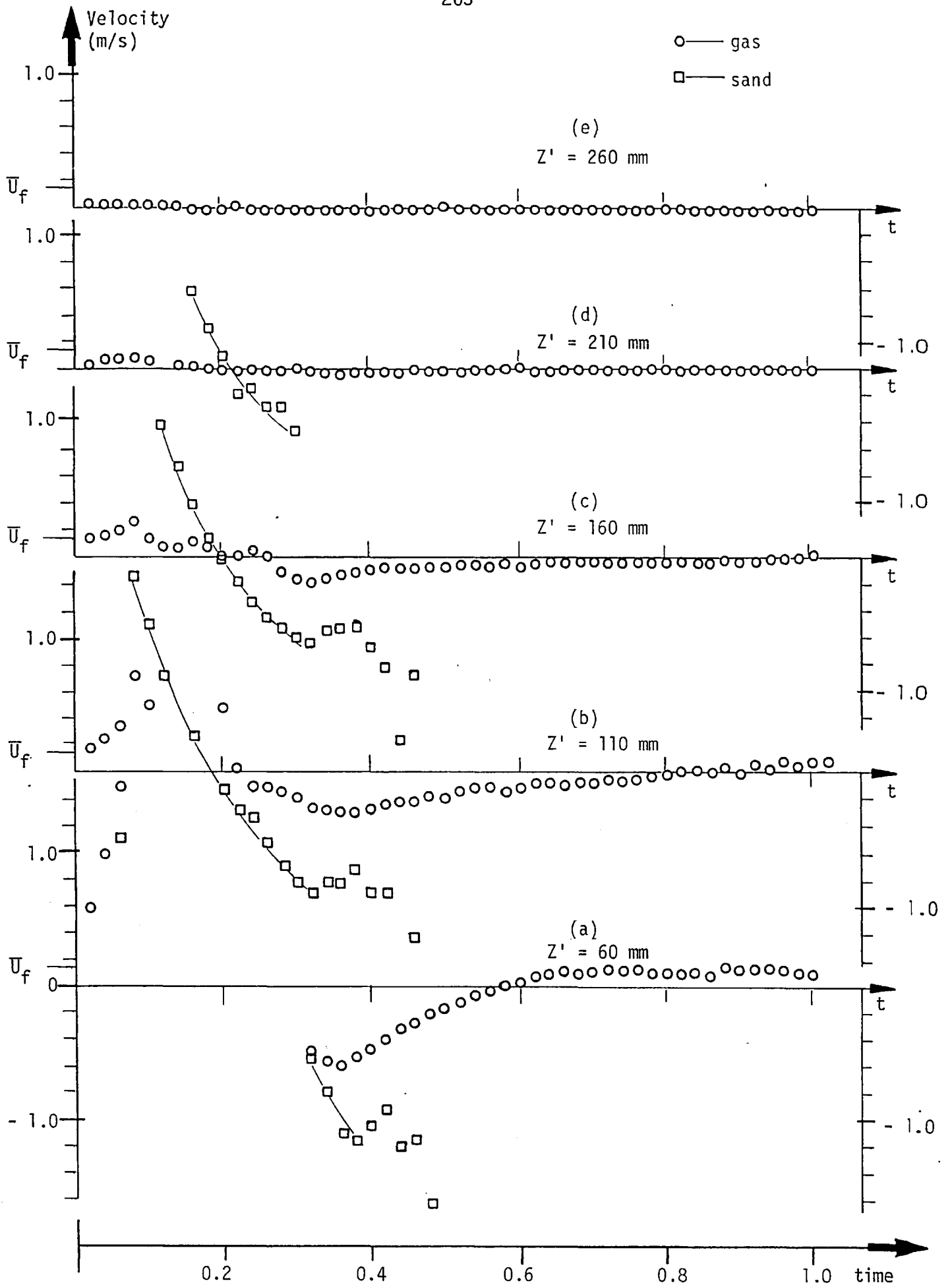
Fig. 6.2.2-2 Time variation of gas and sand velocities along the
vertical axis: X = 0, Y = 0
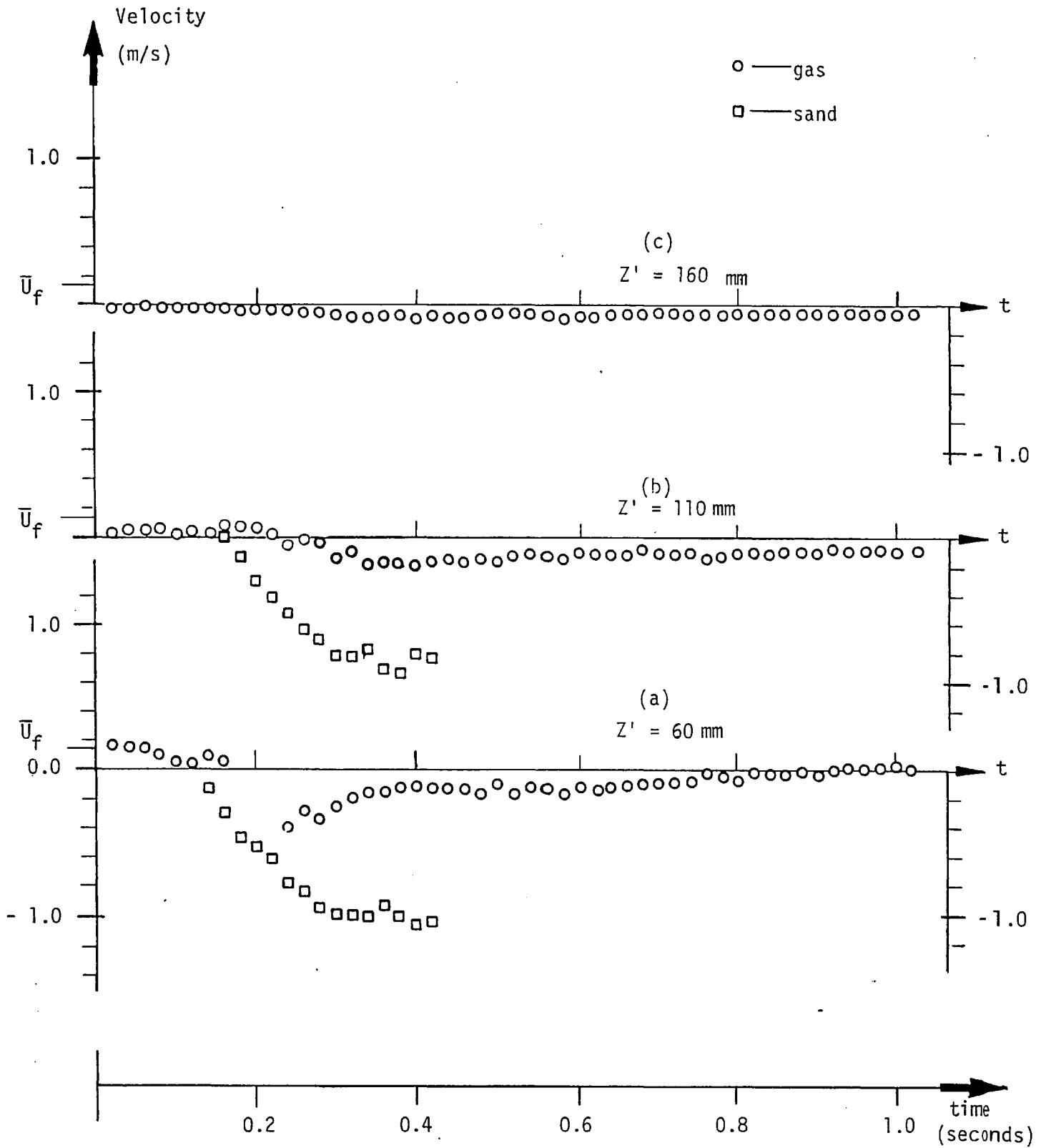
Fig. 6.2.2-3   Time variation of the gas and sand velocities along
the vertical axis: X = 100 mm, Y = 0
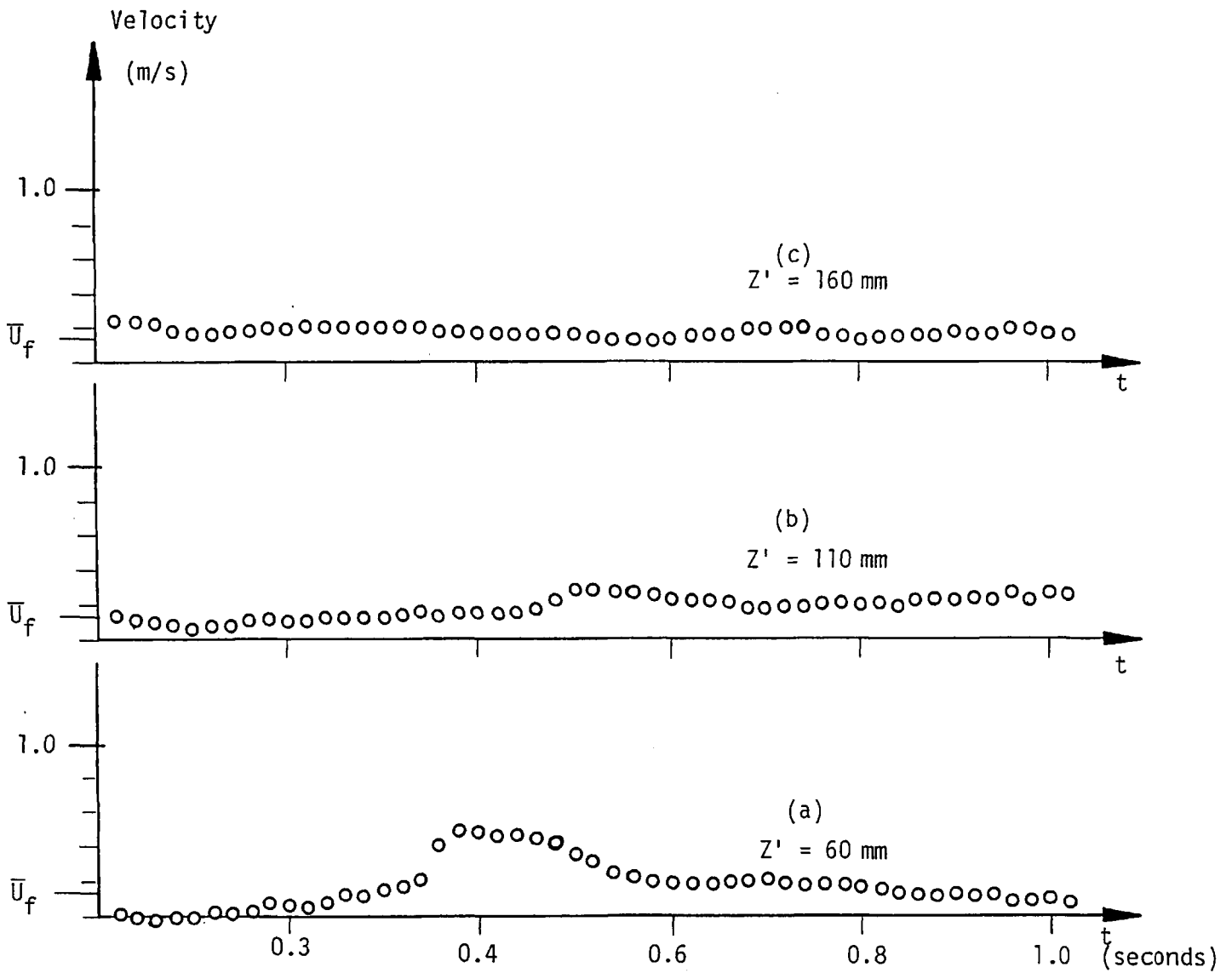
Fig. 6.2.2-4 Time variation of the gas and sand velocities along
the vertical axis: X = 200 mm, Y = 0
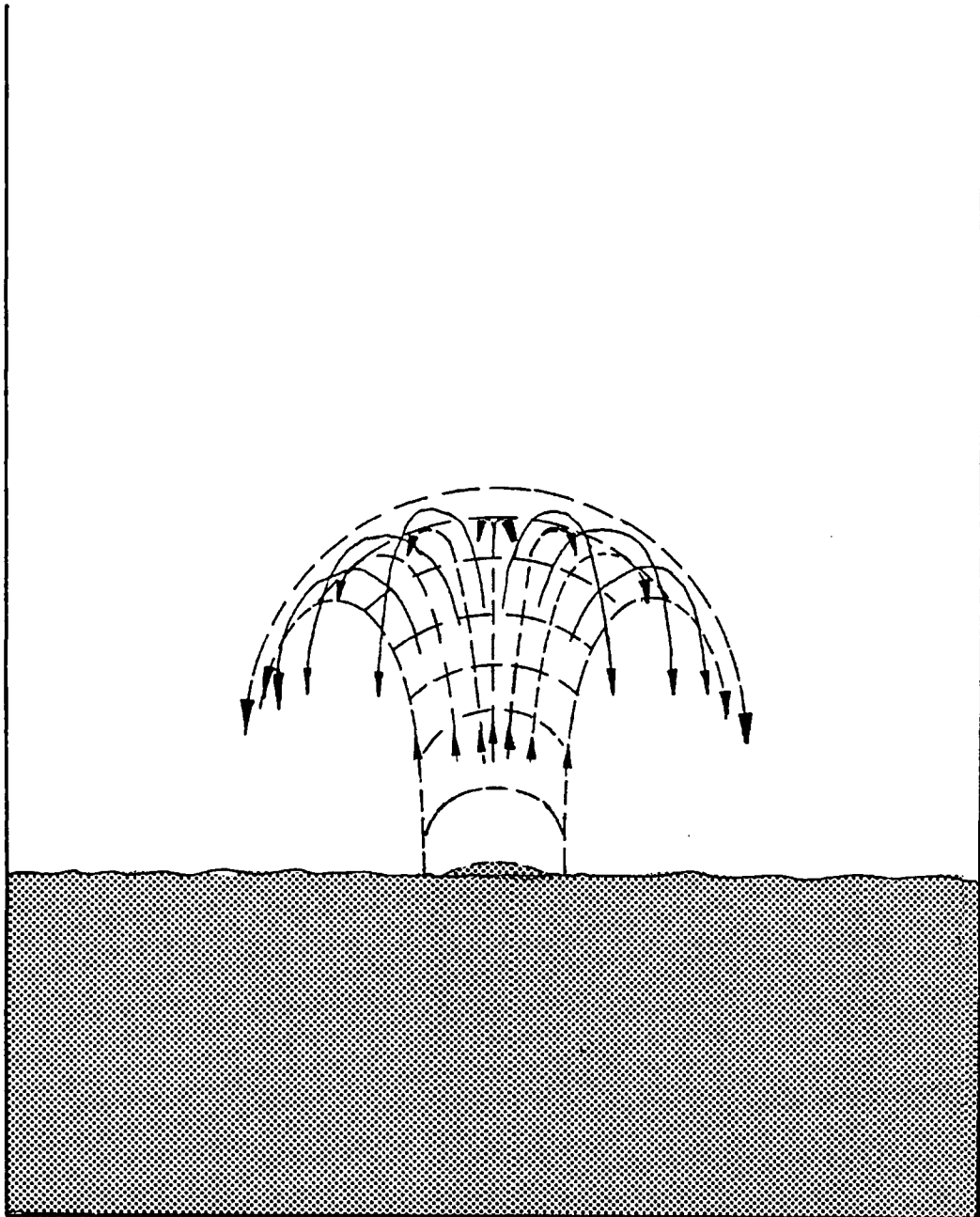
Fig. 6.2.2-5 Schematic illustration of particles movement during
a bubble burst
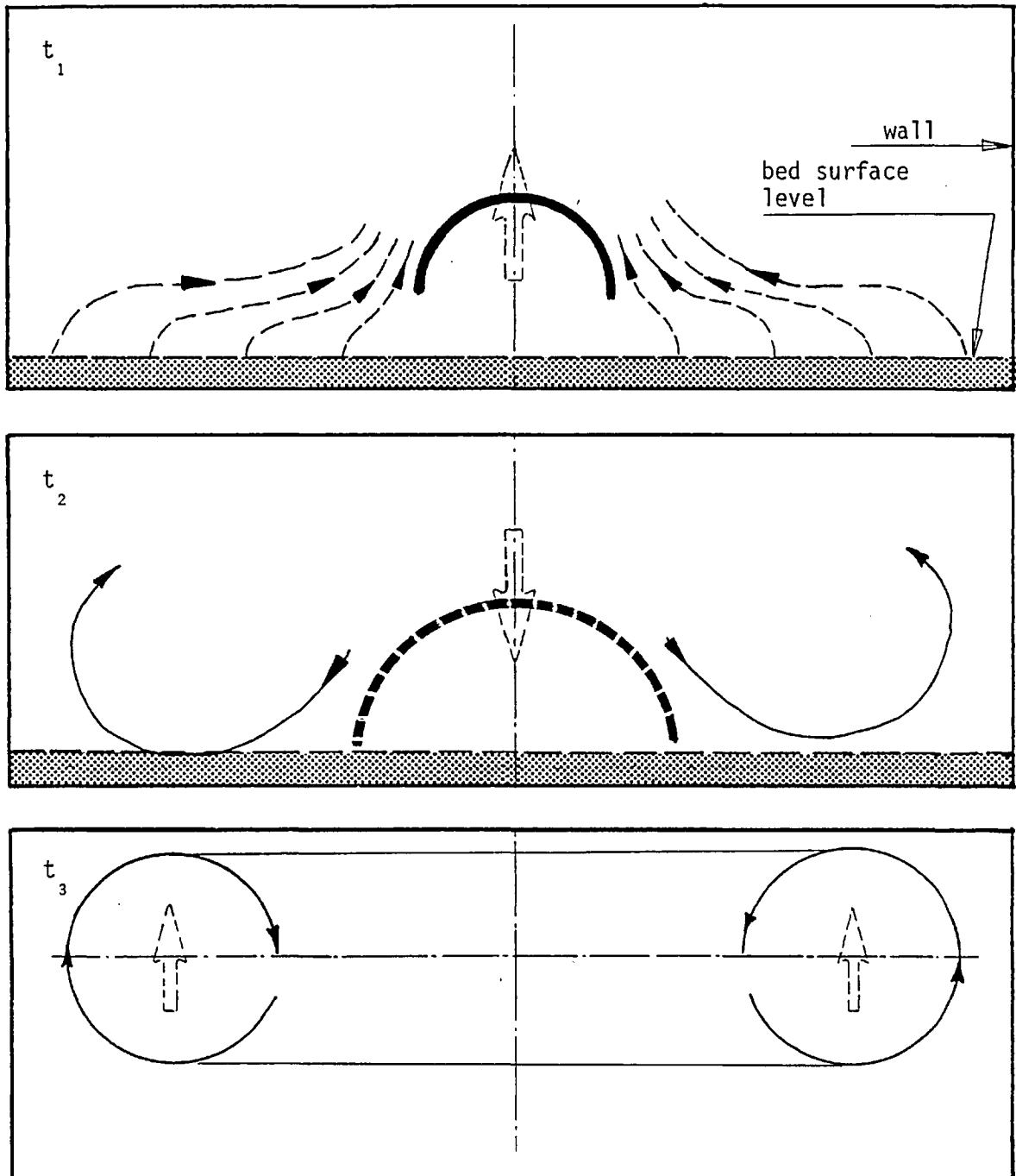
Fig. 6.2.2-6 Schematic illustration of a toroidal circulation created
during a bubble burst
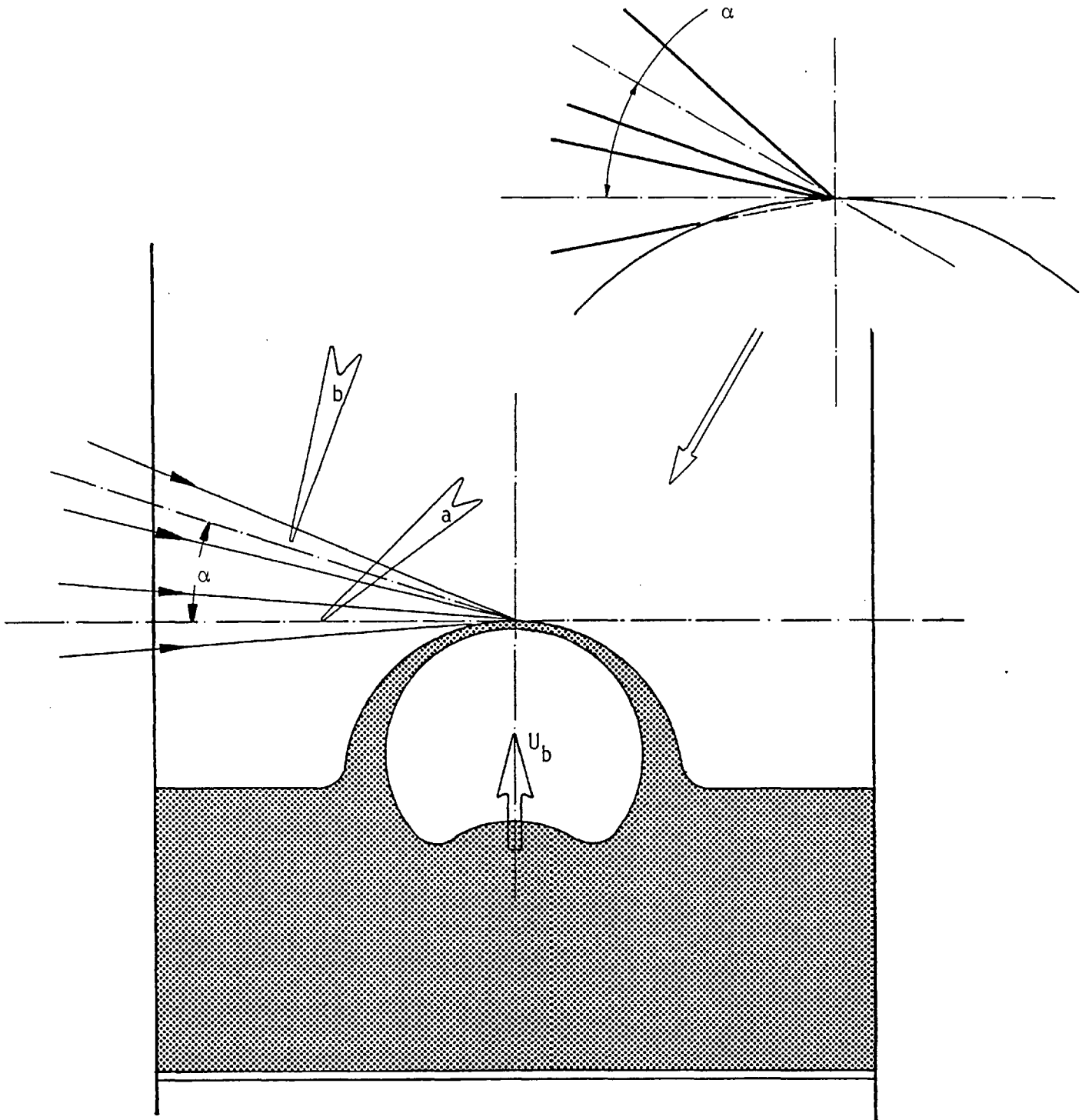
Fig. 6.3-1 Effect of the bubble bulge curvature on the control volume

Velocity (m/s)

o —— gas

□ —— sand

Z' =110 mm

U$_f$

0.0

time
(seconds)

- 1.0

Number of measurements
detected

200

100

0.2   0.4   0.6   0.8   1.0   time
(seconds)
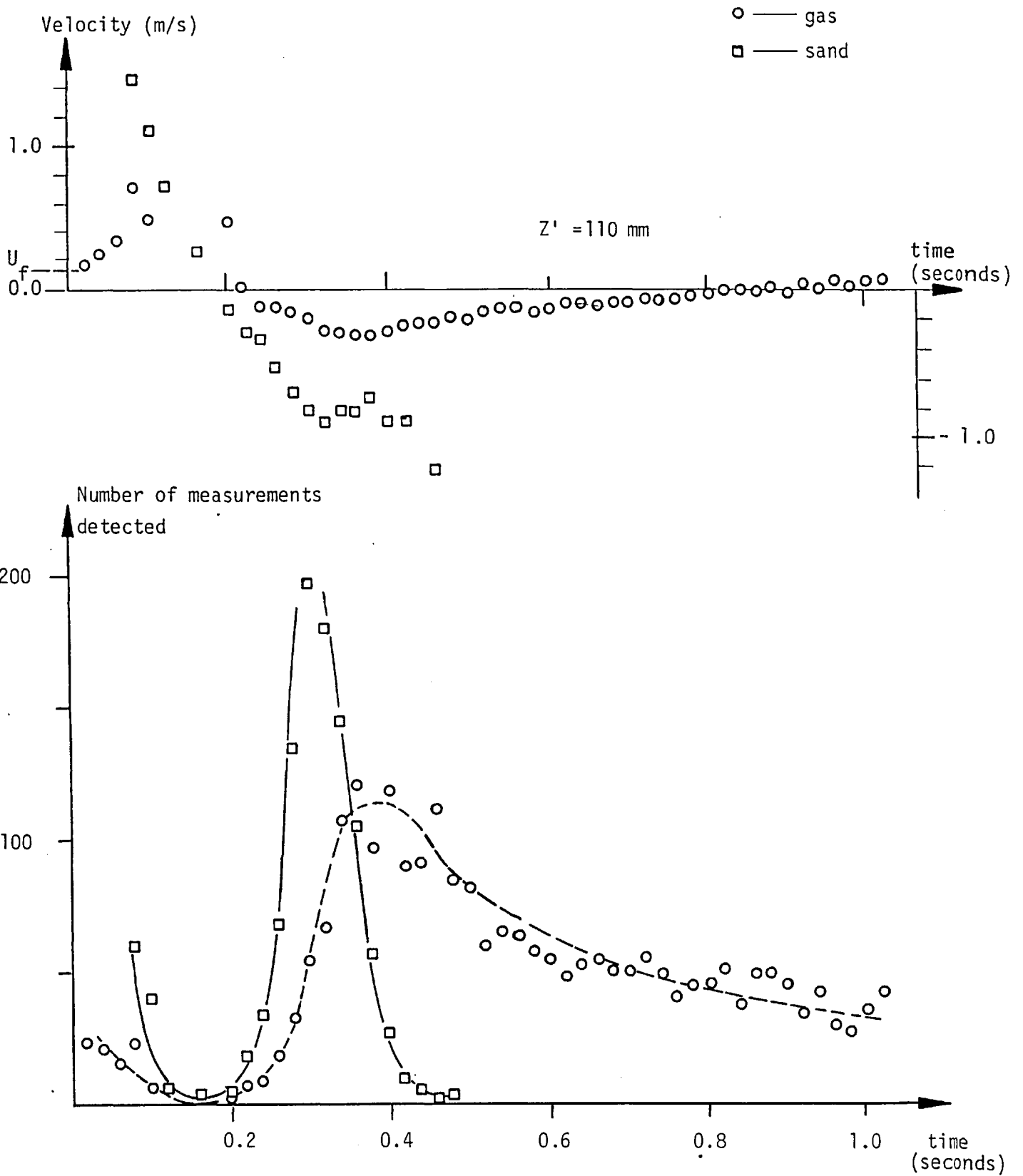
Fig. 6.3-2   Time variation of the gas and sand velocities and
of the number of measurements at the point: X = 0,
Y = 0, Z' = 110 mm

Fig. 6.3-3 Agglomerations of particles ejected upwards
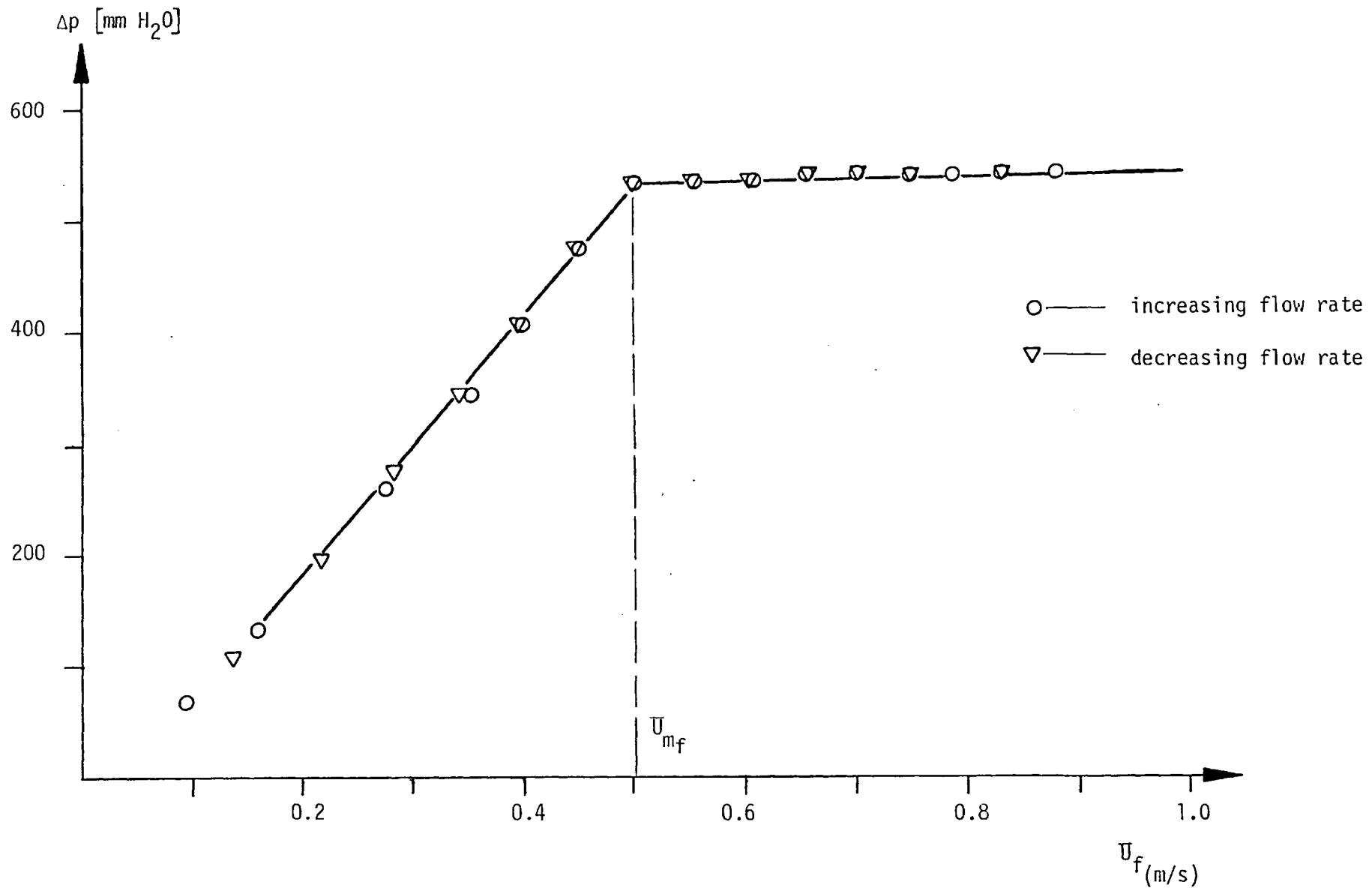
Fig. 6.4.1-1 Variation of bed pressure drop with fluidizing velocity, sand diameter d_p = 1.00 mm
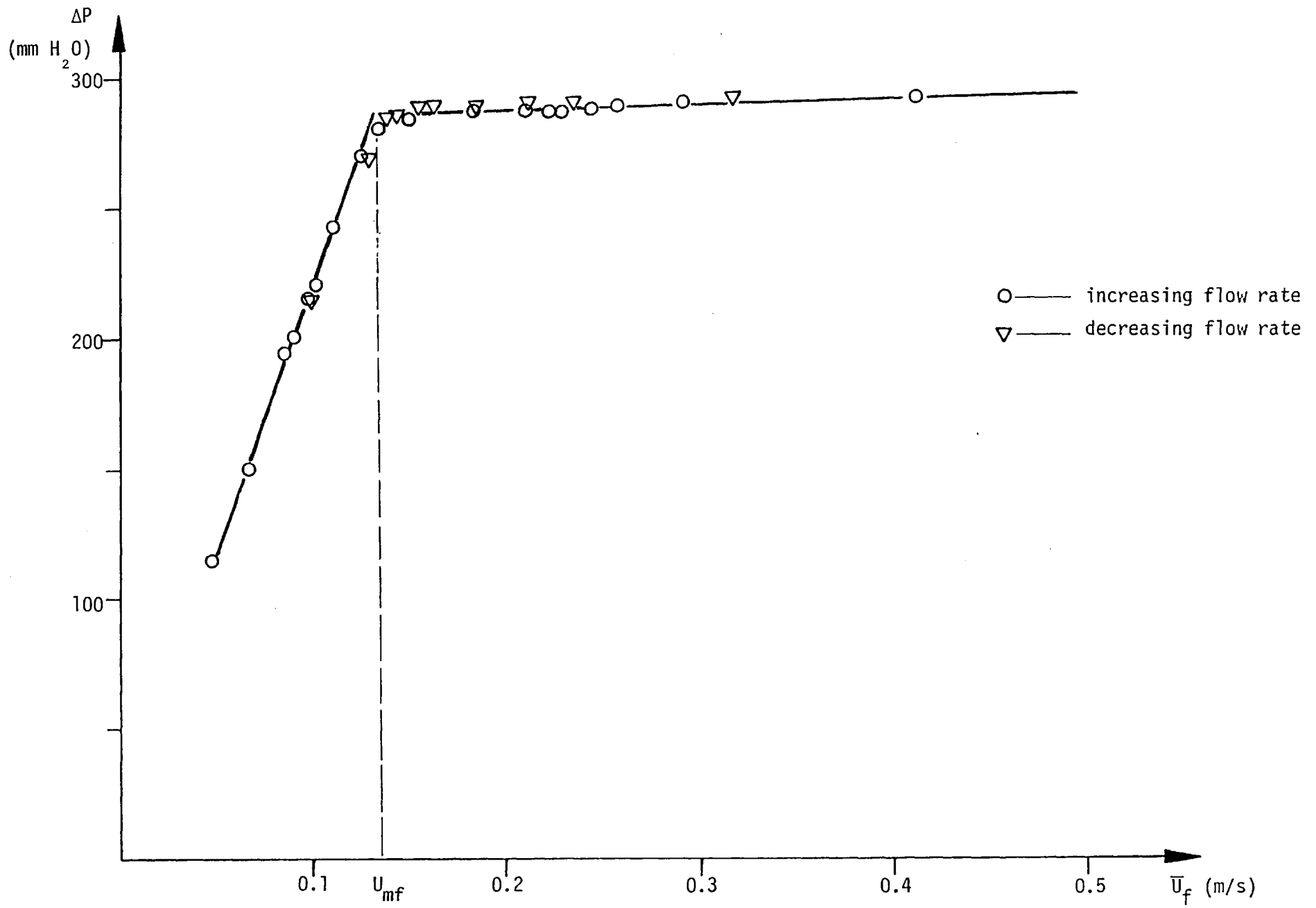
Fig. 6.4.1-2 Variation of bed pressure drop with fluidizing velocity, sand diameter d_p = 0.40 mm

ΔP (distributor)/ΔP (bed)
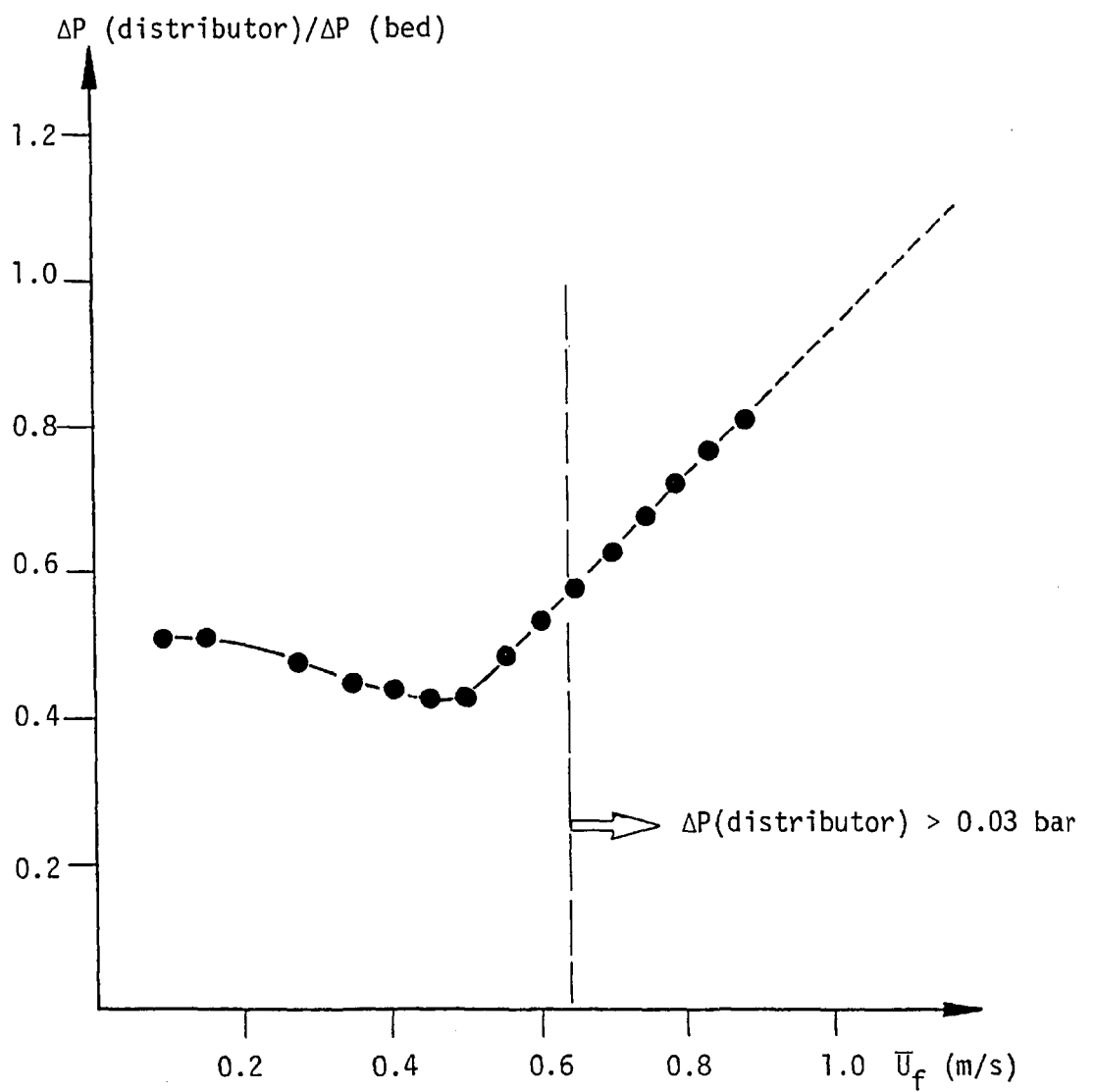
Fig. 6.4.1-3   Variation of pressure drop ratio across the bed and
across the distributor with variation in fluidizing
velocity
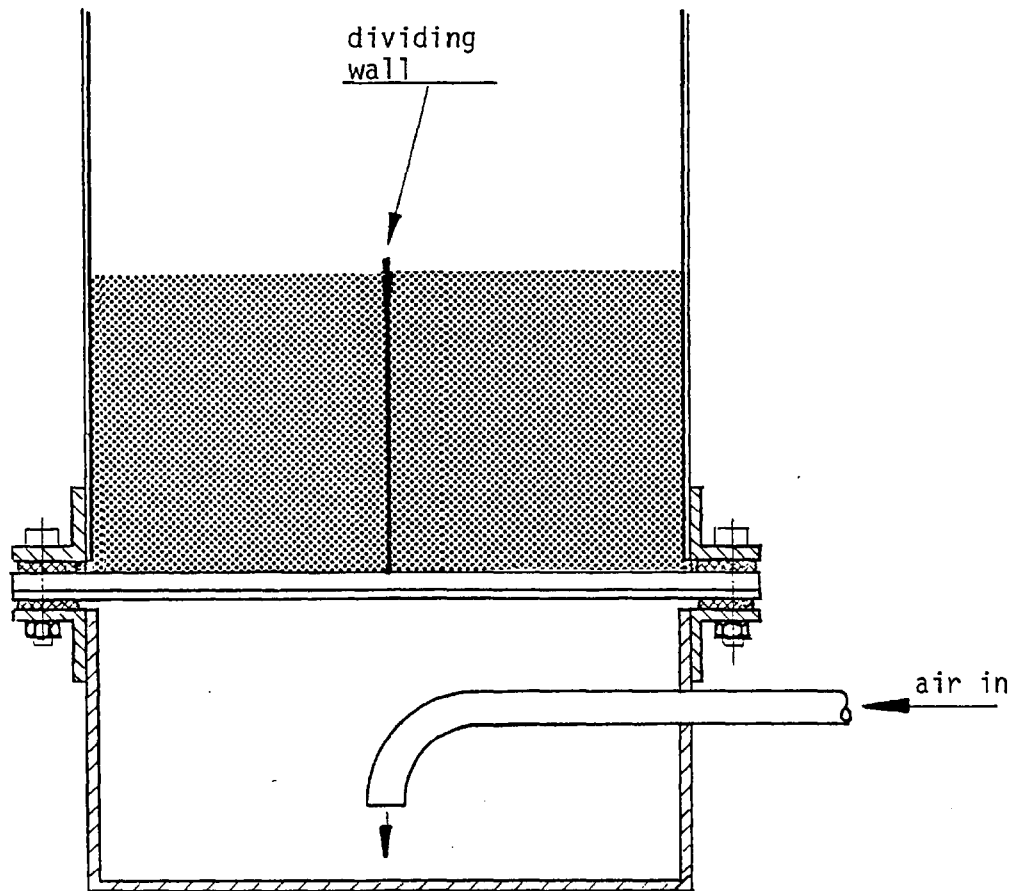
Fig. 6.4.1-4   The fluidizing bed with the dividing wall installed
at its lower level
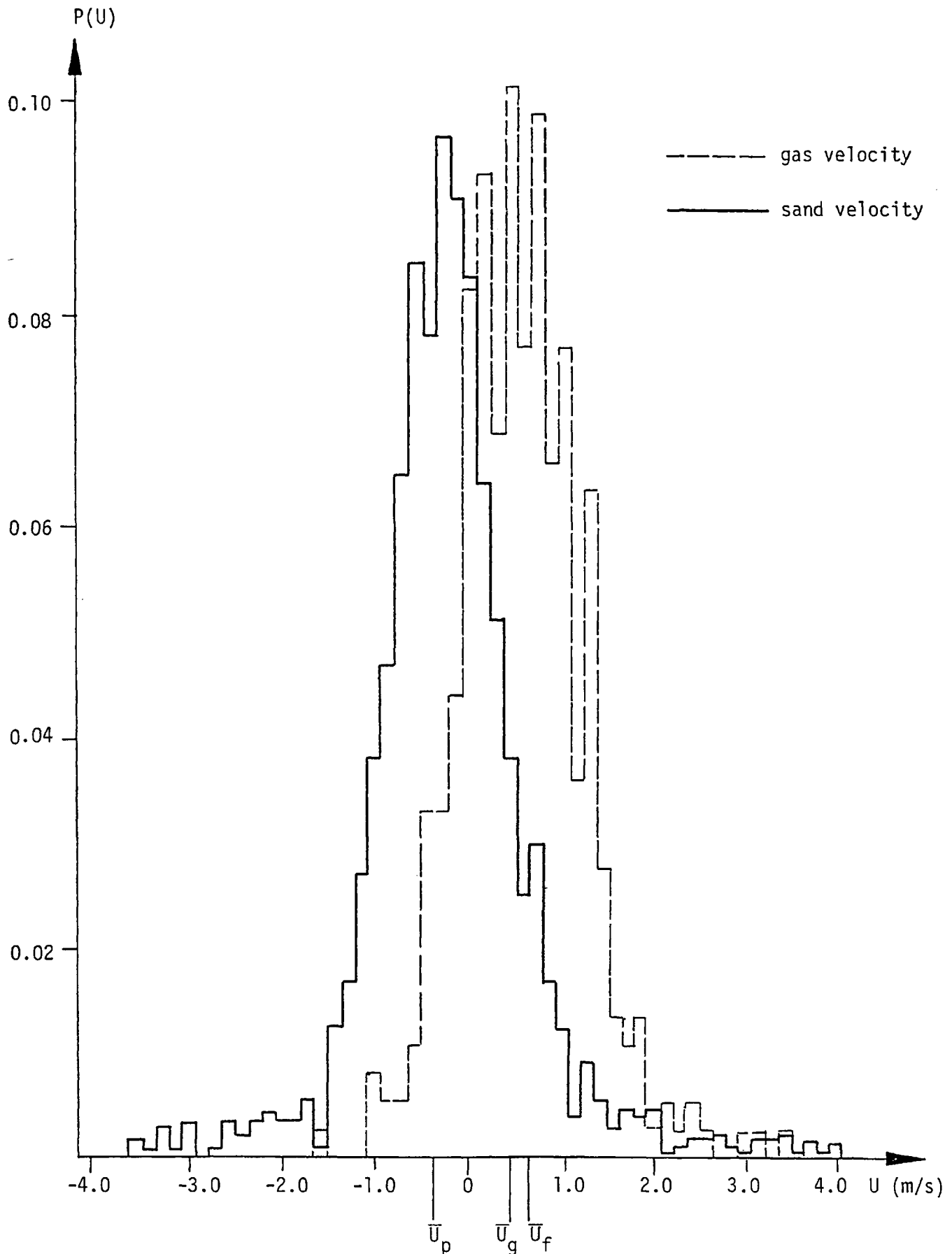
Fig. 6.4.2-1 Gas and sand velocity histogram for d_p = 1.00 mm, Z' = 210 mm, X = Y = 0 and $\overline{U}_f$ = 0.65 m/s (experiment group A1, see Table 6.4.1-1)
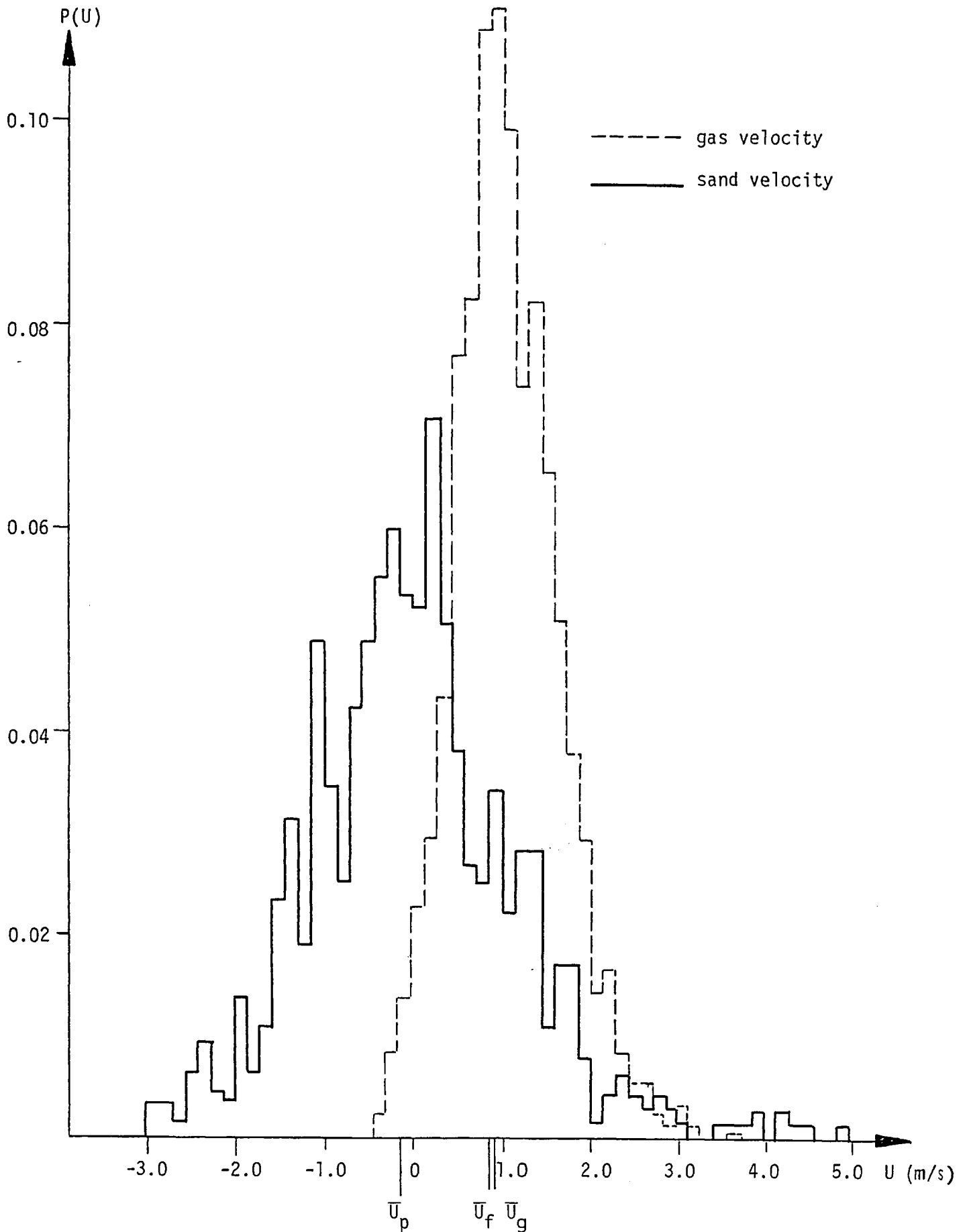
Fig. 6.4.2-2 Gas and sand velocity histogram for d_p = 1.00 mm, Z' = 480 mm, $X = Y = 0$ and $\overline{U}_f$ = 0.875 m/s (experiment group A2, see Table 6.4.1-1)

```
   F[V]

0.108.
      .
      .
      .
0.097.
      .
      .
      .
0.086.
      .
      .
      .
0.075.                                              *
      .                                            * *
      .                                            * *
      .                                            * *
      .                                          0 ** *
0.065.                                         *0 ** *
      .                                         *0 ** *
      .                                         *0 ** *
      .                                         *0 *****
      .                                         *0*******
0.054.                                         *0*******
      .                                         *0*******
      .                                         *0*******
      .                                         *0*******
      .                                         *0*******
0.043.                                        **0*******
      .                                        **0*******  *
      .                                        **0******* **
      .                                        **0**********
      .                                        **0**********
0.032.                                        **0**********
      .                                       ***0**********
      .                                       ***0***********
      .                                       ***0***********
      .                                       ***0*************
0.022.                                      ****0************* *
      .                                      ****0************** *
      .                                      ****0************* *
      .                                      ****0****************
      .                                      ****0*****************
0.011.                                      ****0*****************
      .                                      ****0******************
      .                                      ****0*******************
      .                                   * ****0*******************
      .                                   ******0****************** *
      .                                 ** *******0********************** * *
      ...............................................................................[M/S]
           :       :       :       :       :       :  MF   :       :       :       :       :
        -2.190  -1.825  -1.460  -1.095  -0.730  -0.365  0.000  0.365  0.730  1.095  1.460  1.825
```

Fig. 6.4.2-3 Gas velocity histogram for d_p = 0.40 mm, Z´ = 110 mm, X = Y = 0 and $\overline{U}_f$ = 0.195 m/s (experiment group B1, see Table 6.4.1-1)

F[V]

0.049.

0.044.

0.039.

0.034.

0.029.

0.024.

0.020.

0.015.

0.010.

0.005.

                                                                                                    [M/S]
      :   :   :   :   :   :   M :   F   :   :   :   :   :
   -2.190   -1.825   -1.460   -1.095   -0.730   -0.365   0.000   0.365   0.730   1.095   1.460   1.825

218

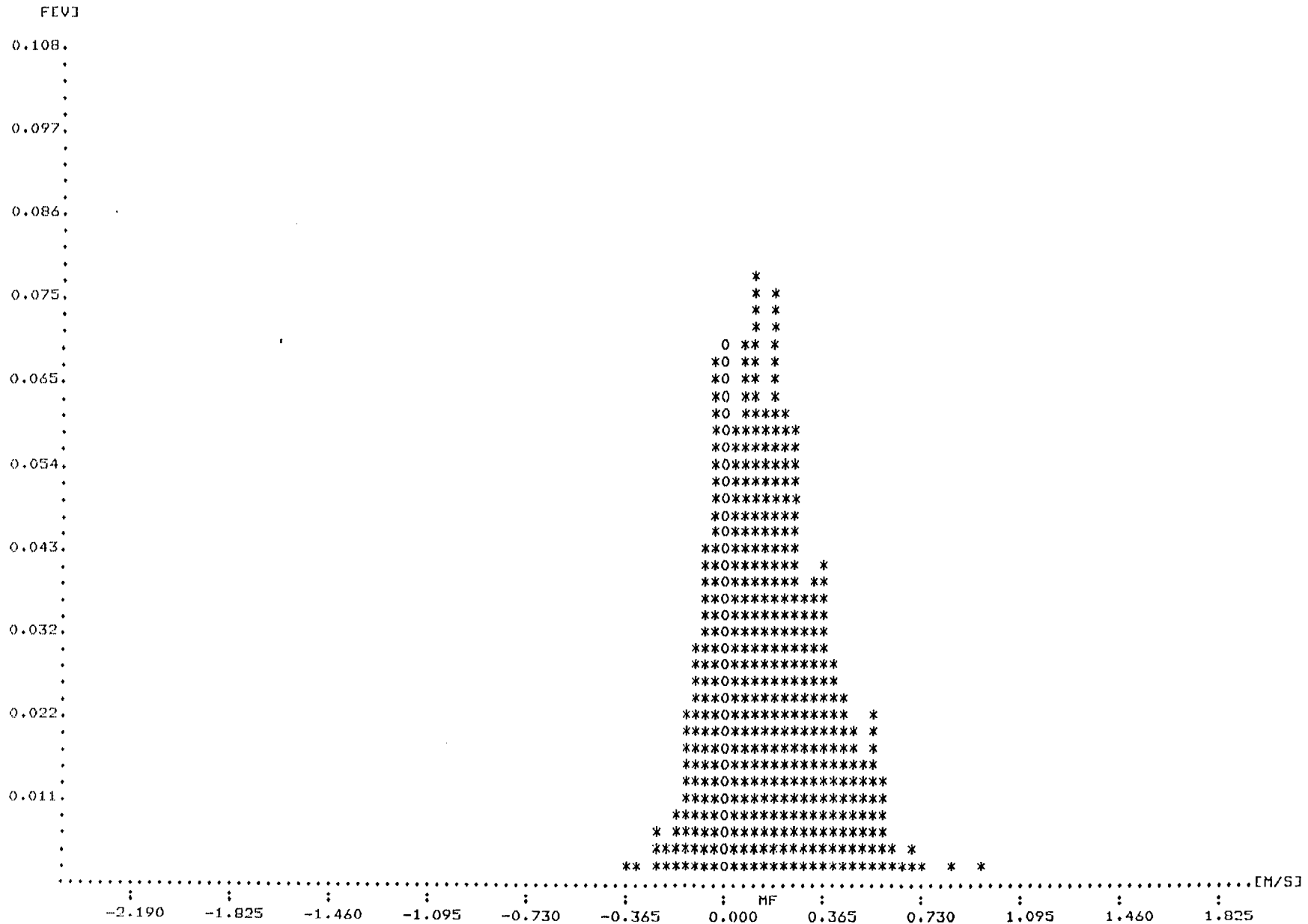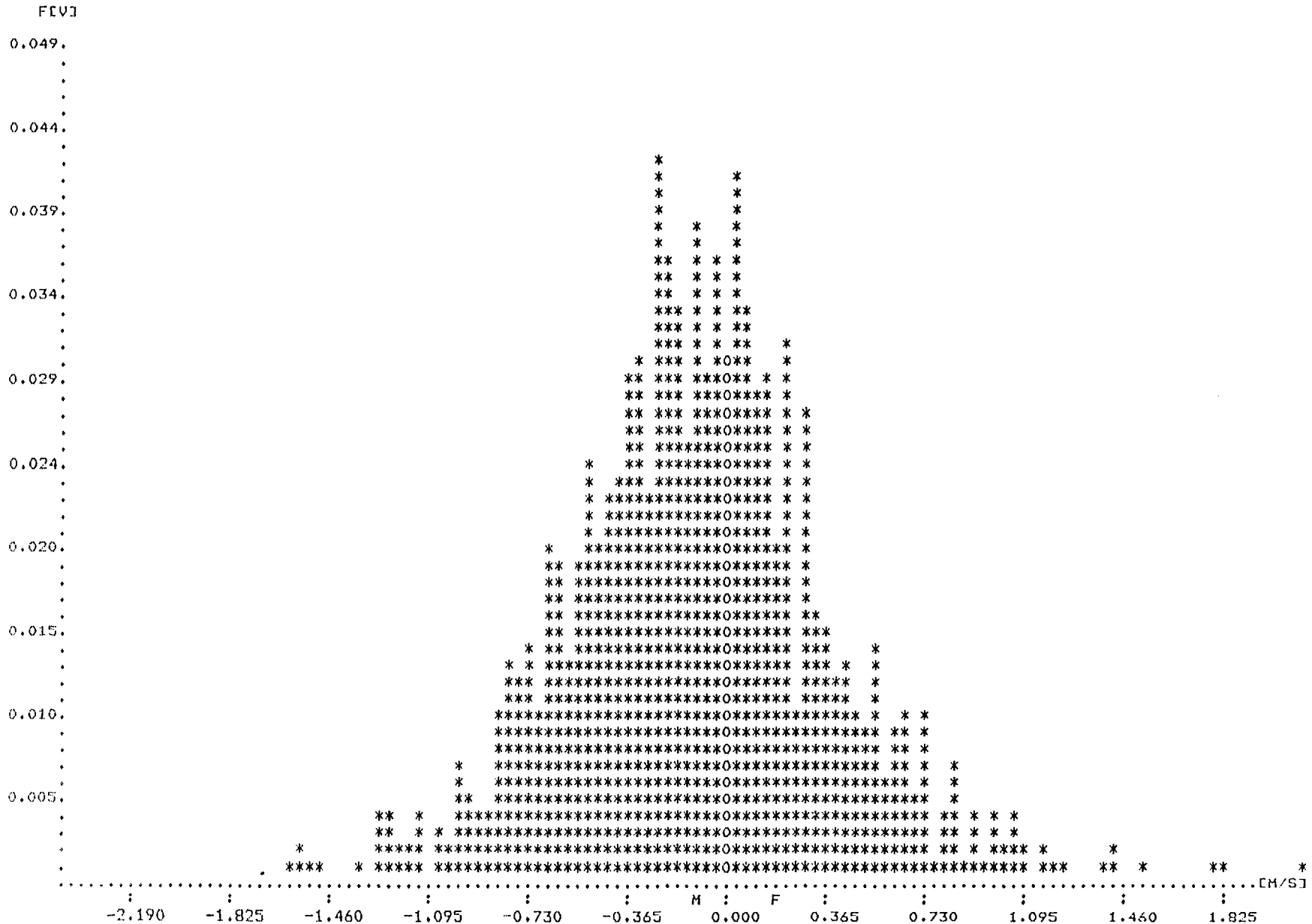Fig. 6.4.2-4   Sand velocity histogram for d_p = 0.40 mm, Z' = 110 mm, X = Y = 0 and $\overline{U}_f$ = 0.195 m/s (experiment group B1, see Table 6.4.1-1)

F[V]

0.085.

0.077.

0.068.

0.060.

0.051.

0.043.

0.034.

0.026.

0.017.

0.009.
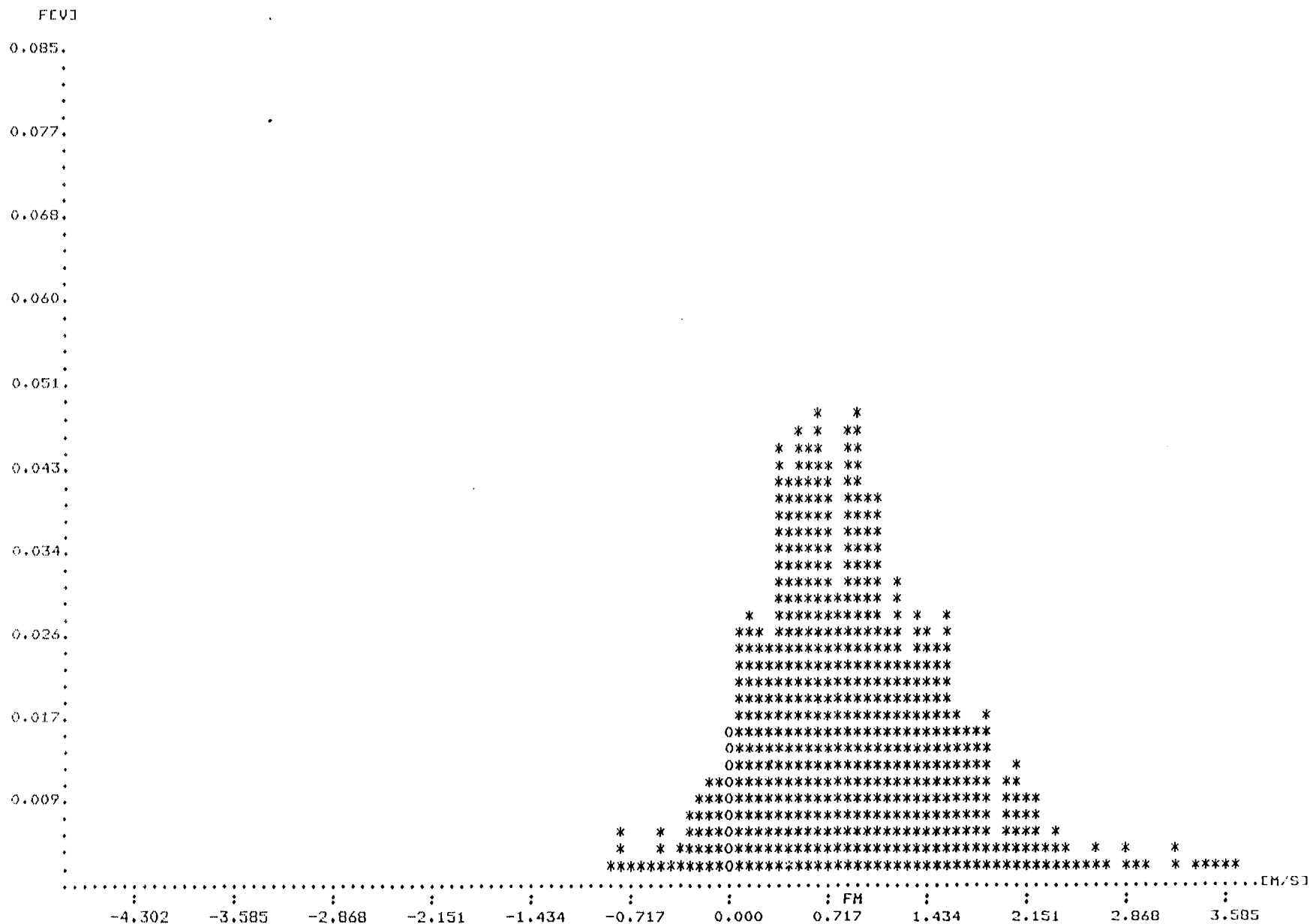
Fig. 6.4.2-5   Gas velocity histogram for d_p = 1.00 mm, X = 295 mm, Y = 0, Z' = 480 mm and $\overline{U}_f$ = 0.875 m/s
(experiment group A2, see Table 6.4.1-1)
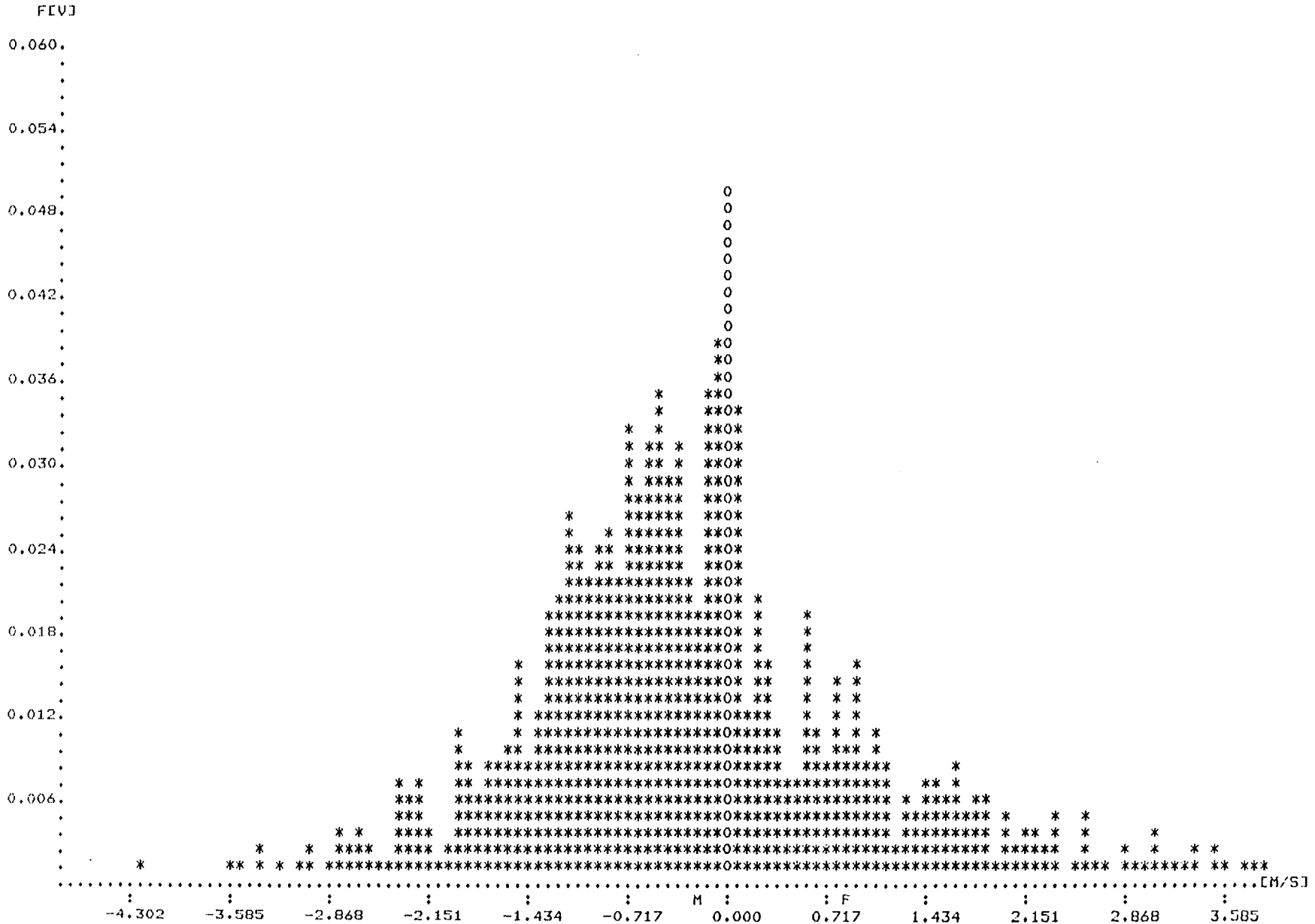
Fig. 6.4.2-6   Sand velocity histogram for d_p = 1.00 mm, X = 295 mm, Y = 0, Z⁻ = 480 mm and $\overline{U}_f$ = 0.875
(experiment group A2, see Table 6.4.1-1)
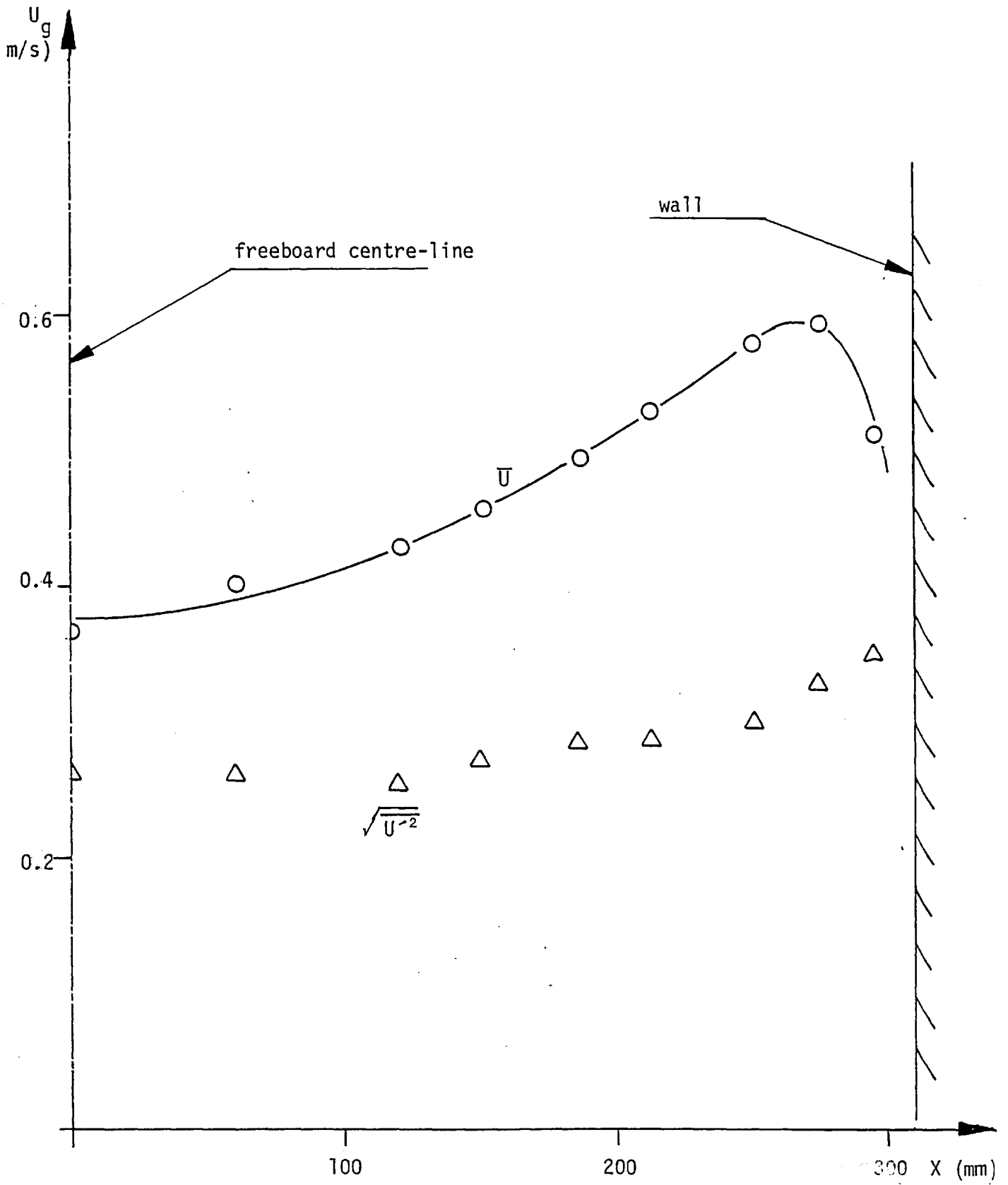
Fig. 6.4.3-1   Variation of gas mean and r.m.s. velocities along
the x axis (Y = 0, Z´ = 500 mm, experiment group HB1,
see Table 6.4.1-1)
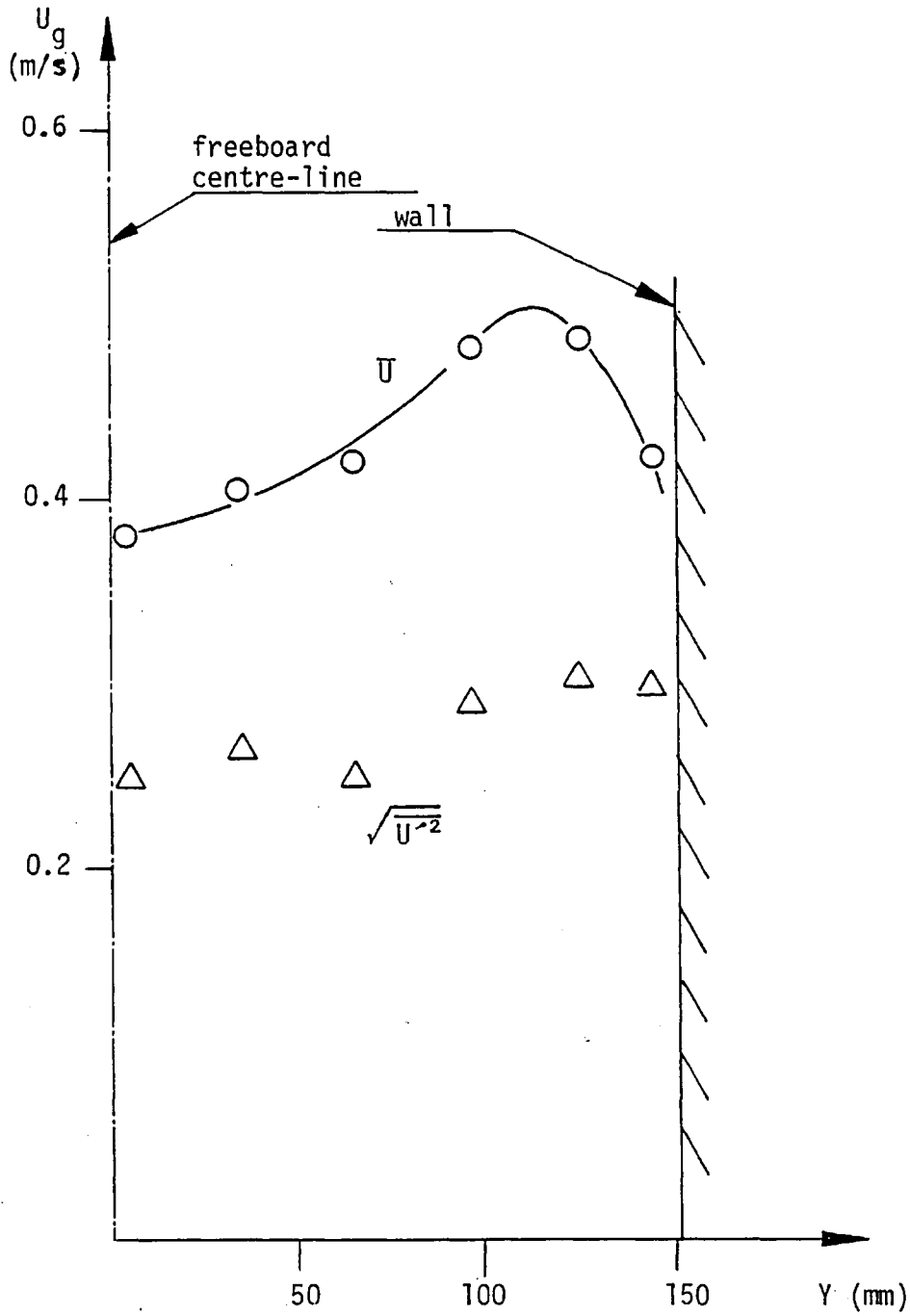
Fig. 6.4.3-2 Variation of gas mean and r.m.s. velocities along the y axis (X = 0, Z´ = 500 mm, experiment group HB1, see Table 6.4.1-1)
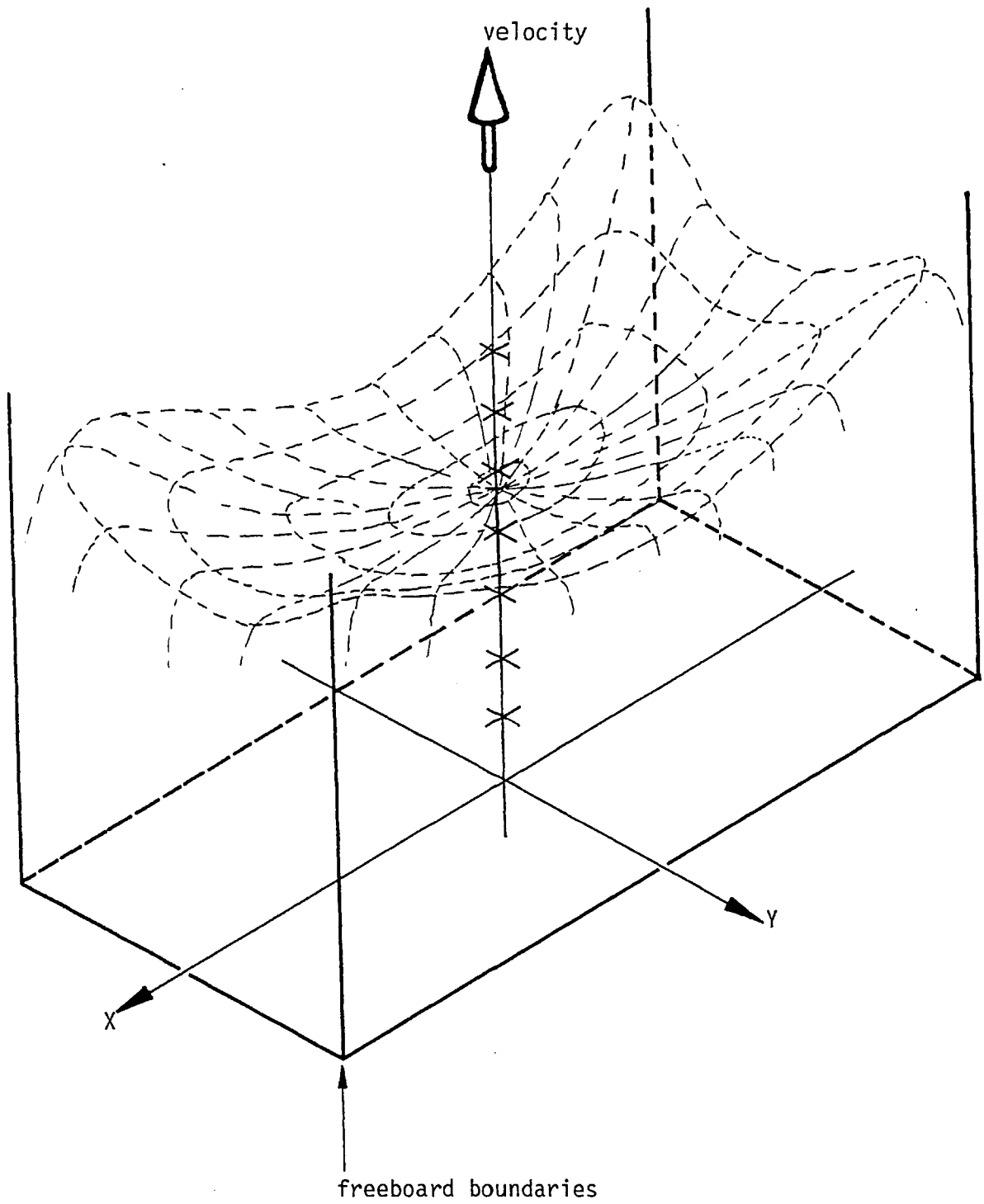
Fig. 6.4.3-3 A three-dimensional sketch of the gas velocity
distribution
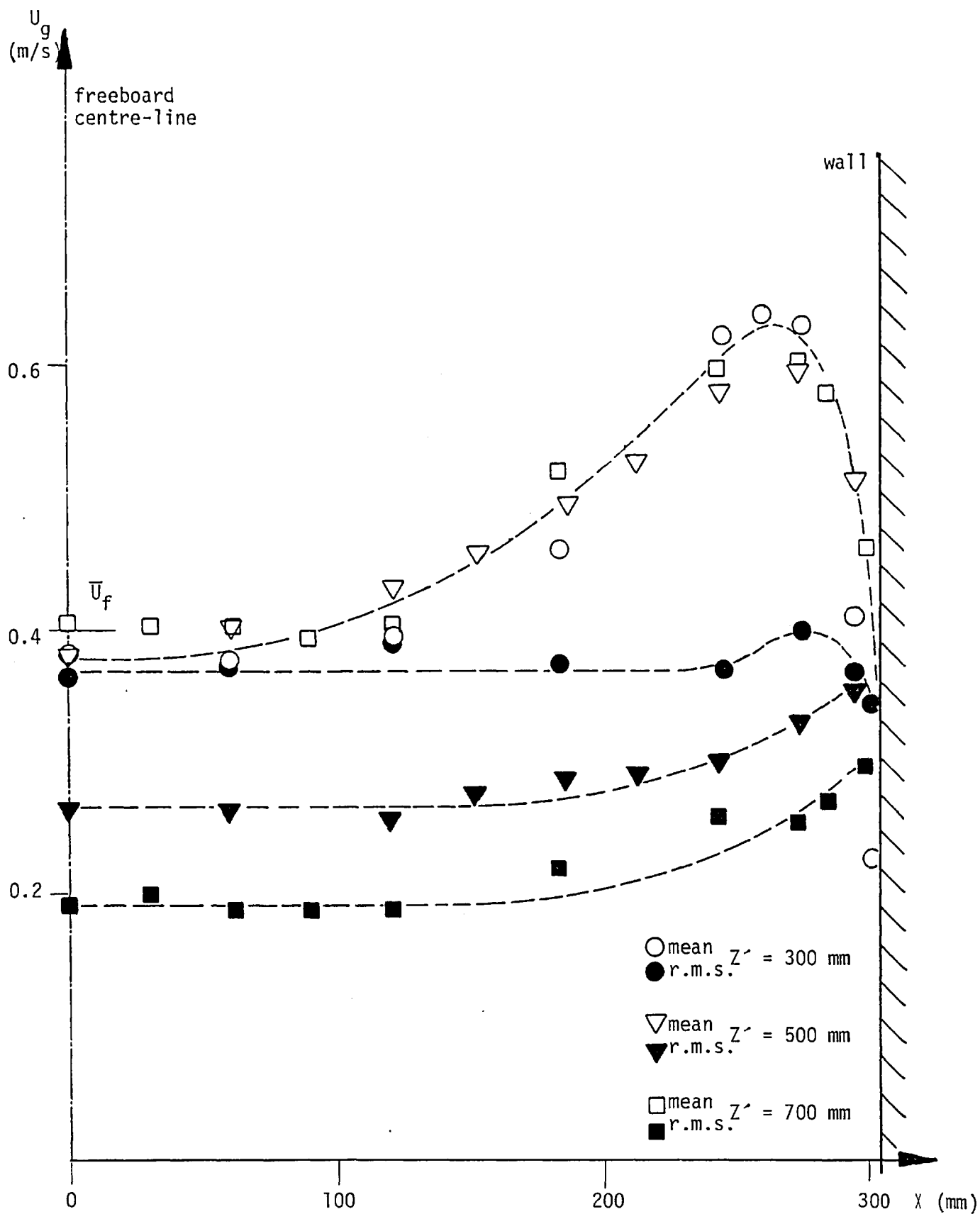
Fig. 6.4.3-4 Variation of gas mean and r.m.s. velocities along the
x axis for three freeboard levels (Y = 0, Z´ = 300,
500, 700 mm; experiment group HB1, see Table 6.4.1-1)
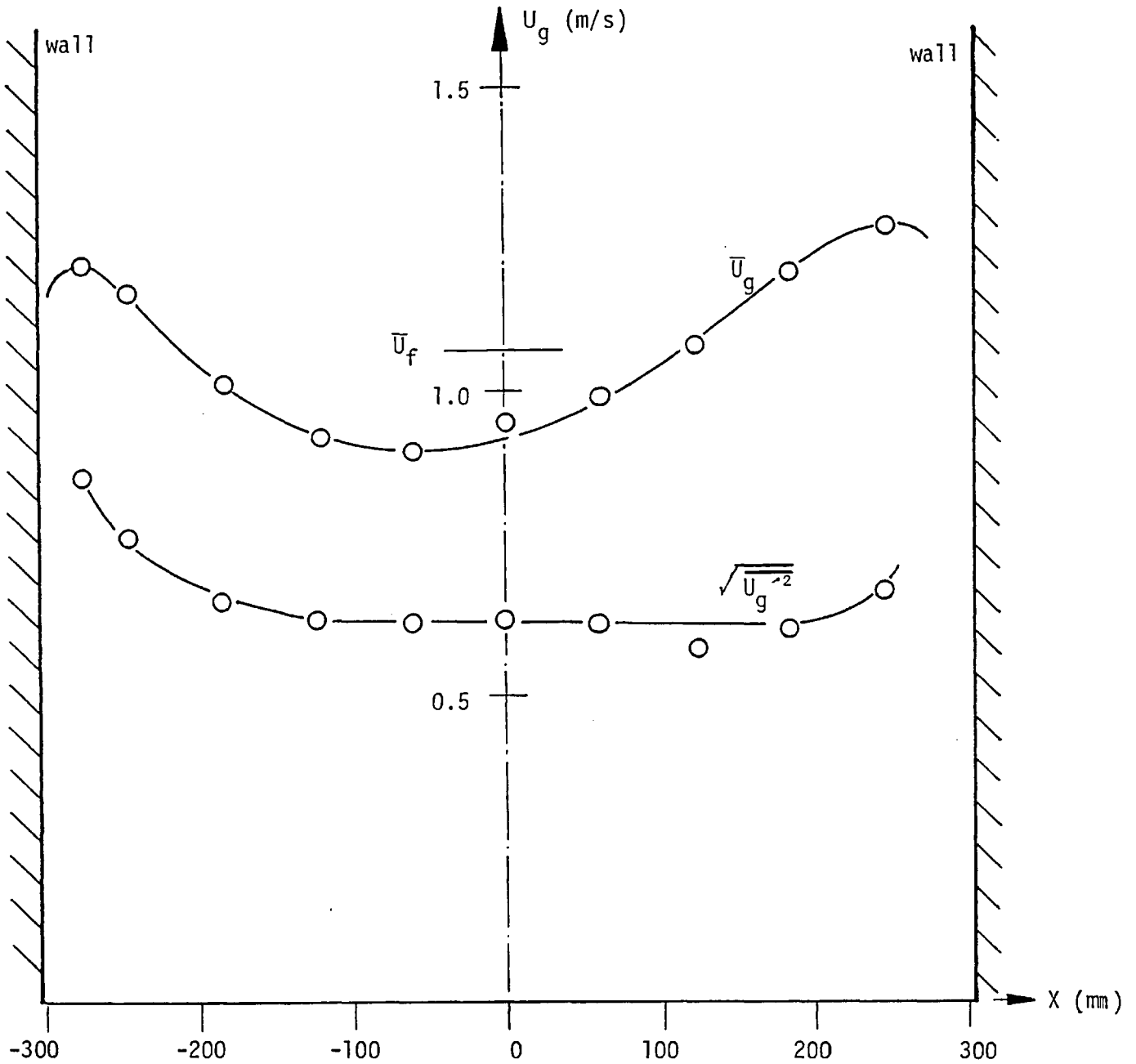
Fig. 6.4.3-5 Variation of gas mean and r.m.s. velocities along the x
axis ($\overline{U}_f$ = 1.07 m/s; Y = 0, Z = 400 mm; experiment
group HA1, see Table 6.4.1-1)
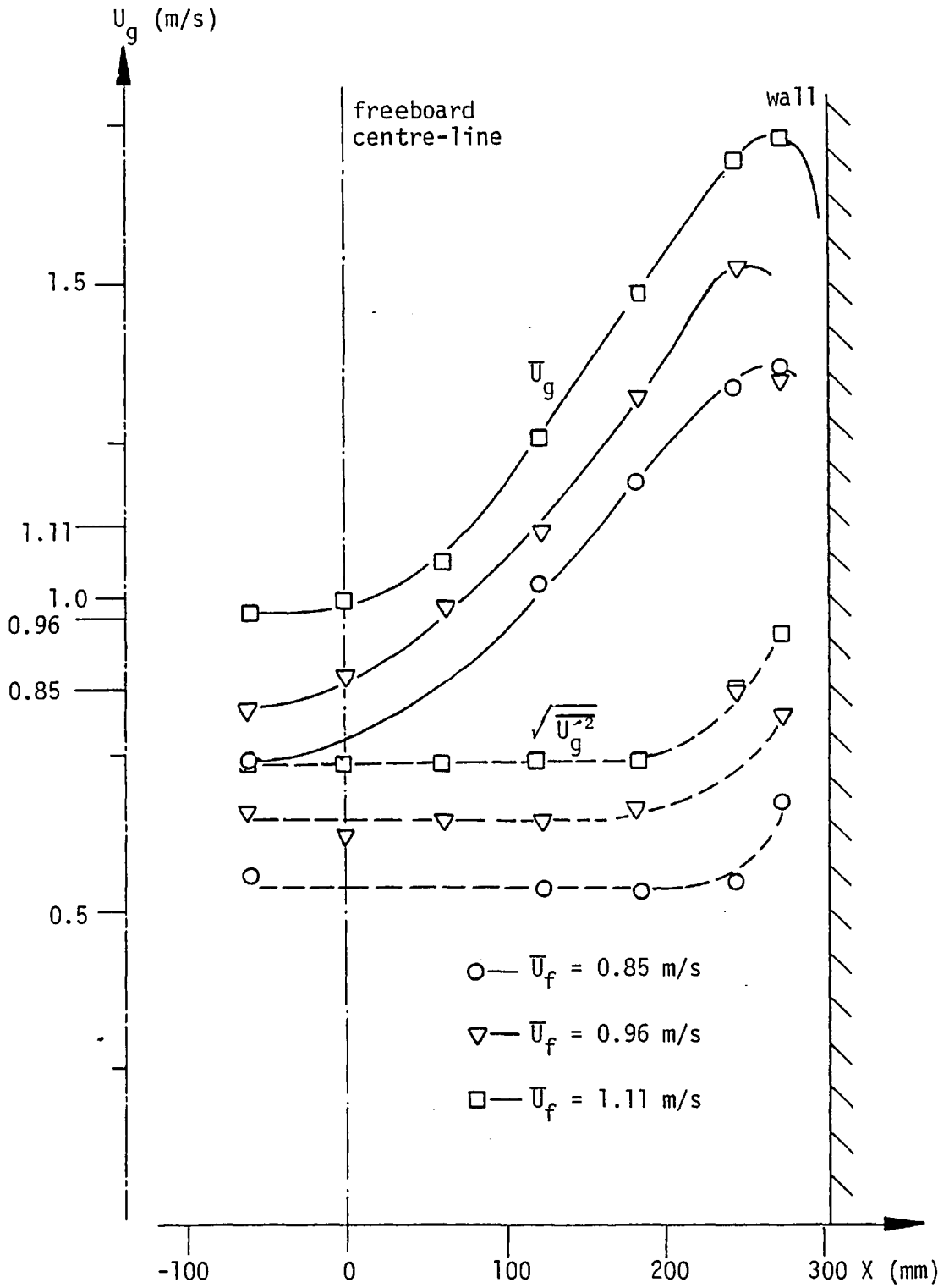
Fig. 6.4.3-6   Variation of gas mean and r.m.s. velocities along the
x axis for three fluidizing velocities (Y = 0, Z´ =
400 mm; experiment group HA1, see Table 6.4.1-1)
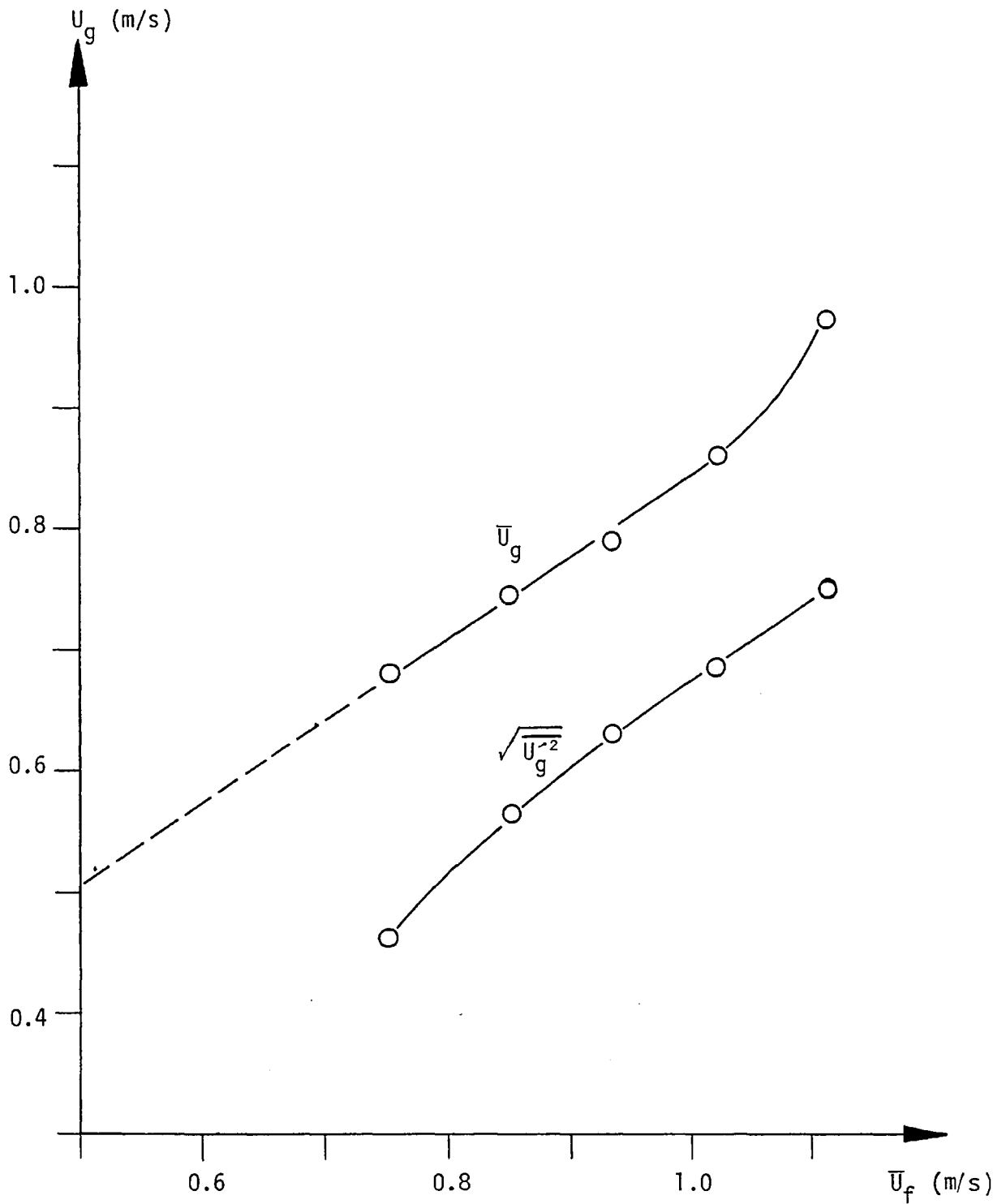
Fig. 6.4.3-7 Variation of freeboard centre-line velocity with
fluidizing velocity (experimental group HA1, see
Table 6.4.1-1)
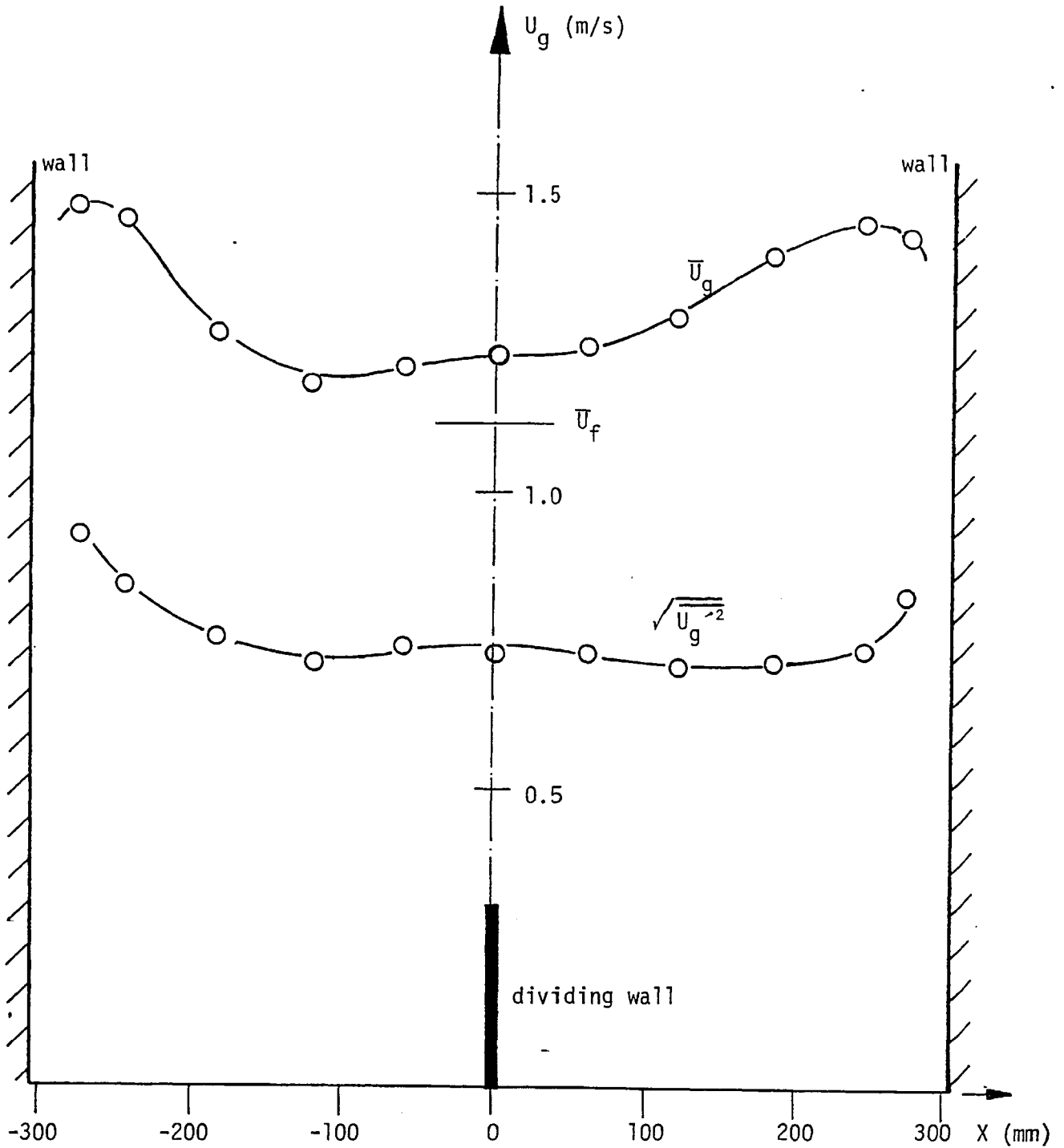
Fig. 6.4.3-8 Variation of gas mean and r.m.s. velocities along the
x axis using the dividing wall installed in the dense
bed (Y = 0, Z´ = 400 mm; experiment group HA2, see
Table 6.4.1-1)

229
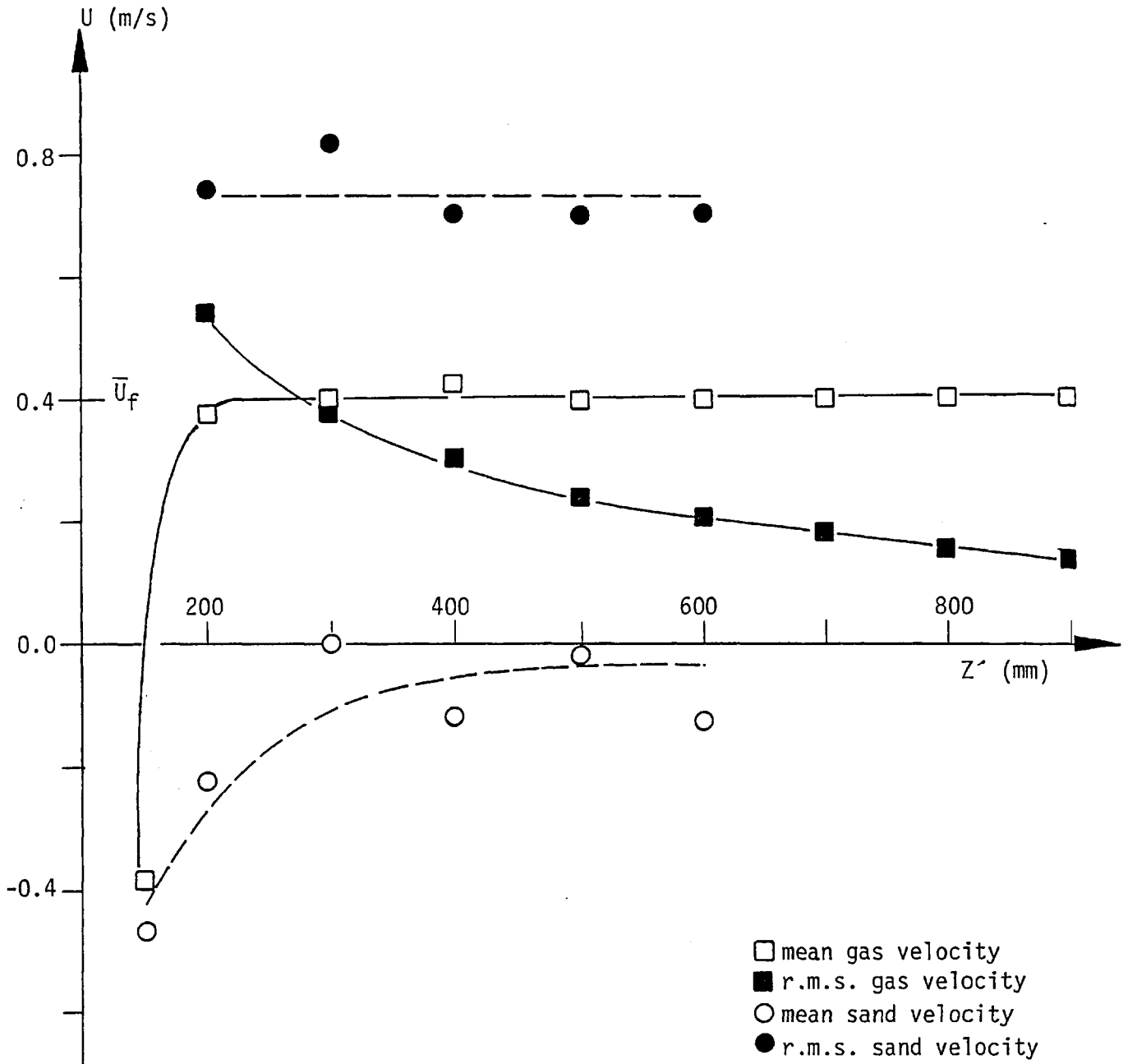
Fig. 6.4.3-9 Variation of gas and sand mean and r.m.s. velocities
with freeboard height for d_p = 0.40 mm and $\overline{U}_f$ = 0.4 m/s
along the z axis (X = Y = 0, experiment group HB1, see
Table 6.4.1-1)
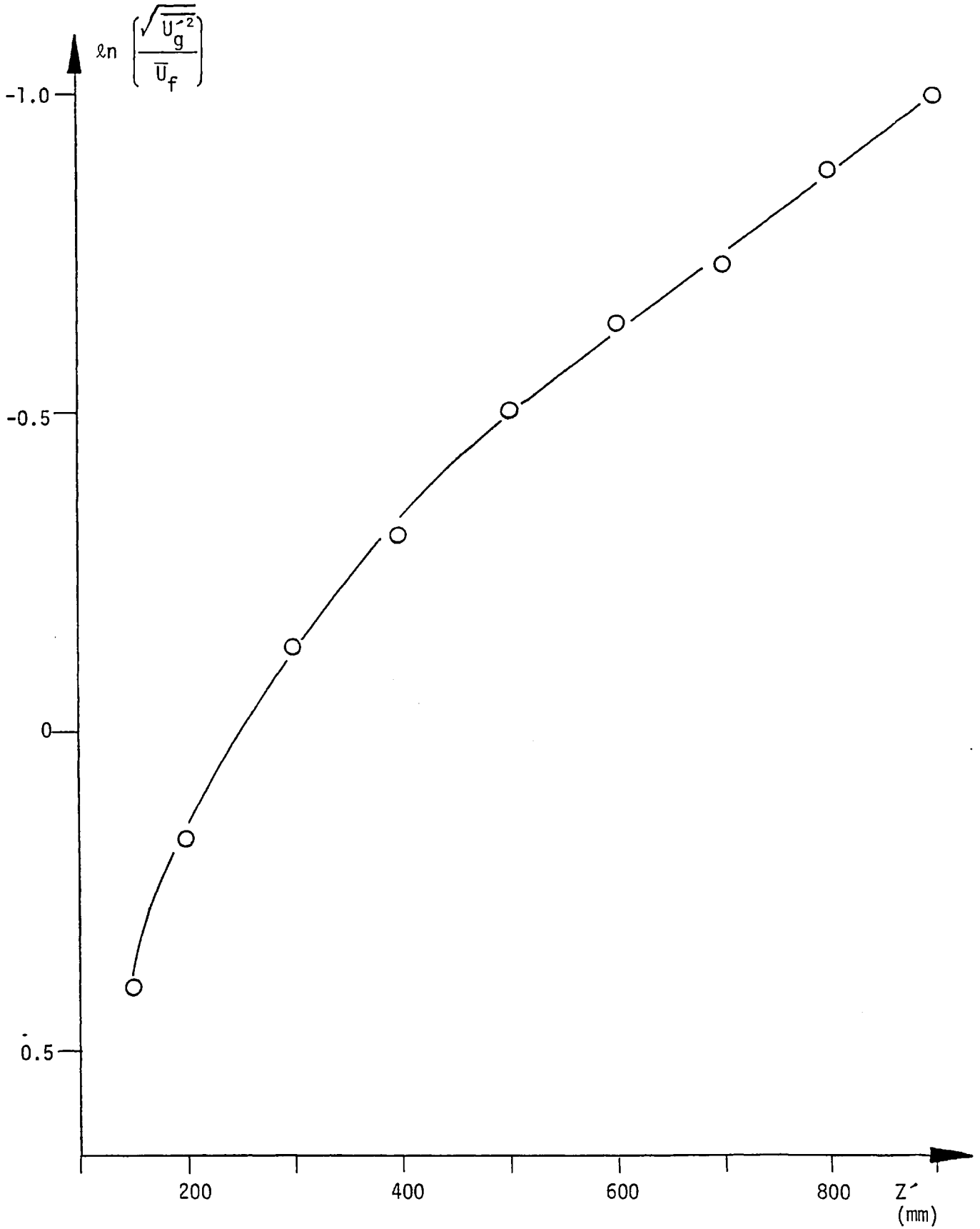
Fig. 6.4.3-10 Variation of the logarithm of the turbulence
intensities with freeboard height

bed static level (mm)
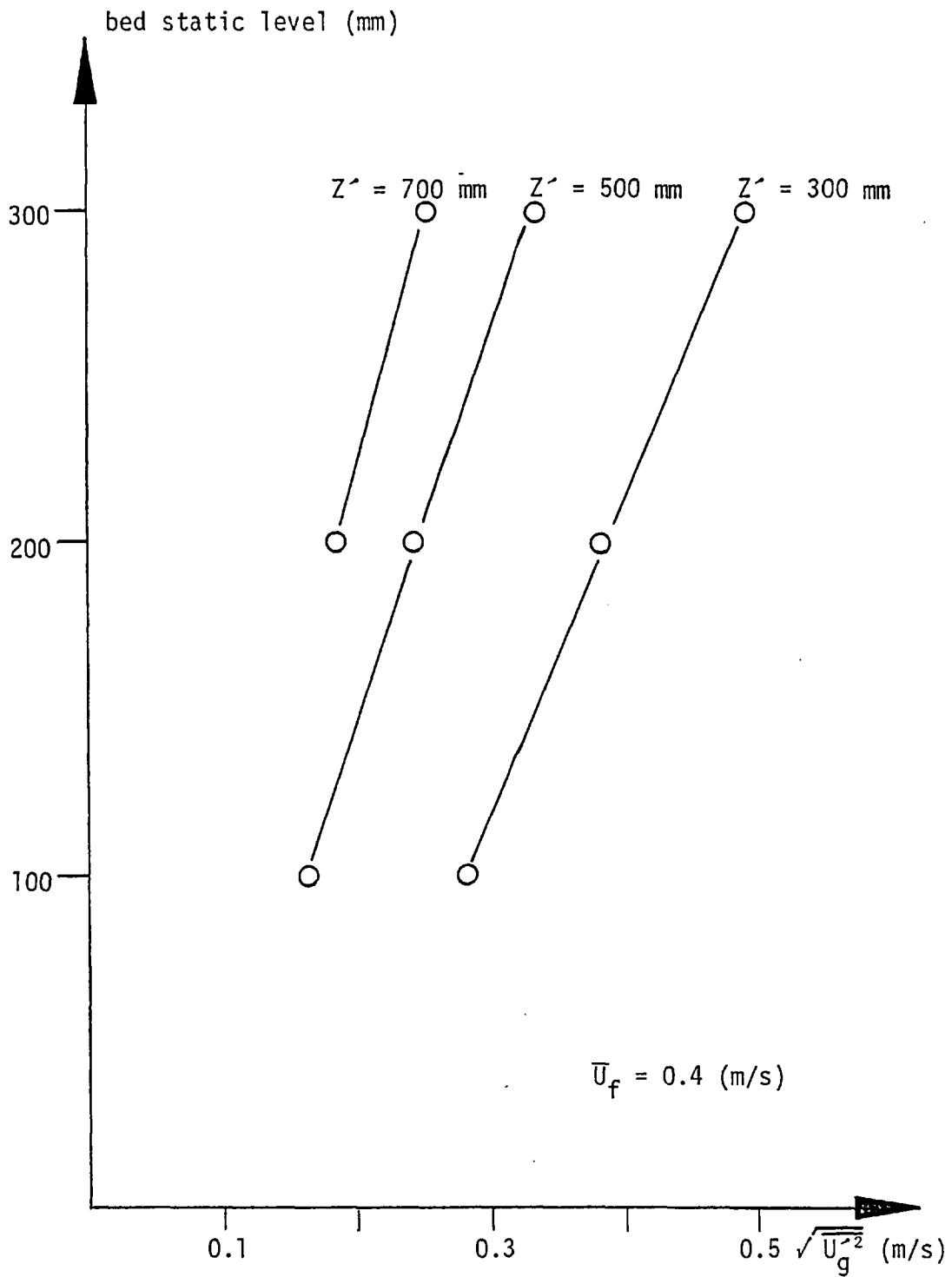
Fig. 6.4.3-11   Variation of mean velocity fluctuation with freeboard
height for different bed levels (X = Y = 0, d_p = 0.40 mm,
experiment group HB2, see Table 6.4.1-1)

232

P(U$_p'$)

(e)

U$_p'$

(d)

U$_p'$

(c)

U$_p'$

(b)

U$_p'$

(a)

U$_p'$
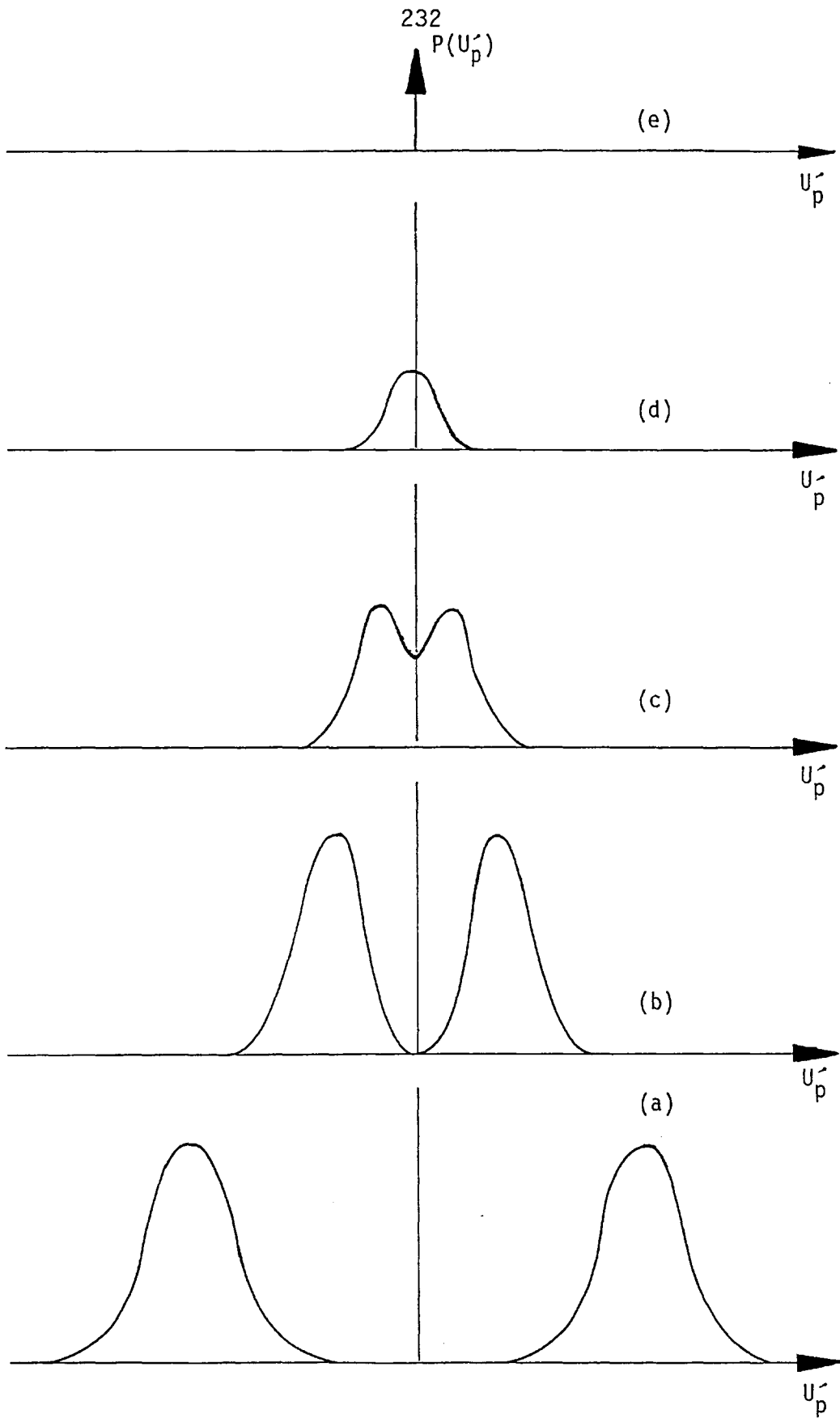
Z$'$(e) > Z$'$(d) > Z$'$(c) > Z$'$(b) > Z$'$(a)

Fig. 6.4.4-1   Schematic illustration of the velocity probability
density functions of the sand particles at different
freeboard levels

F[V]

0.075.

0.068.

0.060.

0.053.

0.045.

0.038.

0.030.

0.023.

0.015.

0.008.

```
                                        *                    *
                                        *                    *
                           *            * *         * *      *
                           *      *     * *    * *  * *      *
                           *      *   * * *  * *     * *     *
                           * *    * * * * ***** **   * *     *
                           * *    * * *** ***** ***   * * * **  *
                           * *   * * *** ***** ***  * ** *** ** *
                           * *   * * * ******** ****  * ***** ** ***   * *
                           * ** * * * ********* *****  * *********** *** * * *
                  *        **** *** *****************0** *********** *** * * *
                  *        **** **********************0*************** *** **** * *
                  *    *   ************************************************ *** ****  *   *
          * *   * *  * ********************************************************** *   *
          *    ***  ****************************************************************** *   *
          *    *** ****************************************0***************************** *    *     * * *
    *     **** **** ****************************************0****************************** *  * * * *  * *
    * ********************************************************0************************************ * * * ** * * *  * *
```
....[M/S]
```
        :         :         :         :         :       M :         :       F :         :         :         :
      -2.907    -2.326    -1.744    -1.163    -0.581   0.000     0.581     1.163     1.744     2.326     2.907     3.488
```

Fig. 6.4.4-2   Velocity histogram of sand particles for d_p = 1.00 mm, U_f = 1.03 m/s, X = Y = 0, Z´ = 400 mm
(experiment group HA1, see Table 6.4.1-1)

F[V]

0.078.

0.070.

0.062.

0.054.

0.047.

0.039.

0.031.

0.023.

0.016.

0.008.

```
       :         :         :         :         :        :M        :        F :         :         :         :         :
    -2.907    -2.326    -1.744    -1.163    -0.581     0.000     0.581     1.163     1.744     2.326     2.907     3.488
```

Fig. 6.4.4-3   Velocity histogram of sand particles for d_p = 1.00 mm, U_f = 1.03 m/s, X = 122 mm, Y = 0, Z' = 400 mm
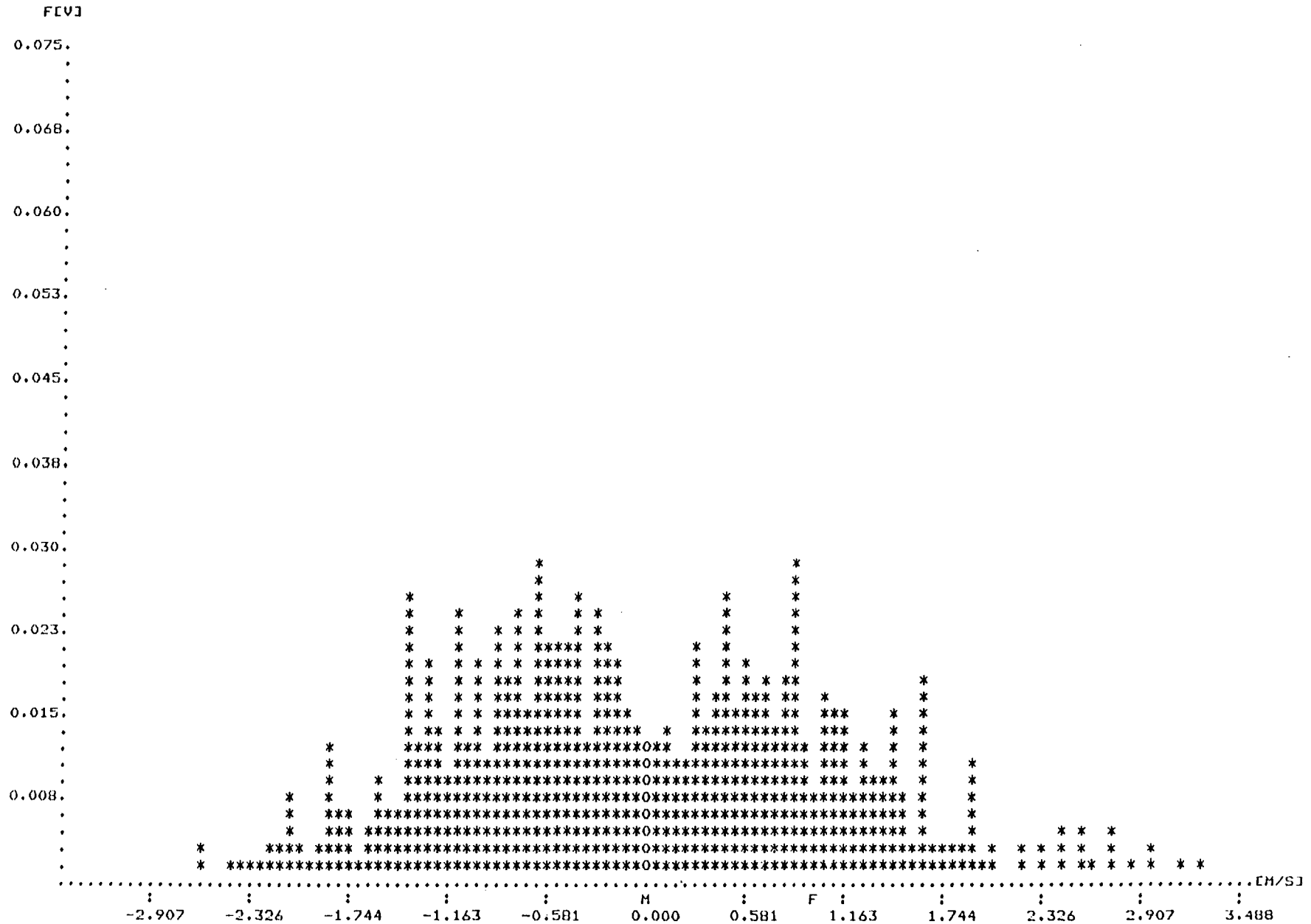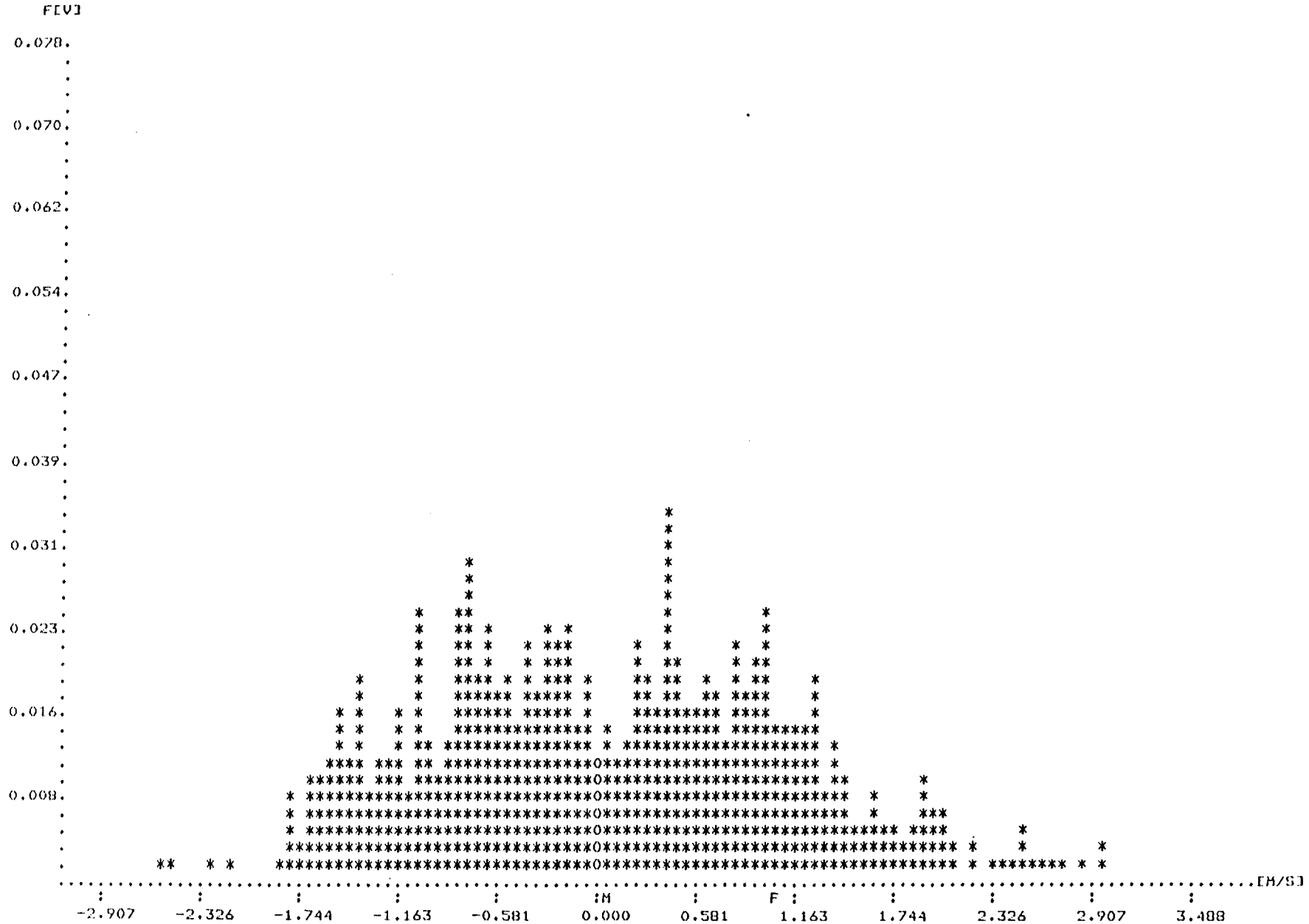(experiment group HA1, see Table 6.4.1-1)

FEVI

0.061.
      .
      .
      .
0.055.
      .
      .
0.049.   * * *
      .   * * *
      .   * * *
      .   **** *   *
      .   **** *   *
0.043.   ***** **   *
      .   ***** **   *
      .   ***** ** * *
      .   ****** **** *
      .   ****** **** *
0.037.   ******* **** *
      .   ******* **** *
      .   ******* **** *
      .   ******* **** *
      .   *************
0.031.   *************
      .   *************
      .   *************
      .   *************
      .   *************
0.025.   ****************
      .   ****************
      .   ****************
      .   *****************
      .   ******************
0.018.   ******************
      .   ********************
      .   ************************O
      .   ************************O
      .   ************************O
0.012.   **************************O*
      .   ***************************O*
      .   * ****************************O* *
      .   ****************************O* **
0.006.   *****************************O* ** *
      .   *****************************O*** *
      .   * *****************************O**** **   *
      .   *** ** *******************************O******** *** *   *
      .   * * ***O*************** * **
....[M/S]
         :   :   :   :   :   M :   : F   :   :   :   :   :
      -2.190 -1.825 -1.460 -1.095 -0.730 -0.365 0.000 0.365 0.730 1.095 1.460 1.825
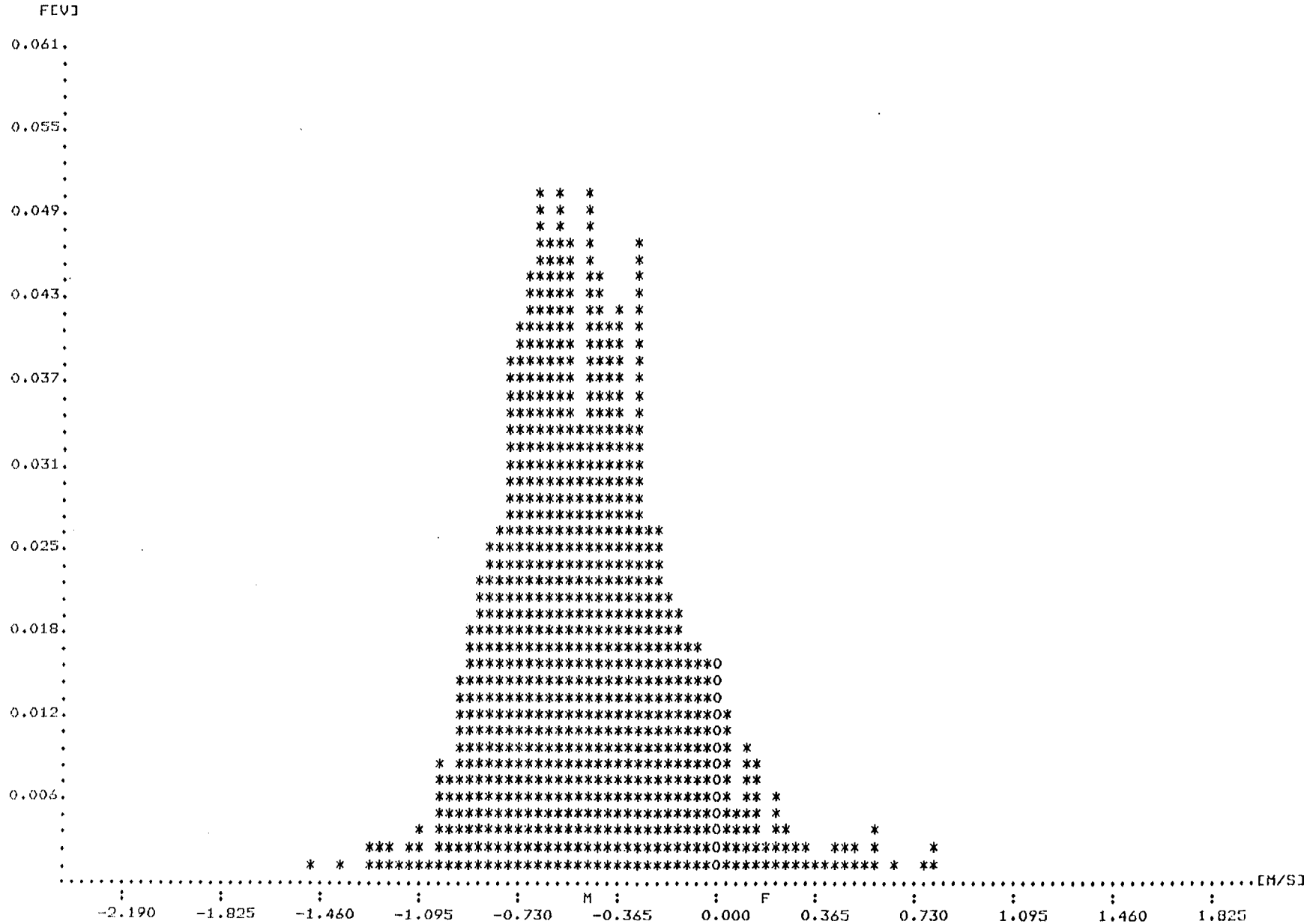
Fig. 6.4.4-4   Velocity histogram of sand particles for d_p = 0.40 mm, $\widetilde{U}_f$ = 0.195 m/s, X = Y = 0, Z' = 50 mm
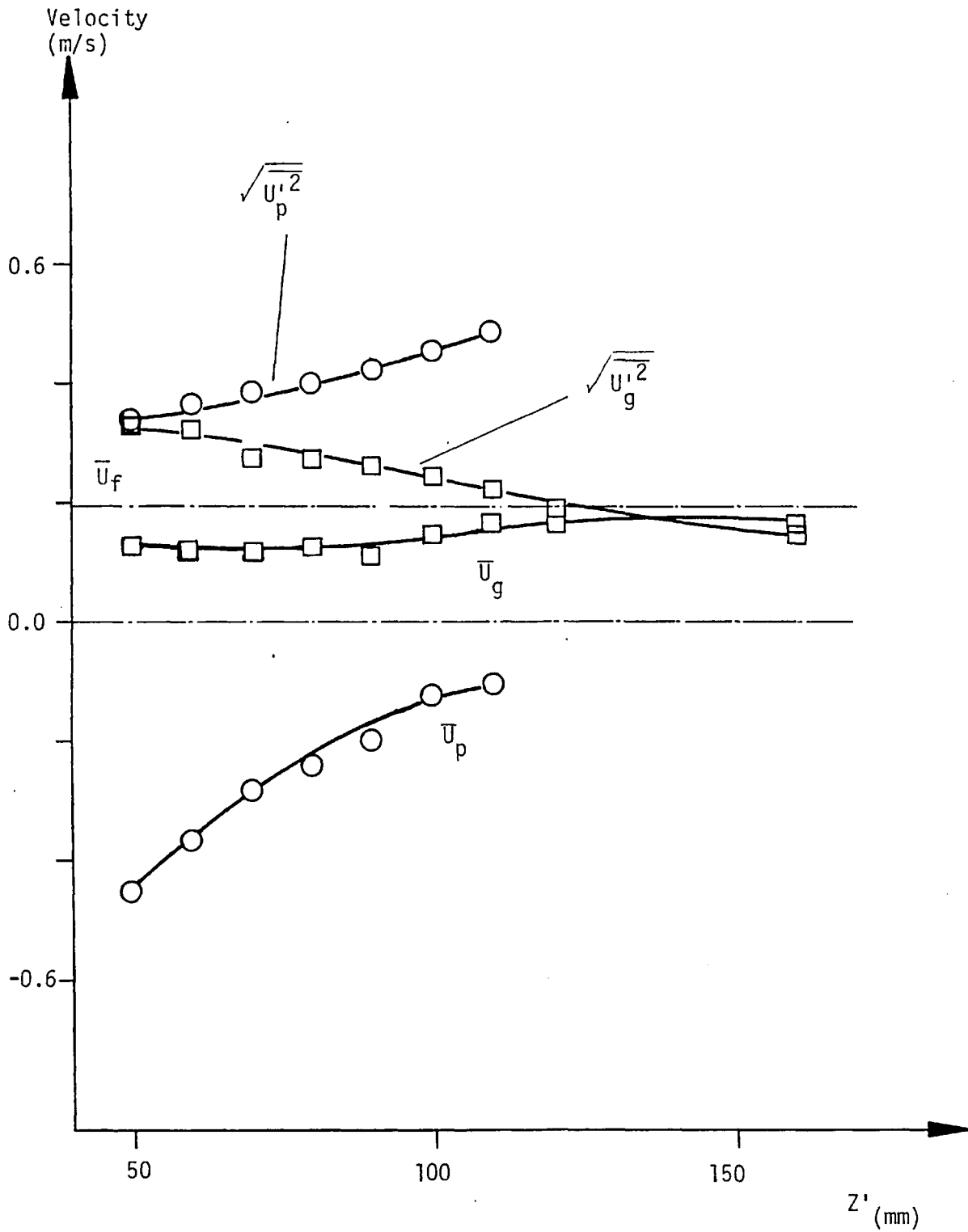   (experiment group B1, see Table 6.4.1-1)

Fig. 6.4.4-5 Variation of gas and sand mean and r.m.s. velocities
with bed height for d_p = 0.40 mm, X = Y = 0 and $\overline{U}_f$ =
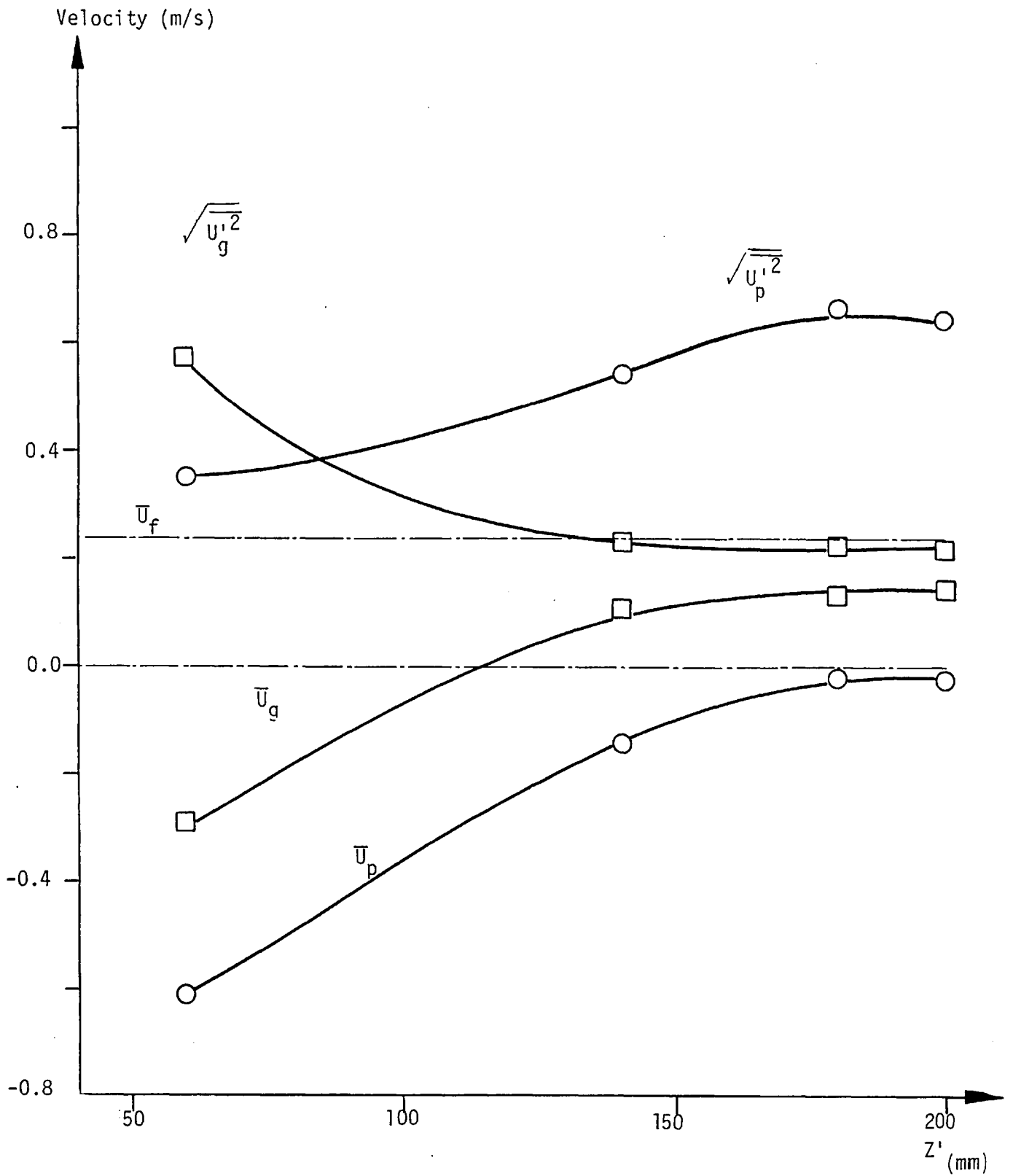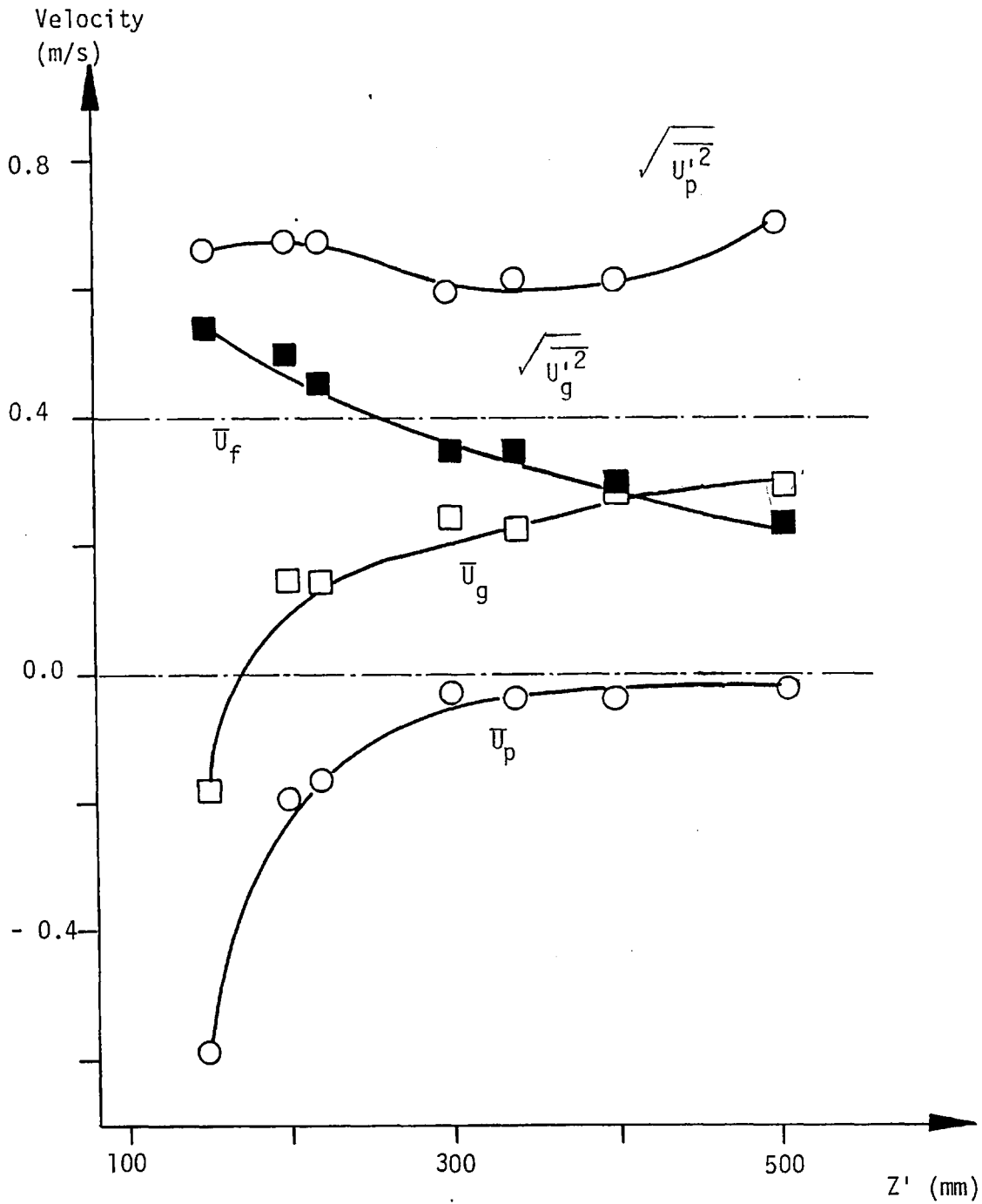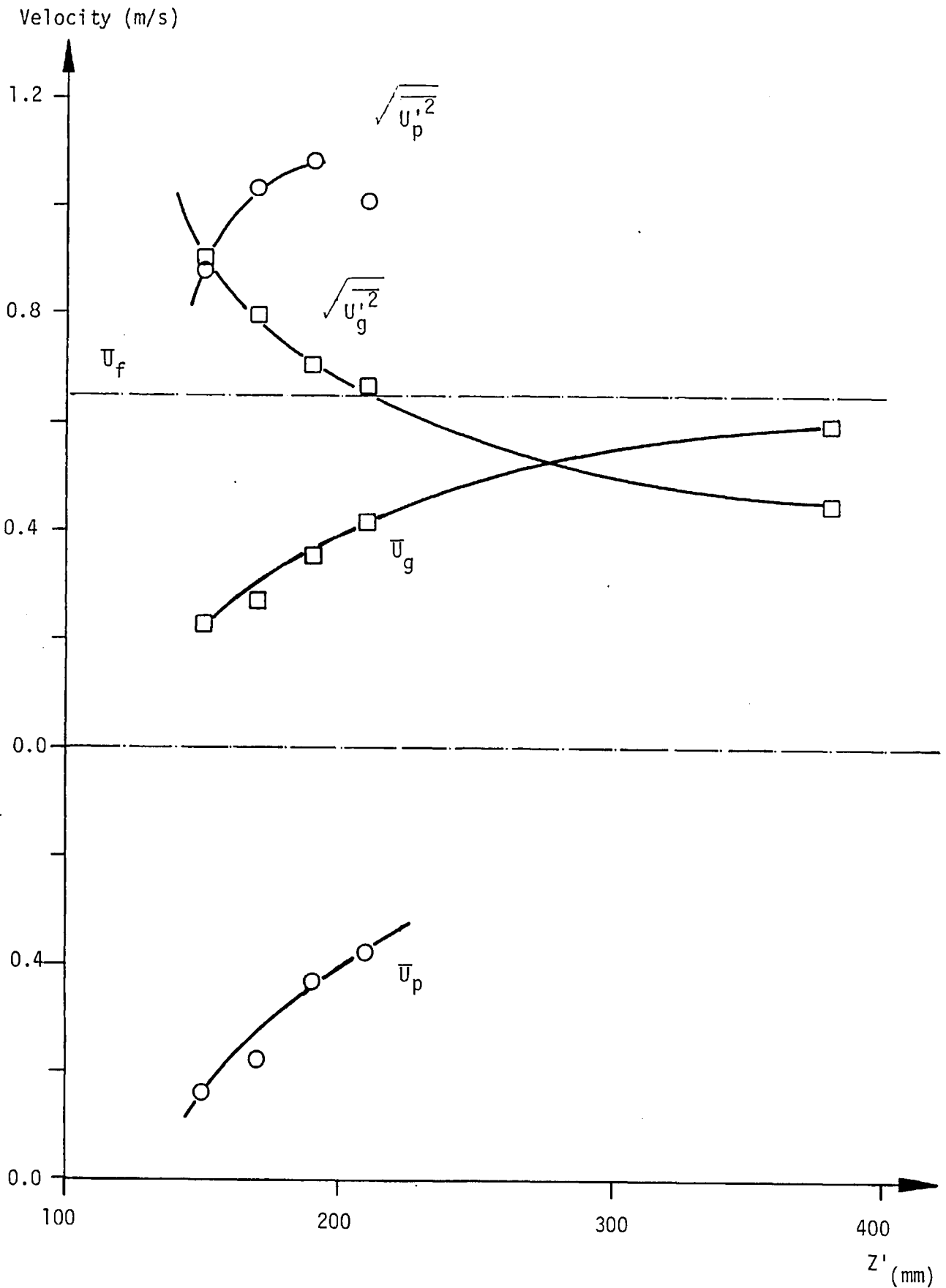0.195 m/s (experiment group B1, see Table 6.4.1-1)
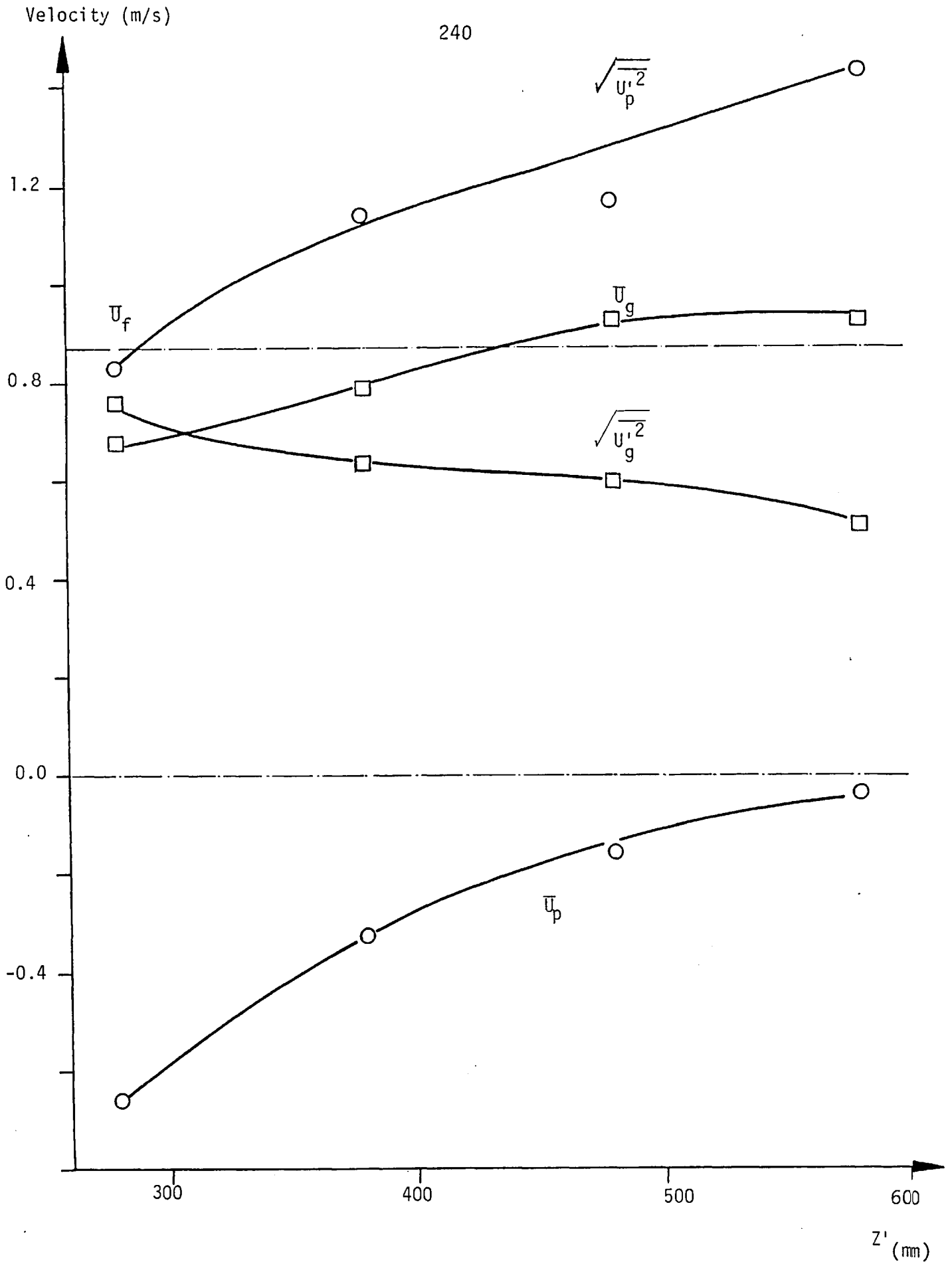
Fig. 6.4.4-6   Variation of gas and sand mean and r.m.s. velocities
with bed height for d_p = 0.40 mm, X = Y = 0 and $\overline{U}_f$ =
0.235 m/s (experiment group B2, see Table 6.4.1-1)

Fig. 6.4.4-7 Variation of gas and sand mean and r.m.s. velocities with bed height for d_p = 0.40 mm, X = Y = 0 and $\overline{U}_f$ = 0.40 m/s (experiment group B3, see Table 6.4.1-1)

Fig. 6.4.4-8 Variation of gas and sand mean and r.m.s. velocities
with bed height for d_p = 1.00 mm, X = Y = 0 and $\overline{U}_f$ =
0.65 m/s (experiment group A1, see Table 6.4.1-1)

Fig. 6.4.4-9 Variation of gas and sand mean and r.m.s. velocities with bed height for $d_p = 1.00$ mm, $X = Y = 0$ and $\overline{U}_f = 0.875$ m/s (experiment group A2, see Table 6.4.1-1)
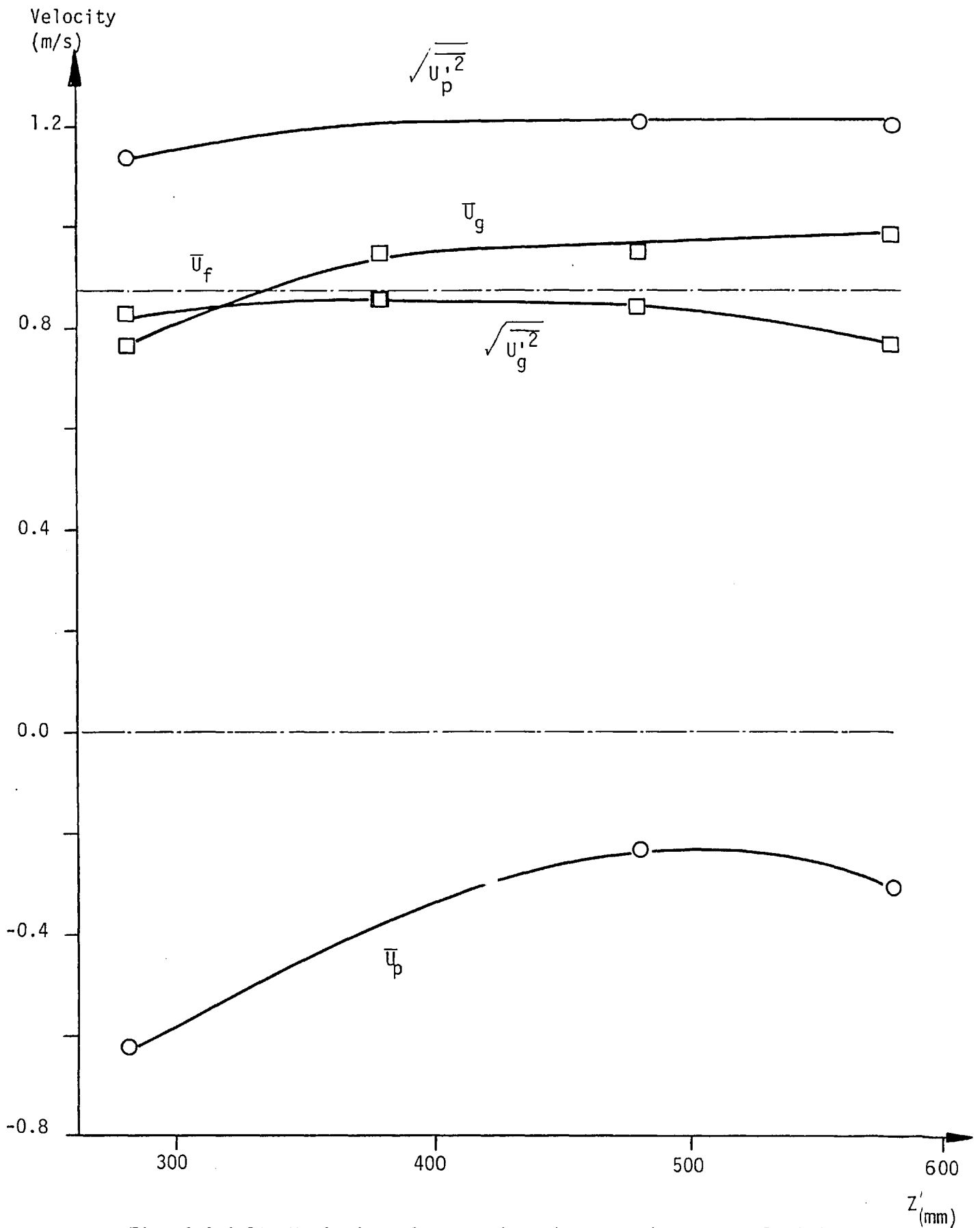
Fig. 6.4.4-10 Variation of gas and sand mean and r.m.s. velocities
with bed height for d_p = 1.00 mm, X = 295 mm, Y = 0
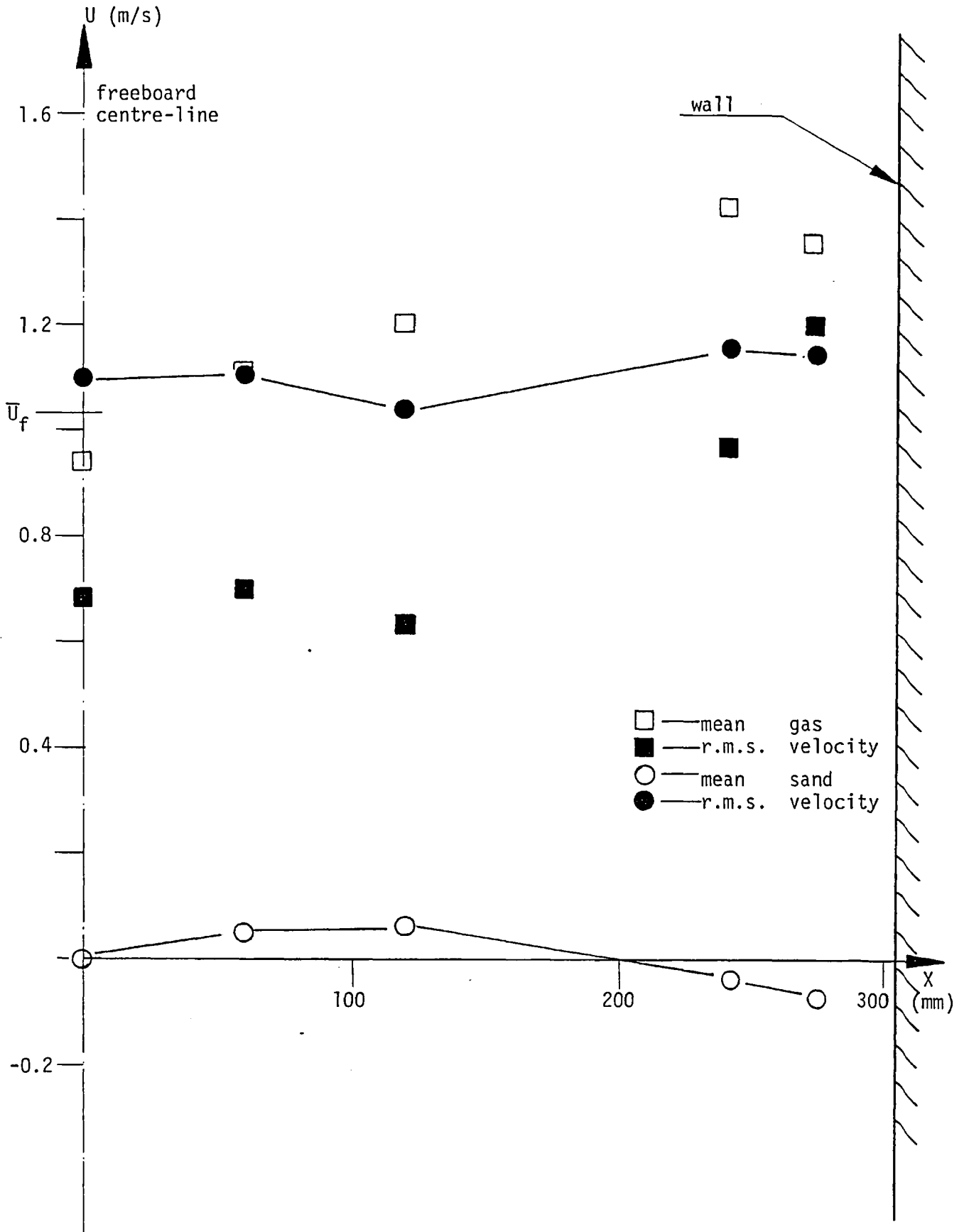and $\overline{U}_f$ = 0.875 m/s (experiment group A2, see Table
6.4.1-1)

Fig. 6.4.4-11 Variation of gas and sand mean and r.m.s. velocities
across a horizontal plane for d_p = 1.00 mm, Y = 0,
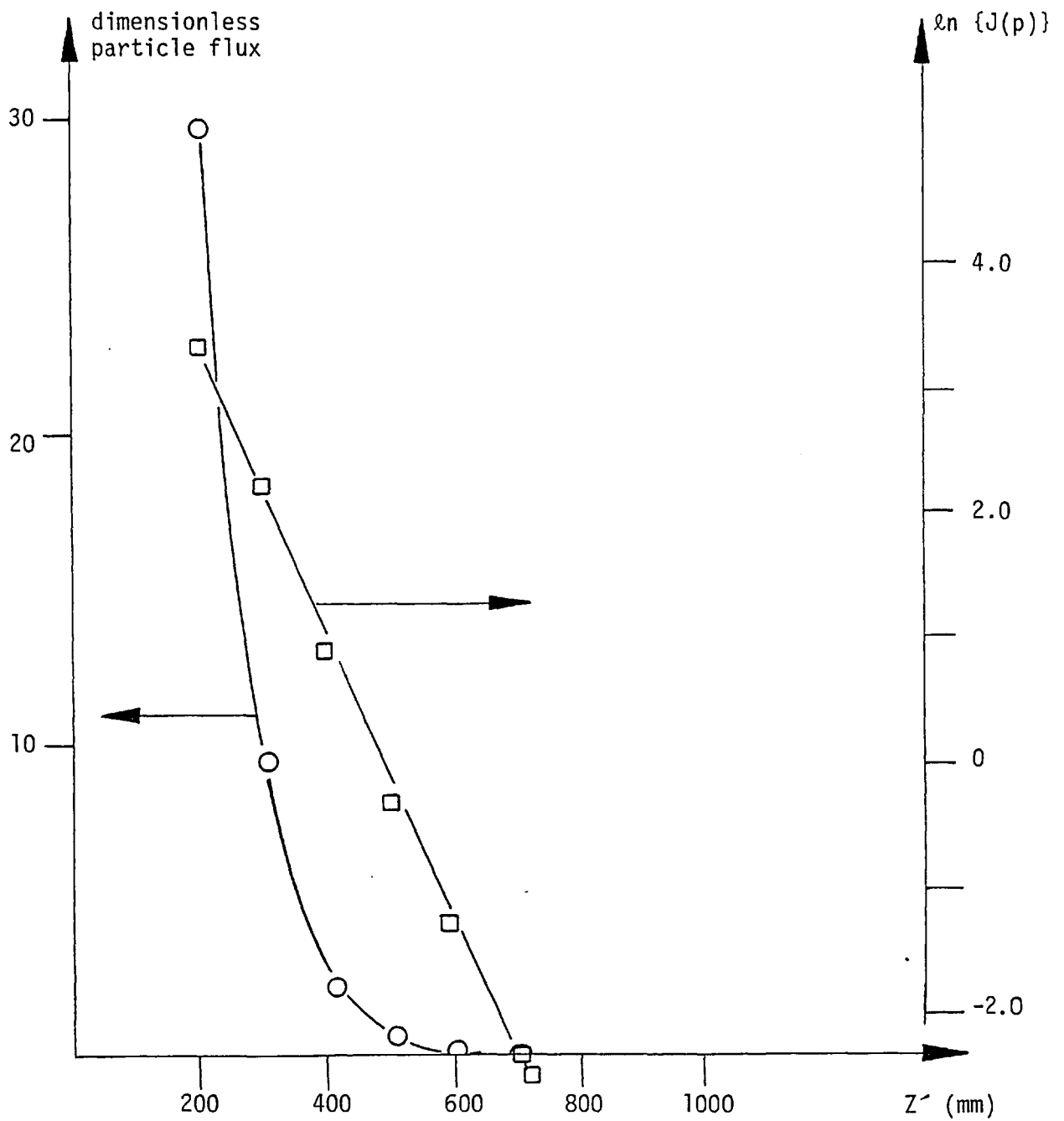Z' = 400 mm, U_f = 1.03 m/s (experiment group HA1,
see Table 6.4.1-1)

Fig. 6.4.4-12 Variation of dimensionless particle flux with freeboard
height for d_p = 0.40 mm, X = Y = 0, U_f = 0.40 m/s
(experiment group HB1, see Table 6.4.1-1)